The Henryk Niewodniczański
INSTITUTE OF NUCLEAR PHYSICS
Polish Academy of Sciences
ul. Radzikowskiego, 31-342 Kraków, Poland

www.ifj.edu.pl/publ/reports/2009/

Kraków, May 2009

Report No. 2027/PL

Study of light exotic and stable nuclei with heavy ion reactions

Stanisław Kliczewski

Habilitation Thesis

CONTENTS

CHAPTER 1

INTRODUCTION

1.1. The main goals of the work.

Nuclear reactions with light and heavy ion beams are one of the most important methods for the investigation of nuclear structure, main features of the nuclear forces and mechanisms of the nuclear processes. At present the most information in these fields is available for the nuclei close to the stability region. The structure and interactions of the nuclei out of this region (*exotic nuclei*) are insufficiently studied yet. There are two experimental methods to perform such investigations: the first one employs experiments with the radioactive (secondary) beams (*direct method*) and the second one is based on experiments with the stable ion beams producing multi-nucleon-transfer reactions. Both methods are used at present and successfully complement one another.

The direct-secondary-beam methods use equipments which produce and form the secondary beams, sometimes with the secondary beam accelerators and storage rings. These equipments are sophisticated and rather expensive. At present, the obtained experimental data are very important but rather poor. The secondary beams have rather small intensities and therefore only elastic and inelastic scattering are studied using this method. The potential parameters of the unstable exotic nuclei interaction and their deformation parameters can be obtained in these experiments. The deformation parameters can only be obtained from the inelastic scattering data from experiments with radioactive nuclei. The next limitation of the exotic nuclei study using the direct method is the fact, that they are possible only for the radioactive ions living longer than several microseconds. More information about the study of exotic nuclei with the method of direct experiments are placed in Section 1.2.

The development of the nuclear reaction theory and of the computational methods give possibilities of wide use of the second method - the stable ion beam experiments with the nucleon-transfer and cluster-transfer reactions. It should be noticed, that investigation of the exotic nuclei interactions, presented in this work, needs of simultaneous investigation of stable nuclei, taking part in the same reactions.

Theoretical analysis of the data, concerning the study of exotic nuclei with heavy-ion reactions is more complex than the investigations using the direct method. The data of elastic and inelastic scattering of radioactive ions are analyzed with the optical model (OM) and coupled-reaction-channels method (CRC) using the nucleus-nucleus potentials of the same systems both in entrance and exit channels On the other hand, the incoming and outgoing reaction systems are different for the transfer reactions. Before the CRC-calculation of the reaction cross section, the potential parameters for the entrance-reaction channel must be deduced from the analysis of the elastic and inelastic scattering data. Moreover, because the parameters of the nucleus-nucleus potentials are energy dependent, studies of the energy dependence of these parameters play important role in investigation of the nuclear reaction of exotic nuclei. For this reason, studies of the elastic and inelastic scattering, based on optical potential parameters and their energy dependence are included in the present work in Chapter 4.

The next problem concerning the transfer reaction studies is connected with the calculations of the nucleon and cluster spectroscopic amplitudes (SA). These calculations for nucleons and clusters can be performed in the frame of Translationary Invariant Shell Model (TISM) using the method described in [91] for the 1s-1p-shell nuclei which includes the light stable and exotic nuclei only. Therefore, the reactions investigated in the present work include only the nuclear processes for the interactions of 1p-shell nuclei. The large base of the TISM cluster SA was calculated and successfully applied in the present reaction studies. Due to their importance for nuclear structure and reaction mechanism studies, the tables of calculated SA are presented in the Appendix.

The present work includes the results obtained by the author and collaborators, presented in Refs. [1-20]. In the CRC-method all possible reaction channels: elastic and inelastic scattering as well as one-step and multi-step transfers of nucleons and clusters are strongly coupled. Then, calculation of optical potential parameters requires determination of contribution of all possible processes to considered reaction. For this reason every investigated reactions are described as separate Sections of Chapters 4 and 5.

This work is devoted to the investigation of the exotic nuclei by nuclear reactions using stable ion beams. This is a traditional method for study of structure of nuclei. These experiments can be performed by many nuclear groups which use the standard experimental equipments. Moreover, a large experimental database, obtained from these experiments already exists. Next, properties of the short living exotic nuclei as well as mechanism of their production can also be studied with nuclear reactions.

The study of the reaction mechanism are very important for deduction of the structure properties of exotic nuclei and of the potential parameters of their interactions. When dominant mechanism of the reaction is found, these parameters are fitted in order to describe the reaction data by the CRC-cross-section. The results of the reaction studies are presented in Chapter 5. Summary and conclusions are presented at the end of the work.

1.2. Present status of exotic nuclei studies.

The term “exotic nuclei” is widely used to name the neutron-rich and proton-rich nuclei, as well as such an unbound nuclei like ^{8}Be. The light nuclei such as $^{5\text{-}8}$He, $^{5,\,8\text{-}11}$Li, $^{7,\,10\text{-}14}$Be etc. are considered as the exotic nuclei, due to their properties different from those of the stable nuclei. The main problems concerning the light exotic nuclei are presented in details in Ref. [21, 23]. The short review of recent main experimental and theoretical problems for light exotic nuclei is presented below.

1.2.1. Masses, energy levels and quantum numbers of ground and excited states of nuclei.

Two main methods are used at present in laboratories for producing the light exotic nuclei. The first one is the ISOL (isotope separation on-line) [22] and the second is the in-flight method [24]. Each method has its own application. The advantage of the first method is good quality of the secondary beam. The ISOL method is suitable for measurements of ground-state properties such as mass, spin and moments of light exotic nuclei. The exact information about nuclear masses is necessary for theoretical calculations and for mapping of nuclei on the nuclear mass surface. The good quality of the secondary beam enables the measurements of such properties even for nuclei out to the drip-line. The advantage of the in-flight method is very short time of the separation process. The disadvantage of this method is rather poor quality of the secondary beam. The measurements of the interaction and reaction cross sections of light exotic nuclei can be performed using this method. A great amount of data for the drip-line nuclei is available in Ref. [24]. The elastic proton scattering experiments at intermediate energies in inverse kinematics technique [25], allow to obtain an information about nuclear matter distributions for short-lived nuclei. We should notice that in this technique a radioactive beam is incident on a hydrogen target. The knockout reaction is a source of spectroscopic information about the states of exotic nuclei [26]. It is especially interesting for the unbound nuclear systems close to the drip-lines. The special example of such a system is called Borromean halo nuclei. The term Borromean was introduced to denote a bound three-body system for which no binary subsystem is bound. The above mentioned reactions, knock-out, transfer and stripping as well as scattering in the inverse kinematics [27] are the main tools for investigation of nuclei in the vicinity of the drip-line.

1.2.2. Shell-model, cluster, molecular and halo-structures.

Some of the light nuclei lying on the drip-line form a neutron or a proton halo. It means that they have a mass distribution in the great distance from the core of the nucleus. The drip-lines are the limits on the map of nuclei, where the neutron or proton separation energy is zero. In other words the drip lines are the boundaries for neutron-rich or proton-rich nuclei existence. Generally, two classes of halo states exist. The first one is the two-body halo with one nucleon in vicinity of the core, for example the one-neutron halos of ^{11}Be and ^{19}C and the one-proton halo of ^{8}B. The second one is so-called Borromean three-body halo with the two valence nucleons in vicinity of the core. The halos of the ^{6}He, ^{11}Li and ^{14}Be nuclei are such examples.

The halo structure of the light nuclei is well described in the few-body and cluster models. According of these models the nucleus consists of the core with one or two valence neutrons as the halo. The similar cluster models can describe also other light nuclei properties. The example is well-known $\alpha - \alpha$-structure of the ^{8}Be ground state [28]. It seems that the cluster structures are a more general feature of light nuclei. For the drip-lines the $\alpha - \{n_1 - n_2 - \ldots - n_i\}$ structure can describe many of the observed data. Theoretical works, using the anti-symmetric molecular dynamics approach, also show the molecular-like forms of many light nuclei [29]. Existing of more exotic molecular structures with possible longer α-chains was also considered. The example can be the ^{16}C nucleus with the $\alpha - 2n - \alpha - 2n - \alpha$ structure [30].

1.2.3. Magic numbers for the exotic nuclei.

The magic numbers are the numbers of protons and neutrons in nuclei for which the energy of separation of a nucleon has a maximum. The existing of these numbers was explained by the shell-model. The magic number nuclei are strongly bound. As we know the existence of magic numbers is connected with big energy gaps between groups of single-particle states. The magic numbers can change for nuclei close to the drip-line. Changing of the single-particle potentials for nuclei in the vicinity of the drip-lines gives other spectrum of the single-particle states [31]. Then the values of magic numbers can be changed. For example, vanishing of the $N = 20$ magic number has been observed in the Coulomb excitation of ^{32}Mg [32]. The new $N = 14$ and 16 magic numbers were observed [33].

For the neutron-rich nuclei in the p- and sd-regions the existence of the new neutron magic number $N = 16$ was reported [34]. This magic number appears due to probably the halo formation. The problem of the magic numbers were discussed in terms of the effective single-particle energies in Ref. [35]. Accordingly to this Ref. [35], in the neutron-rich exotic nuclei, the magic numbers $N = 8, 20$ can disappear, while $N = 6, 16$ can arise. A study, concerning the proton- and neutron-rich nuclei, has given the possibilities of existing of several new magic numbers [36].

1.2.4. Beta-decays.

Beta-decay processes of the exotic nuclei in the vicinity of the drip-line can differ for such processes in the stability region. This is very important for the beta-delayed particle emission processes. In nuclei in the vicinity of the drip-line this process dominate decays to bound states [37]. Also the halo-structure can have an influence on the beta-decay processes. Large spatial extension of the halo-state is one of the reason of this effect. Another effects are connected with the large spatial extension of the halo-state. Another effects are connected with the fact, that the halo states can decay independently from the core. This give specific pattern of decay as for ^{6,8}He and ^{9,11}Li [38] nuclei. It can also lead directly into the continuum of states.

The better understanding of the beta-delayed-neutron and multi-neutron emission processes is important for explanation of the abundance of elements in the Universe. This abundances can be concluded from the rapid neutron-capture process (r-process) [39]. The heaviest neutron drip-line nuclei, for which the beta-decays have been studied, are ^{15}B [40], ^{17}B [41], ^{18}C [42] and ^{19}C [43]. The beta-delayed one- and two-neutron emissions were reported for ^{19}B, ^{22}C and ^{23}N [44].

1.2.5. Astrophysical problems.

Nuclear astrophysics is very important to understand the origin and evolution of the Universe [39, 45]. Nuclear reactions are very important in this evolution. A lot of different elements, from light to very heavy ones, can be formed in nuclear reactions. The conditions for nuclear burning depend on the stellar sites in the stars evolution path, which characterize the scenario of burning such as the CNO-cycle. Observation of the abundance of elements gives also the important data for understanding the evolution of the Universe.

The solar abundance of the heavy elements beyond iron suggests at least the two types of scenarios for the heavy-element nucleosynthesis. The first one is the rapid-neutron-capture process (r-process), and the other one is the slow-neutron-capture process (s-process). There are other complications for the heavy-element synthesis such as the p-process which is considered to be responsible for production of the neutron deficient nuclei in the heavy mass region.

The development of nuclear astrophysics have arose when a variety of the radio-isotope beams have become available. The different characteristics of nuclear burning define the scenario of nucleosynthesis [39]. A chain of nuclear reactions leads the nucleosynthesis-flow to the nuclear regions far from the line of stability. The successive capture reactions take place before beta decays at high temperature and high-density. There are several points in stellar evolution pathway having enough high-temperature and high-density conditions, for involving unstable nuclei. There are a few important astrophysical problems. They include the mechanisms of ignition and termination processes, which are dependent on the nuclear structure of some specific properties of nuclei. There are some critical reaction steps along the nucleosynthesis pathways. They are called bottleneck and waiting points. When the nucleosynthesis flow reaches the proton drip line, there is no way to go further by the (p, γ)-reaction. Then, the nucleosynthesis flow needs to wait for the beta-decay to find the next (p, γ)-reaction. The same situation can be seen if the (p, γ) cross section is very small, or the reaction *Q*-value is small so that the inverse reaction becomes important. The last beta-decay before the next capture reaction primarily defines the waiting time of flow. This is called the waiting point. The first capture reaction after the waiting point is called the bottleneck.

The method to be used for the nuclear astrophysics experiment changes depending on the types of the radioactive ion beams facility. The Coulomb dissociation methods, developed at intermediate and high energies, can provide in some cases the reverse capture cross sections at low energies. Similarly, the direct particle transfer reactions for the bound states provide the particle capture cross sections of the direct capture process. For transitions to the unbound states the direct particle transfer reactions could also provide, the particle-decay width of the resonance. The masses and half-lives of nuclei far from the line of stability can provide important basic information for very rough estimate the pathway of the explosive nucleosynthesis.

The very interesting concepts of nuclear astrophysics are connected with determination of the astrophysical factor *S,* connecting the energy dependent radioactive capture reactions cross sections $\sigma(E)$, for e.g. ^{7}Be(p, γ)^{8}B reaction, and the Sommerfeld parameter $\eta = Z_P Z_T e^2 / \hbar v$ [46, 47, 48]:

$$\sigma(E) = SE\exp(-2\pi\eta).$$

The term $E\exp(-2\pi\eta)$ accounts for the steep energy dependence of $\sigma(E)$, due to the Coulomb penetration of the *S*-wave.

The overall normalization of the astrophysical *S*-factor for each such reaction can be determined from one quantity: the asymptotic normalization coefficient (ANC) of the overlap function of the bound state wave functions for the initial and final particles [49].

The ANC's can be found in many ways:

From an analysis of the classical elastic scattering nuclear reactions.

By extrapolation of the experimental scattering phase shifts to the bound state pole in the energy plane [50, 51].

From peripheral transfer reactions, whose amplitudes contain the same overlap function as the amplitude of the corresponding astrophysical radioactive capture process [52, 53].

From theoretical calculations.

This problem is shown as an example in papers [47, 48]. The differential cross sections for the reactions ^{9}Be(^{10}B, ^{10}B)^{9}Be and ^{9}Be(^{10}B, ^{9}Be)^{10}B have been measured at the incident energy of 100 MeV. At this energy, the elastic scattering data have been used to determine the optical-model parameters for the ^{9}Be + ^{10}B system. These parameters are then used in distorted-wave Born approximation (DWBA) and in the coupled-channels code CHUCK [54] calculations in order to predict the cross sections of the ^{9}Be(^{10}B, ^{9}Be)^{10}B proton-transfer reaction, populating the ground and low-lying states in ^{10}B. By normalizing the theoretical DWBA proton-transfer cross sections to the experimental ones, the asymptotic normalization coefficients (ANC's), defining the normalization of the tail of the ^{10}B bound state wave functions in the two-particle channel ^{9}Be + p, have been found. The ANC for the virtual decay ^{10}B(g.s.) → ^{9}Be + p will be used in the analysis of the $^{10}B(^7Be, ^8B)^9Be$ reaction to extract the ANC's for $^8B \to ^7Be+p$. These ANC's determine the normalization of the $^7Be(p, \gamma)^8B$ radioactive capture cross section at very low energies, which is important for nuclear astrophysics.

1.2.6. Optical potentials for the nucleus-nucleus interaction of exotic nuclei and their deformation parameters.

These problems are solved by the following two methods: 1) with the elastic and inelastic scattering using the exotic radioactive ion beams (direct method) and 2) with the transfer reactions using the stable-ion beams. (transfer-reaction method). The direct method can be applied for the long-lived (above microsecond) unstable exotic nuclei. Some of the main presently existing facilities of such radioactive beams are listed in Table 1.1.

Table 1.1. Facilities of radioactive beams (ISOL and IN-FLIGHT).

Center	*Accelerator facility*	*Beam ion*	*Energy (*MeV)	*Ref.*
CERN	REX-ISOLDE (ISOL)	Number of elements ~ 70 Number of isotopes ~ 600	0.8 – 2.2 MeV/u	[55]
GANIL in Caen	SPIRAL (ISOL)	Radioactive beams A<80	30 keV/u – 80 MeV/u.	[56]
ORNL in Oak Ridge	HRIBF (ISOL)	Radioactive beams A<136 Isobar-separation system	up to few MeV/u.	[57, 58]
GSI in Darmstadt	FRS (IN-FLIGHT)	Radioactive beams up to uranium	up to 1 GeV/u	[59]
GANIL in Caen	LISE3 (IN-FLIGHT)	Radioactive beams up to uranium	20-50 MeV/u	[60]
RIKEN in Tokyo	RIPS (IN-FLIGHT) RIPF (IN-FLIGHT)	Radioactive beams up to uranium Radioactive beams up to uranium	up to 135 MeV/u up to 350 MeV/u	[61] [62]
NSCL in East Lansing	A1900 (IN-FLIGHT)	Radioactive beams A<110	up to 150 MeV/u	[63]
JINR in Dubna	COMBAS (IN-FLIGHT)	Radioactive beams Z<30	20-50 MeV/u	[64, 65]

Table 1.2. Elastic and inelastic scattering investigations with radioactive beams.

Target	*Beam ion*	*Energy (*MeV)	*Scattering*	*Ref.*
^{10}B	^7Be	84 ± 1.6	elastic	[66, 73]
^7Li	^7Be	9.87 MeV.	elastic	[67]
^{14}N and ^{12}C	^7Be	87 MeV	elastic inelastic	[68, 73]
^{12}C	^8B	95 MeV	elastic inelastic	[68, 73]
p	$^{11}C^{4+}$	90 and 125 MeV,	elastic inelastic	[69]
^{13}C	^{13}N	8.15, 10.0 and 14.75 MeV	elastic	[70]
^{208}Pb	^{17}F	170 MeV	elastic inelastic	[71]
^{58}Ni	^7Li,	42 MeV	elastic	[72]

The direct study of the elastic and inelastic scattering with the radioactive beams provides possibility to deduce the optical potential parameters for the interaction of exotic nuclei and their deformation parameters in the usual way by analyzing the data employing the CRC method. Some examples of such investigations are listed in Table 1.2.

The main problems of the exotic nuclei studies with the transfer reactions are presented in the next Section.

1.3. Study of exotic nuclei with transfer reactions.

The transfer reactions *T(P, X)Y* at the stable *P*-ion beams can also be effectively used for the exotic nuclei $X + Y$ studies. Especially, if the neutron-rich ion beams and the neutron-rich targets *T* are applied. For that, the following conditions should be fulfilled:

1) the reaction data must be analyzed using a theoretical model which takes into account the strong-channel couplings and the finite-range interaction that are very important for the light-nuclei reactions. At present, the coupled-reaction-channels (CRC) method [77] can be used for this purpose;

2) the potential parameters for the entrance channel $T + P$ must be carefully studied using the $T + P$ elastic and inelastic scattering data at different energies, because the study of energy dependence of the potential parameters leads to minimization of the parameter uncertainties;

3) the dominant mechanism of the reaction must be found using the well-tested spectroscopic amplitudes of the transferred clusters in CRC-calculations.

If the conditions presented above are fulfilled, one can deduce the potential parameters for the outgoing system $X + Y$ by fitting the CRC angular distribution to the *T(P, X)Y* reaction data. In such a way, it is possible to obtain the nucleus-nucleus potential parameters for the exotic nuclei having a finite life-time. From the analysis of the reaction mechanism, one can obtain also information about the dominant cluster structure of the nuclei at the entrance and exit channels.

As one can conclude, the effective application of the nuclear reactions induced by the stable-ion beams to study the structure of exotic nuclei demands a huge base of the experimental data including the transfer reactions and also the elastic and inelastic scattering at different energies, as well as a careful theoretical analysis of the data within the CRC method. The cluster spectroscopic amplitudes (SA) play very important role in this theoretical analysis. Taking into account these circumstances, we include the experimental and theoretical investigations of many nuclear processes and a set of the SA calculations in the present work. The SA's were tested in the analysis of many reaction data.

The most important information about these theoretical calculations are presented in Chapter 2.

CHAPTER 2

THEORETICAL MODELS OF NUCLEAR PROCESSES

2.1. Optical model for heavy-ion scattering.

The general theory of direct nuclear reactions is presented in [77, 78, 79, 80]. The interaction of the $T + P$ nuclei is a result of interplay of the nucleons belonging to two different nuclei. The summary strength of these nucleon-nucleon interactions is characterized with the Coulomb potential $V_C(\boldsymbol{r})$ and the nuclear potential $U(\boldsymbol{r})$. They are dependent on distance $\boldsymbol{r}$ from their mass centre (CM). The relative motion of the $T + P$ nuclei is described by the wave function $\Psi(\boldsymbol{r})$, which is a solution of the Schrödinger equation

$$\boldsymbol{H}\Psi(\boldsymbol{r}) = E\Psi(\boldsymbol{r}), \tag{2.1}$$

where the Hamilton operator is given as

$$\boldsymbol{H} = \hat{T}(\boldsymbol{r}) + V_C(\boldsymbol{r}) + U(\boldsymbol{r}). \tag{2.2}$$

$\hat{T}(\boldsymbol{r})$ is the kinetic energy operator; E denotes the kinetic energy of the projectile P in the CM system:

$$E = \frac{A_T}{A_T + A_P} E_P, \tag{2.3}$$

where A_T and A_P are the masses of target T and projectile P, respectively; E_P is the kinetic energy of projectile P in LAB system.

For the central potentials $V_C(\boldsymbol{r})$ and $U(\boldsymbol{r})$, the Hamiltonian $\boldsymbol{H}$ in a spherical coordinate system (r, θ, φ) is

$$\boldsymbol{H} = \hat{T}(r) + V_C(r) + U(r) = -\frac{\hbar^2}{2\mu}\left[\frac{d^2}{dr^2} + \frac{\boldsymbol{L}^2}{\hbar^2 r^2}\right] + V_C(r) + U(r), \tag{2.4}$$

where $\mu = A_T A_P / (A_T + A_P)$ is reduced mass of nuclei, $\boldsymbol{L}^2$ is operator of squared orbital momentum, eigenfunctions of which are spherical functions $Y_l^m(\theta,\varphi)$

$$\boldsymbol{L}^2 Y_l^m(\theta,\varphi) = \hbar^2 l(l+1) Y_l^m(\theta,\varphi). \tag{2.5}$$

Using following expansion of the wave function $\Psi(\boldsymbol{r})$:

$$\Psi(\boldsymbol{r}) = \sum_{lm} i^l \frac{1}{r} \chi_l(r) Y_l^m(\theta,\varphi), \tag{2.6}$$

one can obtain next equation for the partial radial functions $\chi_l(r)$ (*distorted waves*):

$$\frac{d^2\chi_l(\rho)}{d\rho^2} + \left[1 - \frac{l(l+1)}{\rho^2} - \frac{V_C(\rho)}{E} - \frac{U(\rho)}{E}\right]\chi_l(\rho) = 0, \tag{2.7}$$

where $\rho = kr,\ k = \sqrt{2\mu E/\hbar^2}$ is wave number.

The uniform-charged-sphere potential

$$V_C(r) = \begin{cases} \dfrac{Z_T Z_P e^2}{2R_C}(3 - \dfrac{r^2}{R_C^2}), & r \le R_C, \\ \dfrac{Z_T Z_P e^2}{r}, & r \ge R_C, \end{cases} \tag{2.8}$$

was used for the Coulomb interaction. Here Z_P and Z_T are proton numbers for P and T nuclei, respectively; e is proton charge; R_C is radius of the Coulomb interaction of $T + P$ nuclei:

$$R_C = r_C(A_P^{1/3} + A_T^{1/3}). \tag{2.9}$$

The nuclear optical potential

$$U(r) = Vf(r, R_V, a_V) + iW_S f(r, R_W, a_W) \tag{2.10}$$

of Woods-Saxon type

$$f(r, R_i, a_i) = 1/\left[1 + \exp\left(\frac{r - R_i}{a_i}\right)\right] \tag{2.11}$$

was used in our calculations. In formulae (2.10) and (2.11), the potential radius is

$$R_i = r_i(A_T^{1/3} + A_P^{1/3})\ (i = V, W), \tag{2.12}$$

where V, r_V and a_V are parameters of real part of $U(r)$-potential; W_S, r_W and a_W are parameters of imaginary part of this potential.

The nuclear potential $U(r) \to 0$ at $r \gg R_V$ and solutions of radial equation (2.7) are regular $F_l(\rho)$ and irregular $G_l(\rho)$ Coulomb functions, having at $\rho \to \infty$ following asymptotic forms:

$$\begin{aligned} &F_l(\rho) \to \sin(\rho - \eta \ln(2\rho) - l\pi/2 + \omega_l), \\ &G_l(\rho) \to \cos(\rho - \eta \ln(2\rho) - l\pi/2 + \omega_l), \end{aligned} \tag{2.13}$$

where $\eta = Z_P Z_T e^2/\hbar v$; ω_l is Coulomb phase shift of wave function $\chi_{l.}(\rho)$.

Matching asymptotic numerical solution $\chi_l(R_m)$ of equation (2.7) to combination of Coulomb functions

$$\chi_l(R_m) = N\,[F_l(R_m) + iG_l(R_m)] + S_l[F_l(R_m) - iG_l(R_m)] \tag{2.15}$$

and to their derivatives

$$\chi_l'(R_m) = N\,[F_l'(R_m) + iG_l'(R_m)] + S_l[F_l'(R_m) - iG_l'(R_m)], \tag{2.16}$$

one can calculate scattering matrix elements $S_l = e^{2i\delta_l}$ and partial nuclear phase shifts δ_l, which are used for calculation of elastic scattering cross-section:

$$\frac{d\sigma(\theta)}{d\Omega} = \frac{1}{k^2}\left| f_c(\theta) + \frac{1}{2i}\sum_{l=0}^{\infty} e^{2i\omega_l}(2l+1)(S_l - 1)P_l(\cos\theta)\right|^2, \tag{2.17}$$

where

$$f_C(\theta) = -\frac{\eta \cdot exp\left[-i\eta\, ln\left(sin^2\frac{\theta}{2}\right)\right]}{2\,sin^2\frac{\theta}{2}} \tag{2.18}$$

is Coulomb scattering amplitude.

The cross section of Coulomb scattering is

$$\frac{d\sigma_R(\theta)}{d\Omega} = \left|f_C(\theta)\right|^2 = \left(\frac{\eta}{2k}\right)^2\left(\sin\frac{\theta}{2}\right)^{-4}. \tag{2.19}$$

The description of heavy-ion elastic scattering, using equation (2.7) with Coulomb and complex nuclear potential $U(r)$ of any form and formulas (2.17) – (2.19) for calculation of elastic-scattering cross-section, is a substance of the optical model (OM) of elastic scattering.

The OM-calculations with fitting $U(r)$ potential-parameters $\{X_i\} = \{V, r_V, a_V, W_S, r_W, a_W\}$ were carried out with the code SPI-GENOA [81]. The fitting procedure based on χ^2-minimization:

$$\chi^2 = \frac{1}{N}\sum_{i=1}^{N}\left|\frac{\sigma_{theor.}(\theta_i) - \sigma_{exp.}(\theta_i)}{\Delta\sigma_{exp.}(\theta_i)}\right|^2, \tag{2.20}$$

where $\sigma_{theor.}(\theta_i)$, $\sigma_{exp.}(\theta_i)$ and $\Delta\sigma_{exp.}(\theta_i)$ are theoretical and experimental cross-sections and data errors, respectively; N is number of experimental points.

It is well known that χ^2-criterion does not guarantee an unambiguous determination of optical potential parameters due to correlations between them of types

$$V\exp\left(\frac{R_V}{a_V}\right) = const.,\quad W_S\exp\left(\frac{R_W}{a_W}\right) = const.. \tag{2.21}$$

For this reason, to deduce realistic potential parameters, one must use realistic limitations on parameter values. Therefore, some parameters were limited also in the present work.

First limitation concerns of the parameter V. Number of nucleons responsible for interaction of colliding nuclei can range from one to min(A_P, A_T), depending on projectile energy and repulsive barrier. Therefore, the parameter V is limited by the following condition:

$$V_{NA} \le V \le V_{NA}\cdot\min\{A_P, A_T\}, \tag{2.22}$$

where $V_{NA} \approx 50$ MeV is a depth of nucleon-nucleus potential.

Second limitation is connected with the relation between parameters V and W_S. Since the elastic scattering dominates in collision of nuclei, then we have

$$W_S \le V. \tag{2.23}$$

Taking into account the Pauli principle, one can use the following compound-nucleus radius

$$R_{comp} = r_0(A_P + A_T)^{1/3}, \tag{2.25}$$

as the lower limit for the parameter R_V :

$$R_{comp} \le R_V = r_V\,(A_P^{1/3} + A_T^{1/3})\,. \tag{2.26}$$

Therefore,

$$r_V \ge \frac{r_0\,(A_P + A_T)^{1/3}}{A_P^{1/3} + A_T^{1/3}}\,. \tag{2.27}$$

The optical nucleus-nucleus potentials $U(r)$ with parameters obtained by fitting elastic-scattering data, were used in the coupled-reaction-channels (CRC) calculations.

2.2. Distorted Wave Born Approximation and Coupled Reaction Channels methods.

According to common theory of *Distorted Wave Born Approximation* (DWBA) the probability of *T(P, X)Y inelastic process* is described by the matrix element

$$\begin{aligned}
\boldsymbol{T_{(P,X)}} &= \int \psi^{*}_{X+Y}(\boldsymbol{r_{XY}})\varphi^{*}_{X}(\xi_X)\varphi^{*}_{Y}(\xi_Y)\left|\boldsymbol{V}\right|\varphi_P(\xi_P)\varphi_T(\xi_T)\psi_{P+T}(\boldsymbol{r_{PT}})\prod d\boldsymbol{r}_{j=\boldsymbol{PT},\,\boldsymbol{XY}}\,d\xi_{i=P,T,X,Y} \equiv \\
&\equiv< \psi_{X+Y}(\boldsymbol{r_{XY}})\varphi_X(\xi_X)\varphi_Y(\xi_Y)\left|\boldsymbol{V}(\boldsymbol{r}_X,\boldsymbol{r_P})\right|\varphi_P(\xi_P)\varphi_T(\xi_T)\psi_{P+T}(\boldsymbol{r_{PT}})>= \\
&=< \psi_{X+Y}(\boldsymbol{r_{XY}})\left|V_{\alpha;\alpha'}(\boldsymbol{r}_X,\boldsymbol{r_P})\right|\psi_{P+T}(\boldsymbol{r_{PT}})>,
\end{aligned} \tag{2.28}$$

where $\Psi_{P+T}(\boldsymbol{r}_{PT})$ and $\Psi_{X+Y}(\boldsymbol{r}_{XY})$ are wave functions (*distorted waves)* of (2.6) type, which describe movements in $P + T$ and $X + Y$ nuclear systems within potential fields $U_{P+T}(r_{PT}) + V_{C(P+T)}(r_{PT})$ and $U_{X+Y}(r_{XY}) + V_{C(X+Y)}(r_{XY})$, respectively;

$\varphi_T(\xi_T)$, $\varphi_P(\xi_P)$, $\varphi_X(\xi_X)$, $\varphi_Y(\xi_Y)$ are wave functions for internal states of *T*, *P, X, Y,* respectively;

$\boldsymbol{V}(\boldsymbol{r}_X,\boldsymbol{r_P})$ is an operator of inelastic process;

$V_{\alpha;\alpha'}$ denotes a matrix element of $\boldsymbol{V}(\boldsymbol{r}_X,\boldsymbol{r_P})$ operator:

$$V_{\alpha;\alpha'}(\boldsymbol{r_P},\boldsymbol{r_X}) =< \varphi_X(\xi_X)\varphi_Y(\xi_Y)\left|\boldsymbol{V}(\boldsymbol{r}_X,\boldsymbol{r_P})\right|\varphi_P(\xi_P)\varphi_T(\xi_T)>. \tag{2.29}$$

For simplicity, in (2.29) we omit the factors dependent on the nuclear spins and their projections.

Using $\boldsymbol{T}_{(P,X)}$-matrices, one can calculate the *T(P, X)Y* reaction cross section:

$$\frac{d\sigma_{(P,X)}(\theta)}{d\Omega} = \frac{1}{E_P E_X}\frac{k_X}{k_P}\frac{1}{(2J_T+1)(2J_P+1)}\sum_{M_T M_P M_X M_Y}\left|T_{(P,X)}(\theta)\right|^2, \tag{2.30}$$

where J_T, J_P, J_X, J_Y and M_T, M_P, M_X, M_Y are spins and their projections of *T*, *P, X, Y* nuclei, respectively.

In calculation of $\boldsymbol{T}_{(P,X)}$ matrix, the expansions of type (2.6) are used for the $\Psi_{P+T}(\boldsymbol{r}_{PT})$ and $\Psi_{X+Y}(\boldsymbol{r}_{XY})$ wave functions. Then the partial distorted waves $\chi_{l(P+T)}(r_{PT})$ and $\chi_{l(X+Y)}(r_{XY})$ are calculated as the solutions of Schrödinger equations (2.7).

The $\boldsymbol{T}_{(P,X)}$ calculation with exact account of relation between vectors $\boldsymbol{r}_{PT}$ and $\boldsymbol{r}_{XY}$ is named *finite-range* approximation [82]. If the relation $\boldsymbol{r}_{PT} = \boldsymbol{r}_{XY} = \boldsymbol{r}$ is assumed then such $\boldsymbol{T}_{(P,X)}$ calculation is called *zero-range* approximation. The zero-range approximation can be used for the elastic and inelastic scattering but it is not useful for transfer reactions. As rule, for transfer reaction calculations, the exact finite-range approximation is used.

The DWBA calculations, in which only one mechanism of *T(P, X)Y* reaction is taken into account, are called by *one-channel DWBA approximations*. Only in some cases such approximation is acceptable. As rule, in heavy-ion reactions, the strong coupled-channels effects take place. Therefore, applying the *Coupled Reaction Channels* (CRC) [74, 83, 84] for the experimental data analysis of heavy ion reactions is important. In the CRC method, for calculation of distorted waves $\chi_\alpha(r_k)$ for k channels, the following system of coupled equations [74] are solved

$$\begin{aligned}&[E_k - \widehat{T}_{kL}(r_k) - V_{Ck}(r_k) - U_k(r_k)]\chi_\alpha(r_k) = \\ &= \sum_{\alpha',\lambda>0} i^{L'-L} V^{\lambda}_{\alpha;\alpha'}(r_k)\chi_{\alpha'}(r_k) + \sum_{\alpha',k'\neq k} i^{L'-L} \int_0^{R_m} V_{\alpha;\alpha'}(r_k, r_{k'})\chi_{\alpha'}(r_k)dr_{k'},\end{aligned} \tag{2.31}$$

where the indeces α and α' denote the sets of quantum numbers for channels k and k', respectively;

$\widehat{T}_{kL}(r_k)$ –kinetic energy operator for the k-channel;

$U_k(r_k)$ and $V_{Ck}(r_k)$ –nuclear and Coulomb potentials for the k-channel;

E_k – kinetic energy of the k-channel;

$V^{\lambda}_{\alpha;\alpha'}(r_k)$ - matrix element (operator) for transitions to discrete states of nuclei with λ-multipolarity (λ is transfered orbital momentum);

$V_{\alpha;\alpha'}(r_k, r_{k'})$ - matrix element (operator) for transfer reactions;

L and L' – orbital momenta of k- and k'- channels.

These matrix-elements are described in next Sections.

2.2.1. Inelastic scattering of ions

In inelastic scattering, projectile and target nuclei do not change their proton and neutron numbers. Only some part of projectile kinetic energy is distributed into an *excitation* of colliding nuclei. There are *collective* and *particle* excitations of nuclei. All or most nucleons of nucleus take part in its *collective* excitation, whereas only single nucleon or few nucleons generating cluster (particle), take part in a *particle* excitation.

Collision of *deformed* nuclei can cause their *rotation* or surface *vibration* [85, 86], e.g.. they can go to the *rotational* or *vibration excited* states. Lower energy excitations of deformed nuclei have such a nature.

The shape of center-symmetric deformed nuclei can be described with the form:

$$R(\boldsymbol{r}) = R_0(r) + \Delta\boldsymbol{R}(\theta) = R_0(r) + \sum_{\lambda\neq 0}\delta_\lambda Y^0_\lambda(\theta), \tag{2.32}$$

where δ_λ is a *length* (*parameter*) *of nuclear deformation* of λ-multipolarity. Using this expansion, the $V^{\lambda}_{\alpha;\alpha'}(r_k)$ matrix element of equation (2.31) for the transitions to the rotational and vibration excited states of deformed nuclei with transfer of orbital momentum λ which can be calculated with the formula [74]

$$V^{\lambda}_{\alpha;\alpha'}(r_k) =< \alpha' \,|\, V_{\lambda}(r_k) Y^{0}_{\lambda}(\theta) \,|\, \alpha >, \qquad (2.33)$$

where

$$V_{\lambda}(r_k) = -\frac{\delta_{\lambda}}{\sqrt{4\pi}} \frac{\mathrm{d}U(r_k)}{\mathrm{d}r_k}, \qquad (2.34)$$

$U(r_k)$ is optical potential in the *k*-channel. For the *vibration* excitations, in (2.34), the δ_λ-parameter represents the vibration amplitude.

Two kinds of rotational transitions can be included into coupled channel scheme in the CRC-calculations. There are rotational transitions $< E^{*}_{ex}, J^{\pi}_{ex} \,|\, V_{\lambda}(r_k) \,|\, E, J^{\pi} >$ with changes of energy of internal state of nuclei, and the quadrupole rotational transitions without energy changes:

$$V^{\lambda=2}_{J^{\pi};J^{\pi}}(r_k) =< E, J^{\pi} \,|\, V_{2}(r_k) \,|\, E, J^{\pi} >. \qquad (2.35)$$

These transitions are called as *reorientations* of nuclei [87]. They are possible for deformed nuclei with spin larger than 1/2. The CRC-analysis of elastic scattering data showed that the *reorientation* processes are important for the scattering of deformed nuclei at large angles.

As it was mentioned above, the nucleus can be excited also by transferring kinetic energy to one or group of nucleons (cluster or particle). These excitations are called the *particle excitations*. In this case, the nucleus A is considered as the system $A = C + x$, where x denotes nucleon or cluster (particle) and C is the core of the nucleus. Then the interaction operator $\boldsymbol{V_\lambda(r)}$ has the form [74]:

$$V(\mathbf{r}) = V_{cc}(\mathbf{r}_c) + V_x(\mathbf{r}') - U(\mathbf{r}), \qquad (2.36)$$

where $V_{cc}(\mathbf{r}_c)$ and $V_x(\mathbf{r}')$ are the potentials of interaction of the partner-nucleus with the core C and with the cluster x in the system $A = C + x$, respectively. The function $U(\mathbf{r})$ denotes the optical potential of interaction of the $T + P$ nuclei.

2.2.2. Transfer reactions

For the $T(P, p)t$ reaction transfer of the cluster x from the system $P = p + x$ to the $t = T + x$ system, the matrix element of the transfer operator has the form:

$$V_{\alpha;\alpha'}(r_k, r_{k'}) = \left\langle \phi_p \phi_t \left| V(r_k, r_{k'}) \right| \phi_P \phi_T \right\rangle, \qquad (2.37)$$

where $\phi_P(\xi)$, $\phi_T(\xi)$, $\phi_p(\xi')$ and $\phi_t(\xi')$ are the wave functions of the internal states of P, T, p, and t nuclei, respectively.

The wave functions $\phi_P(\xi)$, $\phi_t(\xi)$ of the internal states of the $P = p + x$ and $t = T + x$ systems can be presented in following form:

$$\phi_P(\xi) = \sum_x S^P_x \phi_p(\xi) \phi_x(\xi') \varphi_{px}(r_{px}), \qquad (2.38)$$

$$\phi_t(\xi) = \sum_x S^t_x \phi_T(\xi)\phi_x(\xi')\varphi_{Tx}(r_{Tx}) \ , \tag{2.39}$$

where $\phi_x(\xi')$ is the wave function of the internal state of the cluster x transferred in the reaction; $\varphi_{px}(r_{px})$, $\varphi_{Tx}(r_{Tx})$ are the wave functions of the relative motion of x in the systems $P = p + x$ and $t = T + x$ *(wave functions of bound states)*. The values S^P_x, S^t_x are called the *spectroscopic amplitudes* of x in the $P = p + x$ and $t = T + x$ systems, respectively. One can obtain from (2.38) and (2.39) the following formulas for the spectroscopic amplitudes:

$$S^P_x = <\phi_p \phi_x \varphi_{px} | \phi_P>, \tag{2.40}$$

$$S^t_x = <\phi_T \phi_x \varphi_{Tx} | \phi_t>. \tag{2.41}$$

Putting the wave functions (2.38) - (2.39) into (2.37) and taking into account the orthogonality of the wave functions of internal states of the nuclei, one obtains:

$$V_{\alpha;\alpha'}(r_k, r_{k'}) = S^P_x S^t_x \left\langle \varphi_{Tx}(r_{k'}) \middle| V(r_k, r_{k'}) \middle| \varphi_{px}(r_k) \right\rangle, \tag{2.42}$$

where $r_{k'} \equiv r_{Tx}$ and $r_k \equiv r_{px}$.

The *wave functions* $\varphi_{px}(r_k)$, $\varphi_{Tx}(r_{k'})$ of the *bound states* of the nucleons and clusters in the $P = p + x$ and $t = T + x$ systems were calculated, as usual, using the fitting procedure of depths of the real Saxon-Woods potentials $V_{px}(r_k)$ and $V_{Tx}(r_{k'})$ to the experimental values of binding energies of clusters in these systems. In this procedure, the following values of a and r_0 parameters were used:

$$a = 0{,}65 \text{ fm}, \quad r_0 = 1{,}25 A^{1/3} / \left(C^{1/3} + x^{1/3}\right) \text{ fm},$$

where A, C and x are the masses of the nucleus A, core C and cluster x for the $A = C + x$ system.

For CRC calculations of the differential cross sections of nuclear processes the widely spread program FRESCO [74, 76] was used in the present work.

2.3. The spectroscopic amplitudes of nucleons and cluster calculation.

As is visible from the formula (2.35), the *spectroscopic amplitudes* (SA) of the nuclei and clusters should be known for the CRC-calculations. The general theory of the SA calculation of any clusters in nuclei does not exist. Some methods of the SA calculations for some types of clusters and nucleons exist for a limited class of nuclei. In this work, the SA were calculated using the DESNA [88, 89, 90] program. The methods of SA calculations for any clusters and nucleons in the 1p-shell nuclei in the frame of the Translationary Invariant Shell Model (TISM) [91, 92, 93] is used in the DESNA program. For a more detailed explanation of importance of SA in the investigated nuclear reactions and methods of calculations we show the main formulas and algorithms from the DESNA program.

We consider the calculation of SA of the cluster x in the $A = C + x$ system in the frame of the oscillatory TISM. The wave functions Ψ_A, Ψ_C and Ψ_x of the nucleus A, core C and cluster x have the following quantum characteristics respectively:

$$\Psi_A = | AN[f](\lambda\mu)LSTJMM_T >, \tag{2.43}$$

$$\Psi_C = | CN_1 [f_1] (\lambda_1 \mu_1) L_1 S_1 T_1 J_1 M_1 M_{T_1} >, \tag{2.44}$$

$$\Psi_x = | xN_2 [f_2] (\lambda_2 \mu_2) L_2 S_2 T_2 J_2 M_{21} M_{T_2} >, \tag{2.45}$$

where N, N_1, N_2 are the quantum numbers of the oscillatory energy ħω in the corresponding components of the $A = C + x$ system;

$[f]$, $[f_1]$, $[f_2]$ – the Young tableaux, characterizing symmetry of corresponding wave functions of the 1s-1p-shell;

$(\lambda\mu)$, $(\lambda_1\mu_1)$, $(\lambda_2\mu_2)$ – the Elliot symbols, which characterize the wave function symmetry for the nucleons in the 1p-shell; The Elliot symbols have the following relations with the Young tableaux $[f_p] = [f_p^1\ f_p^2\ f_p^3]$ for the nucleons of the 1p-shell: $\lambda = f_p^1 - f_p^2$, $\mu = f_p^2 - f_p^3$;

L, S, T, J, M, M_T are the orbital moments, spin, isospin, total angular momentum, z-projection of the total angular momentum and z-projection of isospin of nucleus; the analogical meanings have the quantum numbers of the wave functions Ψ_C and Ψ_x.

The *spectroscopic amplitude* S_x of cluster x in the $A = C + x$ system is calculated using following method:

$$S_x = \begin{pmatrix} A \\ x \end{pmatrix}^{1/2} \langle \Psi_A | \Psi_C \Psi_x, n\Lambda J_0 \rangle, \tag{2.46}$$

where $\varphi_{Cx} = |n\Lambda J_0>$ is the wave function of the relative motion of the cluster x and core C, characterized by the main quantum number

$$n = N - N_1 - N_2, \tag{2.47}$$

or the main spectroscopic number

$$n_c = (n - \Lambda + 2)/2. \tag{2.48}$$

The orbital Λ and the total J_0 momentum of relative motion are as follows:

$$\Lambda = L - L_1 - L_2, \qquad J_0 = J - J_1, \qquad J_0 = \Lambda + J_2. \tag{2.49}$$

The quantum characteristics of the wave functions, included to SA formula (2.46) are coupled. This relation must be used in a summation of the corresponding vector coefficients [94]:

Clebsch-Gordan - $C^{jm}_{j_1 m_1 j_2 m_2} \equiv (j_1 j_2 m_1 m_2 | jm)$,

Racah - $U(abed;\ cf) = \sqrt{(2c+1)(2f+1)}\, W(abed;\ cf)$ and

Fano (9j-symbols) - $\begin{Bmatrix} a & b & c \\ d & e & f \\ g & h & j \end{Bmatrix}$,

and for direct products of the Young tableaux - $[f] = [f_1] \times [f_2]$ and the Elliot symbols $(\lambda\mu) = (\lambda_1\mu_1) \times (\lambda_2\mu_2)$ - by corresponding coefficients of *SU(3)* and *SU(4)* groups.

The expressions, used for calculations of SA in the DESNA [88, 93, 94] program, have the forms:

$$S_x = Z \sum_{\Im} U(\Lambda L_2 J_0 S_2; \Im J_2) \begin{Bmatrix} L_1 & S_1 & J_1 \\ \Im & S_2 & J_0 \\ L & S & J \end{Bmatrix} \sum_{(\lambda_2'\mu_2')k_2'} D_{(\lambda_2'\mu_2')}(\Im, k_2') G_{(\lambda_2'\mu_2')}(\Im, k_2'), \tag{2.50}$$

where

$$Z=(-1)^{n+\nu_2 N_1}\left(\frac{A}{C}\right)^{n/2}\left(\frac{n!}{n^n}\right)^{1/2}\binom{N}{N_1}^{1/2}\binom{A-N}{\nu_1}^{1/2}\binom{N_2+n}{n}^{1/2}\binom{\nu_2+n}{n}^{1/2}\times$$
$$\times\left(\frac{n_{f_{p1}}n_{f_{p2}}}{n_{f_p}}\right)^{1/2}\Omega_C\Omega_x\sqrt{(2J_1+1)(2J_0+1)(2L+1)(2S+1)}(T_1T_2M_{T_1}M_{T_2}\,|\,TM), \tag{2.51}$$

$$D_{(\lambda_2'\mu_2')}(\Im,k_2')=\left\langle(n0)\Lambda,(\lambda_2\mu_2)k_2L_2\,||\,(\lambda_2'\mu_2')k_2'\Im\right\rangle\times$$
$$\times U([\tilde{\nu}_2],[\tilde{n}],[\tilde{f}_2],[\tilde{f}_{p_2}];[\overline{\nu_2+n}],[\tilde{f}'_{p_2}]), \tag{2.52}$$

$$G_{(\lambda_2'\mu_2')}(\Im,k_2')=\sum_{\varepsilon_1\varepsilon_2}\begin{pmatrix}[\tilde{\nu}_1] & [\tilde{\nu}_2] & [\overline{A-N}]\\ [\tilde{f}_{p_1}] & [\tilde{f}'_{p_2}] & [\tilde{f}_p]\\ [\tilde{f}_1] & [\tilde{f}_2] & [\tilde{f}]\end{pmatrix}_{\varepsilon=\{\varepsilon_1,\varepsilon_2\}}\times$$
$$\times\left\langle(\lambda_1\mu_1)k_1L_1,(\lambda_2'\mu_2')k_2'\Im\,||\,(\lambda\mu)kL\right\rangle_{\varepsilon_1}\times \tag{2.53}$$
$$\times<(st)^A[\tilde{f}]ST\,|\,(st)^{\nu_1+N_1}[\tilde{f}_1]S_1T_1,(st)^{\nu_2+N_2+n}[\tilde{f}_2]S_2T_2>,$$

$$\Omega^2_{A_i}=\sum_{r,[f'_{p_i}]}(-1)^r\binom{\nu_i+r}{r}\binom{A_i-\nu_i}{r}\frac{r!}{A_i^r}\cdot\frac{n_{f'_{p_i}}}{n_{f_{p_i}}}\times$$
$$\times U^2([\tilde{\nu}_i],[\tilde{r}],[\tilde{f}_i],[\tilde{f}'_{p_i}];[\overline{\nu_i+r}],[\tilde{f}_{pi}]),\quad (i=1{,}2;\ \boldsymbol{A_1}=C;\ \boldsymbol{A_2}=x), \tag{2.54}$$

The signs ~ and — over the symbols of Young tableaux show their transposition. For example, in the case of tableau *[f]* = [432] the transposed tableau is $[\tilde{f}]$ = [3321].

The Clebsch-Gordan coefficients with the $(\lambda\mu)$-schemes, which belong to the *SU(3)*-group, are calculated in the DESNA program using the algorithms from the papers [89, 96]. The Racah coefficients and 9*ν*-symbols together with Young tableaux, belonging to the *SU(3)*-group, were calculated using the proper relations with Clebsch-Gordan coefficients of the *SU(3)*-group [89].

For the spin-isospin Clebsch-Gordan coefficients of the *SU(4)*-group, the tabularized data from the papers [93, 97] are used in the DESNA program, because there are no proper methods of their calculation.

The Young tableaux of the 1p-shell nuclei, necessary for the DESNA program calculations, were taken from the Boyarkina tables [98].

The values of the spectroscopic amplitudes S_x and values of the quantum numbers $n = n_c$, $L = \Lambda$ and $J = J_0$ of the wave functions of relative motion of the cluster *x,* core *C* and nucleus $A = C + x$ are presented in the tables in Appendix.

CHAPTER 3

EXPERIMENTAL facilities and METHODS

3.1. Experimental facilities.

The nuclear processes considered in this work, were measured mainly at the Warsaw cyclotron C-200P in Heavy Ion Laboratory at Warsaw University. A part of the results were obtained at the Kiev isochronous cyclotron U-240 in the Institute for Nuclear Research of Ukrainian Academy of Sciences, at the Moscow isochronous cyclotron U-150 in the Russian Research Center "Kurchatov Institute" and at the Tandem/Linac Accelerator in the Florida State University. The light-heavy-ion beams, which were used, and their parameters are listed in Table 3.1. This table contains also the beam energies E_{LAB}, their spreads ΔE_{LAB}, the targets used and their parameters.

Table 3.1. Ion beam and target parameters

Research Center	Accelerator	Ion	E_{LAB} (MeV)	ΔE_{LAB} (%)	Targets			Ref.
					Name	Thickness (μg/cm^2)	Enrichment (%)	
Heavy Ion Laboratory, Warsaw University, Warsaw, Poland	Cyclotron C-200P	^{10}B	51	~ 0.5	^{7}Li	600	92.5	[15]
		^{11}B	49	~ 0.5	^{12}C	200	98.9	[6,11]
		^{11}B	45	~ 0.5	^{9}Be	600	100.0	[8,10,18, 19]
		^{11}B	45	~ 0.5	^{13}C	500	90.0	[9]
		^{11}B	45	~ 0.5	^{14}C	280	86.0	[12]
		^{11}B	44	~ 0.5	^{7}Li	500	92.5	[13]
		^{18}O	114	~ 0.5	^{7}Li	900	92.5	[16]
Institute for Nuclear Research, Kiev, Ukraine	Cyclotron U-240	^{14}N	116	< 1	^{12}C	500	98.9	[1]
		^{12}C	65	~ 0.6	^{9}Be+Ni	300+ 300	100.0+ natural	[3,4,5]
		^{14}N	110	~ 0.5	^{7}Li	500	92.5	[7]
Russian Research Center, Moscow, Russia	Cyclotron U-150	^{6}Li	93	~ 0.7	^{14}C	270	80.0	[2]
		^{7}Li	82	~ 0.7	^{12}C	400	98.9	[14]
Florida State University, USA	Tandem/ Linac	^{7}Li	42	< 0.1	^{16}O+^{6}Li	150 (sum)		[20]

3.2. Experimental setup at the Warsaw cyclotron C-200P.

3.2.1. Scattering chamber and geometry.

The experimental chambers, detectors, electronics and data processing procedures were similar for all these experiments. Therefore, their details are explained for the example of the Warsaw experiments.

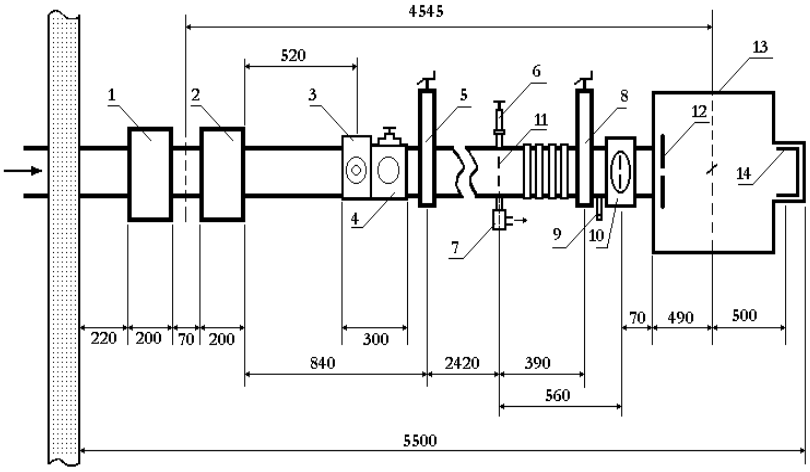

Fig. 3.1. The experimental setup. 1, 2 – quadrupole lenses, 3 – TV camera, 4 – the beam diagnostic system, 5, 8 – valves, 6 – holder for the 1st collimator, 7, 9 valves for venting, 10, 11- defining collimator, 12 – anti-scattering collimator, 13 – scattering chamber, 14 – Faraday cup.

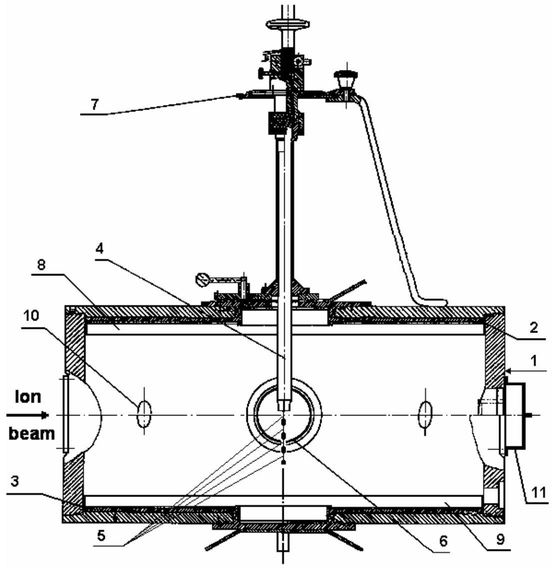

Fig. 3.2. The scattering chamber. 1-body of the reaction chamber, 2, 3 - upper and lower platforms, 4 - rod with the frame with targets, 5 - set of targets, 6 – viewing port, 7 – scale for the adjustment of the target angle, 8,9 – angular scales, 10 – viewing port for control of the vacuum system, 11 - Faraday cup.

The scheme of the Warsaw setup is shown in Fig. 3.1. and the scheme of the scattering chamber [17] is shown in Fig 3.2. The diameter of the chamber is 800 mm and the heigth is 400 mm. Two movable platforms (2,3) are placed inside the chamber. In the center of the chamber, a frame with the targets is fixed on a movable rod (4,5). The platforms with the detectors can be rotated with the accuracy up to 0.6 degrees.

The relative positions of the spectrometers inside the scattering chamber are shown in Fig. 3.3. The ion beam passed through the two defining collimators and through the anti-scattering collimator with the apertures of 10 mm, 2.9 mm and 4.5 mm, placed before the target. The ion beam was stopped in the Faraday cup, connected to a charge integrator. An additional monitoring of the beam was provided by a silicon detector, placed at the angle of 15° with respect to the direction of the ion beam. The three-channel *ΔE-E* spectrometer, with the ionization chamber working as the *ΔE* – detector, was mounted on the lower platform.

This chamber has a shape of the complex of the three parallel-sided prisms 79 mm × 40 mm, in the central line. On the backward side of each ionization chamber, the two silicon E_1 (~ 500 µm) and E_2 (~ 2 mm) detectors, which stopped the reaction products, were mounted. For identification of the products with $Z > 2$, the ΔE-E_1 spectrometers were used and for the products with $Z < 3$, the E_1-$E_2 \equiv \Delta E_2$-E_2 spectrometers were applied. The angular separation between the spectrometers was 9.5°. The distance between the silicon-detectors and the target was approximately 246 mm. On the front side, there are three entrance windows (8) with the diameters of 6 mm each, covered with the 0.5 µm thickness Mylar film, resistant to the pressure of a working gas up to 760 mbar. Each of the entrance windows has the 40-mm long tubular collimator (3) with the rectangular diaphragm 93 mm high and 1.75 mm width). The resolution of approximately 0.3° for measurements of the angular distributions was achieved (this corresponds to the solid angle of 1.5×10^{-4} sr). The scheme of the ionization chamber is shown in Fig. 3.4.

On the upper platform the ΔE-E spectrometer with the silicon ΔE (~ 60 µm) and E (~ 500 µm) detectors was placed.

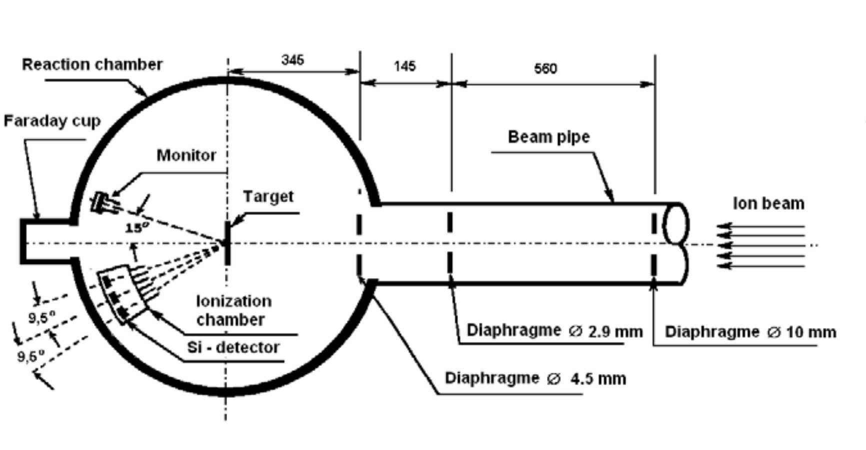

Fig. 3.3. Relative position of spectrometers and collimators inside the reaction chamber.

3.2.2. **Measurements using the spectrometers with ionization chambers.**

Each section of the ionization chamber has an anode (5) and a cathode (6). The cathodes are grounded and signals are taken from the anodes. Each of the anodes is supplied with the voltage of 80 - 120 volts. The Frish grid (7), which is supplied with 5-15 volts, is used to regulate the charge collection.

The regulated flux of argon with the pressure of 200 mbar served as a working gas in the ionization chamber. Such conditions were equivalent to the 15 µm thickness of silicon for ^{11}B, ions at the incident energy of around 50 MeV. The consumption of working gas in the ionization chamber was about one liter per hour.

In the ^{9}Be(^{11}B,X) reaction, for the ion beam energy E_{LAB}(^{11}B) = 45 MeV and for the beam energy spread about 1%, the self-supported ^{9}Be foil with thickness of 600 µg/cm^2 was used as a target. The admixture of oxygen and heavier elements was not greater than 10%.

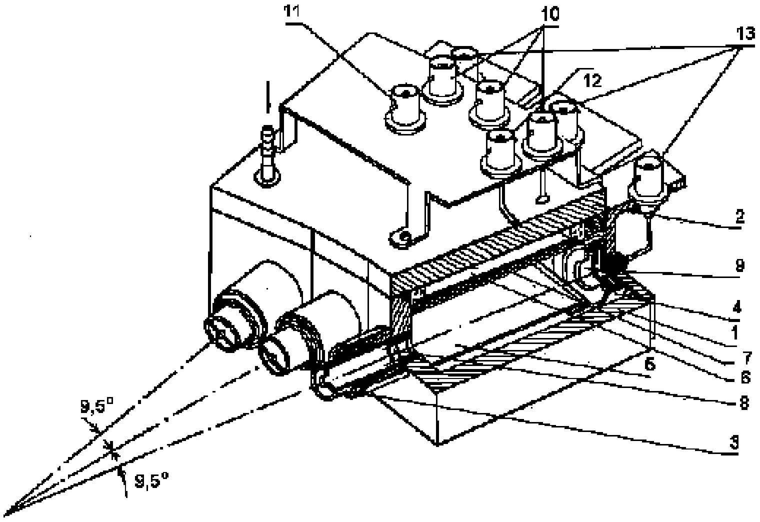

Fig. 3.4 . The scheme of the ionization chamber. 1- body, 2 - upper side of the chamber,3 - collimator, 4 - coaxial connector for a silicon detector, 5 - anode, 6 - cathode, 7 - Frish grid, 8 – entrance window of the chamber, 9 - silicon detector, 10 - anode coaxial connectors, 11 - cathode coaxial connector, 12 - coaxial connector of Frish grid, 13 – coaxial connectors of silicon detectors.

The standard CAMAC electronics was used in the experiment. The ΔE and E signals were collected by the data acqusition system using analog-to-digital converters ADC. A digital signal from ADC's is going to the computer, which was operated with the data acquisition system SMAN [99]. The digital spectroscopic information was stored in the computer buffer in the form of separate ΔE-E-N blocks (N is the number of the ADC) and then stored on a hard disc. Typical spectra are shown in Figs. 3.5 and 3.6. The reaction products were detected by a three-layer telescope consisting of an ionization chamber ($\Delta E1$ detector) and 0.5-mm ($E1 = \Delta E2$) and 2-mm ($E2$) silicon detectors. The heavy ($2 < Z < 8$) and light ($Z < 3$) ejectiles were detected by $\Delta E1$-$E1$ and $\Delta E2$-$E2$ telescopes, respectively.

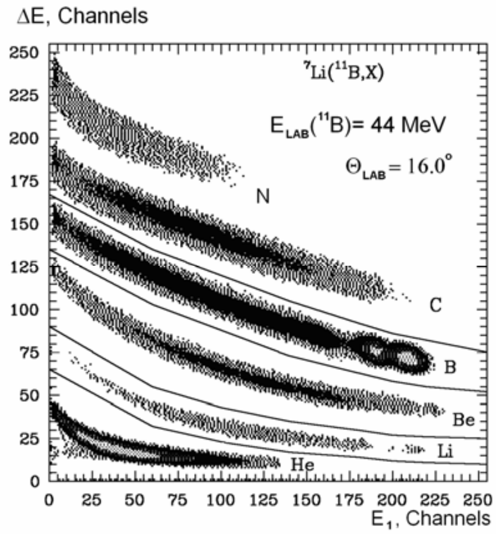

Fig. 3.5. The typical two-dimension $\Delta E(E_1)$-spectrum of ^{7}Li(^{11}B,X) reaction products for E_{LAB}(^{11}B) = 44 MeV energy [13], measured with ΔE-E_1-E_2-spectrometer with ionization chamber as the ΔE-detector.

It is visible, that this experimental method gives the possibility of indentification of heavy products from lithium to nitrogen along the charges only (Fig. 3.5) and light products along charges and masses (Fig. 3.6). The yield of ^{3}He from ^{18}O compound-nucleus decay ^{18}O and from ^{7}Li(^{11}B, ^{15}C)^{3}He reaction was small and the corresponding line in Fig. 3.6 has a small intensity.

The loci of the lithium and boron isotopes are chosen and shown in Fig. 3.5. The energy spectra $N(E_i)$

$$N(E_i) = \sum_{j=\Delta E_i^{\min}}^{\Delta E_i^{\max}} n_j(E_i) \qquad (3.1)$$

for the boron and lithium isotopes were calculated by the projection and summing of loci. The analysis of these spectra and the obtained differential cross sections for the elastic and inelastic scattering of ^{7}Li + ^{11}B nuclei is described in Chapter 4.

The *ΔE-E*-spectrometers with the ionization chamber were also used for investigation of the ^{12}C(^{11}B, ^{15}N)^{8}Be reaction for E_{LAB}(^{11}B) = 49 MeV energy, at the Warsaw cyclotron. The carbon target had the thickness of ~ 0.200 mg/cm^2 and the isotopic abundance (^{12}C – 98.9 %).

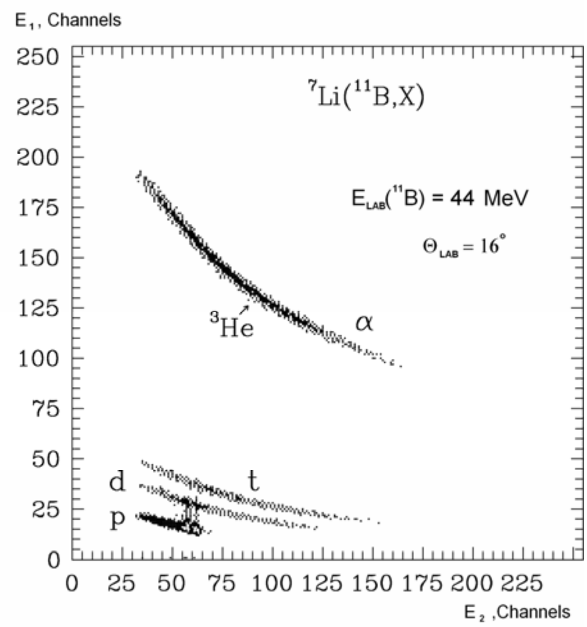

Fig. 3.6. The typical two-dimensional *E*$_1$(*E*$_2$)-spectrum of the ^{7}Li(^{11}B,X) reaction products for E_{LAB}(^{11}B) = 44 MeV energy [101], measured with *ΔE-E*$_1$-*E*$_2$-spectrometer with *E*$_1$ silicon detector as the *ΔE*-detector.

The typical two-dimensional *ΔE(E)*-spectrum of the ^{12}C(^{11}B, *X*) reaction products is shown in Fig. 3.7.

It is visible that these experimental methods give a possibility of good identification of the reaction products along charges from lithium to fluor. The nitrogen isotope products of the ^{12}C(^{11}B, N)Be reaction were separated and shown in Fig. 3.7. The energy resolution of the *ΔE-E* spectrometer, with the ionization chamber as the *ΔE* detector, was estimated from the one- and two-dimension spectra of α particles from the standard ^{226}Ra source. From the analysis of the one-dimensional spectra of α particles, the energy resolution of the spectrometer was equal to about 1.5%

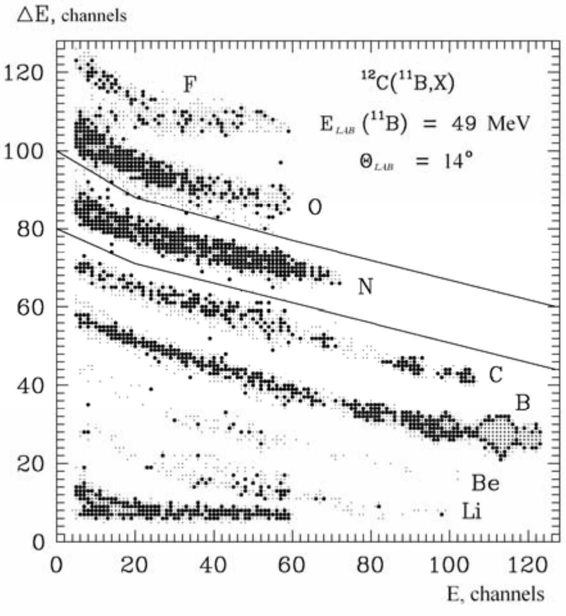

Fig. 3.7. The typical two-dimensional *ΔE(E)*-spectrum of the ^{12}C(^{11}B,*X*) reaction products for E_{LAB}(^{11}B) = 49 MeV [11].

In the experiments, the energy resolution was worse, because of 1% beam energy spread. The worst energy resolution was for low intensity spectra, for example in the case of beryllium isotopes from the ^{9}Be(^{11}B, Be) reaction at $E_{LAB.}$(^{11}B) = 45 MeV energy. For this case, the energy resolution was ~ 4.5%. The worsening of the peak splitting in the spectrum was caused by the beam energy spread and by the kinematical spread of the reaction products due to the solid angle of the spectrometer. This energy resolution allowed to study the inelastic scattering of ^{11}B on the ^{9}Be nuclei for transitions to different excited states of the ^{11}B nucleus.

3.2.3. The measurements using ΔE-E-silicon detectors.

In the ^{7}Li(^{18}O, *X*) reaction experiment for E_{LAB}(^{18}O) = 114 MeV, the *ΔE-E*-spectrometer with the *ΔE*-silicon detector of 67 µm thickness with high energy resolution was used. Thickness of the *E*-detector was 1 mm. This spectrometer gives a possibility of good identification of reaction produts *X* not only along charge and also by masses. The typical two-dimensional spectra are presented in Fig. 3.8.

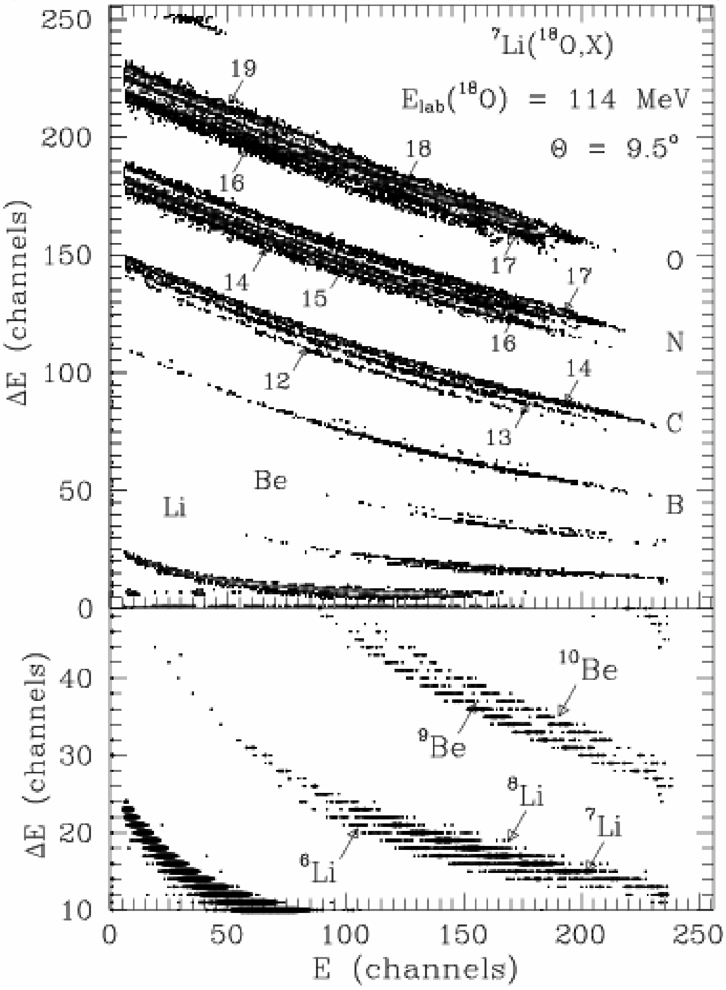

Fig.3.8. The typical two-dimensional spectra *ΔE(E)*-spectra of the ^{7}Li(^{18}O, X) reaction products for E_{LAB}(^{18}O) = 114 MeV energy [16].

This is visible, that the experimental method presented here, gives a possibility of identification of the ^{16,17,18,19}O, ^{14,15,16,17}N, ^{12,13,14}C, ^{10,11,12}B, ^{9,10}Be and ^{6,7,8}Li isotopes as reaction products. Then, the analysis of reactions with stable and unstable nuclei in the exit channel was possible. The first stage of this research program was investigation of the elastic and inelastic scattering of all studied reactions. As an example of this procedure, the calculations for the ^{7}Li + ^{18}O reaction is shown. This is the basis for investigation of the reactions with unstable nuclei in the exit channels, in frame of the present theoretical approach with coupling of the reaction channels. Instead of them, the experimental data of elastic and inelastic scattering are the basis for determination of the nucleon-nucleon potentials. For example, we obtained the information about the potential of interaction of the ^{7}Li + ^{18}O nuclei and about their differences from the analogous potential of interactions for the ^{7}Li + ^{16}O nuclei (so called *isotopic effects).*

The use of this spectrometer with the 67 µm thickness *ΔE*-silicium detector was not possible for exact investigations of the ^{7}Li(^{11}B, *X*) reaction at E_{LAB}(^{11}B) = 44 MeV energy and for the ^{12}C(^{11}B, ^{15}N)^{8}Be reaction at E_{LAB}(^{11}B) = 49 MeV energy, because for these experiments the *ΔE*-silicium detector with the 20 µm thickness is necessary. The energy resolution of these silicium detectors is rather low. The energy resolution of the *ΔE-E* spectrometer with the *ΔE* – silicium detector was estimated from experimental data. For example, in the ^{7}Li + ^{18}O, E_{LAB}(^{18}O) = 114 MeV experiment, the energy resolution of 0.2 MeV was estimated. This resolution allowed for resolving the first excited (0.48 MeV) state of ^{7}Li.

3.3. The analysis of the *ΔE - E* spectra.

As was mentioned above, the measured two-dimensional *ΔE-E*-spectra were transformed into the one-dimensional *E*-spectra.

A typical example of the *E*-spectrum for the boron isotopes from the ^{7}Li(^{11}B, B)Li reaction at E_{LAB}(^{11}B) = 44 MeV, obtained by projection and summing of the isotopes of boron loci on the *E*-axis (Fig. 3.5), is shown in Fig. 3.9.

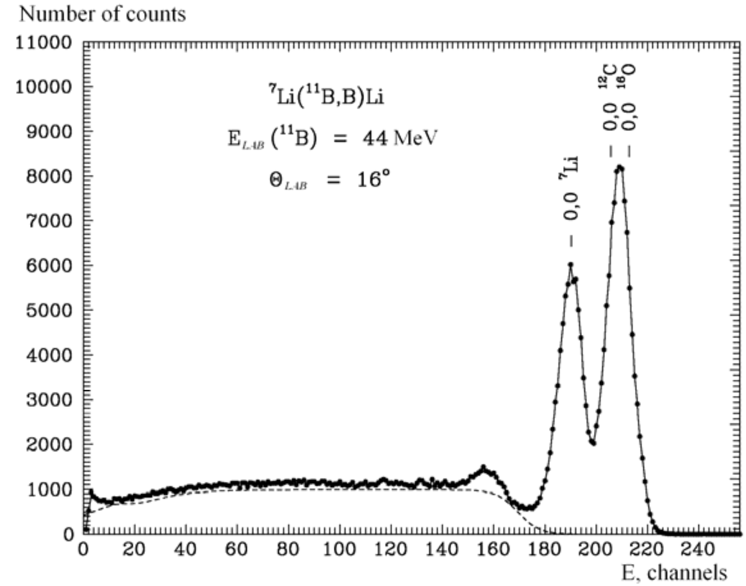

Fig. 3.9. The typical energy spectrum of the boron isotopes from the ^{7}Li(^{11}B, B)Li reaction at E_{LAB}(^{11}B) = 44 MeV energy [101], for the scattering angle θ_{LAB} = 16^{o} registered using the spectrometer with ionization chamber as the *ΔE*-detector. The dashed line denotes the multiparticle reaction background.

One can see that in the energy spectra of boron isotopes, except the peak of the elastic scattering of ^{11}B ions on the ^{7}Li target nuclei, also the peaks for elastic scattering of these ions on ^{12}C and ^{16}O nuclei (contaminations of the lithium target – lithium oxide and the rest of vacuum oil) are visible. Although the number of counts from the contaminations are large, this is not a result of a strong contamination in the target because for small angles the Coulomb scattering of ^{11}B ions on ^{12}C and ^{16}O nuclei is much more greater than on the ^{7}Li nuclei. In the energy spectra for large angles, the peak amplitude of the elastic scattering ^{7}Li + ^{11}B is greater than the amplitudes of the corresponding peaks for the ^{12}C, ^{16}O + ^{11}B elastic scatterings.

It is visible from Fig. 3.9 that in the inelastic scattering area of the spectrum for the ^{11}B ions the continuous background exists, due to the multiparticle reactions ^{7}Li(^{11}B,^{11}B)*xy*, where *x, y* denote the clusters from the nucleus ^{7}Li = *x* + *y*. This background can be approximated by the so-called *background function* from the PEAKFIT program [100]. These approximations are shown as the dashed lines in Fig. 3.9. The background line was fitted to the minima of the spectrum. Using the PEAKFIT program, the continuous background can be substracted from the experimental spectrum. As a result, we obtain the so called "*residual, background-free spectrum",* approximated in the PEAKFIT program by the sum of the symmetric Gauss functions

$$N(E) = \sum_{i=1}^{n} N_{0i} \exp\left(-\frac{\left(E - E_{0i}\right)^2}{h_i^2} \right), \qquad (3.2)$$

where N_{0i}, E_{0i} and h_i denote the amplitude, the position and the half-width of the *i* peak, respectively.

Before approximation of the residual spectrum by the functions (3.2), the calibration procedure should be done. This procedure transfer the x-axis scale of the spectrum from channels to the absolute energy scale (MeV). The kinetic energies of the scattered ^{11}B ions in the ground and most probable excited states were taken into account as a base.

The residual (background-free) spectrum of the boron nuclei with the *E*-axis in absolute energy units, obtained from the experimental spectrum, is shown in Fig. 3.10. Energies of the excited states of ^{11}B and ^{7}Li nuclei were shown above the peaks.

During approximation of the background-free spectrum by the function (3.2), the values of kinetic energies for the corresponding states of nuclei, obtained from kinetic calculations of scattering and reactions, were used for positions of the E_{0i} peaks. Then, the parameters E_{0i} were not changed. Also, the peak-width parameters were fixed. This same fixed half-width h_i value, obtained from fitting of a well isolated peak, was applied for each peak. The *E*-spectrum is approximated by a sum of the Gaussian functions via fitting of the peak amplitudes N_{0i} only. It makes the approximation of the experimental spectra by the function (3.2) much more ambiguous. Also the area of peaks is a result of the PEAKFIT program. These areas are necessary for calculation of the differential cross sections for particular processes.

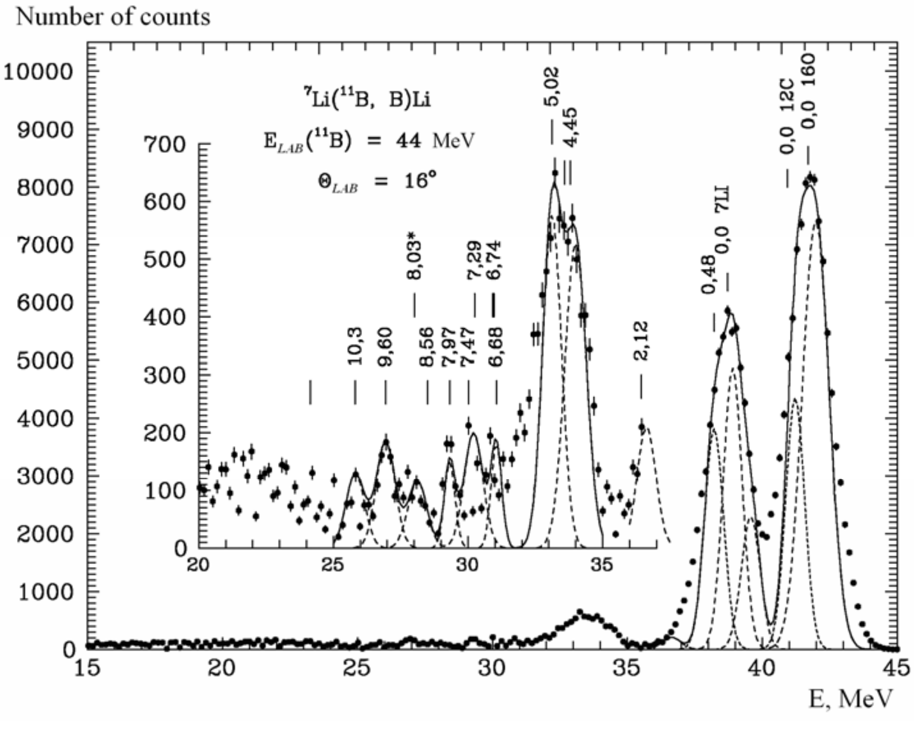

Fig. 3.10. The background-free (residual) spectrum of the boron nuclei from the ^{7}Li(^{11}B, B)Li reaction at E_{LAB}(^{11}B) = 44 MeV [13] and for the scattering angle $\theta_{LAB} = 16^o$.

The approximations of the *E*-spectrum of boron isotopes by the function (3.2) is shown in Fig. 3.10. The methods of expansion of the experimental energy spectrum in terms of the components described above, give the accuracy of the peak area from 10% to 30%, depending on overlapping of the peaks.

3.4. The energy dependences of the nucleus-nucleus potentials.

The conventional optical potential parameters are: $\{X_i\} = \{V, r_V, a_V, W_S, W_{CRC}, r_W, a_W\}$. The errors ΔX_i of the parameters were estimated using the following simple criterion [4]:

$$\min\left\{|\chi^2(X_i) - \chi^2(X_i + \Delta X_i)|, |\chi^2(X_i) - \chi^2(X_i - \Delta X_i)|\right\} / \chi^2(X_i) \approx 1 \qquad (3.3)$$

If the error ΔX_i determined in such a way was smaller than $0.1\times X_i$, then it was assumed to be $\Delta X_i = 0.1\times X_i$.

The sets of the OM parameters $\{X_i\}$ for different energies were parameterized by the following simple functional forms [4 – 6]:

$$X(E)=\begin{cases} X_i^{max}-(X_i^{max}-X_i^{min})g(E,E_x,\Delta E_x) & \text{for } \{X_i\}=\{V_0,W_S,a_V,a_W\} \\ X_i^{max}+(X_i^{max}-X_i^{min})g(E,E_x,\Delta E_x) & \text{for } \{X_i\}=\{r_V,r_W\} \end{cases} \tag{3.4}$$

where

$$g(E,E_x,\Delta E_x)=\left[1+exp\left(\frac{E-E_x}{\Delta E_x}\right)\right]^{-1} \tag{3.5}$$

$X_i^{min}, X_i^{max}, E_x, \Delta E_x$ - fitted parameters.

Due to the causality principle, which states that the scattered wave cannot be emitted before the interaction has occurred. Then, the real part *V(r,E)* of the OM potential is connected to the imaginary part *W(r,E)* by the dispersion relation [219, 75]:

$$V(r,E)=V_0(r,E)+\Delta V_W(r,E), \qquad \text{where} \tag{3.6}$$

where

$$\Delta V_W=\frac{P}{\pi}\int_0^\infty \frac{W(r,E')}{E'-E}dE'. \tag{3.7}$$

where P denotes the principal value of the integral $\Delta V_W(r,E)$, which was calculated at $r = 0$ using the method described in Refs. [4, 219]. The use of the dispersion relation can help to minimize ambiguities in the optical potential. The dispersion relation is related to the so called “threshold anomaly” (see Section 4.2).

For brevity, we shall use the following notation [6]:

$\Delta V(E) = \Delta V_W(0,E)$, $\quad V_0(E) = V_0(0,E)$,
$V(E) = V(0,E) = V_0(E) + \Delta V(E)$.

The parameters in Eqs (3) and (4), were fitted to describe the sets $\{X_i\}$ of the OM potential parameters using a code PARE [220]. Then parameters predicted by the code, were used as the starting values in the analysis of the data at next experimental energy. The OM parameters obtained for the next energy were added to the sets $\{X_i\}$ and the fitting procedure of energy dependence was repeated. Thus the energy dependence of OM parameters was obtained with such a step-by-step fitting procedure.

CHAPTER 4.

Nucleus-nucleus scattering

4.1. The $^{10,\,11}$B + ^{7}Li, ^{9}Be, $^{12,\,13,\,14}$C scattering.

4.1.1. Scattering of ^{11}B + ^{12}C nuclei, optical potential and influence of ^{11}B reorientation.

The angular distributions of the elastic and inelastic scattering of ^{11}B ions by ^{12}C nuclei at the energy $E_{LAB}(^{11}\text{B})$ = 49 MeV in the angular range $\theta_{CM} \approx 24^{\circ} - 156^{\circ}$ were measured [6]. The experimental data with their absolute errors are shown in Figures 4.1.1 – 4.1.3. The error of the cross section normalization is about 10%. The data of the ^{11}B + ^{12}C elastic scattering at the energies E_{CM} = 5.42 – 52.17 MeV [169 – 178] and our data at E_{CM} = 25.57 MeV ($E_{LAB}(^{11}\text{B})$ = 49 MeV) were analyzed within OM using potential of Woods–Saxon type with imaginary part W_S. The OM potential parameters $\{X_i\} = \{V, r_V, a_V, W_S, r_W, a_W\}$ were fitted to describe the experimental angular distributions of the elastic scattering in the angular range where potential scattering dominates (full angular range at low energies and $\theta_{CM} < 90^{\circ}$ at E_{CM} > 10 MeV). The radius of the Coulomb potential was fixed at r_{C} = 1.25 MeV. The OM potential parameters obtained for the elastic scattering were used as starting values for the calculations of angular distributions for different processes within CRC method. The elastic and inelastic scattering as well as transfer reactions corresponding to diagrams of Fig. 4.1.4 were included in the coupling scheme. Low-energy states of the ^{11}B and ^{12}C nuclei were assumed to be of rotational nature.

The standard fit of parameters in CRC approach is not possible in practice. Then, analysis was performed in a few steps. At the beginning the deformation length parameters δ_2 and δ_4 for ^{11}B and ^{12}C nuclei as well as the parameter W_S were fitted to describe the inelastic scattering data for transitions to the 2.125 MeV ($1/2^-$), 5.02 MeV ($3/2^-$) and 4.44 MeV (2^+) excited states of ^{11}B and ^{12}C at $E_{LAB}(^{11}\text{B})$ = 49 MeV in the angular range where rotational transitions dominate. In this step the elastic and inelastic scattering and reorientation of ^{11}B were included in the coupled channel scheme. Then preliminary values W_{CRC} (W_S), δ_2 and δ_4 were obtained and used in the next steps of the CRC-calculations. Next, the CRC angular distributions of individual transfer reactions were calculated using spectroscopic amplitudes (see Appendix). The most probable transfers contributing to the elastic and inelastic scattering were selected and included in the coupling scheme. Finally, using full coupling scheme, all OM potential parameters and deformation length parameter δ_2 and δ_4 where corrected to describe the angular distributions of all experimental data in full angular range. The errors ΔX_i of the parameters $\{X_i\} = \{V, r_V, a_V, W_S, W_{CRC}, r_W, a_W\}$ were estimated using the simple criterion (see sub-Section 3.4).

To obtain the energy dependence of the optical potential parameters, we used the procedure presented above to describe the present data and the earlier measured data [169 – 178]. As the result, the sets of optical potential parameters were determined at the experimental beam energies. The optical potential parameters obtained in the analysis of elastic and inelastic scattering data at different energies are collected in Table 4.1.1.

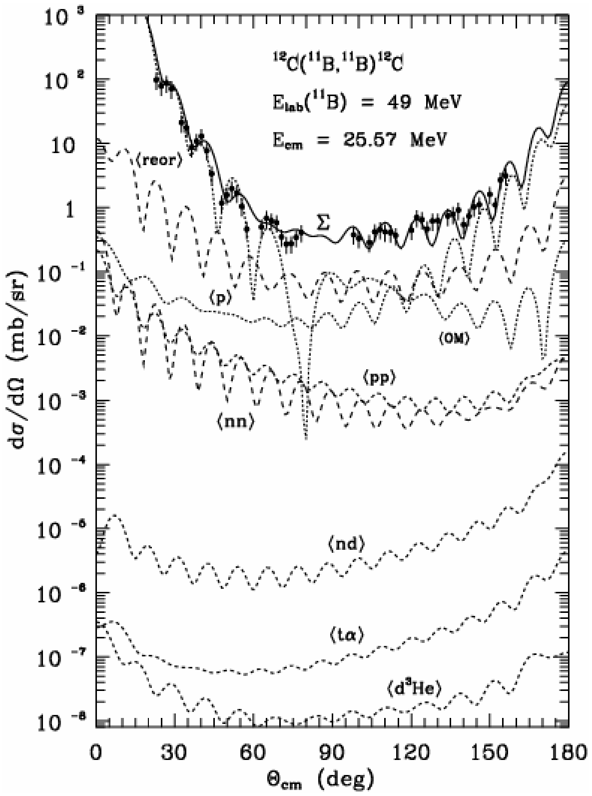

Fig. 4.1.1. Angular distribution of the ^{11}B + ^{12}C elastic scattering at the energy E_{LAB}(^{11}B) = 49 MeV. The dashed curves marked by <OM> and <reor> show the OM and reorientation cross sections, respectively. Other dashed curves <p>, <pp>, <nn>, <nd>, <tα> and <d^{3}He> represent the CRC cross sections for the transfers corresponding to diagrams shown in Fig. 4.1.4. The solid curve Σ shows the sum of the CRC cross sections for all processes.

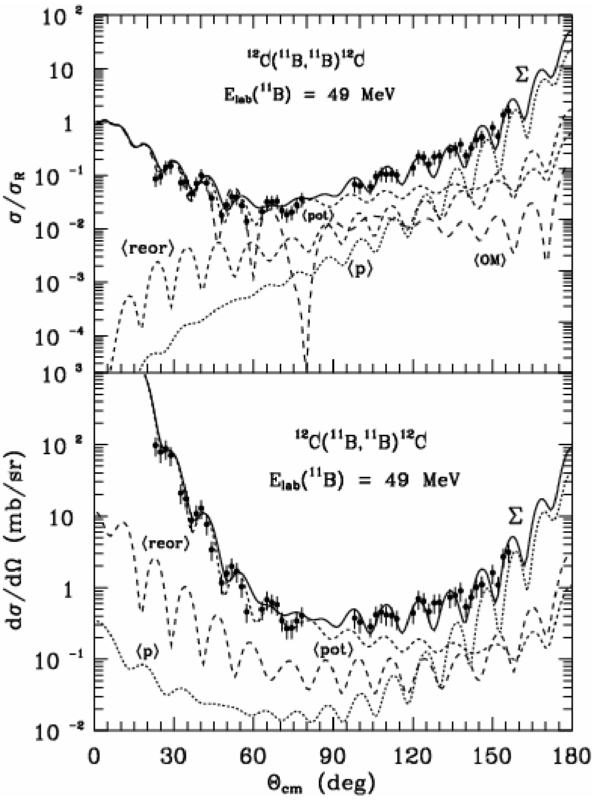

Fig. 4.1.2. The same as in Fig. 4.1.1, but for the potential scattering (curve <pot>), the ^{11}B reorientation (curve <reor>) and proton transfer (curve <p>). The solid curve Σ shows the CRC sum of these processes.

As it can be seen in Fig. 4.1.1, the optical model describes oscillations of the cross section for elastic scattering only at forward angles. The contributions of the two-step processes to the ^{11}B + ^{12}C elastic scattering are very small. The contribution of the elastic knock-on reaction (see the last diagram in Fig. 4.1.4) was shown to be small for the similar reactions [180]. Therefore the two-step nucleon and cluster transfers were not included in the coupled channel scheme.

The one-step processes, which give noticeable contributions to the ^{11}B + ^{12}C elastic scattering at E_{LAB}(^{11}B) = 49 MeV, are shown separately in Fig. 4.1.2. The angular distributions of the potential scattering calculated in the CRC approach, proton transfer, reorientation of ^{11}B and their coherent sum calculated in the CRC approach is also displayed here together with the experimental data. The deformation length δ_2 = 1.2 fm obtained in the analysis of inelastic scattering was used in the CRC calculation of the ^{11}B reorientation. One can see that the potential scattering and the proton transfer dominate at angles $\theta_{CM} < 60^{\circ}$ and $\theta_{CM} > 140^{\circ}$, respectively. All three mechanisms mentioned above explain the angular distribution in the angular interval $\theta_{CM} \approx 60^{\circ} - 140^{\circ}$. The coherent sum of these three processes describes well the experimental data.

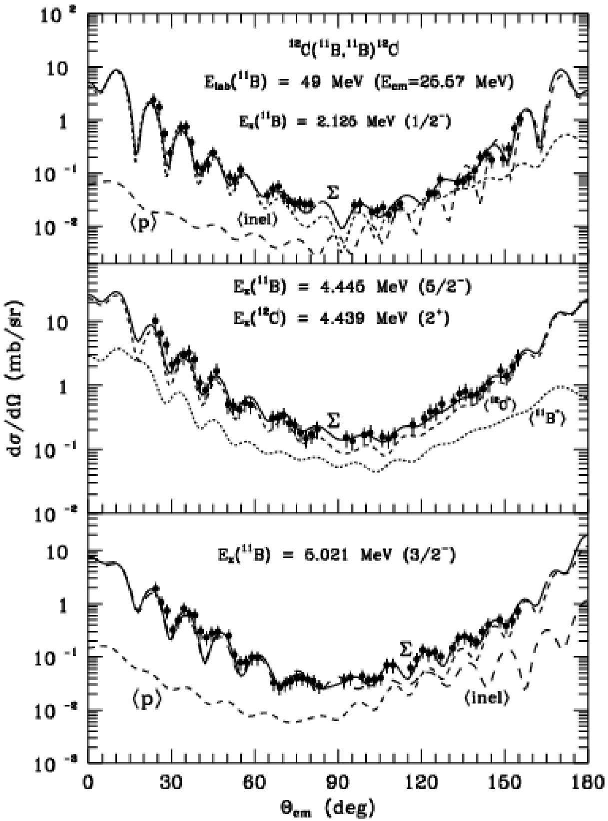

Fig. 4.1.3. Angular distributions of the ^{11}B + ^{12}C inelastic scattering at the energy E_{LAB}(^{11}B) = 49 MeV for the transitions to the 2.125 MeV (1/2$^-$), 4.445 MeV (5/2$^-$) and 5.021 MeV (3/2$^-$) excited states of the ^{11}B nucleus and to the 4.439 MeV (2$^+$) excited state of the ^{12}C nucleus. Dashed curves <p> and <inel> show the contributions of proton transfer and rotational excitation of the ^{11}B nucleus, respectively. The CRC cross sections for the 4.439 MeV and 4.445 MeV excitation of the ^{12}C and ^{11}B nuclei are shown by the curves <^{12}C*> and <^{11}B*>, respectively. The solid curves Σ represent the sums of CRC cross sections for all processes.

Different other processes like the compound-nucleus formation or the formation of isolated resonances of the molecular character can also contribute to the ^{11}B + ^{12}C cross section at low energies. These processes were ignored in the present analysis.

One can see that the mentioned above processes describe the inelastic scattering well. The curves <inel> shown in Fig. 4.1.3, were obtained for δ_2 = 1.2 fm and δ_4 = 1.0 fm. These deformation parameters are shown in Table 4.1.4. The deformation length $\delta_2 = -1.0$ fm [181] was used for the ^{12}C nucleus. It is visible from Fig. 4.1.3 that the nuclear excitation (curves <inel>) and the proton transfer (curves <p>) dominate at angles $\theta_{CM} < 110^o$ and $\theta_{CM} > 110^o$, respectively, for transitions to the 2.125 MeV and 5.021 MeV excited states of the ^{11}B nucleus. The same is also observed for the transitions to the 4.445 MeV + 4.439 MeV excited states of the ^{11}B and ^{12}C nuclei, respectively. The coherent sums (curves Σ) of these processes well describe the data in the whole angular range for the transitions to both the 2.125 MeV and 5.021 MeV excited states of the ^{11}B nucleus.

The optical potential parameters from Table 4.1.1 versus the center-of-mass energy E_{CM} are shown in Fig. 4.1.5. They have been described by the functional forms by fitting the parameters X_i^{min} , X_i^{max} , E_{Xi} *and* ΔE_{Xi}. These values, obtained in the fitting procedure are listed in Table 4.1.2.

Table 4.1.1 Parameters of Woods–Saxon OM potentials for the ^{11}B + ^{12}C elastic scattering. ($R = r_i(A^{1/3}_T + A^{1/3}_P)$, $i = V,W,C$)

E_{CM} (MeV)	V (MeV)	r_V (fm)	a_V (fm)	W_S (MeV)	W_{CRC} (MeV)	r_W (fm)	a_W (fm)	r_C	Ref. (data)
5.43	76.0	0.940	0.600	3.4	3.4	1.500	0.600	1.25	[175]
6.47	77.0	0.890	0.640	3.7	3.4	1.500	0.640	1.25	[175]
7.17	81.0	0.850	0.660	4.0	3.5	1.440	0.660	1.25	[171]
7.62	82.0	0.850	0.660	4.1	3.7	1.360	0.660	1.25	[175]
7.65	83.0	0.850	0.660	4.1	3.6	1.360	0.660	1.25	[172]
8.13	84.0	0.850	0.660	4.3	3.7	1.330	0.660	1.25	[171]
8.61	103.0	0.860	0.670	4.6	4.0	1.330	0.670	1.25	[172]
9.57	115.0	0.810	0.670	5.0	4.4	1.320	0.670	1.25	[171]
10.52	128.0	0.788	0.670	5.4	4.5	1.300	0.670	1.25	[172]
11.48	142.0	0.788	0.670	5.9	5.0	1.270	0.670	1.25	[171, 172]

13.04	169.3	0.788	0.670	6.5	5.2	1.260	0.670	1.25	[173]
14.59	215.0	0.788	0.670	7.0	6.1	1.250	0.670	1.25	[178]
14.61	215.0	0.788	0.670	7.0	6.1	1.250	0.670	1.25	[171, 174]
18.26	240.0	0.788	0.670	9.0	7.0	1.250	0.670	1.25	[178]
20.87	252.0	0.788	0.670	10.0	7.4	1.250	0.670	1.25	[173, 178]
22.17	251.0	0.788	0.670	10.3	8.0	1.250	0.670	1.25	[176]
23.48	252.0	0.788	0.670	10.7	8.1	1.250	0.670	1.25	[178]
25.04	241.8	0.788	0.670	11.0	8.5	1.250	0.670	1.25	[177]
25.57	241.6	0.788	0.670	11.1	9.0	1.250	0.670	1.25	this work [6]
26.09	242.0	0.788	0.670	11.2	9.0	1.250	0.670	1.25	[173, 178]
26.78	242.0	0.788	0.670	11.3	8.9	1.250	0.670	1.25	[178]
29.22	240.0	0.788	0.670	11.6	9.0	1.250	0.670	1.25	[178]
31.30	244.0	0.788	0.670	11.8	9.4	1.250	0.670	1.25	[178]
33.48	237.0	0.788	0.670	12.0	9.5	1.250	0.670	1.25	[178]
33.91	236.7	0.788	0.670	12.1	9.9	1.250	0.670	1.25	[178]
36.52	235.0	0.788	0.670	12.1	10.2	1.250	0.670	1.25	[178]
39.13	233.5	0.788	0.670	12.2	10.3	1.250	0.670	1.25	[178]
41.61	232.0	0.788	0.670	12.2	10.3	1.250	0.670	1.25	[170]
41.74	232.0	0.788	0.670	12.2	10.3	1.250	0.670	1.25	[178]
52.17	227.2	0.788	0.670	12.2	10.3	1.250	0.670	1.25	[176]

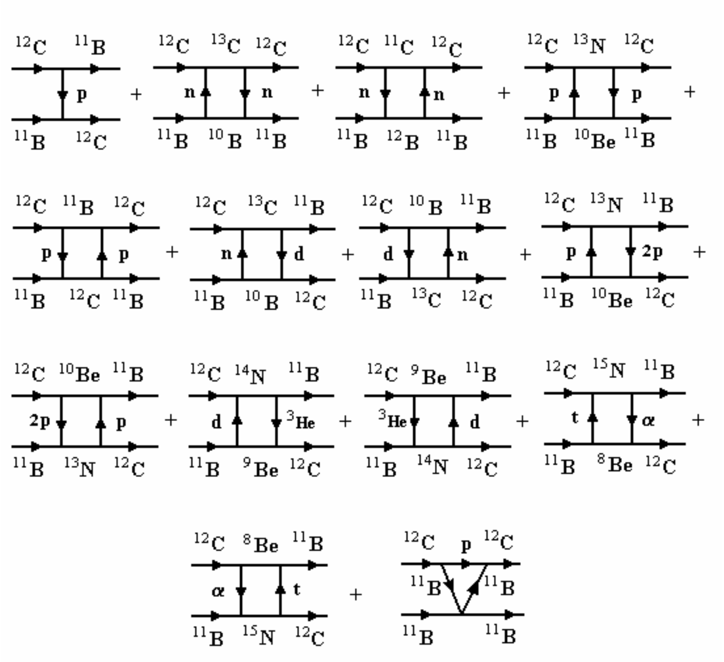

Fig. 4.1.4. Diagrams of the one- and two-step processes for the ^{12}C(^{11}B, ^{12}C)^{11}B reaction.

The energy dependence of the optical potential parameters was also studied for the ^{9}Be + ^{12}C (sub-Section 4.2.2), ^{8}Be + ^{13}C (sub-Section 5.2.1) and ^{10}B + ^{11}B (sub-Section 5.2.2) interactions. It is interesting to compare those results with the present ones for the ^{11}B + ^{12}C interaction. Such a comparison is made in Fig. 4.1.6, where the fitted curves of the energy dependence of the ^{11}B + ^{12}C and ^{9}Be + ^{12}C, ^{8}Be + ^{13}C interactions are presented together. Particularly large differences are observed in the low-energy range ($E_{CM} \leq 10$ MeV) for the parameters $a_V = a_W$, r_V and r_W. Why at low energies are these parameters so different, whereas they are rather equal at larger energies? It seems that a common behavior of r_V and r_W in the low-energy range can be explained by the dominance of the Coulomb repulsion between the interacting nuclei at low energies. This leads to an increase of the minimal distance between the nuclei (so, the parameters r_V and r_W increase) and to a decrease of the nuclear overlap (consequently, parameters V, W, a_V and a_W decrease). Different values of W_S for the different systems ^{11}B + ^{12}C, ^{9}Be + ^{12}C and ^{8}Be + ^{13}C are due to their different structure.

Table 4.1.2 Parameters of energy dependence of the ^{11}B + ^{12}C interaction.

X_i	V_0	W_S	W_{CRC}	r_V	r_W	a_V	a_W
	(MeV)	(MeV)	(MeV)	(fm)	(fm)	(fm)	(fm)
X_i^{min}	83.1	1.2	2.6	0.788	1.25	0.48	0.48
X_i^{max}	272.4	12.3	10.3	1.152	1.63	0.67	0.67
E_{Xi} (MeV)	13.0	13.6	17.6	4.821	6.70	4.80	4.80
ΔE_{Xi} (MeV)	2.5	5.8	5.1	1.820	1.50	1.00	1.00

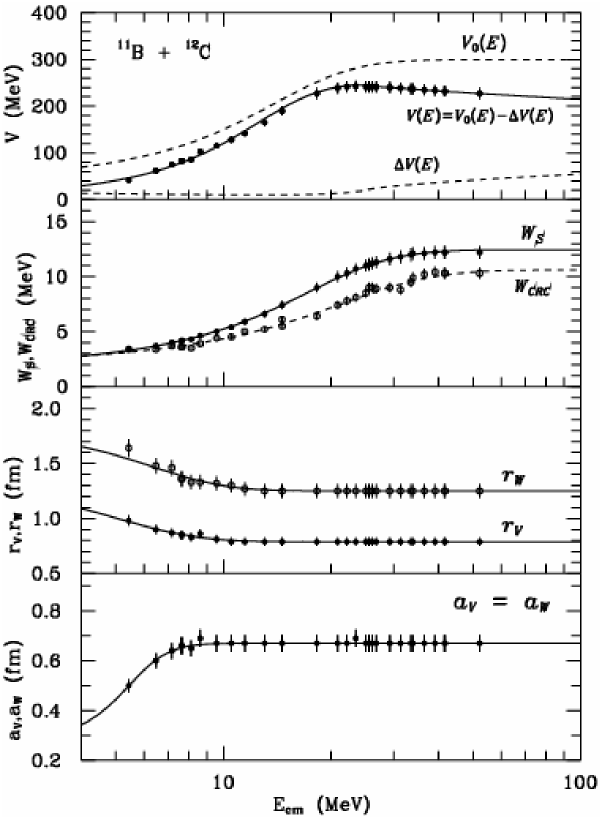

Fig. 4.1.5. Energy dependence of the OM potential parameters for the ^{11}B + ^{12}C interactions.

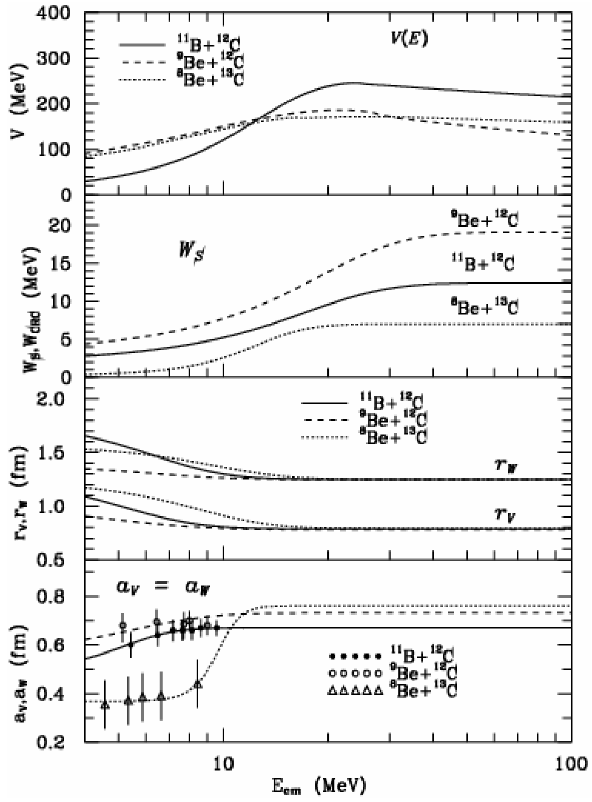

Fig. 4.1.6. A comparison of the energy dependence of the OM potential parameters for the ^{11}B + ^{12}C and ^{9}Be + ^{12}C [4], ^{8}Be + ^{13}C [3] interactions.

4.1.2. Scattering of ^{11}B + ^{13}C nuclei, optical potential, the ^{11}B reorientation and ^{11}B, ^{13}C deformation parameters and the ALAS phenomenon.

The analysis of the isotopic effects in the ^{11}B + ^{13}C and ^{11}B + ^{12}C elastic and inelastic scattering [9] is presented. This analysis includes the study of differences between the OM parameters for the two scattering systems, the change of deformation parameter with the number of neutrons as well as the study of the ALAS (anomalous large angle scattering) mechanisms of the ^{11}B + $^{12,\,13}$C scattering. The ALAS phenomenon is also considered in this work for scattering of ^{11}B + ^{9}Be [8] in the sub-Section 4.1.4 and for ^{14}N + ^{7}Li [7] scattering in the sub-Section 4.3.1. Although the oblate deformation of the ^{12}C ground state is well established [181], the sign of the ^{13}C quadrupole deformation is still not determined convincingly. It was found to be positive in the analysis of the inelastic scattering of ^{3}He + ^{13}C [182], p + ^{13}C [184] and $\pi^{\pm}$ + ^{13}C [185], while from the analysis of the inelastic scattering of α + ^{13}C [183] and t + ^{13}C [186] it was deduced to be negative. This discrepancy can be partly explained by the fact that only the forward angle scattering data of the inelastic scattering were used in the analysis in above mentioned papers. It is known that the forward angle distribution of inelastic scattering is weakly sensitive to the sign of nuclear deformation. In the present sub-Section, the measured ^{11}B + ^{13}C elastic and inelastic scattering in the full angular range are presented.

The angular distributions of the ^{13}C + ^{11}B elastic and inelastic scattering at $E_{LAB}(^{11}B)$ = 45 MeV are shown in Figs. 4.1.7 – 4.1.13. together with results of theoretical calculations [9]. The error of the cross section normalization is about 10%. One can observe in these Figures an anomalously large enhancement of the cross section at large angles. The angular distribution of the ^{13}C + ^{11}B elastic scattering was analyzed within the optical model. The simultaneous analysis of the ^{13}C + ^{11}B elastic and inelastic scattering data was performed using the method of coupled-reaction-channels. The elastic and inelastic scattering as well as the reorientation of ^{11}B and the most probable transfer reactions corresponding to the diagrams in Figures 4.1.14 – 4.1.16, were included in the coupling scheme. The optical potential parameters, obtained in the fitting procedures are listed in Table 4.1.3. The optical potential parameters for ^{11}B + ^{12}C nuclei for E_{CM} = 23.48 MeV and E_{CM} = 25.57 MeV were taken from Table 4.1.1. The rotational model was applied to calculation of the transitions to the excited states of ^{13}C and ^{11}B. The deformation parameters of ^{13}C and ^{11}B estimated from the fitting of inelastic scattering data, are listed in Table 4.1.4.

Table 4.1.3 Parameters of Woods–Saxon OM potentials for the ^{11}B + ^{13}C elastic scattering. ($R = r_i(A^{1/3}_T + A^{1/3}_P)$, $i = V,W,C$)

$P + T$	E_{CM} (MeV)	V (MeV)	r_V (fm)	a_V (fm)	W_S (MeV)	r_W (fm)	a_W (fm)	r_C (fm)
^{11}B + ^{13}C	24.38	256.7	0.788	0.740	8.0	1.250	0.740	1.250

The OM cross section (curve <OM> in Figs. 4.1.7 and 4.1.8) fitted to the forward-angle data of the ^{11}B + ^{13}C elastic scattering cannot describe the data at large angles. To explain the observed ALAS in the ^{11}B + ^{13}C elastic scattering, we performed the CRC calculations for many one-step and two-step processes corresponding to the diagrams shown in Fig. 4.1.14. One can see that only the potential scattering (curve <OM>) and the ^{11}B reorientation (curve <reor>) dominate at large angles. The coherent sum of these two processes cross section (curves Σ) describes satisfactorily the data in the full angular range.

The ^{11}B + ^{12}C versus the ^{11}B + ^{13}C elastic scattering are shown in Fig. 4.1.8 in order to demonstrate the isotopic effects. Except the usual difference of the diffraction picture at small angles, which originates from the difference of the ^{12}C and ^{13}C radii as well as from the difference of E_{CM}, a strong difference in ALAS is observed for these scatterings. The ^{11}B + ^{12}C ALAS is much stronger than for ^{11}B + ^{13}C. It is presented in [6] that the^{11}B + ^{12}C ALAS is satisfactorily described by the CRC cross section sum (dotted curves <23.48> and <25.57>) of the potential scattering, the ^{11}B reorientation and the proton transfer (dashed curves <p> in Fig. 4.1.8). Due to the ^{11}B + ^{13}C ALAS is caused by only two first ones of these mechanisms, the proton transfer in the ^{11}B + ^{12}C elastic scattering leads to the observed difference between the large angle scattering of ^{11}B on ^{12}C and ^{13}C.

Table 4.1.4 The ^{11}B and ^{13}C transition multi-polarities λ and deformation parameters δ_λ ($\beta_\lambda = \delta_\lambda/R$ for $R = 1.25A^{1/3}$ fm).

Nuclei	E_x (MeV)	j^π	λ	δ_λ (fm)	β_λ	Ref.
^{11}B	2.125	$1/2^-$	2	1.20	0.43	[6]
	4.445	$5/2^-$	2	1.20	0.43	[6]
			4	1.00	0.36	[6]
	5.020	$3/2^-$	2	1.20	0.43	[6]
	6.743	$7/2^-$	2	1.20	0.43	[6]
			4	1.00	0.36	[6]
	6.792	1/2+	1	1.00	0.36	
	7.286	5/2+	1	1.00	0.36	
			3	1.20	0.43	
	7.978	$3/2^+$	1	1.00	0.36	
			3	1.20	0.43	
	8.560	$3/2^-$	2	1.80	0.65	
^{13}C	3.088	$1/2^+$	1	1.00	0.34	
	3.684	$3/2^-$	2	0.94	0.32	[182] ^{13}C+^{3}He
				-1.11	-0.37 (0.19^b)	[183] ^{13}C+α
				1.44	0.49	[184] ^{13}C+p
				1.23	0.42	[185] ^{13}C+$\pi^\pm$
				-1.26 (-1.11^a)	-0.428	[186] ^{13}C+t
				0.90	0.31	[9]
	3.854	5/2+	3	0.50	0.17	
	6.864	5/2+	3	0.50	0.17	
	7.490	7/2+	3	0.50	0.17	
	7.547	5/2−	2	0.94	0.32	[182]
				1.23	0.42	[184]
				1.23	0.42	[185]
				−1.26 (−1.11^a)	−0.428	[186]
				0.90	0.31	[9]
	7.680	3/2+	1	1.00	0.34	
	8.200	3/2+	1	1.00	0.34	

[a] δ_λ from Ref. [186].

[b] β_λ from Ref. [183].

The angular distributions of the ^{11}B + ^{13}C inelastic scattering at E_{LAB}(^{11}B) = 45 MeV (E_{CM} = 24.38 MeV) for the transitions to the excited states of ^{11}B are shown in Figs. 4.1.9 – 4.1.11. The ^{11}B + ^{12}C inelastic scattering data at E_{CM} = 25.57 MeV [6] are also shown in Fig. 4.1.9. As in the case of the ^{11}B + ^{13}C elastic scattering, the transfer reactions are negligible in the ^{11}B + ^{13}C inelastic scattering (see, for example, curve <d> in Fig. 4.1.9). The ^{11}B + ^{12}C inelastic ALAS is stronger than for the ^{11}B + ^{13}C inelastic scattering, due to the proton transfer dominating in the ^{11}B + ^{12}C inelastic scattering. The deformation parameter of ^{11}B deduced from the analysis of the ^{11}B + ^{13}C inelastic scattering data is the same as in [6], where this parameter was obtained from the analysis of the ^{11}B + ^{12}C inelastic scattering data (see Table 4.1.4). The δ_λ values for ^{11}B and ^{13}C, deduced from fitting of theoretical cross sections to the back angle data of the transitions to excited state of these nuclei are presented also in Table 4.1.4.

The angular distributions of the ^{11}B + ^{13}C inelastic scattering are also shown in Figs. 4.1.12 and 4.1.13. The curves represent the CRC cross sections calculated within the rotational model using deformation parameters of ^{13}C listed in Table 4.1.4. A special attention was given to determine the sign of the ^{13}C quadrupole deformation length δ_2. This parameter for ^{12}C is negative [6]. It is apparent from the analysis of the data for the transitions to the 3.684 MeV ($3/2^-$) + 3.854 MeV ($5/2^+$) excited states of ^{13}C (see the two lower panels of Fig. 4.1.12), that only the CRC angular distribution for the transition to the 3.684 MeV ($3/2^-$) state of ^{13}C describes satisfactorily the oscillations of the data at forward angles (see curve <3.68> in Fig. 4.1.12). The CRC cross section for the transition to the 3.854 MeV ($5/2^+$) state of ^{13}C has oscillations of opposite phase (see curve <3.85> in Fig. 4.1.12). The CRC cross sections for positive and negative δ_2 differ slightly at forward angles. This helps us to determine the ^{13}C deformation length $|\delta_2|$ = 0.9 fm using the CRC cross section for the transition to the 3.684 MeV ($3/2^-$) excited state of ^{13}C at forward angles. The deformation length $\delta_3 = 0.5$ fm fitting the CRC cross section for the transition to the 3.854 MeV ($5/2^+$) state of ^{13}C to the data in full angular range was determined. Finally, the incoherent sums of CRC cross sections of both the transitions were obtained for the positive and negative δ_2 of ^{13}C. The lower panel of Fig. 4.1.12 shows these sums using the solid and dotted curves, respectively. Positive δ_2 gives better description of the experimental data in the full angular range. One can see in Fig. 4.1.13 that the difference between these incoherent sums is small in the angular range $\theta_{CM} < 90^{\circ}$. The same is also observed for the transition to the 8.2 MeV ($3/2^+$) excited states of ^{13}C (see lower panel of Fig. 4.1.13). The solid and dotted curves show the CRC cross sections for the positive and negative δ_2, respectively. This analysis suggests that the sign of the ^{13}C deformation parameter δ_2 is positive.

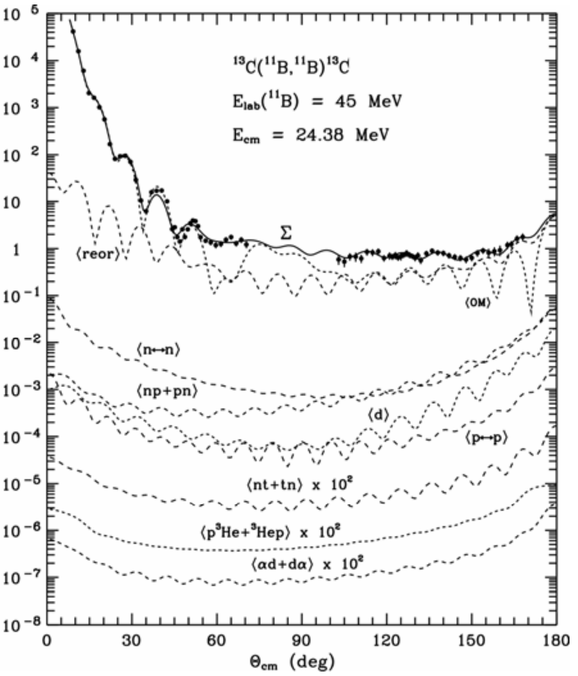

Fig. 4.1.7. Angular distribution of the ^{13}C(^{11}B, ^{11}B) elastic scattering at the energy E_{LAB}(^{11}B) = 45 MeV. The dashed curves marked by <OM> and <reor> show the OM and CRC cross sections for the potential scattering and reorientation of ^{11}B, respectively. Other dashed curves <d>, <p↔p>, <n↔n>, <np + pn>, <nt + tn>, <αd + dα> and <p^{3}He+^{3}Hep> represent the CRC cross sections for the transfer reactions corresponding to diagrams shown in Fig. 4.1.14. The solid curve Σ shows the sum of CRC cross sections for all processes.

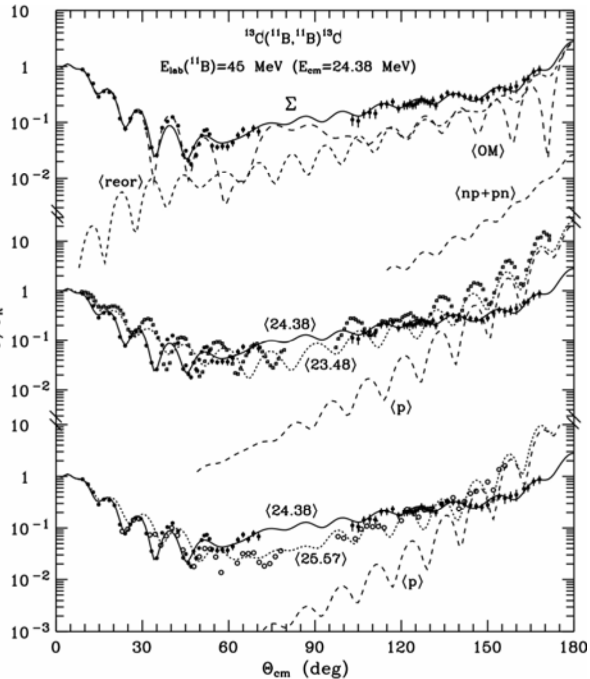

Fig. 4.1.8.. Angular distribution of the ^{13}C(^{11}B, ^{11}B) elastic scattering at the energy E_{LAB}(^{11}B) = 45 MeV (E_{CM} = 24.38 MeV) versus the angular distributions of the ^{12}C(^{11}B, ^{11}B) elastic scattering at E_{CM} = 23.48 MeV [178] (open points) and E_{CM} = 25.57 MeV [6] (open points). The solid curves Σ and <24.38> show the CRC sum of the potential scattering (dashed curve <OM>) and reorientation of ^{11}B (dashed curve <reor>) in the ^{13}C + ^{11}B elastic scattering at E_{CM} = 24.38 MeV. Other curves for this scattering are the same as in Fig. 4.1.7. The dotted curves <23.48> and <25.57> represent the CRC sums of the ^{11}B reorientation and proton transfer (dashed curves <p>) [6] for the ^{12}C + ^{11}B elastic scattering at E_{CM} = 23.48 MeV and 25.57 MeV, respectively.

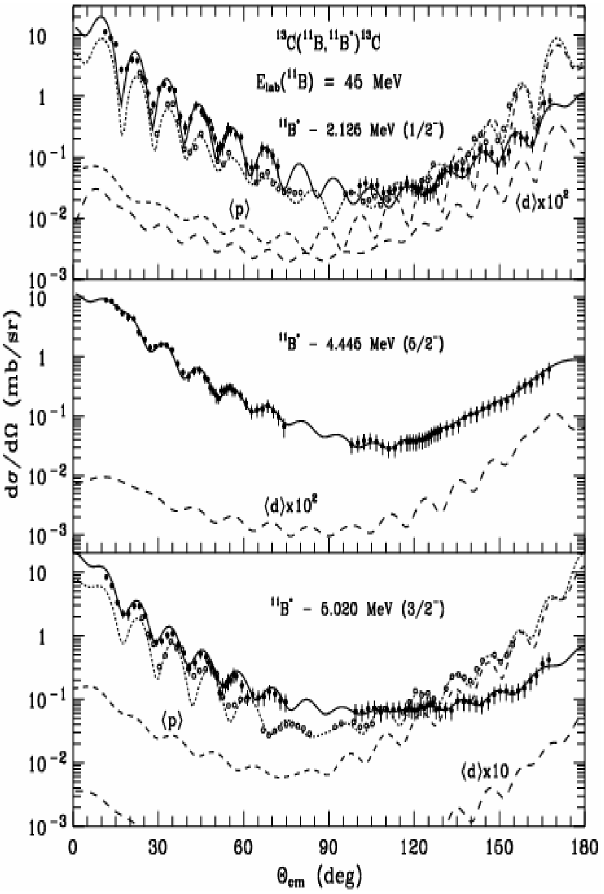

Fig. 4.1.9. Angular distributions of the $^{13}C(^{11}B, ^{11}B^*)^{13}C$ inelastic scattering at the energy $E_{LAB}(^{11}B)$ = 45 MeV (E_{CM} = 24.38 MeV) for the transitions to the 2.125 MeV (1/2⁻), 4.445 MeV (5/2⁻) and 5.020 MeV (3/2⁻) excited states of the ^{11}B (full points) versus the $^{12}C(^{11}B, ^{11}B^*)^{12}C$ inelastic scattering at E_{CM} = 25.57 MeV [6] (open points). The solid and dotted curves represent the CRC cross sections of the ^{11}B scattering on ^{13}C and ^{12}C, respectively, for the rotational model with the transition multipole and deformation parameters of ^{11}B listed in Table 4.1.4. The dashed curves <d> and <p> show the CRC cross sections of the deuteron and proton transfer reactions for the $^{11}B + ^{13}C$ and $^{11}B + ^{12}C$ inelastic scattering, respectively.

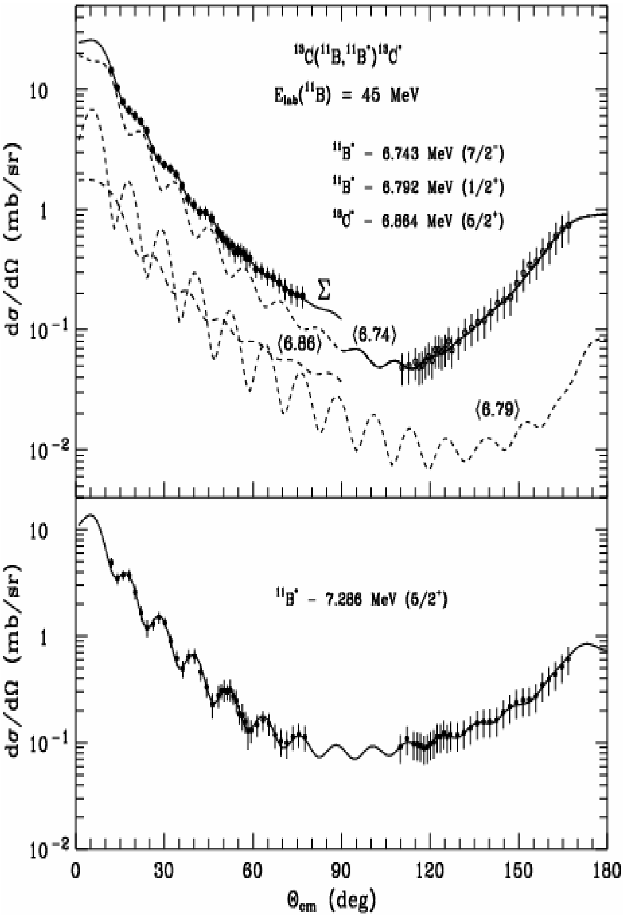

Fig. 4.1.10. The same as in Fig. 4.1.9 but for the transitions to the 6.743 MeV (7/2⁻) + 6.792 MeV (1/2⁺) excited states of ^{11}B (open points and solid curve <6.74> at large angles) and for the transitions to the 6.743 MeV (7/2⁻) + 6.792 MeV (1/2⁺) + 6.864 MeV (5/2⁺) (^{13}C) excited states of ^{11}B and ^{13}C (full points and solid curve Σ) (upper panel) and for the transition to the 7.286 MeV (5/2⁺) excited state of ^{11}B (lower panel). The dashed curves <6.74>, <6.79> and <6.76> show the CRC cross sections for the individual transitions. The solid curve *Σ* is incoherent sum of these individual transitions at forward angles. The solid curve in lower panel is the CRC cross section for the coherent sum of the rotational model transition to the 7.286 MeV *(5/2⁺)* excited state of ^{11}B and reorientation of ^{11}B in this state.

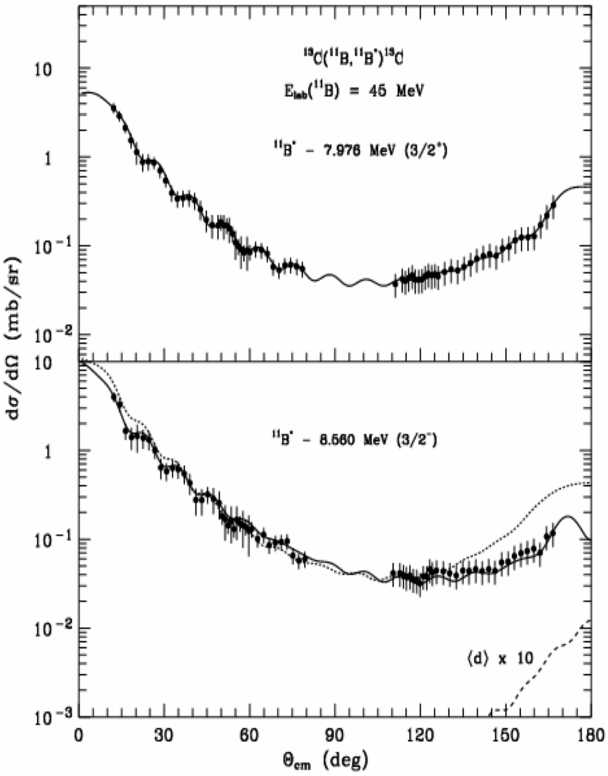

Fig. 4.1.11. The same as in Fig. 4.1.9 but for the transitions to the 7.976 MeV (3/2$^+$) excited state of ^{11}B (upper panel) and for the transition to the 8.560 MeV (3/2$^-$) excited state of ^{11}B. The solid curves are the CRC cross sections of these transitions. The dashed curve marked by <d> represents the CRC cross section for the deuteron transfer reaction. The dotted curve (lower panel) shows the CRC cross section for the transition to the 8.560 MeV (7/2$^-$) state of ^{11}B.

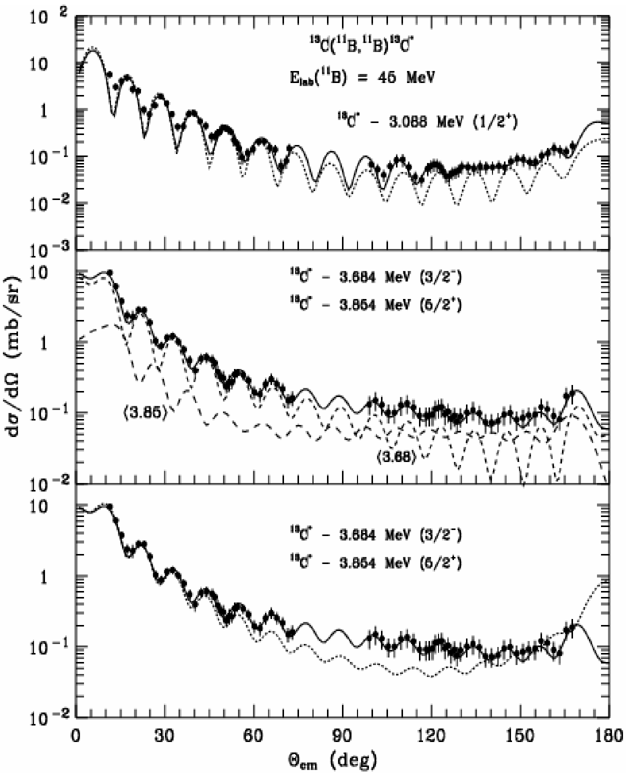

Fig. 4.1.12. Angular distributions of the ^{13}C(^{11}B, ^{11}B)^{13}C* inelastic scattering at the energy E_{LAB}(^{11}B) = 45 MeV (E_{CM} = 24.38 MeV) for the transitions to the 3.088 MeV (1/2$^+$) (upper panel) and 3.684 MeV (3/2$^-$)+3.854 MeV (5/2$^+$) (lower panel) excited states of ^{13}C, respectively. The solid and dotted curves show the CRC cross sections for the positive and negative deformation parameter δ_2 of ^{13}C. The dashed curves <3.68> and <3.85> represent the CRC cross sections for the individual transitions.

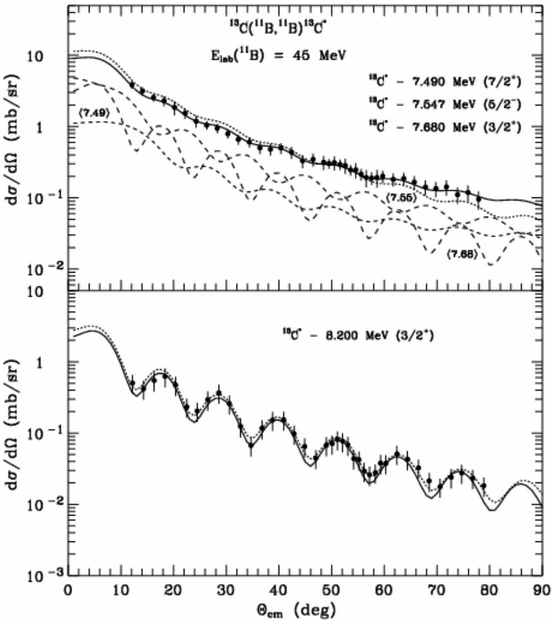

Fig. 4.1.13. The same as in Fig. 4.1.12 but for the transitions to the 7.490 MeV (7/2$^+$) + 7.547 MeV (5/2$^-$) + 7.680 MeV (3/2$^+$) (upper panel) and 8.2 MeV (3/2$^-$) (lower panel) excited states of ^{13}C, respectively. The solid and dotted curves show the CRC cross sections for the positive and negative deformation parameter δ_2 of ^{13}C. The dashed curves <7.49>, <7.55> and <7.68> represent the CRC cross sections for the individual transitions.

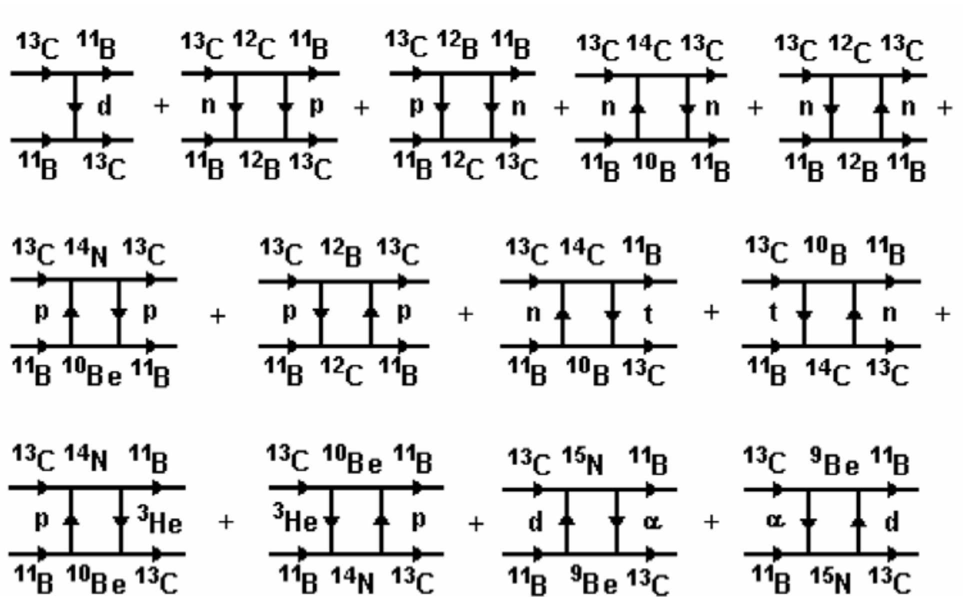

Fig. 4.1.14. Transitions to the excited states of ^{11}B and ^{13}C and diagrams of one- and two-step transfers in the ^{11}B + ^{13}C reactions.

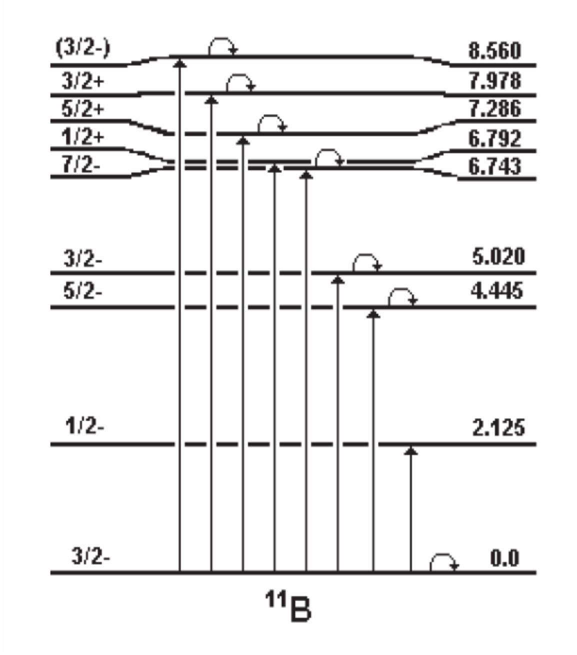

Fig. 4.1.15. Transitions to the excited states of ^{11}B. The transitions of the ^{11}B reorientations are marked with arc arrows.

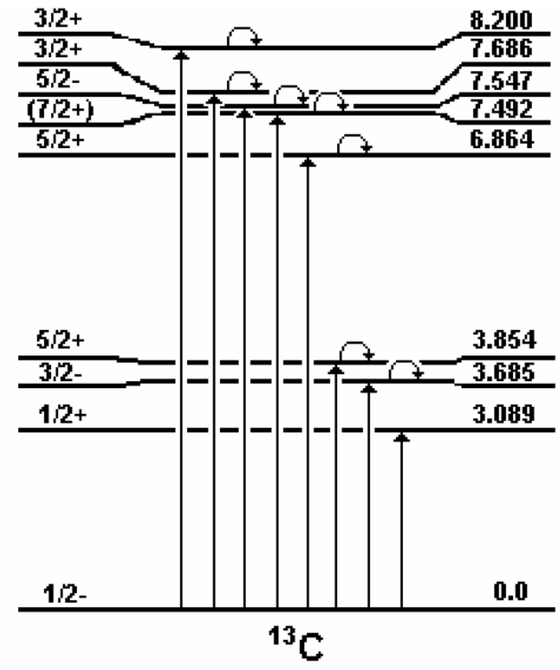

Fig. 4.1.16. Transitions to the excited states of ^{13}C. The transitions of the ^{13}C reorientations are marked with arc arrows.

The differences between the angular distributions of the ^{11}B + ^{13}C and ^{11}B + ^{12}C elastic and inelastic scattering at the close energies E_{CM} = 24.38 MeV (^{13}C), 23.48 MeV [178] and 25.57 MeV [6] (^{12}C) were illustrated above in Figs. 4.1.8 and 4.1.9. To analyze these differences (isotopic effects) in detail, it is useful to apply the following function describing the asymmetry

$$D(\theta) = \frac{\sigma_{13C} - \sigma_{12C}}{\sigma_{13C} + \sigma_{12C}} \ ,$$

where $\sigma_{13C}(\theta)$ and $\sigma_{12C}(\theta)$ are equal to $\sigma(\theta)/\sigma_R(\theta)$ for the ^{11}B + ^{13}C and ^{11}B + ^{12}C elastic scattering, respectively. For the inelastic scattering $\sigma_i(\theta) = d\sigma_i/d\Omega$.

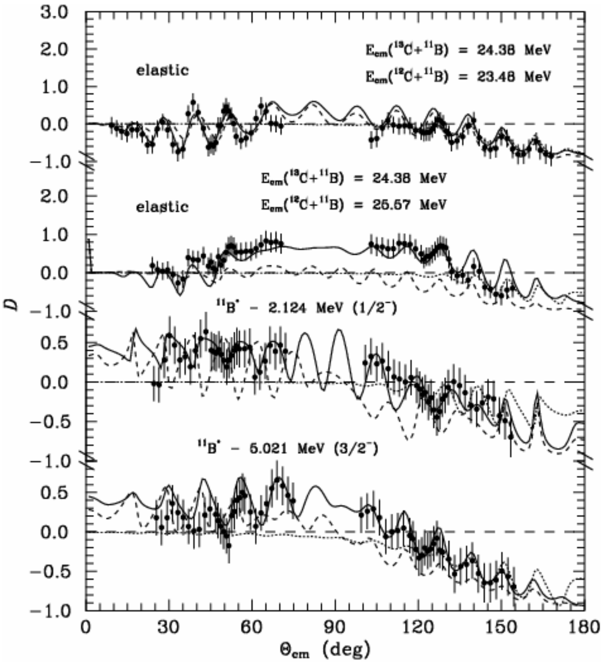

Fig. 4.1.17. Isotopic asymmetries $D(\theta) = (\sigma_{13C}(\theta) - \sigma_{12C}(\theta))/(\sigma_{13C}(\theta) + \sigma_{12C}(\theta))$ for the elastic and inelastic scattering ^{11}B + ^{13}C versus the ^{12}C + ^{11}B at $E_{LAB}(^{11}$B$)$ = 45 MeV and 49 MeV (E_{CM} = 24.38 MeV and 25.57 MeV), respectively. The dashed and solid curves show the $D(\theta)$-asymmetries for the corresponding CRC cross sections ($\sigma(\theta)/\sigma_R(\theta)$ for the elastic scattering) calculated for the ^{11}B + ^{13}C and ^{11}B + ^{12}C scattering with the same and individual OM parameters, respectively. The dotted curves represent the isotopic asymmetries $D(\theta)$ when only proton and deuteron transfers in the ^{12}C(^{11}B, ^{12}C)^{11}B and ^{13}C(^{11}B, ^{13}C)^{11}B reactions, respectively, are included.

The isotopic asymmetries $D(\theta)$ for and the inelastic scattering for the transitions to the 2.124 MeV (1/2$^-$) and 5.021 MeV (3/2$^-$) excited states of ^{11}B are shown in Fig. 4.1.15. The points and the curves represent $D(\theta)$ for the data and for the CRC cross sections, respectively. Two sets of the asymmetries $D(\theta)$ for the ^{11}B + ^{13}C elastic scattering at E_{CM} = 24.38 MeV versus the ^{11}B + ^{12}C elastic scattering at E_{CM} = 23.48 MeV [178] and 25.57 MeV [6] are illustrated in Fig. 4.1.17. This is done to compensate the lack of the ^{11}B + ^{12}C elastic scattering data at E_{CM} = 24.38 MeV. The asymmetries $D(\theta)$ have the diffraction structure, which is evidently caused by the angular shifts between the ^{11}B + ^{13}C and ^{11}B + ^{12}C angular distributions. The CRC asymmetries $D(\theta)$ describe the observed oscillations satisfactorily only if the individual OM potentials (see Table 4.1.3) were used for the ^{11}B + ^{13}C and ^{11}B + ^{12}C scattering (solid curves). If the same potential parameters are used for the both scattering, the CRC asymmetries $D(\theta)$ fail in description of the most data (dashed curves). Thus, a conclusion can be done that the OM potentials for the ^{11}B + ^{13}C and ^{11}B + ^{12}C scattering are different. However, as it is seen from Tables 4.1.1 and 4.1.3, the OM potentials differ only by the values of the parameters $a_V = a_W$ ($\Delta a_V = \Delta a_W$ = 0.07 fm). Other OM parameters are the same or differences between them are rather small.

For the large angles (θ_{CM} > 130°) the asymmetries $D(\theta) < 0$. It means that the cross sections for the ^{12}C(^{11}B, ^{12}C)^{11}B and ^{12}C(^{11}B, ^{12}C)^{11}B* reactions (proton transfer) are greater than for the ^{13}C(^{11}B, ^{13}C)^{11}B and ^{13}C(^{11}B, ^{13}C)^{11}B* reactions (deuteron transfer).

4.1.3. Scattering of ^{11}B + ^{14}C nuclei and quadrupole deformation of ^{14}C.

Angular distributions of the ^{11}B + ^{14}C elastic scattering and inelastic scattering for transitions to a few excited states of ^{14}C were measured at $E_{LAB}(^{11}$B$)$ = 45 MeV over the full angular range [12]. The data were analyzed within the coupled-reaction-channels method. The features of neutron-rich carbon isotopes was recently widely discussed [187 – 190]. A sign of the quadrupole deformation of the carbon isotopes is determined by the summary configuration of the proton and neutron distributions. The oblate + oblate, oblate + prolate and oblate + spherical proton and neutron distributions would lead, probably, to the negative (^{12}C, ^{18}C, ^{20}C, ^{22}C), positive or negative (^{10}C, ^{16}C) and negative (^{14}C) quadrupole deformations, respectively. However, a positive quadrupole deformation of ^{14}C was found from d(pol) + ^{14}C [191], α + ^{14}C [192] and ^{3}He + ^{14}C [193] inelastic scattering.

The angular distributions corresponding to the ^{11}B + ^{14}C elastic and inelastic scattering are shown in Figs. 4.1.18., 4.1.20. – 4.1.22. The errors for the poorly resolved peaks in the experimental energy spectra were less than 20%. The similar errors for the well resolved peaks were of about 10%.

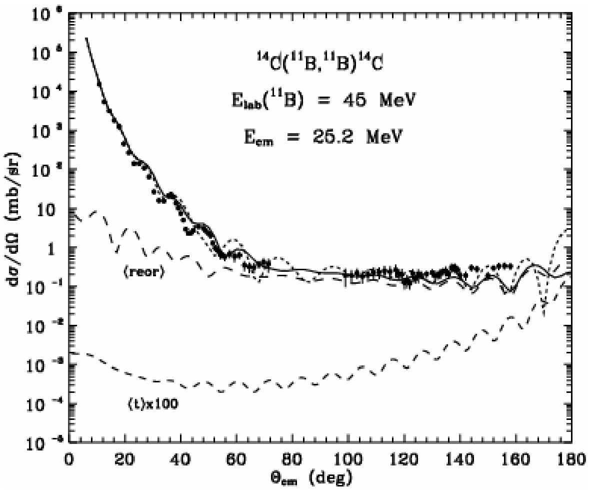

Fig. 4.1.18. Angular distribution of the ^{11}B + ^{14}C elastic scattering at $E_{LAB}(^{11}\text{B})$ = 45 MeV (E_{CM} = 25.2 MeV). The curves show the OM cross section for potential scattering (short-dashed) as well as contributions from the reorientation of ^{11}B (g.s.) (<reor>) and the triton transfer (<t>). The solid curve represents the coherent sum of all the processes in the elastic channel.

The elastic scattering data were fitted by the optical model calculations with four free parameters: N, the normalization factor of the real part V and the three parameters of the imaginary part: W, r_W and a_W. The following values of the parameters were found: N = 0.88, W = 5.8 MeV, r_W = 1.450 fm and a_W = 0.67 fm. The results of the optical model calculations are plotted in Fig. 4.9.18. Then, the couplings to the excited states of ^{14}C as well as reorientation of the ^{11}B ground state (see Fig. 4.1.19.) were included. The coupling scheme shown in Fig. 4.1.19. was limited to the states observed experimentally plus the (3^-) state, which was strongly populated in the ^{3}He [193] and α [192] scattering from ^{14}C. Since the direct transitions from the ground state to the 6.903 MeV (0^-) and 7.341 MeV (2^-) states are forbidden, these states were not included in the coupling scheme. In order to simplify the calculations, we also omitted the transitions between the ground and excited states of ^{11}B, since in previous investigations sub-Sections 4.1.1 and 4.1.2 only the ^{11}B ground state reorientation was found to play a significant role in the elastic channel. The values of the deformation lengths for transitions to different excited states observed experimentally were extracted from the fit to the experimental data at forward angles.

The contribution from t-exchange, which could play a significant role for the elastic channel for the backward scattering angles, was found to be negligible. In Figure 4.1.16, the curve labeled by <t> shows the calculated cross section for the triton transfer process in the ^{14}C(^{11}B, ^{14}C)^{11}B reaction. The process of ^{11}B reorientation (curve labeled <reor>), was found to be important at large angles. The solid curve shows the result of the coupled reaction channel calculation for the elastic channel. In this calculation, the depth of the imaginary part of the OM potential was reduced to 5.3 MeV.

The results of the coupled reaction channels calculation for the transition to the 7.012 MeV (2^+) state are shown in Fig. 4.1.20. According to Refs [191 – 193], this state was assumed to be rotational with the positive quadrupole deformation $\beta_2 \approx 0.25$ (see Table 4.1.5) that corresponds to $\delta_2 = \beta_2 R \approx 0.8$ fm for $R = 1.25A^{1/3}$ (dotted curve in Fig.

4.1.20). For quadrupole deformation $\beta_2 \approx 0.25$ value a phase mismatch is observed between the CRC angular distribution and the experimental data in the angular range 30° – 80°. In the present CRC calculations, when the sign of the quadrupole deformation was changed to negative the phase agreement was significantly improved. The best fit to the experimental data for the transition to the 7.012 MeV (2^+) state was obtained with $\delta_2 = -0.6 \pm 0.09$ fm, e.g., $\beta_2 = -0.2 \pm 0.03$ (Table 4.1.5). The results are plotted in Fig. 4.1.20 using the solid curve. A good agreement was obtained in the forward angle hemisphere. The results of CRC calculations with the positive quadrupole deformation ($\delta_2 = 0.8$ fm) for the transition to the 8.318 MeV (2^+) state are represented in Fig. 4.1.21 by the dotted curve. In this case, the calculated curve also does not reproduce the experimental data. However, in papers [189 – 190] the 8.318 MeV (2^+) state was predicted to have the oblate configuration. The calculations with $\delta_2 = -0.6 \pm 0.09$ fm gave good agreement with the experimental data, as it is shown in Fig. 4.1.21 using the solid curve.

The quadrupole deformation of the ^{14}C ground state was deduced to be negative ($\delta_2 = -\ 0.60 \pm 0.09$ fm), which is in a good agreement with the theoretical predictions [187], but in contradiction to the results of the previous analyses [191 - 193] of inelastic scattering, where the sign of the ^{14}C quadrupole deformation was found to be positive.

The CRC calculations with the assumption that the 6.094 MeV (1^-) state is of collective nature did not lead to as good description of the measured angular distribution. The results of the calculations with the dipole deformation length $\delta_1 = 0.4$ fm are presented in Fig. 4.1.22. using the solid curve. This value was extracted from the fit to the experimental data at the forward scattering angles. The estimated error is of the order of 15% (Table 4.1.5). Assuming the standard radius of the ^{14}C nucleus, $R = 1.25A^{1/3}$, the calculated value of the parameter β_1 is smaller than the values found in the deuteron and α scattering experiments [191, 192] (Table 4.1.5). However, taking into account the uncertainty of the order of 15% and assuming a similar error for β_1 extracted from the deuteron scattering [191], the two values are in good agreement.

Table 4.1.5 Parameters δ_λ and β_λ for ^{14}C.

$J_i^\pi \to J_f^\pi$	λ	δ_λ (fm)	β_λ (a)	β_λ [191]	β_λ [192]	β_λ [193]
$0^+ \to 1^-$	1	0.40±0.06	0.13±0.02	0.18	0.22	
$0^+ \to 3^-$	3	< 0.55	< 0.18	0.32	0.40	0.27, 0.20
$0^+ \to 2^+$ 7.012 MeV	2	–0.60±0.09	–0.20±0.03	0.27	0.29	0.25, 0.19
$0^+ \to 2^+$ 8.318 MeV	2	–0.60±0.09	–0.20±0.03	0.26	0.22	0.15, 0.09

(a) $\beta_\lambda = \delta_\lambda / R$ (for $R = 1.25A^{1/3}$, this work).

It was found that reorientation of the ^{11}B ground state plays an important role in the excitation of the (1^-) state. If this process is omitted, the calculated angular distribution becomes very oscillatory at backward angles (short-dashed curve in Fig. 4.1.22.).

The excited state 6.728 MeV (3^-) of ^{14}C could not be resolved experimentally from the two excited states of ^{11}B, 6.743 MeV ($7/2^-$) and 6.792 MeV ($1/2^+$). The calculations with $\delta_3 = 0.7$ fm (assuming the ratio $\delta_3/\delta_1 \approx 1.8$ as in [191 - 192]) has been done. This very strong octupole coupling had, of course, strong influence on the results for all the other channels. The most clearly visible effect was observed for the transition to the 8.318 MeV (2^+) state. Increasing δ_3 strongly damps the oscillations of the calculated curve and leads to values of the differential cross section that are too large. The best agreement was obtained with the octupole deformation length reduced to 0.2 fm.

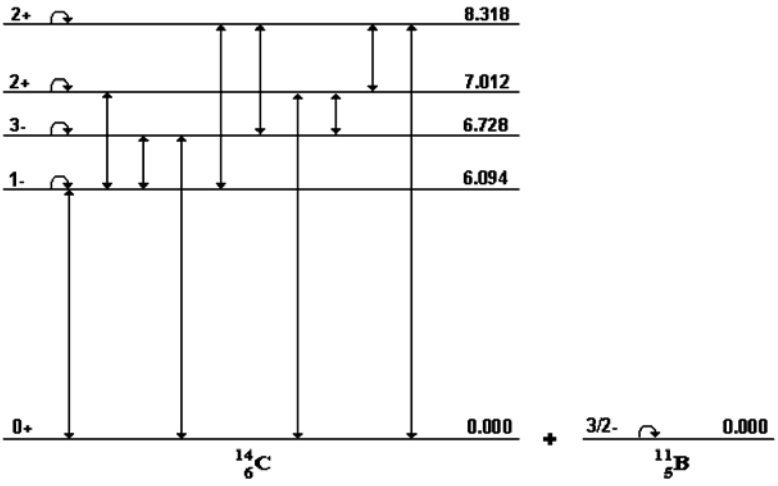

Fig. 4.1.19. Coupling scheme used in the CRC calculations.

A good review of the experimental and theoretical results concerning the structure of ^{14}C is given in the recent publication by von Oertzen et al. [190]. Most of the states of ^{14}C are predicted to be of the single particle nature, and their structure can be described by coupling of the two neutrons to the ground or the first excited states of the ^{12}C core.

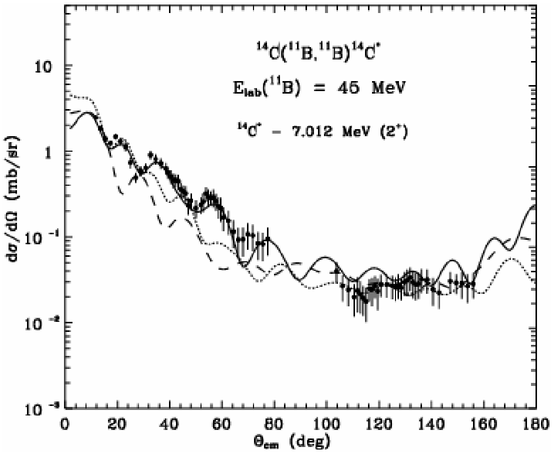

Fig. 4.1.20. Angular distribution of the $^{14}C(^{11}B, ^{11}B)^{14}C^*$ inelastic scattering at $E_{LAB}(^{11}B)$ = 45 MeV for the transition to the 7.012 MeV (2^+) excited state of ^{14}C. The curves show the CRC-calculations with δ_2 = 0.8 fm (dotted) and $\delta_2 = -0.6$ fm (solid). The long dashed curve corresponds to the $^{14}C = {}^{12}C$ (g.s.) + 2n model calculations.

The results of calculations for the transition to the 6.094 MeV (1^-) state are plotted in Fig. 4.1.23. using the dashed curve. The depth of the imaginary part of the projectile – core (^{11}B + ^{13}C) potential, W = 1.7 MeV, was deduced from the fit to the experimental data at backward angles. The dashed curve oscillates in the backward region, while the experimental data show rather smooth dependence on the scattering angle, within the error bars. Inclusion of the ^{11}B (g.s.) reorientation in the coupling scheme damped the oscillations and led to considerable improvement of the fit to the experimental data (dotted curve in Fig. 4.1.23.).

In order to account deformation of the ^{13}C core, we followed the procedure proposed in the paper by Keeley et al. [194], where for the ^{13}C ($1/2^+$) = ^{12}C + n system the effect of ^{12}C core deformation was simulated by a considerable enhancement of the binding potential radius. It was found from the best fit to the experimental data at backward angles that the binding potential radius for the ^{14}C (1^-) = ^{13}C (g.s.) + n system has to be increased to $R_V = 1.7 \times 13^{1/3}$ fm. The well depth of the binding potential was adjusted so that to obtain a correct binding energy of the ^{14}C (1^-) = ^{13}C (g.s.) +n system. The results are plotted in Fig. 4.1.21 using the solid curve. With this large value of the binding potential radius the rms radius of the valence neutron was found to be 5.157 fm. This suggests that the 6.094 MeV (1^-) state of ^{14}C can be a good candidate for the neutron halo state [195].

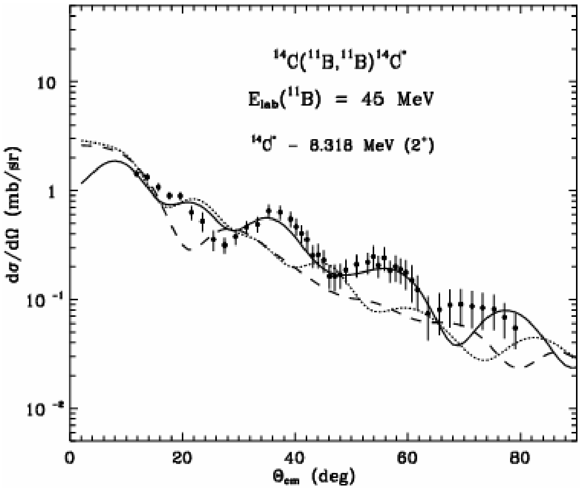

Fig. 4.1.21. As in Fig. 4.1.20 but for the transition to the 8.318 MeV (2^+) excited state of ^{14}C.

The 3.089 MeV ($1/2^+$) state of ^{13}C has long been described by a weak coupling of the sd shell nucleon to the ground and to the first excited states of the ^{12}C core, see e.g., [196]. The ground state of ^{13}C ($1/2^-$) has a dominant structure of the $P_{1/2}$ neutron coupled to the ground state of ^{12}C. The wave functions for the ground and first excited states of ^{13}C, calculated in the weak coupling basis in Ref. [197], were used in the analysis. The spectroscopic amplitudes are given in Appendix. The potential for the projectile – core (^{11}B + ^{12}C) interaction was taken from [198]. The depth of its imaginary part W = 5.0 MeV was deduced from the fit to the experimental data at backward angles. The potential for the projectile – particle ^{11}B + n interaction was taken from the global systematics [199]. The potential parameters were kept fixed. Finally, the potential binding the neutron to the ^{12}C core was taken to be of the Woods – Saxon form with the conventional radius $R_V = 1.25 \times 12^{1/3}$ fm and the diffuseness parameter $a_V = 0.65$ fm adopted from the paper of Keeley et al. [194]. The depth of this potential was adjusted to give the correct binding energies of the respective ^{13}C (g.s., exc.) = ^{12}C + n systems.

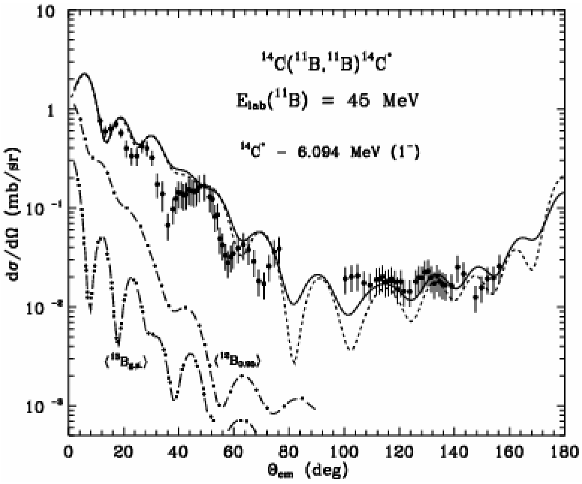

Fig. 4.1.22. Angular distribution of the $^{14}C(^{11}B, ^{11}B)^{14}C^*$ inelastic scattering at $E_{LAB}(^{11}B)$ = 45 MeV for the transition to the 6.094 MeV (1^-) excited state of ^{14}C. The solid and dashed curves correspond to the CRC-calculations using the deformation length δ_1 = 0.4 fm with and without ^{11}B (g.s.) reorientation included in the coupling scheme, respectively. The curves labeled <$^{12}B_{0.95}$> and <$^{13}B_{g.s.}$> show the calculated contributions from the $^{14}C(^{11}B, ^{12}B_{0.95})^{13}C$ and $^{14}C(^{11}B, ^{13}B)^{12}C$ transfer reactions, respectively.

The results of the calculations for the transition to the 3.089 MeV ($1/2^+$) state of ^{13}C are plotted in Fig. 4.1.24 using the dashed curve. Similarly, as in the previous case, the dashed curve oscillates at backward angles, while the experimental data do not show such structure, despite the large error bars. Inclusion of the ^{11}B (g.s.) reorientation in the coupling scheme damps the oscillations in the backward angle region (dotted curve in Fig. 4.1.24). Keeley et al. [194] has shown that the wave function of the $2S_{1/2}$ neutron, calculated in a spherical ^{12}C + n potential with an enlarged radius ($R_V = 2.0 \times 12^{1/3}$ fm), will be equivalent to the wave function calculated in a deformed ^{12}C + n potential with the conventional radius ($R_V = 1.25 \times 12^{1/3}$ fm). When, following this method, the binding-potential radius of the ^{13}C ($1/2^+$) = ^{12}C + n system increases to $R_V = 2.0 \times 12^{1/3}$ fm, the best agreement with the backward-region data (solid curve in Fig. 4.1.24) was obtained. Thus, taking into account the reorientation of the ^{11}B nucleus in its ground state and a large quadrupole oblate deformation of the ^{12}C core

[194], one can obtain the improvement of the fit to the experimental data in the backward angle region. In this case, the rms radius of the valence neutron wave function in the 3.088 MeV ($1/2^+$) state has turned out to be 5.453 fm, which is in a good agreement with the value of 5.04±0.75 fm obtained in Ref. [200]. Thus, this result supports the prediction of Liu et al. [195] that this state is the candidate for the nuclear halo state.

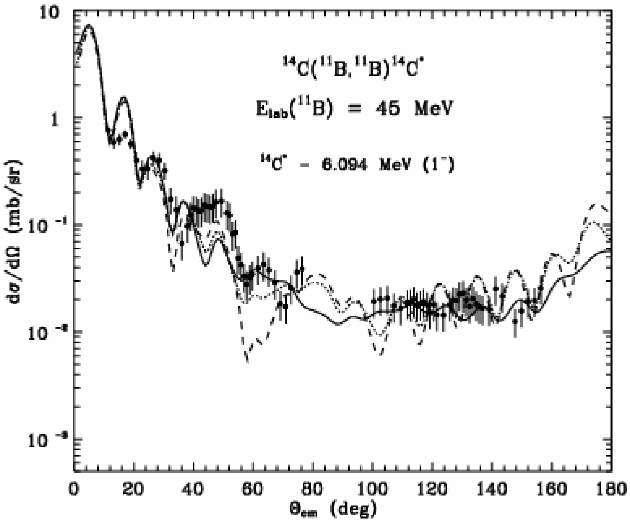

Fig. 4.1.23. Angular distribution of the ^{14}C(^{11}B, ^{11}B)^{14}C* inelastic scattering at E_{LAB}(^{11}B) = 45 MeV for the transition to the 6.094 MeV (1^-) excited state of ^{14}C. The dashed curve shows the ^{14}C = $^{13}C_{\text{g.s.}}$ + n model calculations with the conventional radius of the binding potential and without ^{11}B$_{\text{g.s.}}$ reorientation included in the coupling scheme, the dotted curve corresponds to the same calculations but with the ^{11}B$_{\text{g.s.}}$ reorientation included. The solid curve shows the results with the enlarged radius of the binding potential and with the ^{11}B$_{\text{g.s.}}$ reorientation included.

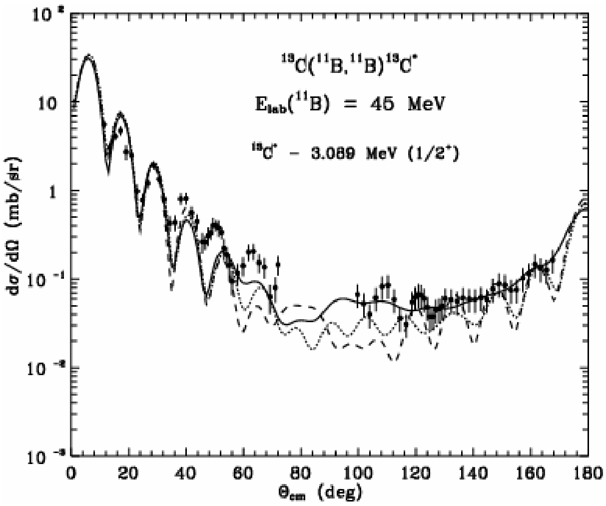

Fig. 4.1.24. As in Fig. 4.1.23. but for the ^{13}C(^{11}B, ^{11}B)^{13}C* inelastic scattering at E_{LAB}(^{11}B) = 45 MeV leading to the 3.089 MeV ($1/2^+$) excited state of ^{13}C.

The results of CRC calculations for the transition to the 7.012 MeV (2^+) state of ^{14}C are plotted in Fig. 4.1.20. as the long-dashed curve. This curve underestimates the data in the angular range 30° – 80°. The depth W = 3.0 MeV of the imaginary part of the projectile – core (^{11}B + ^{12}C) potential was obtained from the fit to the experimental data at backward angles. In Figure 4.1.20, the results of the ^{12}C$_{\text{g.s.}}$ + 2n model calculations for the transition to the 8.318 MeV (2^+) state are plotted using the long-dashed curve. In this case the depth of the projectile–core imaginary potential was reduced to zero. The long-dashed curve does not reproduce the experimental data. These calculations suggest that both the 7.012 MeV (2^+) and 8.318 MeV (2^+) states of ^{14}C have a predominantly the collective nature. However, it seems that the model used in the present calculations may be inappropriate for the 7.012 MeV and 8.318 MeV (2^+) states of ^{14}C, since in the paper of von Oertzen et al. [190] it was suggested that these states are based rather on the 4.439 MeV (2^+) excited state of the ^{12}C core.

The quadrupole deformation of the ^{14}C ground state was deduced to be negative ($\delta_2 = -0.60 \pm 0.09$ fm), which is in a good agreement with the theoretical predictions [187], but in contradiction to the results of the previous analyses [191, 192, 193] inelastic scattering, where the sign of the ^{14}C quadrupole deformation was found to be positive.

4.1.4. Scattering of ^{11}B + ^{9}Be nuclei optical potential, the ALAS phenomenon and ^{9}Be and ^{11}B reorientation.

The results of the study of the ^{11}B + ^{9}Be elastic and inelastic scattering measured in the full angular range at the energy $E_{LAB}(^{11}\mathrm{B})$ = 45 MeV (E_{CM} = 20.25 MeV) are presented in this sub-Section [8]. The experimental data with their absolute errors and results of theoretical calculations are shown in Figures 4.1.25 – 4.1.30. The error of the cross section normalization is about 10%. In these figures one can observe an anomalously large enhancement of the cross-section at the backward angles (ALAS). The ALAS phenomenon is also considered in this work for scattering of ^{11}B + ^{13}C [9] in the sub-Section 4.1.2 and for ^{14}N + ^{7}Li [7] scattering in the sub-Section 4.3.1. In the past, ALAS was studied, for example, in the scattering of ^{12}C + ^{24}Mg [110], ^{16}O + ^{28}Si [111], ^{7}Li + ^{12}C [112 – 114], ^{6}Li + ^{12}C [115 – 120], α particles by ^{16}O and ^{40}Ca [121], ^{24}Mg and ^{28,30}Si [122]. A review of the theoretical approach to the ALAS problem is presented in e.g. [121]. It was found that in each case the ALAS has specific mechanism, different for different reaction. The data for energies $E_{\mathrm{CM}} \approx 9 - 22$ MeV [149, 150], known from the literature, were also included in the CRC analysis.

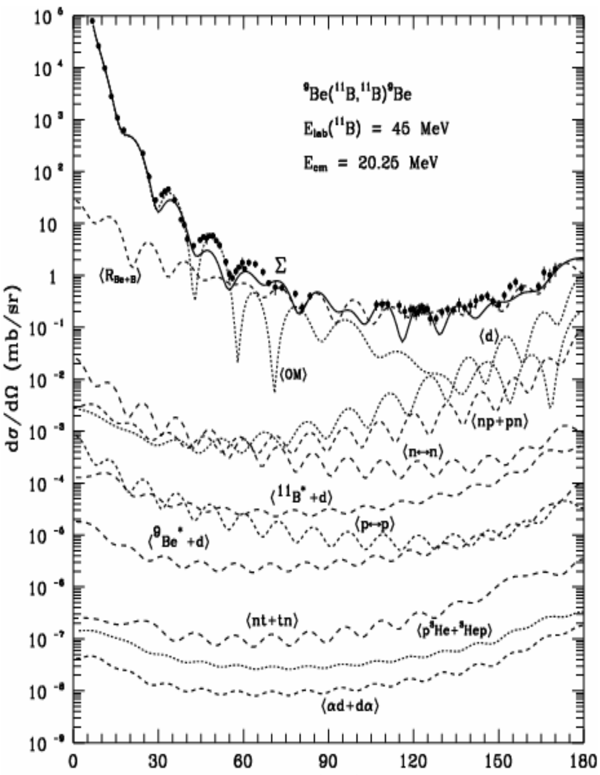

Fig. 4.1.25. Angular distribution of the ^{9}Be(^{11}B, ^{11}B) elastic scattering at the energy $E_{LAB}(^{11}\mathrm{B})$ = 45 MeV (E_{CM} = 20.25 MeV). The dashed curves marked by <OM> and <R_{Be+B}> show the OM cross section and a coherent sum of the ^{9}Be+^{11}B reorientations, respectively. The other dashed curves <d>, <^{11}B* +d>, <^{9}Be* +d>, <np + pn>, <nt + tn>, <αd + dα>, <p ^{3}He + ^{3}He p>, <n ↔n> and <p↔ p> represent the CRC cross sections for the transfers corresponding to diagrams shown in Fig. 4.1.31. The curves marked by <^{11}B* + d> and <^{9}Be* + d> correspond to the 2.125 MeV ($1/2^{-}$) state of ^{11}B and 2.429 MeV ($5/2^{-}$) state of ^{9}Be, respectively. The solid curve Σ shows the sum of CRC cross sections for all processes.

The data for the ^{11}B + ^{9}Be elastic scattering were analyzed within the optical model using potential of Woods–Saxon type with imaginary part W_S. The CRC cross section was fitted to the data of the ^{11}B + ^{9}Be elastic scattering at large angles by varying only the parameter W_S. Transitions and transfers corresponding to diagrams in Fig. 4.1.31 were included in calculations. The sets of the optical potential parameters, obtained in the fitting procedures within the OM and CRC method, are listed in Table 4.1.6. The multipole deformation lengths δ_λ obtained in the analysis of the data are listed in Table 4.1.7.

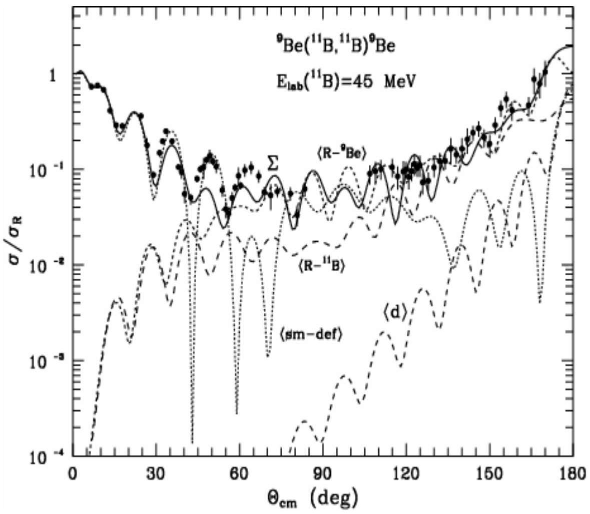

Fig. 4.1.26. Angular distribution of the ^{9}Be(^{11}B, ^{11}B) elastic scattering in units of the Rutherford cross section at the energy E_{LAB}(^{11}B) = 45 MeV. The dashed curves <R–^{9}Be>, <R–^{11}B>, <d> and <sm–def> show the ratio $\sigma(\theta)/\sigma_R(\theta)$ for the reorientations of ^{9}Be, ^{11}B, deuteron transfer reaction and (weakly-deformed) potential elastic scattering, respectively. The solid curve Σ shows the CRC coherent sum of the reorientations and deuteron transfer for a deformed potential with the deformation lengths listed in Table 4.1.7.

Table 4.1.6. Parameters of Woods–Saxon OM potentials for the $P + T$ scattering ($R = r_i(A^{1/3}{}_T + A^{1/3}{}_P)$, $i = V,W,C$)

$P+T$	E_{CM} (MeV)	V (MeV)	r_V (fm)	a_V (fm)	W_S (MeV)	r_W (fm)	a_W (fm)	r_C (fm)
^{11}B + ^{9}Be	8.80	81.0	1.150	0.690	7.0	1.350	0.690	1.250
^{11}B + ^{9}Be	14.85	153.8	0.860	0.716	9.2	1.250	0.716	1.250
^{11}B + ^{9}Be	20.25	187.3	0.788	0.730	10.4	1.236	0.730	1.250
^{11}B + ^{9}Be	20.35	180.0	0.788	0.750	11.4	1.236	0.750	1.250
^{11}B + ^{9}Be	22.00	202.0	0.788	0.760	12.7	1.236	0.760	1.250

The reorientation mechanism was applied in both elastic and inelastic scattering channels It was found that the cross section for the reorientation equals about 10 – 20% of the integrated cross section, for a given channel. The reorientation mechanism is expected to be rather small for the inelastic scattering. Previously we have already found that reorientation plays a crucial role for the elastic scattering of ^{12}C + ^{9}Be [4] and ^{14}N + ^{7}Li [7] at backward angles. The contribution of the reorientations to the forward hemisphere is rather small, due to the dominance of the Coulomb scattering in this angular range. Transitions in the reverse direction (not shown in Fig. 4.1.31) were also included in the coupling scheme.

The CRC analysis was performed in the following steps. At the beginning, the ^{11}B + ^{9}Be elastic and inelastic channels for the transitions to the excited states of ^{11}B only were included in the coupling scheme to fit W_S and the deformation lengths δ_λ for ^{11}B. In the second step, the elastic and inelastic channels for the transitions to the excited states of ^{9}Be were included in the coupling scheme to correct W_S and fit the deformation lengths δ_λ for ^{9}Be. In the next step, the CRC cross section of each transfer reaction corresponding to the diagrams of Fig. 4.1.31, was calculated. The optical potential parameters for the intermediate channels were used the same as for the ^{11}B + ^{9}Be elastic scattering (see Table 4.1.6).

Our data of angular distribution of the ^{11}B + ^{9}Be elastic scattering are shown in Figs. 4.1.25 and 4.1.26. As one can see in Fig. 4.1.26, the OM cross section (curve <OM>) fitted to the forward angle data cannot describe the data at large angles. To explain the observed ALAS, we have investigated many one-step and two-step processes corresponding to diagrams of Fig. 4.1.31 and 4.1.32.

Table 4.1.7. Transition multipolarity and deformation parameters of nuclei (β_λ for $R = 1.25A^{1/3}$ fm)

Nuclei	E_x (MeV)	J^π	λ	δ_λ (fm)	β_λ
^{9}Be	1.684	$1/2^+$	1	2.0	0.77
	2.429	$5/2^-$	2	2.4	0.92
			4	0.4	0.15
	2.78, 7.94	$1/2^-$	2	2.4	0.92
	3.049	$5/2^+$	1	2.0	0.77
			3	1.0	0.38
	4.704	$3/2^+$	1	2.0	0.77
			3	1.0	0.38
	6.760	$7/2^-$	2	2.4	0.92
			4	0.4	0.15
^{11}B	2.125	$1/2^-$	2	1.2	0.43
	4.445	$5/2^-$	2	1.2	0.43
			4	1.0	0.36
	5.020	$3/2^-$	2	1.2	0.43
	6.743	$7/2^-$	2	1.2	0.43
			4	1.0	0.36
	6.792	$1/2^+$	1	1.0	0.36
	7.286	$5/2^+$	1	1.0	0.36
			3	1.2	0.43
	7.978	$3/2^+$	1	1.0	0.36
			3	1.2	0.43
	8.560	$3/2^-$	2	1.8	0.65

All the transfer reactions, especially the three and four-nucleon cluster transfers, contribute rather weakly to the elastic channel. Only the direct deuteron transfer plays a certain role in the large-angle elastic scattering. The two-step deuteron transfers were calculated for all the intermediate excited states of ^{11}B and ^{9}Be presented in level diagrams of Fig. 4.1.31. The corresponding CRC cross sections were found to be small as in the cases shown in Fig. 4.1.25 (curves <^{11}B* + d>) and <^{9}Be* + d>).

As one can see in Figs. 4.1.25 and 4.1.26, the reorientations of ^{9}Be and ^{11}B are the dominant processes at large angles. To illustrate in detail the nuclear interaction processes, in Fig. 4.1.26 we present the experimental data of the ^{11}B + ^{9}Be ^{9}Be + ^{11}B elastic scattering and the CRC angular distributions in the units of the Rutherford cross section, $\sigma(\theta)/\sigma_R(\theta)$. The dashed curves <R–^{9}Be>, <R–^{11}B> and <d> show the angular distributions for the ^{9}Be, ^{11}B reorientations and for the direct deuteron transfer, respectively. To illustrate the importance of the nuclear-potential deformation in elastic scattering, the CRC angular distribution was calculated with the small deformation lengths $\delta_\lambda = 0.001$ fm for ^{11}B (see dashed curve <sm–def>). In this case the optical potential form is very close to the spherically symmetric one and the CRC and OM angular distributions are practically identical. As one sees in Fig. 4.1.26, the data for the large-angle elastic scattering cannot be described using a weakly-deformed OM potential. Fig. 4.1.25 shows that the reorientations of ^{9}Be and ^{11}B dominate at large angles $\theta_{CM} > 130^\circ$.

The angular distributions of the ^{11}B + ^{9}Be inelastic scattering at $E_{LAB}(^{11}\mathrm{B}) = 45$ MeV are shown in Figs. 4.1.27 for different excited states of ^{9}Be and ^{11}B. Figure 4.1.27 shows the angular distributions of the ^{11}B + ^{9}Be inelastic scattering for the transitions to the excited states of ^{9}Be. The CRC angular distributions satisfactorily describe the ^{11}B + ^{9}Be inelastic scattering data in the angular range $\theta_{CM} \approx 20^\circ$–$80^\circ$.

Figure 4.1.28 shows the angular distributions of the ^{11}B + ^{9}Be inelastic scattering for the transitions to the excited states of ^{11}B. Only the direct deuteron transfer gives a considerable contribution at the backward angles (see dashed curves <d>). The indirect deuteron transfers are rather negligible. The difference between the solid and dotted curves at large angles shows that the direct deuteron transfer contributes only at $\theta_{CM} > 130^\circ$.

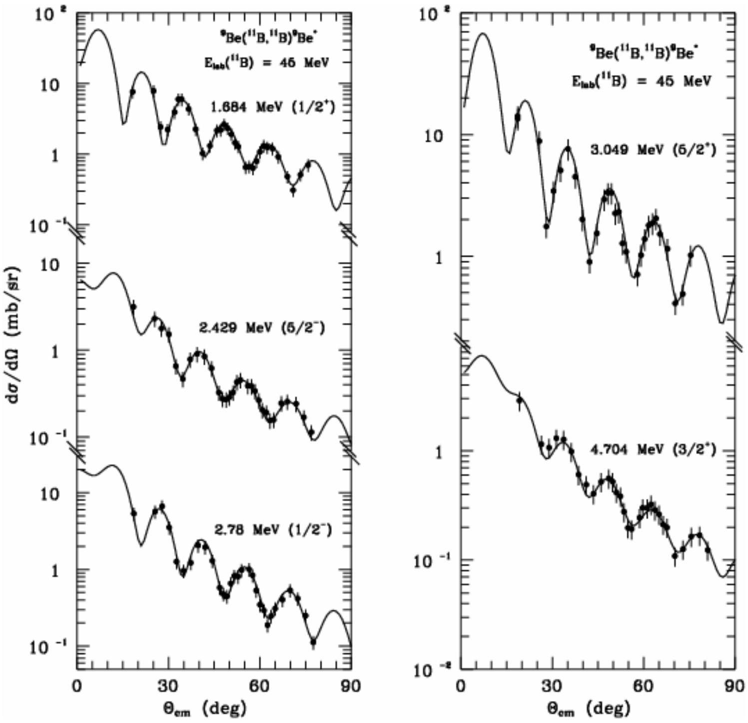

Fig. 4.1.27. Angular distributions of the ^{9}Be(^{11}B, ^{11}B)^{9}Be* inelastic scattering at the energy E_{LAB}(^{11}B) = 45 MeV for the transitions to the 1.684 MeV ($1/2^+$), 2.429 MeV ($5/2^-$), 2.78 MeV ($1/2^-$), 3.049 MeV ($5/2^+$) and 4.704 MeV ($3/2^+$) excited states of ^{9}Be. The solid curves represent the CRC cross sections for the rotational model with the transition multipolarity and deformation parameters of ^{9}Be listed in Table 4.1.7.

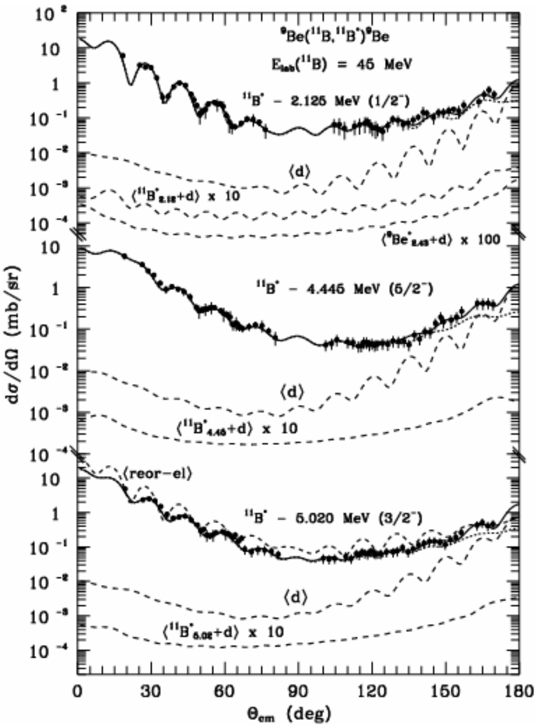

Fig. 4.1.28. The same as in Fig. 4.1.27 but for the transitions to the 2.125 MeV ($1/2^-$), 4.445 MeV ($5/2^-$) and 5.020 MeV ($3/2^-$) excited states of the ^{11}B nucleus. The dashed curves marked by <d>, <^{11}B*$_{2.12}$ + d>, <^{11}B*$_{4.45}$ + d>, <^{11}B*$_{5.02}$ + d> and <^{9}Be*$_{2.43}$ + d> represent the cross sections for the one-step deuteron transfer and two-step deuteron transfers through the intermediate 2.125 MeV ($1/2^-$), 4.445 MeV ($5/2^-$), 5.02MeV ($3/2^-$) states of ^{11}B and 2.429 MeV ($5/2^-$) state of ^{9}Be, respectively. The dotted curves represent the CRC cross sections for the rotational model with the transition multipolarity and deformation parameters of ^{9}Be listed in Table 4.1.7. The solid curves show the coherent sums of all processes. The dashed curve <reor–el> represents the reorientation of ^{11}B in the ground state.

The role of reorientations in the excited nuclear states was studied for the transitions to the 7.286 MeV ($5/2^+$) state of ^{11}B (see Fig. 4.1.29). It is rather small for this excited state of ^{11}B, as well as for the other excited states. In this case, the direct deuteron transfer is forbidden and the two-step processes are negligible. The solid curve for this transition shows the CRC cross section of the rotational model, which in this case predicts an enhancement of the large angle inelastic scattering.

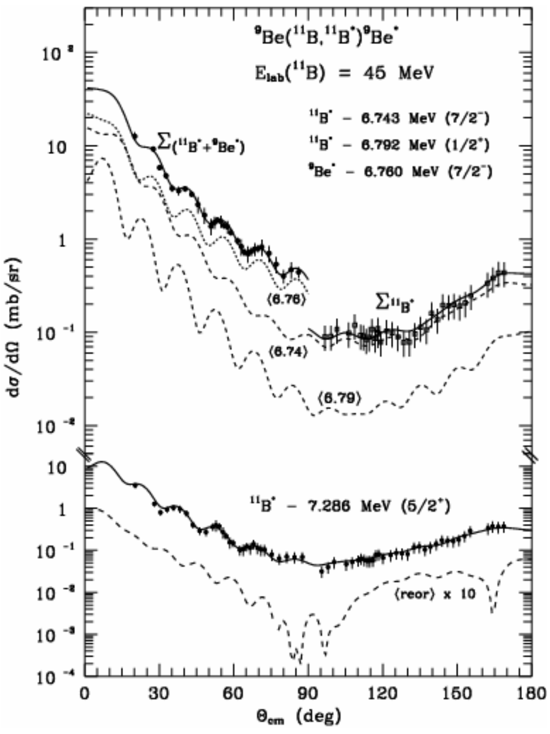

Fig. 4.1.29. The same as in Fig. 4.1.27 but for the transitions to the 6.743 MeV (7/2$^-$) + 6.792 MeV *(*1/2$^+$*)* excited states of ^{11}B (open points and curve Σ_{11B*}) and for the transitions to the 6.743 MeV (7/2$^-$) + 6.792 MeV (1/2$^+$) + 6.760 MeV (7/2$^-$) (^{9}Be) excited states of ^{11}B and ^{9}Be (the full points and the curve $\Sigma_{(11B*+9Be*)}$) and for the transition to the 7.286 MeV (5/2$^+$) excited state of ^{11}B. The dashed curves <6.74>, <6.79> and <6.76> show the CRC cross sections for the individual transitions. The solid curves $\Sigma_{(11B*+9Be*)}$ and Σ_{11B*} are incoherent sums of these individual transitions (unresolved in the experiment) for forward and backward angles, respectively. The solid and dashed <reor> curves for the transition to the 7.286 MeV *(*5/2$^+$*)* excited state of ^{11}B show the direct transition 3/2$^-$ →5/2$^+$ and reorientation 5/2$^+$ →5/2$^+$, respectively.

Figure 4.1.29 shows also the angular distribution of the ^{11}B + ^{9}Be inelastic scattering. The description of the transition to the 6.792 MeV (1/2$^+$) excited state of ^{11}B is rather poor in the full angular range. The incoherent sum of the CRC cross sections for all the transitions (solid curve <$\Sigma_{(11B*+9Be*)}$>) gives a good description of the data at the forward angles. The transition to the 6.743 MeV (7/2$^-$) excited state of ^{11}B is dominant at the backward angles. The dashed curve <6.74> shows the coherent sum of the CRC cross sections of the direct transition, reorientation of ^{11}B in the 6.743 MeV (7/2$^-$) excited state and in the deuteron transfer. The solid curve <Σ_{11B*}>, which represents the incoherent sum of the CRC cross sections for the transitions to the 6.743 MeV (7/2$^-$) + 6.792 MeV (1/2$^+$) excited states of ^{11}B, well describes the data at $\theta_{CM} > 90^o$.

Figure 4.1.30 shows the angular distributions of the ^{11}B + ^{9}Be inelastic scattering for the transitions to the 7.978 MeV (3/2$^+$) + 7.940 MeV (1/2$^-$) (^{9}Be) excited states of ^{9}Be and ^{11}B, unresolved in the experiment at forward angles. The dashed curves <7.94>, <7.98> and <$\Sigma_{(11B*+9Be*)}$> show the CRC cross sections for the individual transitions and their incoherent sum, respectively, at $\theta_{CM} < 90^o$. The open points and the solid curve <7.98> at backward angles represent the data and the CRC cross section for the transition to the 7.978 MeV (3/2$^+$) excited states of ^{11}B. The solid curves <$\Sigma_{(11B*+9Be*)}$> and <7.98> well describe the data for the above mentioned transitions.

The angular distributions for the transition to the 8.56 MeV (3/2$^-$) excited state of ^{11}B are presented in Fig. 4.1.30. The dashed curve <d> shows the direct deuteron transfer, which gives a non-negligible contribution only at $\theta_{CM} > 150^o$ (see the difference between the solid and dotted curves). The coherent sum (solid curve) of the CRC cross sections for direct transition, the reorientation of ^{11}B in the excited state and the deuteron transfer well describe the data. The direct transition dominates and provides the observed ALAS for this transition.

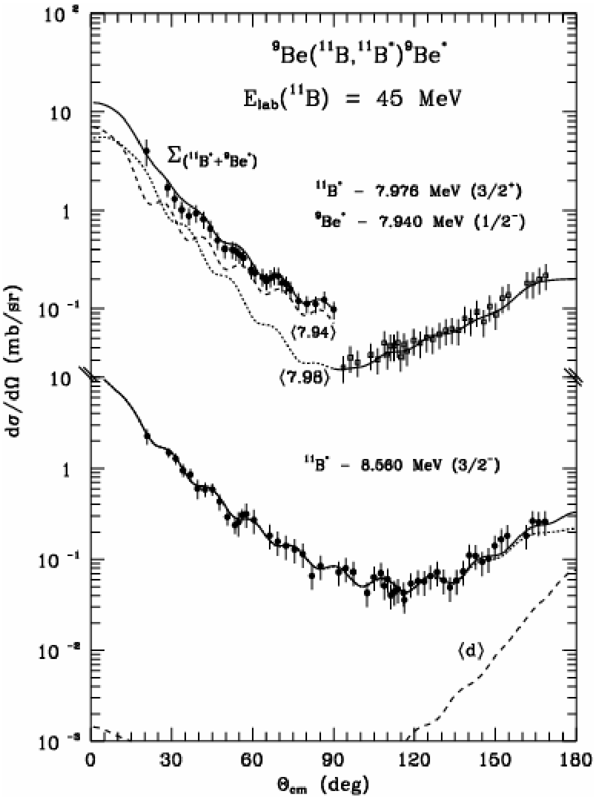

Fig. 4.1.30. The same as in Fig. 4.1.27 but for the transitions to the 7.976 MeV (3/2$^+$) + 7.940 MeV (1/2$^-$) (^{9}Be) excited states of ^{11}B and ^{9}Be (the full points and the curve $\Sigma_{(11B*+9Be*)}$) and for the transitions to the 7.976 MeV (3/2$^+$) excited state of ^{11}B (the open squares at large angles and the solid curve <7.98>) and for the transition to the 8.560 MeV (3/2$^-$) excited state of ^{11}B. The dashed curves <7.94> and <7.98> show the CRC cross sections for the individual transitions. The solid curves $\Sigma_{(11B*+9Be*)}$ are incoherent sums of these individual transitions. The dashed curve marked by <d> represents the CRC cross section for the deuteron transfer.

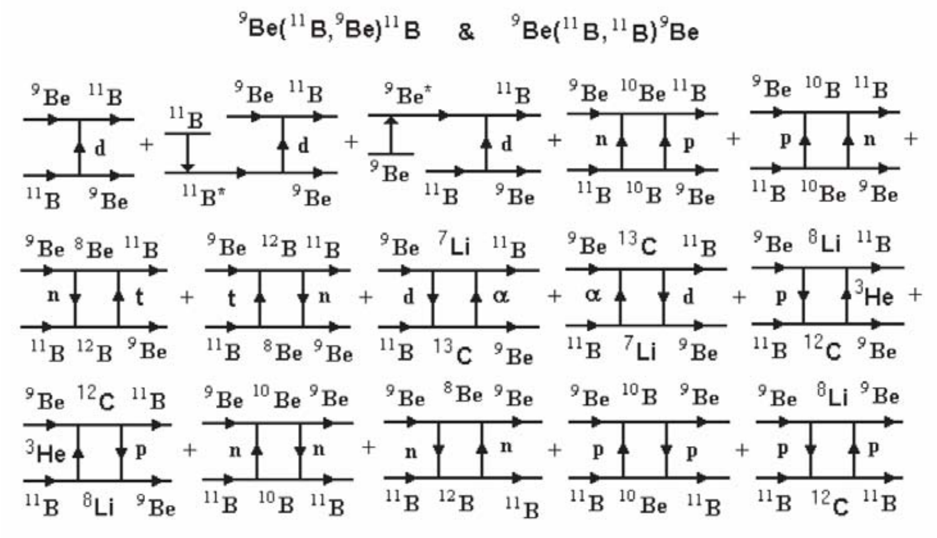

Fig. 4.1.31. Diagrams of the one- and two-step transfers in the ^{9}Be(^{11}B, ^{9}Be)^{11}B and ^{9}Be(^{11}B, ^{11}B)^{9}Be reactions. and transitions to the excited states of ^{11}B and ^{9}Be. The transitions of the ^{11}B and ^{9}Be reorientations are marked with arc arrows.

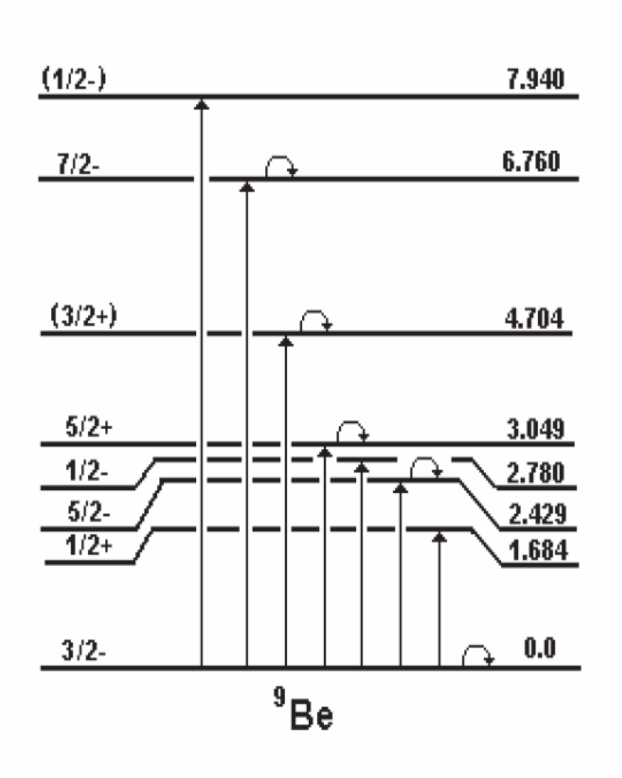

Fig. 4.1.32. Transitions to the excited states of ^{9}Be. The transitions of the ^{9}Be reorientations are marked with arc arrows. Transitions to the excited states of ^{11}B are shown in Fig. 4.1.15.

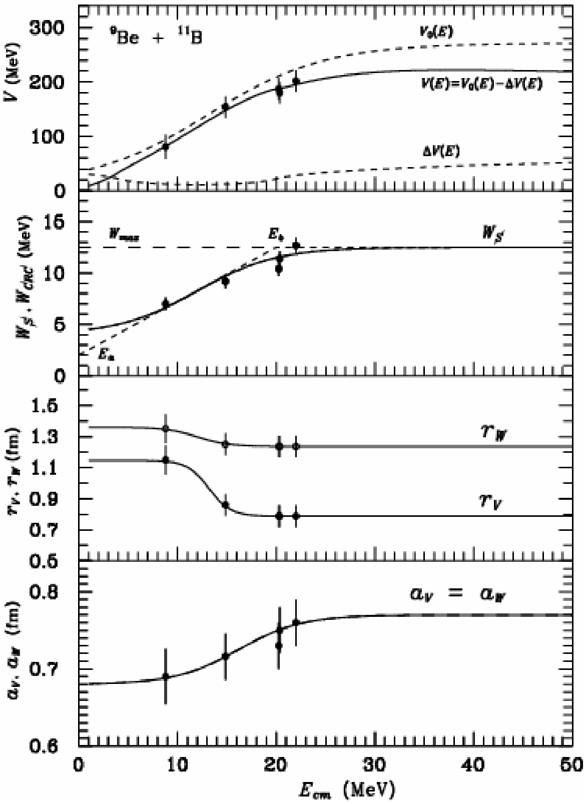

Fig. 4.1.33. Energy dependence of the OM potential parameters for the ^{11}B + ^{9}Be interactions.

Table 4.1.8. Parameters of the energy dependence for the OM potential of the ^{11}B + ^{9}Be elastic scattering.

X_i	V_0 (MeV)	W_S (MeV)	r_V (fm)	r_W (fm)	a_V (fm)	a_W (fm)
$X_i^{\min}$	9.1	4.0	0.788	1.236	0.680	0.680
$X_i^{\max}$	270.9	12.5	1.146	1.360	0.770	0.770
E_{Xi}(MeV)	13.1	12.0	13.175	12.000	16.200	16.200
E_{Xi}(MeV)	5.9	4.0	1.100	1.600	3.200	3.200

The energy dependence parameters E_{Xi}, ΔE_{Xi}, $X_i^{\max}$ and $X_i^{\min}$ of the optical potential of the ^{9}Be + ^{11}B nuclei are listed in Table 4.1.8. The energy dependence of OM parameters for these nuclei are shown in Fig. 4.1.33.

Different explanations of the ALAS phenomenon in the elastic scattering had been proposed in the literature, e.g., a weak absorption in the collision process (a small imaginary part of the optical potential), direct cluster transfer or compound nucleus process. In the reaction under consideration we have found that the ^{9}Be and ^{11}B reorientations in the ground states combined with the weak absorption dominate in the large angle elastic scattering. On the contrary, the reorientations of these nuclei in the excited states is rather marginal as being a higher order process.

4.1.5. The elastic and inelastic scattering of ^{11}B + ^{7}Li nuclei, optical potential and ^{7}Li deformation parameters.

The angular distributions of the ^{11}B + ^{7}Li elastic and inelastic scattering [13] were measured at $E_{LAB}(^{11}\mathrm{B}) = 44$ MeV for the transitions to the ground and excited states of ^{7}Li and ^{11}B. The present data and data taken from the literature at $E_{LAB}(^{7}\mathrm{Li}) = 34$ MeV [108, 109] were analyzed within the optical model and the coupled-reaction-channels methods.

The measured angular distributions of the elastic and inelastic scattering of ^{7}Li + ^{11}B together with results of theoretical calculations [9] are shown in Figs. 4.1.34 –4.1.35. The error of the cross section normalization is about 15%.

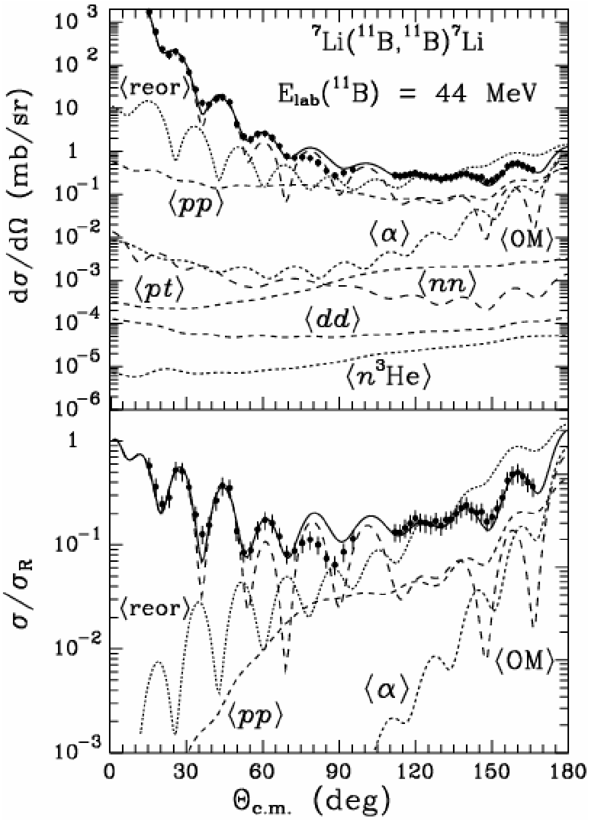

Fig. 4.1.34. Angular distributions of ^{11}B + ^{7}Li elastic scattering at $E_{LAB}(^{11}\mathrm{B}) = 44$ MeV. The curves show the OM and CRC angular distributions of the potential scattering (curves <OM>), reorientations of ^{7}Li and ^{11}B (curves <reor>) and transfers (other curves). The solid curves represent the coherent sums of these processes.

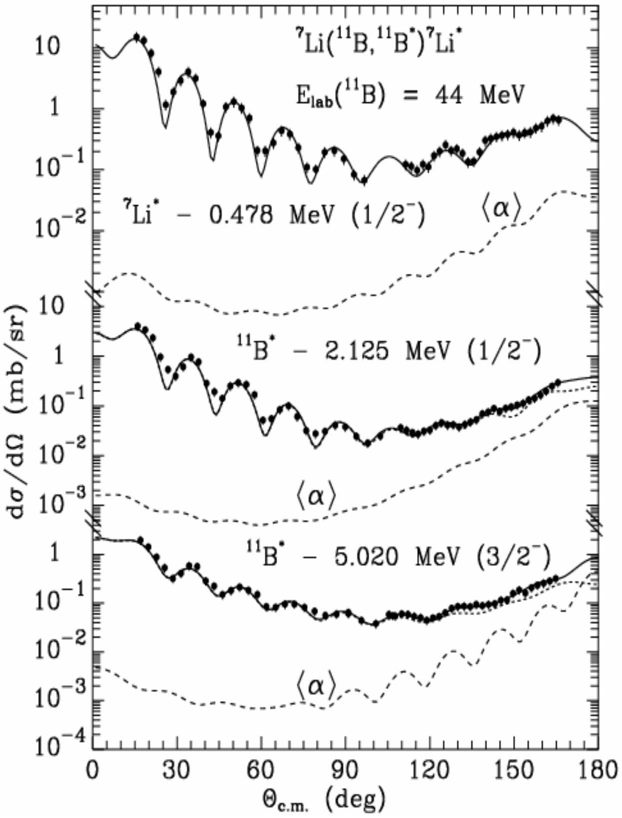

Fig. 4.1.35. Angular distributions of ^{11}B + ^{7}Li inelastic scattering at $E_{LAB}(^{11}\mathrm{B}) = 44$ MeV for the transition to the 0.478 MeV (1/2^{-}) state of ^{7}Li and 2.125 MeV (1/2^{-}) and 5.02 MeV (3/2^{-}) excited states of ^{11}B. The curves show the CRC angular distributions of collective nature excitations (dotted curves) and α-cluster transfers (curves <α>). Solid curves represent the coherent sums of these processes.

In the first step of analysis, the ^{11}B + ^{7}Li elastic scattering data at $E_{LAB}(^{11}\mathrm{B}) = 44$ MeV ($E_{CM} = 17.11$ MeV) (this work) and $E_{LAB}(^{7}\mathrm{Li}) = 34$ MeV ($E_{CM} = 20.78$ MeV [108, 109]) were analyzed within OM. In the second step, the obtained OM parameters $\{X_i\}$ were used as the input in the CRC fit. The CRC calculations were performed including the elastic and inelastic scattering, reorientations of ^{7}Li and ^{11}B, and the α-cluster and p + p transfers in the coupling-channel scheme. The deduced OM parameters $\{X_i\}$ are listed in Table 4.1.10.

In the CRC analysis, the ^{11}B + ^{7}Li elastic and inelastic scattering for the transitions to the ground and excited states of ^{7}Li and ^{11}B (up to 9.85 MeV) as well as the most important transfer reactions were included in the coupled-channels scheme. The transitions to the excited states of ^{7}Li are shown in Fig. 4.1.40 and of ^{11}B in Fig. 4.1.15. The reorientations of these nuclei in the excited states were also included in the CRC calculations. The diagrams of one-step and two-step transfers which contribute to the ^{11}B + ^{7}Li scattering are presented in Fig. 4.1.39.

We assume that the rotations and vibrations of the deformed ^{7}Li and ^{11}B nuclei dominate in the low-energy excitations. The deformation parameters are listed in Table 4.1.9.

Table 4.1.9. Deformation parameters of ^{7}Li and ^{11}B (β_λ for $R = 1.25A^{1/3}$ fm).

Nuclei	E_x (MeV)	J^π	λ	δ_λ (fm)	β_λ	Ref.
^{7}Li	0.0	$3/2^-$	2	2.0	0.84	[109]
	0.478	$1/2^-$	2	2.0	0.84	[109]
	4.630	$7/2^-$	2	2.0	0.84	
			4	1.0	0.42	
	6.680	$5/2^-$	2	2.0	0.84	
			4	1.0	0.42	
	7.460	$5/2^-$	2	2.0	0.84	
			4	1.0	0.42	
	9.670	$7/2^-$	2	2.0	0.84	
			4	1.0	0.42	
	9.850	$3/2^-$	2	2.0	0.84	
^{11}B	2.125	$1/2^-$	2	1.2	0.43	[8]
	4.445	$5/2^-$	2	1.2	0.43	[8]
			4	1.0	0.36	[8]
	5.020	$3/2^-$	2	1.2	0.43	[8]
	6.743	$7/2^-$	2	1.2	0.43	[8]
			4	1.0	0.36	[8]
	6.792	$1/2^+$	1	1.0	0.36	[8]
	7.286	$5/2^+$	1	1.0	0.36	[8]
			3	1.2	0.43	[8]
	7.978	$3/2^+$	1	1.0	0.36	[8]
			3	1.2	0.43	[8]
	8.560	$3/2^+$	2	1.8	0.65	[8]
	8.920	$5/2^+$	2	1.2	0.43	
			4	1.0	0.36	

Contributions of the reorientation and transfer reactions to the elastic scattering data were calculated. They are shown in Fig. 4.1.34 and 4.1.41 by the curves labeled *process name* (curves *reor* show the cross section of the ^{7}Li and ^{11}B reorientations, the curve *pt* corresponds to the coherent sum of $p + t$ and $t + p$ transfers, and so on). One can see that the contribution of most transfer reactions to the elastic scattering are negligible. Only the α-cluster and sequential $p + p$ transfers (curves α and *pp*, respectively) give small contributions to the data at large angles. Figure 4.1.34 and 4.1.41 shows that the reorientations of ^{7}Li and ^{11}B (curves *reor*) cause mostly the large-angle enhancement of the elastic scattering. The coherent sums of the potential scattering, reorientations, and the transfers of α and $p + p$ (solid curves) describe the ^{11}B + ^{7}Li elastic-scattering data quite satisfactorily.

The angular distributions of the ^{11}B + ^{7}Li inelastic scattering at $E_{LAB}(^{11}\mathrm{B}) = 44$ MeV are shown in Figs. 4.1.34 – 4.1.38 and Figs. 4.1.41 and 4.1.42. The curves represent the CRC cross sections calculated with the deformation and OM parameters listed in Tables 4.1.9 and 4.1.10, respectively. The OM parameters for the ^{11}B + ^{7}Li* and ^{11}B* + ^{7}Li exit channels were fitted to the inelastic-scattering data. As in the previous case, the contributions of the transfer reactions to the data were estimated. It was found that they are negligible (curves α and *pp* in Figs. 4.1.34 – 4.1.38, 4.1.41 and 4.1.42). The reorientations of ^{7}Li and ^{11}B in excited states were found to give small contributions to the data.

Table 4.1.10. Parameters of the Woods-Saxon OM potentials.

Channels	E_{CM}(MeV)	V_0(MeV)	r_V(fm)	a_V(fm)	Ws(MeV)	r_W(fm)	a_W(fm)
^{7}Li$_{9.85}$+^{11}B	7.26	90.5	0.874	0.580	7.1	1.370	0.533
	10.93	138.5	0.815	0.614	7.7	1.288	0.574
^{7}Li$_{9.67}$+^{11}B	7.44	92.3	0.872	0.581	7.1	1.367	0.535
	11.11	140.9	0.813	0.616	7.8	1.284	0.576
^{7}Li+^{11}B$_{8.92}$	8.19	100.5	0.860	0.587	7.2	1.350	0.542
	11.86	150.6	0.806	0.624	8.0	1.274	0.586
^{7}Li+^{11}B$_{8.56}$	8.55	104.7	0.854	0.590	7.2	1.342	0.546
	12.22	154.9	0.803	0.628	8.2	1.270	0.590
^{7}Li+^{11}B$_{7.98}$	9.13	111.8	0.844	0.596	7.3	1.327	0.552
	12.80	161.6	0.800	0.634	8.4	1.264	0.597
^{7}Li$_{7.47}$+^{11}B	9.64	118.4	0.835	0.601	7.3	1.315	0.558
	13.31	167.1	0.798	0.639	8.7	1.261	0.603
^{7}Li+$_{11}$B$_{7.29}$	9.83	120.8	0.832	0.602	6.4	1.310	0.560
	13.49	168.9	0.797	0.641	5.8	1.260	0.604
^{7}Li+$_{11}$B$_{6.79}$	10.32	127.5	0.824	0.608	7.5	1.299	0.566
	13.98	173.6	0.796	0.645	9.0	1.257	0.609
^{7}Li+$_{11}$B$_{6.74}$	10.37	128.2	0.823	0.608	7.5	1.298	0.567
	14.03	174.0	0.796	0.645	9.0	1.257	0.610
^{7}Li$_{6.68}$+^{11}B	10.43	129.1	0.822	0.609	7.5	1.297	0.568
	14.10	174.6	0.795	0.646	9.1	1.257	0.611
^{7}Li+^{11}B$_{5.02}$	12.09	152.2	0.804	0.627	6.2	1.270	0.588
	15.76	196.5	0.793	0.580	3.5	1.252	0.540
^{7}Li$_{4.63}$+^{11}B	12.48	157.5	0.802	0.631	8.8	1.266	0.593
	16.15	188.3	0.793	0.660	10.0	1.252	0.627
^{7}Li+^{11}B$_{4.45}$	12.67	159.8	0.801	0.633	8.9	1.265	0.595
	16.33	189.1	0.793	0.600	4.5	1.252	0.540
^{7}Li+^{11}B$_{2.13}$	14.99	183.9	0.794	0.653	10.2	1.254	0.619
	18.65	189.4	0.792	0.671	10.7	1.250	0.639
^{7}Li$_{0.48}$+^{11}B	16.63	188.2	0.792	0.663	11.0	1.251	0.630
A	20.30	189.2	0.792	0.674	11.5	1.250	0.644
B	20.30	189.2	0.792	0.675	13.0	1.350	0.644
^{7}Li+^{11}B	17.11	188.0	0.792	0.665	11.0	1.251	0.633
	20.78	189.2	0.792	0.675	10.2	1.250	0.644

The large-angle scattering data for the 0.478 MeV transition at 34 MeV are described by the CRC angular distribution (see lower panel in Fig. 4.1.41). The set *A* of OM parameters satisfactorily describes the data only to $\theta_{CM} \approx 140^o$. By increasing the absorption potential, it is possible to improve the description of the large-angle data (set *B*) but description of the middle-angle data becomes worse.

The transitions to the excited states of ^{7}Li (Fig. 4.1.36) as well as to the excited states of ^{11}B (Fig. 4.1.37) were unresolved in the experiment at the forward hemisphere angles. As one can see, transitions to the excited states of ^{7}Li dominate in the both cases. The solid curves Σ and Σ_B show the incoherent sums of the unresolved states. The CRC angular distributions describe the data satisfactorily.

Figure 4.1.38 shows that the transition to the excited state 9.67 MeV ($7/2^-$) of ^{7}Li dominates the data for the unresolved excited states 9.67 MeV ($7/2^-$) + 9.85 MeV ($3/2^-$) of ^{7}Li.

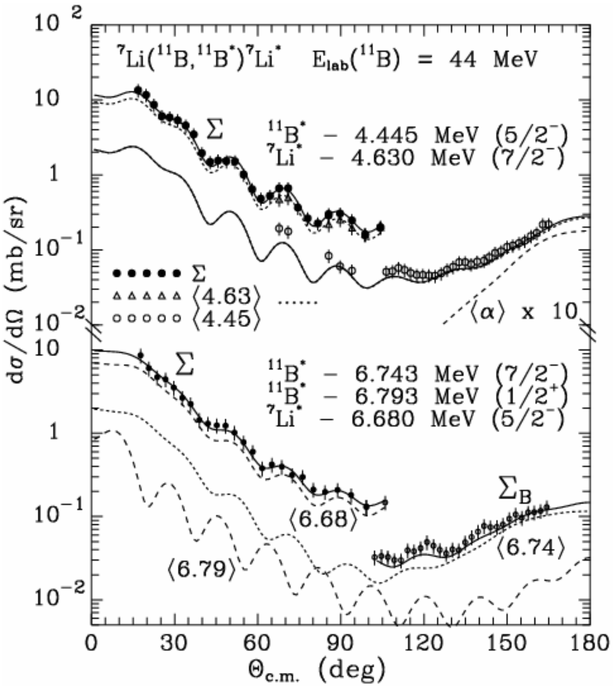

Fig. 4.1.36. The same as in Fig. 4.1.35 but for the 4.63 MeV (7/2$^-$) and 6.68 MeV (5/2$^-$) excited states of ^{7}Li and the 4.445 MeV (5/2$^-$), 6.743 MeV (7/2$^-$), and 6.793 MeV (1/2$^+$) excited states of ^{11}B. Curves *Σ* and *Σ$_B$* show the incoherent sums of these transitions, respectively.

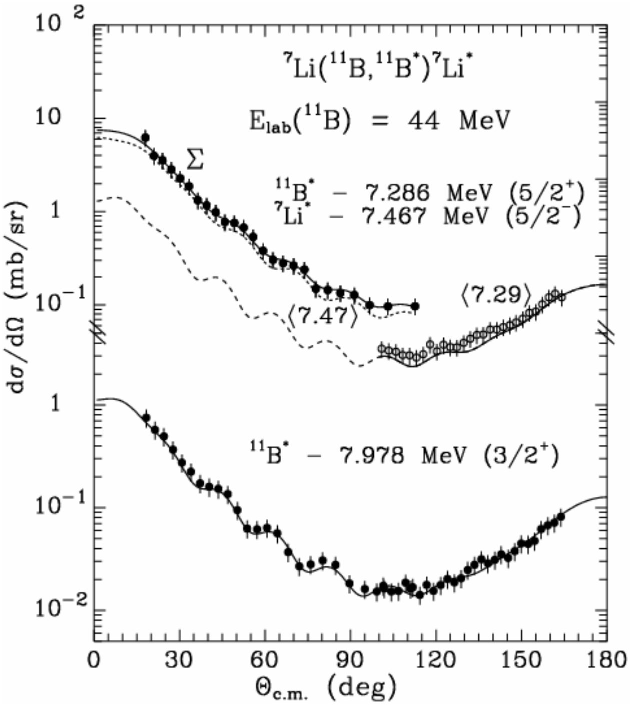

Fig. 4.1.37. The same as in Fig. 4.1.35 but for the 7.467 MeV (5/2$^-$) excited state of ^{7}Li and the 7.286 MeV (5/2$^+$), and 7.978 MeV (3/2$^+$) excited states of ^{11}B.

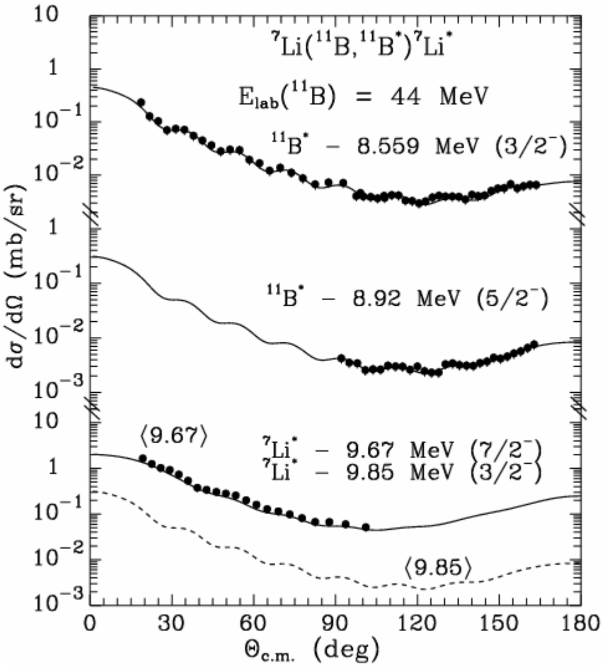

Fig. 4.1.38. The same as in Fig. 4.1.35 but for the 9.67 MeV (7/2$^-$) and 9.85 MeV (3/2$^-$) excited states of ^{7}Li and the 8.559 MeV (3/2$^-$) and 8.92 MeV (5/2$^-$) excited states of ^{11}B.

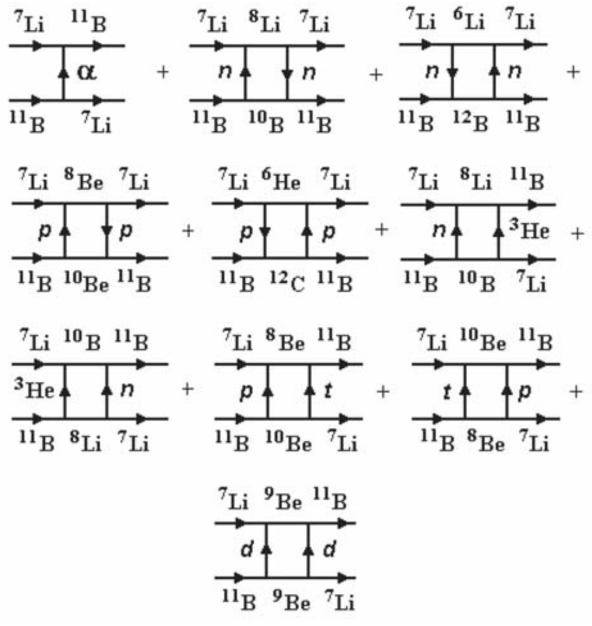

Fig. 4.1.39.. Diagrams of one- and two-step transfers contributing to the ^{11}B + ^{7}Li elastic- and inelastic-scattering calculations.

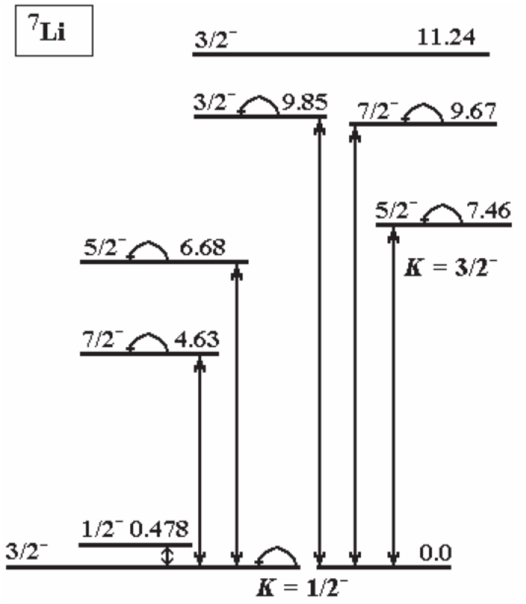

Fig. 4.1.40. The coupling schemes for the transitions to the excited states of ^{7}Li. Coupling schemes for the transitions to the excited states of ^{11}B are shown in Fig. 4.1.15.

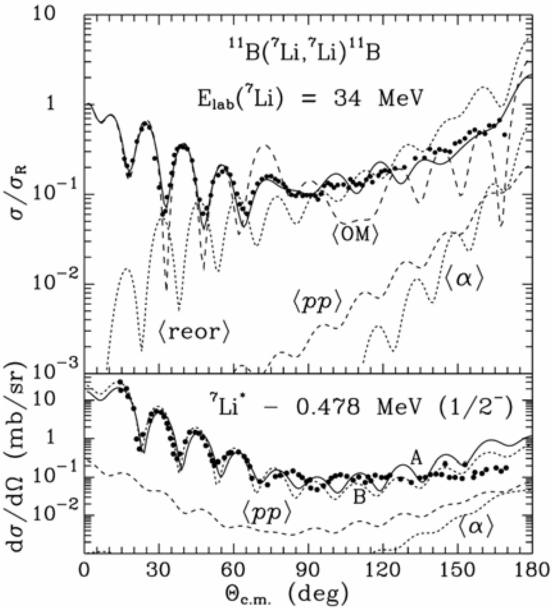

Fig. 4.1.41. Angular distributions of ^{7}Li + ^{11}B scattering at the energy $E_{\mathrm{LAB}}(^7\mathrm{Li})$ = 34 MeV [108, 109] for the transitions to the ground states of these nuclei (upper panel) and 0.478 MeV (1/2$^-$) state of ^{7}Li (lower panel). The curves are the same as those in Fig. 4.1.34 but for the energy $E_{\mathrm{LAB}}(^7\mathrm{Li})$=34 MeV.

The obtained OM parameter sets $\{X_i\} = \{V, W_S, r_V, r_W, a_V, a_W\}$ for the excited ^{7}Li and ^{11}B are given in Table 4.1.10.

The energy dependence of the ^{11}B + ^{7}Li optical potential parameters is described in the next sub-Section 4.1.6 together with the energy dependence of the ^{10}B + ^{7}Li optical potential parameters

In the^{11}B + ^{7}Li elastic channel, the potential scattering and the reorientations of ^{7}Li and ^{11}B dominate at the forward and backward angles, respectively. The rotational transitions to the excited states of ^{7}Li and ^{11}B dominate the inelastic channels. The contributions of the one-step and two-step transfers to the elastic and inelastic channels are small. The α-cluster and the sequential proton + proton transfers dominate the transfer channels.

As the result, the ^{11}B + ^{7}Li OM parameters for the ground and excited states of ^{7}Li and ^{11}B, as well as the deformation parameters of these nuclei were deduced. It was also found that the OM parameter W_S for the ^{11}B* + ^{7}Li channels with the 4.445 MeV (5/2$^-$), 5.021 MeV (3/2$^-$), and 7.286 MeV (5/2$^-$) states of ^{11}B is smaller (weaker absorption) when compared to the other states of these nuclei. The energy dependence of the ^{11}B + ^{7}Li OM parameters for the ground and excited states of ^{7}Li and ^{11}B was obtained at energies E_{CM} = 7 – 21 MeV.

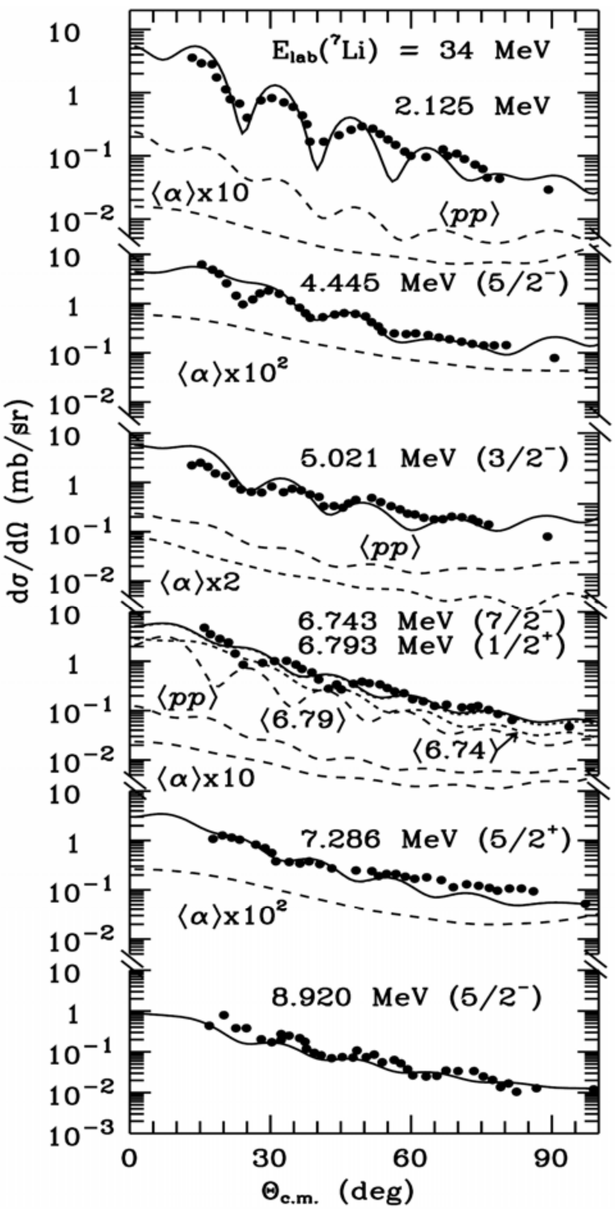

Fig. 4.1.42. The same as in Fig. 4.1.35 but for the excited states of ^{11}B at energy E_{LAB}(^{7}Li) = 34 MeV [108, 109].

4.1.6. The elastic and inelastic scattering of ^{10}B + ^{7}Li nuclei, optical potential and ^{10}B deformation parameters.

The angular distributions of the ^{10}B + ^{7}Li elastic and inelastic scattering were measured at the energy E_{LAB}(^{10}B) = 51 MeV (E_{CM}(^{10}B) = 21 MeV) [15]. The present data and data taken from the literature at E_{LAB}(^{7}Li) = 24 MeV [102] and E_{LAB}(^{7}Li) = 39 MeV [103], were analyzed using the optical model (OM) and the coupled-reaction-channels (CRC) method to determine the energy dependence of the parameters of the scattering potential and to find the difference between these parameters and obtained for the ^{11}B + ^{7}Li scattering [13] (isotopic effect). It was found that the ^{11}B + ^{7}Li potential parameters fail to describe the ^{10}B + ^{7}Li scattering data. The biggest difference is observed between the depths of the imaginary potentials that describe these scatterings.

The resulting angular distribution of the elastic scattering of ^{10}B + ^{7}Li at $E_{\rm LAB}(^{10}$B) = 51 MeV are shown in Fig. 4.1.43 The data for the elastic scattering at $E_{\rm LAB}(^{7}$Li) = 24 MeV [102] and 39 MeV [103], which were included in the analysis, are presented in Fig. 4.1.44. The data of the inelastic scattering ^{10}B + ^{7}Li at $E_{\rm LAB}(^{10}$B) = 51 MeV, obtained in the present work, are shown in Figs. 4.1.45 and 4.1.46. The results of theoretical calculations are also shown in these Figures. The error of the cross section normalization is smaller than 15%.

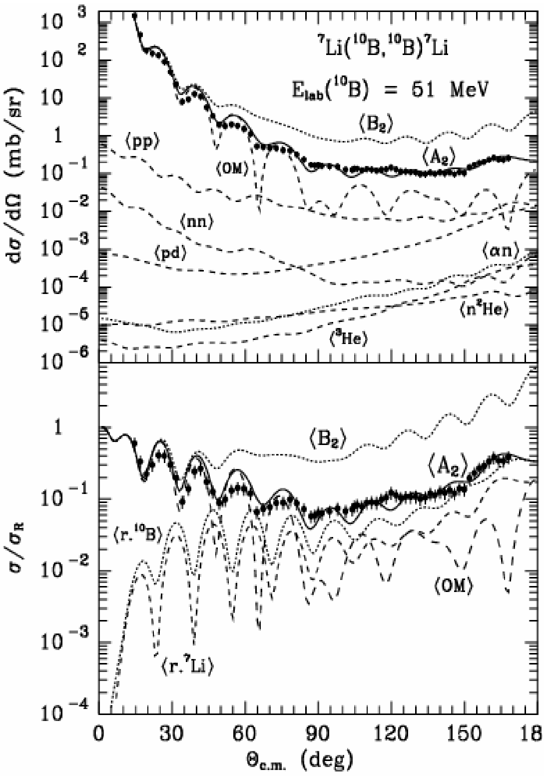

Fig. 4.1.43. Angular distributions of the ^{7}Li(^{10}B, ^{10}B) elastic scattering at the energy $E_{LAB}(^{10}$B) = 51 MeV in the absolute units (upper panel) and in units of the Rutherford cross section (lower panel). The curves show the OM cross section (curves <OM>) and CRC-calculations for the reorientation of ^{7}Li (curve <r.^{7}Li>, ^{10}B (curve <r.^{10}B>), transfer of ^{3}He-cluster (curve <^{3}He>) and sequential transfers of protons (curve <pp>), neutrons (curve <nn>), p + d (curve <pd>), α + n (curve < αn>) and n + 2p (curve <n^{2}He>). The curves <A$_2$> and <B$_2$> represent the coherent sums of CRC-calculations of all processes for A$_2$- and B$_2$-parameters, respectively (see Table 4.1.12).

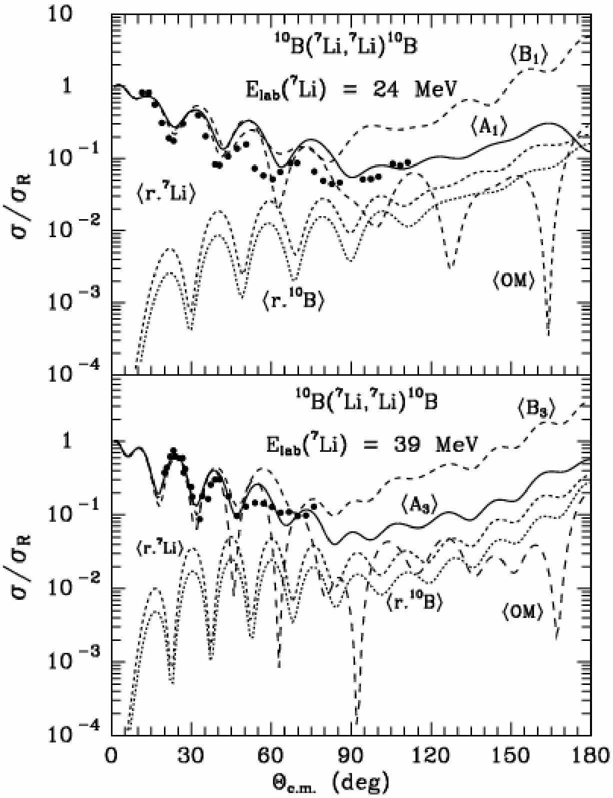

Fig. 4.1.44. Angular distributions of the ^{7}Li(^{10}B, ^{10}B) elastic scattering at the energies $E_{LAB}(^{7}$Li) = 24 MeV [102] (upper panel) and $E_{LAB}(^{7}$Li) = 39 MeV [103] (lower panel). The curves are the same as described for Fig. 4.1.43 but for other energies and potential parameters.

The optical potential parameters were fitted in the framework of the optical model to obtain a good description of the elastic scattering data for θ_{CM} < 90°. The optimal set of these parameters was used as the initial one in the CRC-calculations.

The ^{10}B + ^{7}Li elastic and inelastic scattering for the transitions to the ground and excited states of ^{10}B + ^{7}Li, reorientations of ^{7}Li and ^{10}B as well as the most important transfer reactions were included in the channel-coupling scheme in the CRC-analysis. The diagrams of the one-step and two-step transfers, which contribute to the ^{10}B + ^{7}Li scattering calculations, are presented in Fig. 4.1.47. The transitions to the excited states of ^{10}B are shown in Fig. 4.1.48 and to excited states of ^{7}Li in Fig. 4.1.15.

We assume that the rotations of the deformed ^{7}Li and ^{10}B nuclei as well as vibrations dominate in the low-energy excitations. The deformation parameters of ^{7}Li taken from [13], were used in the present CRC-calculations. The deformation lengths of δ_λ for ^{10}B were fitted. The values of these parameters for ^{10}B, estimated in the present work and presented in Ref. [104-107], are listed in Table 4.1.11.

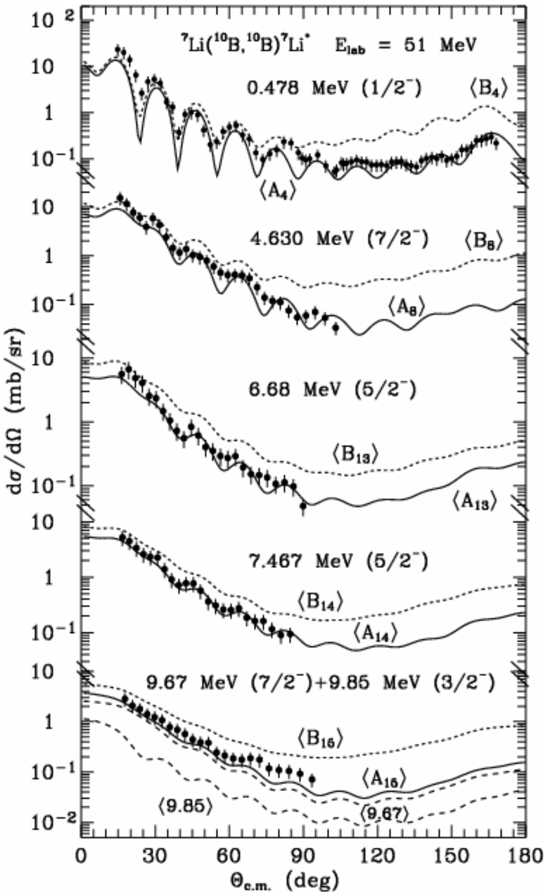

Fig. 4.1.45. Angular distributions of the ^{10}B + ^{7}Li inelastic scattering at E_{LAB}(^{10}B) = 51 MeV for the transition to the excited states of ^{7}Li. The curves <A$_i$> and <B$_i$> (i = 4, 8, 13, 15) show the CRC cross sections for collective nature excitations of ^{7}Li calculated with A$_i$- and B$_i$-parameters, respectively (see Table 4.1.12).

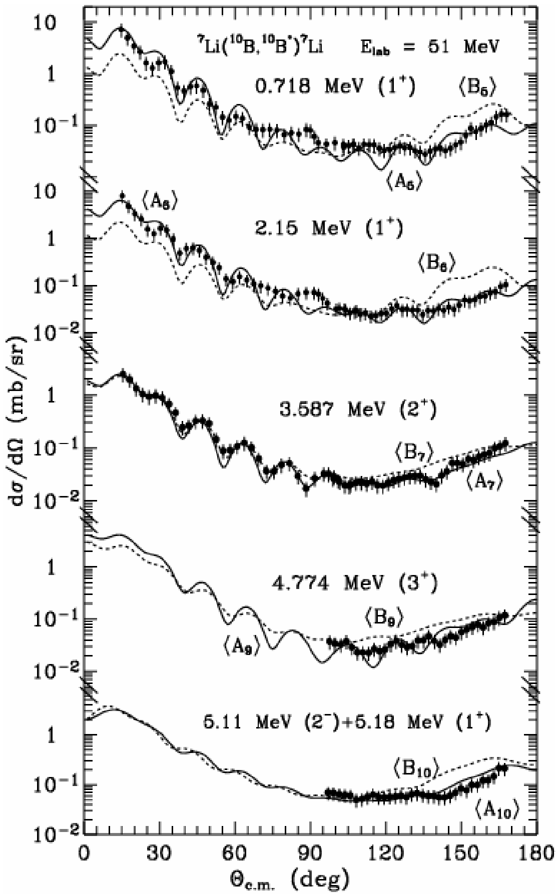

Fig. 4.1.46. Angular distributions of the ^{7}Li + ^{10}B inelastic scattering at E_{LAB}(^{10}B) = 51 MeV for the transition to the excited states of ^{10}B. The curves are the same as described for Fig. 4.1.45 but for excited states of ^{10}B and other potential parameters.

The curves shown in Fig. 4.1.43 represent the OM- and CRC- calculations with parameters A$_i$ (i = 1 - 15) listed in Table 4.1.12. The parameters A$_n$ (n = 1 - 3) were first obtained from the OM-fitting to the ^{10}B + ^{7}Li elastic-scattering data at the angles $\theta_{\mathrm{CM}} < 90^{\mathrm{o}}$. Then, they were corrected in the CRC-calculation.

The values of c_V and c_W, presented in Table 4.1.12, will be used for explaining the isotopic effects.

Table 4.1.11. Deformation parameters of ^{10}B.

E_x (MeV)	J^π	λ	δ_λ (fm)	β_λ (a)	Ref.
0.000	3^+	2	1.8	0.67	
0.718	1^+	2		0.67	(p,p’) [107]
		2		0.62	(d,d’) [105]
		2		0.37	(^{3}He,^{3}He’) [104]
		2	1.8	0.67	
2..154	1^+	2		0.69	(n,n’) [106]
		2		0.49	(p,p’) [107]
		2		0.61	(d,d’) [105]
		2		0.36	(^{3}He,^{3}He’) [104]
		2	1.8	0.67	
		4	1.0	0.37	
3.587	2^+	2		0.45	(p,p’) [107]
		2		0.36	(^{3}He,^{3}He’) [104]
		2	1.8	0.67	
		4	1.0	0.37	
		2	1.8	0.67	
		4	1.0	0.37	
5.110	2^-	3		0.45	(p,p’) [107]
	2^-	1	1.0	0.37	
		3	1.0	0.37	
5.180	1^+	2	1.8	0.67	
		4	1.0	0.37	

(a) In this table $\beta_\lambda = \delta_\lambda/R$, $R = 1.25A^{1/3} = 2.69$ fm.

One can see from Fig. 4.1.43 that the potential scattering (curves <OM>) dominates at the forward angles. The large-angle scattering are mainly caused by reorientations of ^{7}Li and ^{10}B. The transfer contributions are small compared to the calculated cross-section of the elastic scattering channel. The curve <A_2> shows the coherent sum of all the processes.

It is shown in Fig. 4.1.44 that the same effect is observed also in the description of the ^{10}B + ^{7}Li data at E_{LAB}(^{7}Li) = 24 MeV [102] and 39 MeV [103] with the potential parameters A_1 and A_3, fitted to the data (see Table 4.1.12). The curves <A_1> and <A_3> are the results of the CRC calculations of the coherent sums all the processes for the above parameters.

It is interesting to compare the obtained ^{10}B + ^{7}Li parameters with those of the ^{11}B + ^{7}Li scattering. The last parameters were calculated using their energy dependence coefficients [13] for corresponding energies. The calculated ^{11}B + ^{7}Li parameters are listed in Table 4.1.12 as the B_i-sets (i = 1 - 15). One can see that the ^{10}B + ^{7}Li absorption potentials are deeper than those of the ^{11}B + ^{7}Li scattering, at the same energies.

The CRC-calculations of the ^{10}B + ^{7}Li scattering with the B_i-parameters (i = 1-3) are shown in Figs. 4.1.43 and 4.1.44 One can see that there are substantial differences between the CRC calculations with the potential parameters A_i and B_i. The parameters B_i do not correctly describe the ^{10}B + ^{7}Li data at large angles.

From the above analysis, one can conclude that there is a remarkable difference between the ^{10}B + ^{7}Li and the ^{11}B + ^{7}Li absorption potentials.

The curves in Fig. 4.1.45 and 4.1.46 show the CRC-calculations within the rotational and vibrational models with the deformation parameters δ_λ of ^{10}B listed in Table 4.1.11 and the same parameters for ^{7}Li taken from ref. [13]. The parameters δ_λ for ^{10}B were fitted to the inelastic scattering data.

Table 4.1.12. Parameters of Woods-Saxon potential for the ^{10}B + ^{7}Li scattering (r_C = 1.25 fm).

Nuclei	E_{CM}	Set	V	r_V	a_V	W_S	r_W	a_W	c_V	c_W
	(MeV)		(MeV)	(fm)	(fm)	(MeV)	(fm)	(fm)		
^{7}Li+^{10}B	14.12	A_1	150.0	0.790	0.660	11.0	1.250	0.660	9.88	10.10
		B_1	176.1	0.795	0.646	9.2	1.257	0.611	10.26	10.73
	21.00	A_2	189.9	0.790	0.660	14.5	1.250	0.660	10.11	10.38
		B_2	189.1	0.792	0.676	10.9	1.250	0.645	10.09	10.41
	22.94	A_3	191.8	0.790	0.660	14.8	1.250	0.660	10.12	10.40
		B_3	187.2	0.792	0.678	10.9	1.250	0.647	10.06	10.38
^{7}Li$_{0.478}$+^{10}B	20.52	A_4	191.8	0.790	0.660	11.0	1.250	0.660	10.12	10.10
		B_4	189.3	0.792	0.675	10.8	1.250	0.644	10.10	10.41

$^7Li+^{10}B_{0.718}$	20.28	A_5	187.0	0.790	0.650	12.3	1.230	0.650	10.17	10.21
		B_5	189.4	0.792	0.674	10.8	1.250	0.643	10.11	10.42
$^7Li+^{10}B_{2.154}$	18.84	A_6	185.5	0.790	0.649	13.0	1.250	0.649	10.17	10.40
		B_6	189.4	0.792	0.671	10.8	1.250	0.640	10.13	10.46
$^7Li+^{10}B_{3.587}$	17.41	A_7	182.5	0.790	0.645	8.8	1.250	0.645	10.19	10.06
		B_7	188.7	0.792	0.666	10.6	1.251	0.634	10.16	10.52
$^7Li_{4.630}+^{10}B$	16.37	A_8	184.4	0.790	0.640	11.9	1.252	0.640	10.24	10.43
		B_8	190.2	0.793	0.661	10.3	1.252	0.629	10.21	10.57
$^7Li+^{10}B_{4.774}$	16.22	A_9	173.1	0.790	0.639	8.8	1.256	0.639	10.18	10.17
		B_9	189.9	0.793	0.661	10.3	1.252	0.628	10.21	10.58
$^7Li+^{10}B_{5.110}$	15.89	A_{10}	168.3	0.791	0.636	7.5	1.251	0.636	10.18	10.01
		B_{10}	188.8	0.793	0.659	10.1	1.252	0.625	10.22	10.60
$^7Li+^{10}B_{5.920}$	15.08	A_{11}	176.2	0.792	0.643	11.0	1.251	0.643	10.10	10.61
		B_{11}	184.4	0.794	0.653	9.8	1.254	0.619	10.25	10.66
$^7Li+^{10}B_{6.127}$	14.87	A_{12}	174.5	0.792	0.642	10.8	1.252	0.642	10.10	10.59
		B_{12}	182.8	0.794	0.652	9.7	1.254	0.618	10.25	10.67
$^7Li_{6.680}+^{10}B$	14.32	A_{13}	170.7	0.793	0.648	9.9	1.256	0.648	10.12	10.18
		B_{13}	178.2	0.795	0.648	9.4	1.256	0.613	10.26	10.72
$^7Li_{7.467}+^{10}B$	13.53	A_{14}	164.2	0.795	0.641	9.2	1.259	0.641	10.14	10.21
		B_{14}	170.2	0.797	0.641	8.9	1.259	0.605	10.28	10.80
$^7Li_{9.670}+^{10}B$	11.33	A_{15}	144.2	0.809	0.619	7.7	1.281	0.619	10.29	11.46
		B_{15}	142.0	0.811	0.619	7.7	1.281	0.579	10.38	11.19

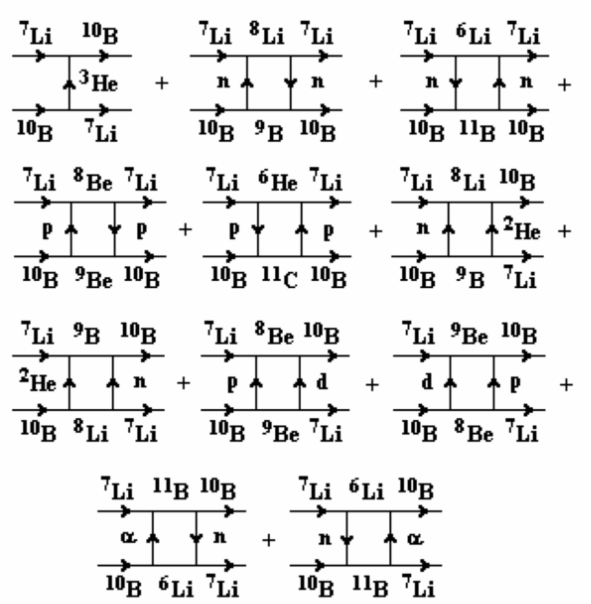

Fig. 4.1.47. Diagrams of one- and two-step transfers contributing to the $^{10}B + ^7Li$ elastic-scattering calculations.

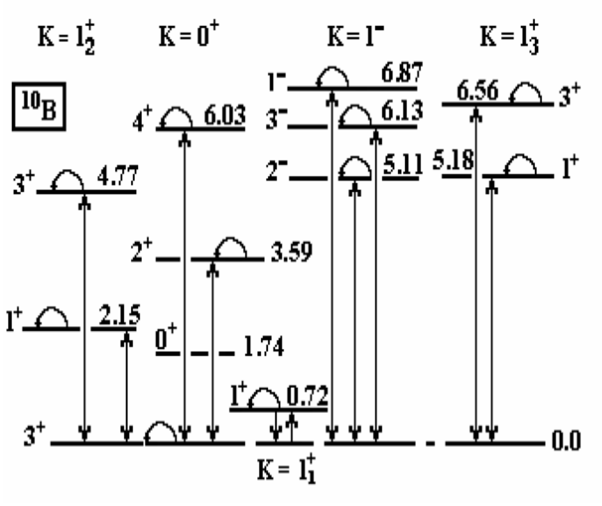

Fig. 4.1.48. Coupling schemes for the transitions to the excited states of ^{10}B. The circles denote reorientations processes. The coupling schemes for the transitions to the excited states of ^7Li are shown in Fig. 4.1.15.

In the conclusion one can state, that in the $^{10}B + ^7Li$ elastic channel, the potential scattering and reorientations of ^7Li and ^{10}B dominate at forward and backward angles, respectively. The contributions of one- and two-step transfers to the elastic and inelastic channels are small. One can conclude from the data, that absorbing part of the optical potential for ^{10}B is stronger than for ^{11}B at large-momentum transfer.

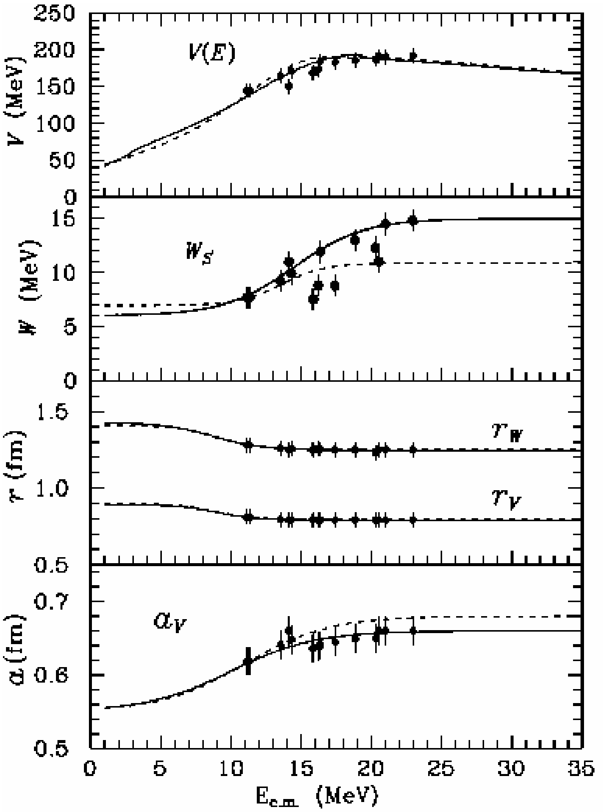

Fig. 4.1.49. Energy dependence of the $^{10}B + {}^{7}Li$ [15] potential parameters (dots and solid curves) versus the same for the $^{11}B + {}^{7}Li$ interaction [13] (dashed curves).

The parameters of the energy dependence of the optical potential parameters $X_i = X_i^{\min}$; X_i^{max}; E_{Xi} ; ΔE_{Xi}, estimated for the $^{10}B + {}^{7}Li$ potential, taken from [15] paper, are listed in Table 4.1.13 and presented by the solid curves in Fig. 4.1.49.

The energy dependence of the optical potential parameters for $^{10}B + {}^{7}Li$, taken from [13] paper, are also shown in Fig. 4.1.49 using the dashed curves. The energy dependence parameters are listed in Table 4.1.13. It is visible that only the energy dependence of the imaginary potential is distinctly different for the two systems. Therefore, the isotopic effect in the $^{10,11}B + {}^{7}Li$ scattering arises from the difference in the structure of the ^{10}B and ^{11}B. The observed isotopic effect for the $^{10,11}B + {}^{7}Li$ systems is due to different reaction channels possible for the two isotopes.

Table 4.1.13. Energy dependence of the $^{10}B + {}^{7}Li$ OM potential parameters.

X_i	V_0 (MeV)	W_S (MeV)	r_V (fm)	r_W (fm)	a_V (fm)	a_W (fm)
X_i^{min}	110.0	6.0	0.790	1.246	0.550	0.550
X_i^{max}	270.0	15.0	0.890	1.430	0.660	0.660
E_{Xi} (MeV)	12.5	14.5	9.100	8.700	10.000	10.000
ΔE_{Xi} (MeV)	3.5	2.5	1.400	1.800	3.000	3.000

The energy dependence of the optical potential parameters for $^{11}B + {}^{7}Li$, taken from [13] paper, are also shown in Fig. 4.1.50, together with energy dependence of the $^{14}N + {}^{7}Li$ OM parameters for V and W_S (curves ^{14}N) taken from sub-Section 4.3.1. One can see that the parameters for the $^{14}N + {}^{7}Li$ interaction achieve their maxima at higher energies than in the case of $^{11}B + {}^{7}Li$ scattering. This effect is due to the higher potential barrier for the first system.

Table 4.1.14. Energy dependence of the $^{11}B + {}^{7}Li$ OM potential parameters

X_i	V_0 (MeV)	W_S (MeV)	r_V (fm)	r_W (fm)	a_V (fm)	a_W (fm)
$X_i^{\min}$	113.1	7.0	0.792	1.250	0.550	0.500
$X_i^{\max}$	307.0	10.9	0.899	1.412	0.680	0.650
E_{Xi} (MeV)	11.7	13.6	9.044	8.970	11.000	11.000
Δ_{Xi} (MeV)	3.1	1.6	1.490	1.633	3.000	3.000

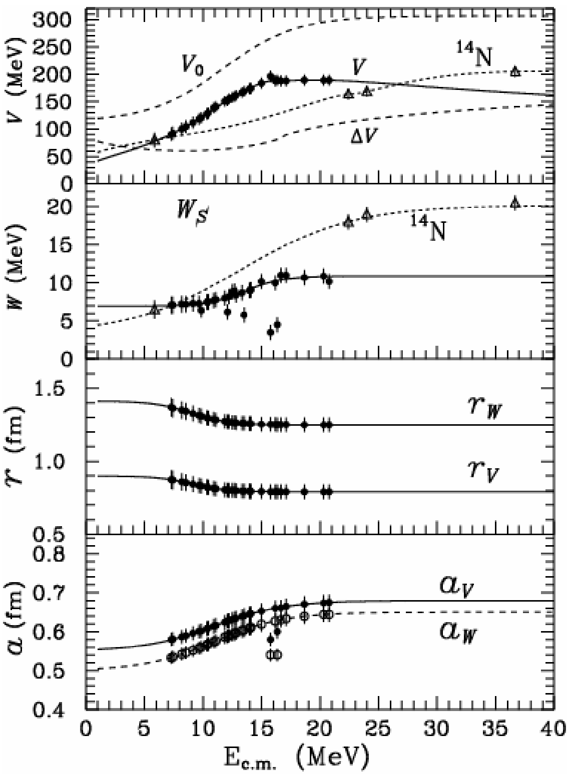

Fig. 4.1.50. Energy dependence of OM potential parameters for the interaction of ^{7}Li and ^{11}B in ground and excited states versus the same for the ^{14}N + ^{7}Li interaction (curves ^{14}N) [7]. Note that $V = V_0 - \Delta V$.

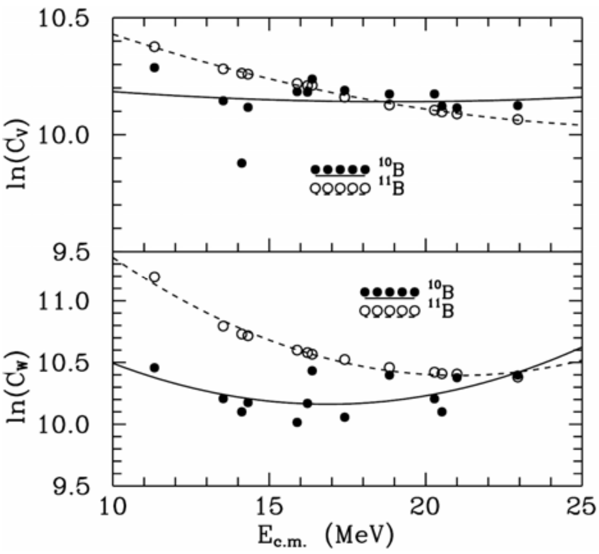

Fig. 4.1.51. Energy dependence of c_V and c_W for the ^{10}B + ^{7}Li potential parameters versus the same for the ^{11}B + ^{7}Li interaction.

The values of

$$\ln c_V = \ln(V \exp(R_V/a_V)),$$
$$\ln c_W = \ln(W_S \exp(R_W/a_W))$$

taken from Table 4.1.12 are shown in Fig. 4.1.51. The curves show the fits of these values by the polynomials:

$\ln c_V = 10.33 - 0.0204E + 0.0005E^2$ for ^{7}Li + ^{10}B,
$\ln c_V = 10.99 - 0.0686E + 0.0012E^2$ for ^{7}Li + ^{11}B,
$\ln c_W = 12.16 - 0.2368E + 0.0070E^2$ for ^{7}Li + ^{10}B,
$\ln c_W = 13.87 - 0.3307E + 0.0079E^2$ for ^{7}Li + ^{11}B.

One can see a noticeable difference between the c_W values of these potentials. It is apparent in Fig. 4.1.51 that both the potentials are similar in the peripheral scattering region.

The following conclusions can be drawn out from the reaction discussed above. In the ^{7}Li + ^{10}B elastic channel, the potential scattering and reorientations of ^{7}Li and ^{10}B dominate at forward and backward angles, respectively. The contributions of one- and two-step transfers to the elastic and inelastic channels are small. The data for ^{10}B shows it to be more strongly absorbing at large-momentum transfer than that for ^{11}B. The energy dependence of the ^{7}Li + ^{10}B potential parameters for the ground and excited states of ^{7}Li and ^{10}B was obtained. It was found that this energy dependence is different from that of the ^{7}Li + ^{11}B interaction [13] especially for the imaginary potential. The observed isotopic effect for the ^{7}Li + ^{10,11}B systems is indicative of the different reaction channels possible for the two isotopes.

4.2. The ^{12}C + ^{9}Be scattering.

Scattering of ^{12}C + ^{9}Be nuclei, optical potential and influence of ^{9}Be reorientation processes.

This sub-Section is devoted to the study of the energy dependence of the optical model potential for the ^{12}C + ^{9}Be interaction in a rather broad range of energy E_{CM} = 5.14 – 90.46 MeV [152 – 158]. In the past, many articles were devoted to the study of this dependence (see [151] and references therein). Recently, the interest in the energy dependence of optical model potential parameters has increased due to the observation of the threshold anomalies in the elastic scattering of heavy ions (see Refs. [159 – 164] and references therein).

Due to the causality principle, a scattered wave cannot be emitted before the interaction has occurred. Then, this principle implies the existence of a dispersion relation between the real and the imaginary parts of the optical potential (see formulas (3.6) and (3.7) in Chapter 3). This relation gives a possibility to minimize the ambiguities in the optical potential. In the case of nucleus-nucleus scattering, the dispersion relation predicts that the absolute value of the $V(E)$ real part of the optical potential in function of energy has a bell-shaped maximum, while their $\Delta V_W(E)$ imaginary part approaches minimum, mainly for energies near the top of the Coulomb barrier. This phenomenon is so called threshold anomaly [256].

The absolute value of the imaginary potential for heavy ions falls down while the energy drops below the Coulomb barrier because the non-elastic channels are being effectively closed. More detailed studies [251] take into account the specific channels available and the requirements of momentum and angular moments matching. In some special cases, these may result in the decrease of absolute value of the imaginary potential occurring at energies appreciably above the top of the Coulomb barrier. The systems ^{16}O + ^{28}Si [255] and α + ^{40}Ca [252, 253, 254] are examples of this. It is probably due to contributions of other channels, coupling to the elastic scattering and modifying the real potential [255]. One can conclude from the dispersion relation that the anomalous behavior of the real potential is also associated with the closing of the non-elastic channels. The non-elastic couplings can produce changes in the real potential through virtual excitations even below the thresholds where the corresponding channels are energetically closed and where their contribution to the imaginary potential has to vanish.

Although this effect is well established for the scattering of tightly bound nuclei, there are some conclusions that the breakup of weakly bound nuclei influence the threshold anomaly [257]. For systems in which at least one of the participants is a weakly bound nucleus, it has been recently shown that the breakup cross section does not diminish so fast in the vicinity of the Coulomb barrier but, rather, that it can have values much larger than the fusion cross sections. As a consequence of this at these energies the imaginary part of the optical potential does not necessarily decrease and the threshold anomaly may disappear. Moreover, it has been suggested [162, 164] that the effect of coupling of the breakup channel to the continuum may produce a repulsive polarization potential that affects the overall dynamic polarization potential in such a way that the usual threshold anomaly may vanish. This fact has been taken as a possible explanation of the absence of the usual threshold anomaly for systems involving the weakly bound nuclei ^{6}Li or ^{7}Li such as ^{6,7}Li + ^{28}Si [258, 259].

The coupled-reaction-channel model was used in the analysis of the data. The elastic and inelastic scattering, the reorientation of ^{9}Be and the transfer reactions were included in the coupled channel scheme. The energy-dependent optical-model potential for this interaction, determined in the coupled-reaction-channel analysis, can be useful for the study of common properties of the nucleus–nucleus interaction and also for the study of the ^{9}Be(^{12}C, X) reactions.

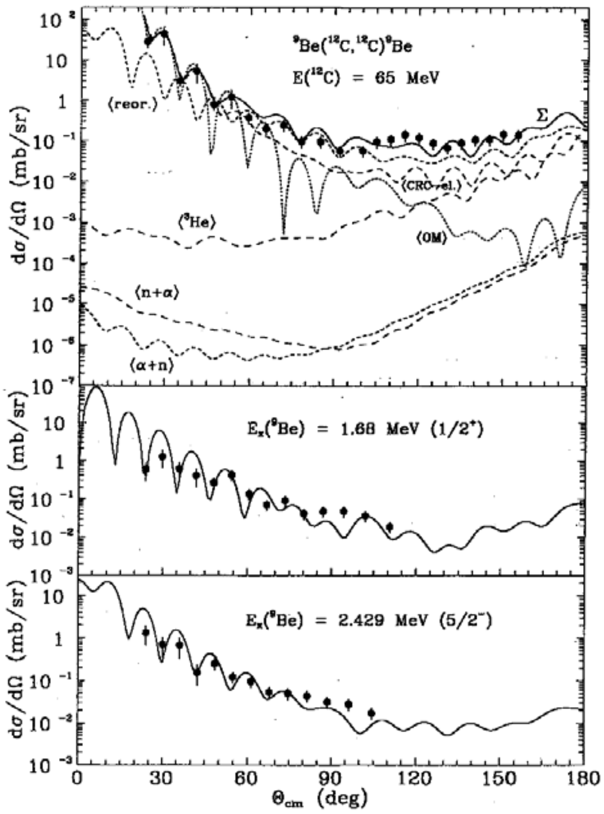

Fig. 4.2.1. Angular distributions of the ^{9}Be(^{12}C, ^{12}C)^{9}Be elastic and inelastic scattering at the energy E_{LAB}(^{12}C) = 65 MeV. The solid curves *Σ* and dashed curves *<OM>*, *<reor.>*, *<CRC -el.>*, <3He>, <n+α>, and <α+n> show the angular distributions corresponding to the sum of all processes, OM elastic scattering, ^{9}Be reorientation, CRC elastic scattering and ^{3}He-cluster, sequential n + α and α + n transfers, respectively. The solid curves, presented in the two lower panels, show the angular distributions calculated for the inelastic scattering.

The angular distributions of elastic and inelastic scattering of ^{12}C ions by the ^{9}Be nuclei at 65 MeV for the transitions to the 1.68 MeV (1/2$^+$) and 2.429 MeV states of ^{9}Be nucleus are shown in Fig. 4.2.1. Our data [4] at E_{CM} = 27.86 MeV (E_{LAB}(^{12}C) = 65 MeV) are in good agreement with the data of Ref. [156] at very close E_{CM} = 28.57 MeV.

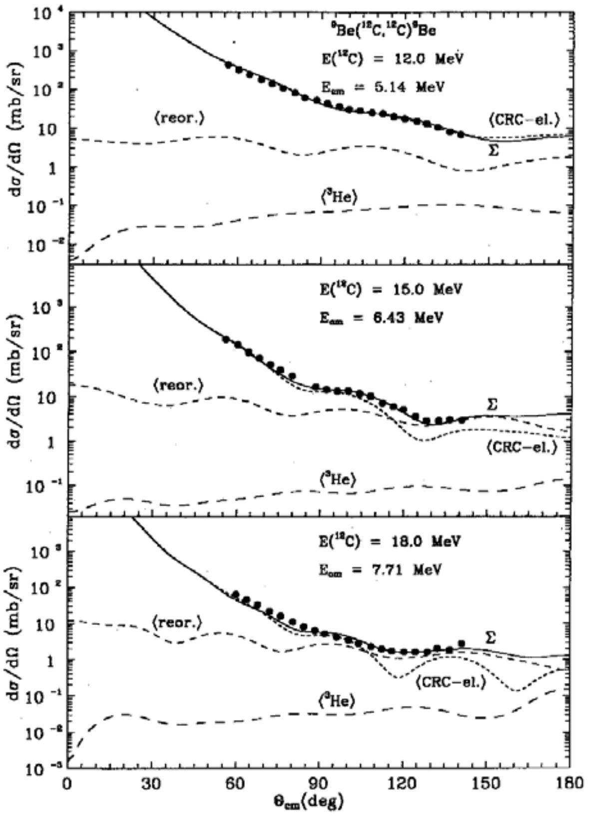

Fig. 4.2.2. Angular distributions of the ^{9}Be(^{12}C, ^{12}C)^{9}Be elastic scattering at the energies E_{LAB}(^{12}C) =12, 15 and 18 MeV [151] . The solid curves *Σ* and dashed curves *<reor.>*, *<CRC-el.>*, <^{3}He> show the angular distributions corresponding to the sum of all processes, ^{9}Be reorientation, CRC elastic scattering and ^{3}He-cluster transfer, respectively.

The OM potential parameters obtained from the analysis of our experimental data of the elastic scattering ^{12}C + ^{9}Be at E_{LAB}(^{12}C) = 65 MeV and others at the energies E_{CM} = 5.14 – 90.46 MeV [152 – 158] are given in Table 4.2.1. The corresponding cross sections are represented in Figs.

4.2.1 – 4.2.6 by the dashed curves <OM> . It can be seen that the angular range in which the potential scattering is dominant became narrower with increasing energy from $\theta_{CM} \approx 0^o - 150^o$ at E_{CM} = 5.14 MeV to $\theta_{CM} \approx 0^o - 60^o$ at E_{CM} = 90.46 MeV. Therefore, any analysis of the ^{12}C + ^{9}Be elastic scattering data at energies larger than 5 MeV/nucleon must take into account the contributions to the elastic channel from the multi-step transitions through the intermediate inelastic channels, the ^{9}Be reorientation and the transfer reactions.

The values of deformation parameters of the ^{9}Be nucleus parameters, obtained from the CRC analysis of inelastic scattering, are given in Table 4.2.2. It was found that the deformation length δ_2 = 2.4 fm (β_2 = 1.4), which is in a good agreement with the values obtained in Ref. [165] (δ_2 = 2.448 fm), Ref. [155] (δ_2 = 2.5 fm), Ref. [166] (δ_2 = 2.9 and 2.5 fm), Ref. [167] (δ_2 = 1.97 fm), and Ref. [168] (δ_2 = 2.5 fm). To improve the description of the data for the 2.429 MeV transition at large angles (lower panel in Fig. 4.2.1), a transition with λ = 4 and deformation length δ_4 = 0.4 fm was added into calculations.

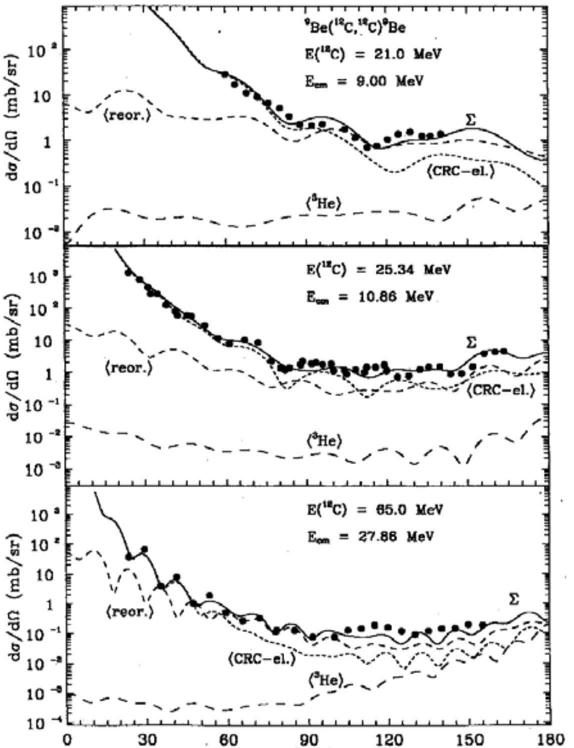

Fig. 4.2.3. Angular distributions of the ^{9}Be(^{12}C, ^{12}C)^{9}Be elastic scattering at the energies E_{LAB}(^{12}C) = 21 MeV [151], 25.34 MeV [163] and 65 MeV. The solid curves Σ and dashed curves <*reor.*>, <*CRC-el.*>, <^{3}He> show the angular distributions corresponding to the sum of all processes, ^{9}Be reorientation, CRC elastic scattering and ^{3}He-cluster transfer, respectively.

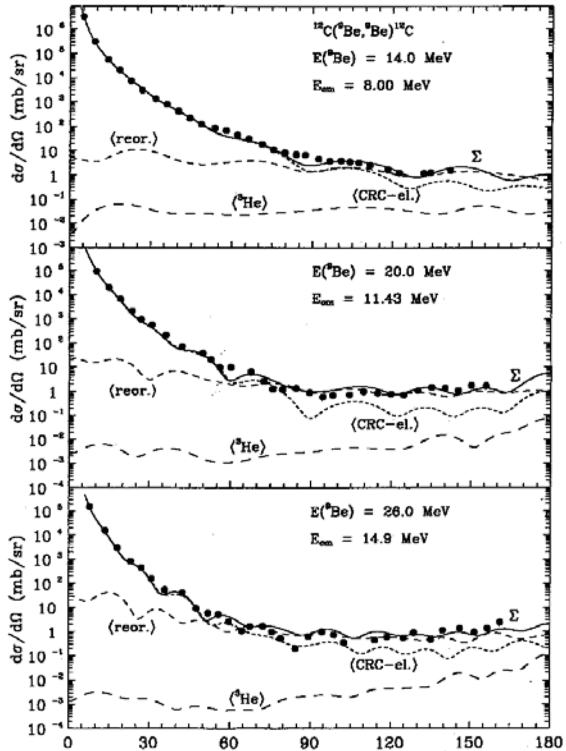

Fig. 4.2.4 Angular distributions of the ^{12}C(^{9}Be, ^{9}Be)^{12}C elastic scattering at the energies E_{LAB}(^{9}Be) = 14, 20 and 26 MeV [159 – 161]. The solid curves Σ and dashed curves <*reor.*>, <*CRC-el.*>, <^{3}He> show the angular distributions corresponding to the sum of all processes, ^{9}Be reorientation, CRC elastic scattering and ^{3}He-cluster transfer, respectively.

The OM potential of the entrance channel (Table 4.2.1) was also used for the intermediate channels in the CRC calculations of the two-step transfer reactions (Fig. 4.2.7). The OM potential parameter W_S was additionally fitted to the data of elastic scattering in order to describe the angular distributions at small angles. The corresponding values of W_{CRC} obtained in the analysis are given in Table 4.2.1.

The angular distributions of the ^{12}C + ^{9}Be elastic scattering, which were calculated within the CRC model using the above-mentioned processes in the coupled channel scheme, are plotted in Figs. 4.2.1 – 4.2.6 using the solid curves Σ (coherent sum of all processes) and the dashed curves labeled by the (process name) are shown for each individual term separately. All the experimental data are well described by the CRC angular distributions in a broad angular range. The potential scattering and the ^{9}Be reorientation (curves labeled by <reor.>) are dominant at large angles for all energies. The next important process contributing to the data at large angles is the ^{3}He-cluster transfer reaction. The contributions of two-step transfer reactions are negligibly small, as it can be seen from Fig. 4.2.1 (upper panel) for the n + α and α + n transfers.

At higher energies (E_{CM} = 90.46 MeV [157]), only the experimental data at forward angles are available. Therefore, in this case, we could not use our fitting procedure which requires the description of the angular distribution at backward angles. As the result, the two sets (*A* and *B)* of optical-potential parameters were obtained (see Table 4.2.1). The both sets give a good description of the data at forward angles and slightly different angular distributions at large angles.

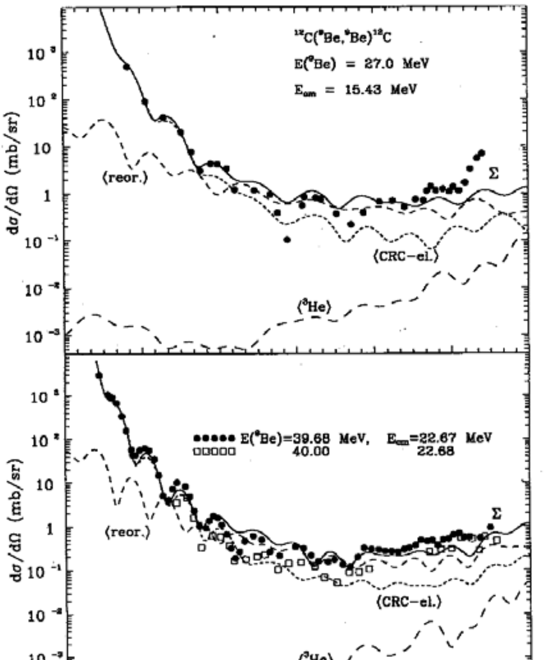

Fig. 4.2.5. Angular distributions of the ^{12}C(^{9}Be, ^{9}Be)^{12}C elastic scattering at the energies E_{LAB}(^{9}Be) = 27 MeV [153], 39.68 MeV [162] and 40 MeV [153] open square . The solid curves Σ and dashed curves <*reor.*>, <*CRC-el.*>, <^{3}He> show the angular distributions corresponding to the sum of all processes, ^{9}Be reorientation, CRC elastic scattering and ^{3}He-cluster transfer, respectively.

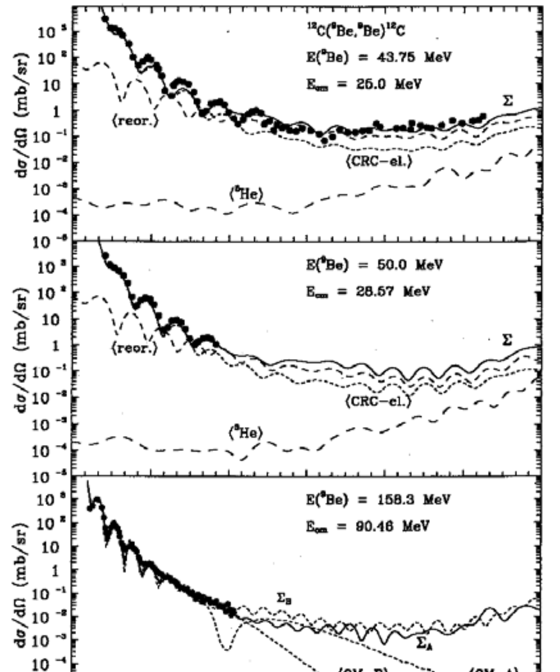

Fig. 4.2.6. Angular distributions of the ^{12}C(^{9}Be, ^{9}Be)^{12}C elastic scattering at the energies E_{LAB}(^{9}Be) = 43.75 MeV [162], 50 MeV [164] and 158.3 MeV [153] . The solid curves Σ and dashed curves <*reor.*>, <*CRC-el.*>, <^{3}He> show the angular distributions corresponding to the sum of all processes, ^{9}Be reorientation, CRC elastic scattering and ^{3}He-cluster transfer, respectively.

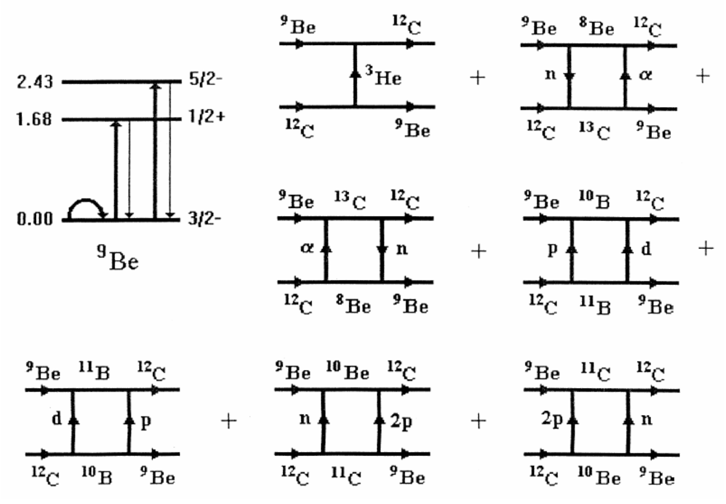

Fig. 4.2.7. A scheme of the transitions included in the coupled channel scheme and diagrams of one- and two-step transfer reactions.

The values of the OM potential parameters listed in Table 4.2.1 are plotted in Fig. 4.2.8. The values of the energy dependence parameters $X_i^{\min}$, $X_i^{\max}$, E_{Xi} and ΔE_{Xi} obtained in the fitting procedure are listed in Table 4.2.3.

Table 4.2.1 Parameters of the Woods–Saxon optical model potentials for the ^{12}C + ^{9}Be elastic scattering ($R = r(A^{1/3}_T + A^{1/3}_P)$, i=V,W,C)

P	E_{LAB}	E_{CM}	V	r_V	a_V	W_S	W_{CRC}	r_W	a_W	r_C
	MeV	MeV	MeV	fm	fm	MeV	MeV	fm	fm	fm
^{12}C	12.00	5.14	108.0	0.843	0.76	4.9	3.5	1.35	0.60	0.843
^{12}C	15.00	6.43	115.0	0.810	0.79	5.5	3.8	1.34	0.60	0.810
^{12}C	18.00	7.71	118.0	0.797	0.80	7.0	5.3	1.31	0.57	0.797
^{9}Be	14.00	8.00	140.0	0.794	0.80	7.0	6.5	1.28	0.60	0.794
^{12}C	21.00	9.00	145.9	0.793	0.76	8.0	7.0	1.27	0.60	0.793
^{12}C	25.34	10.86	161.8	0.793	0.80	8.5	6.5	1.27	0.68	0.793
^{9}Be	20.00	11.43	167.1	0.789	0.80	8.6	8.0	1.27	0.68	0.789
^{9}Be	26.00	14.86	172.9	0.791	0.80	12.0	9.9	1.25	0.60	0.791
^{9}Be	27.00	15.43	174.1	0.791	0.76	12.0	9.9	1.25	0.60	0.791
^{9}Be	39.68	22.67	180.0	0.789	0.80	15.0	12.2	1.25	0.68	0.789
^{9}Be	40.00	22.86	180.0	0.789	0.80	15.0	12.2	1.25	0.68	0.789
^{9}Be	43.75	25.00	181.4	0.789	0.80	15.5	13.0	1.25	0.68	0.789
^{12}C	65.00	27.86	181.4	0.789	0.76	16.0	14.5	1.25	0.68	0.789
^{9}Be	50.00	28.57	181.4	0.789	0.80	16.0	14.5	1.25	0.68	0.789
^{9}Be	158.30	90.46	132.0*A*	0.789	0.83	20.6	18.0	1.25	0.69	0.789
			181.4*B*	0.789	0.80	21.0	19.0	1.25	0.68	0.789

Table 4.2.2 Deformation parameters δ_λ and β_λ for the ^{9}Be nucleus.

E_x(MeV)	J^π	λ	δ_λ(fm)	β_λ
0.000	3/2-	2	2.40	1.40
1.680	1/2+	1	2.00	1.17
2.429	5/2-	2	2.40	1.40
		4	0.40	0.23

In the past attention was paid mainly to the energy dependence of the depths *V* and *W* of the OM potential for the nucleus – nucleus interaction (see for instance Refs. [167, 239] and references therein). The *V* and *W* parameters obtained in the fitting procedure were approximated with linear energy-dependent forms in a limited energy range. Recently, the interest in the energy dependence of OM potential parameters increased due to the observation of the threshold anomalies in the interaction potentials for elastic scattering [159 – 164]. It was found that these anomalies can be explained by the relation between the real and imaginary parts of the OM potential and obey the dispersion relation Refs [159, 160]. Recently the threshold anomalies were studied for the elastic scattering of ^{6}Li and ^{7}Li ions on heavy nuclei [162 – 164]. The anomaly was observed for the ^{7}Li + ^{138}Ba elastic scattering and not observed for the ^{6}Li + ^{138}Ba scattering [164]. The absence of the anomaly for the ^{6}Li + ^{138}Ba scattering was explained by the fact that the breakup threshold for the ^{6}Li nucleus is lower than its first exited state [164]. The ^{9}Be nucleus has a structure similar to the ^{7}Li nucleus and one can expect the existence of the threshold anomaly for the ^{9}Be + ^{12}C scattering. The results of our investigations of ^{9}Be + ^{12}C scattering are presented in this section.

It can be seen from Fig. 4.2.8 that the potential radius parameters r_V and r_W have a weak energy dependence at energies above the Coulomb barrier. The parameters a_V and a_W have a tendency to increase with rising energy. W_S converges to a constant at higher energies. The dispersion term $\Delta V(E)$ (see the upper panel in Fig. 4.2.8) has a shallow broad minimum near the Coulomb barrier (~ 10% of V) and consequently a small broad peak is observed in $V(E)$ at the energies E_{CM} = 12 – 30 MeV. This peak can be considered as the threshold anomaly of the ^{12}C + ^{9}Be elastic scattering, although it only slightly exceeds the uncertainty of V. The dispersion term $\Delta V(E)$ increases at higher energies and leads to a significant change of V.

Table 4.2.3 Parameters of the energy dependence of the OM potentials for ^{12}C + ^{9}Be elastic scattering.

X_i	V_0 (MeV)	W_S (MeV)	W_{CRC} (MeV)	r_V (fm)	r_W (fm)	a_V (fm)	a_W (fm)
$X_i^{\min}$	0.00	0.00	0.00	0.78	1.25	0.71	0.50
$X_i^{\max}$	202.00	19.12	18.00	1.22	1.41	0.84	0.73
E_{Xi}(MeV)	1.87	12.86	15.51	1.90	4.90	9.00	9.00
ΔE_{Xi}(MeV)	4.50	7.33	8.93	2.30	2.10	40.00	40.00

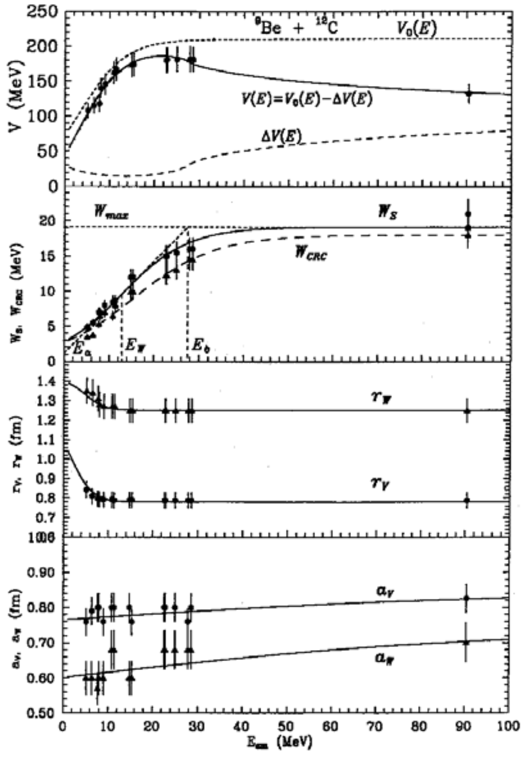

Fig. 4.2.8. Energy dependence of the OM potential parameters for the ^{9}Be + ^{12}C interaction. The values of E_a, E_W, E_b and W_{max} are for simple parametrization of V and W parameters [4]. The Coulomb barrier height is $E_{Coul.}$ = 5.49 MeV (CM).

The data were analyzed within the optical and CRC models using above mentioned coupling scheme. The strong coupled-channels effects were observed. A good description of the experimental data was achieved. We have found an interesting result of dominance of the ^{9}Be reorientation process in the cross section at large angles. This is in good agreement with an analogous result obtained earlier for the ^{9}Be + ^{40}Ca elastic scattering [168]. At the same time, we found a rather small contribution of the ^{3}He-cluster transfer in the backward hemisphere. In the past, the latter process was commonly believed to be the dominant process in the large angle region for the ^{9}Be + ^{12}C elastic scattering.

4.3. The ^{14}N + ^{7}Li, ^{12}C scattering.

4.3.1. Scattering of ^{14}N + ^{7}Li nuclei, optical potential, the ALAS phenomenon and influence of reorientation processes.

This sub-Section is devoted to the study of the backward angle enhancement in the ^{14}N + ^{7}Li elastic scattering – the so called anomalous large-angle scattering (ALAS). The ALAS mechanism was already considered in sub-Section 4.1.2 for ^{11}B + ^{13}C [9] and sub-Section 4.1.4 for ^{11}B + ^{9}Be [8] nuclei interaction. It seems that each individual reaction has its own ALAS mechanism: weak absorption, quasi-molecular resonances, sequential α-cluster transfers, reorientation etc. The mechanisms of the backward-angle enhancement are strongly dependent on the structure and quantum numbers of the colliding nuclei.

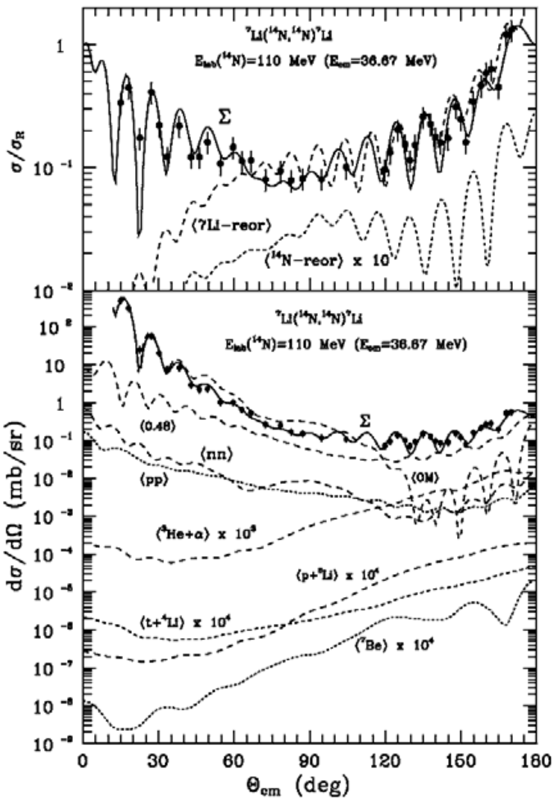

Fig. 4.3.1. Angular distributions of the elastic scattering ^{14}N + ^{7}Li at E_{LAB}(^{14}N) = 110 MeV. The dashed curves <^{7}Be>, <nn>, <pp>, <^{3}He + α>, <p + ^{6}Li>, <n + ^{6}Be>, <d + ^{5}Li>, <t + ^{4}Li> show the CRC cross sections for individual mechanisms corresponding to diagrams shown in Fig. 4.3.4. The curves marked by <OM> and <^{7}Li-reor>, <^{14}N-reor> show the OM and ^{7}Li, ^{14}N reorientation cross sections, respectively. The solid curves Σ shows the coherent sum of CRC cross sections for the potential elastic scattering and reorientation of ^{7}Li.

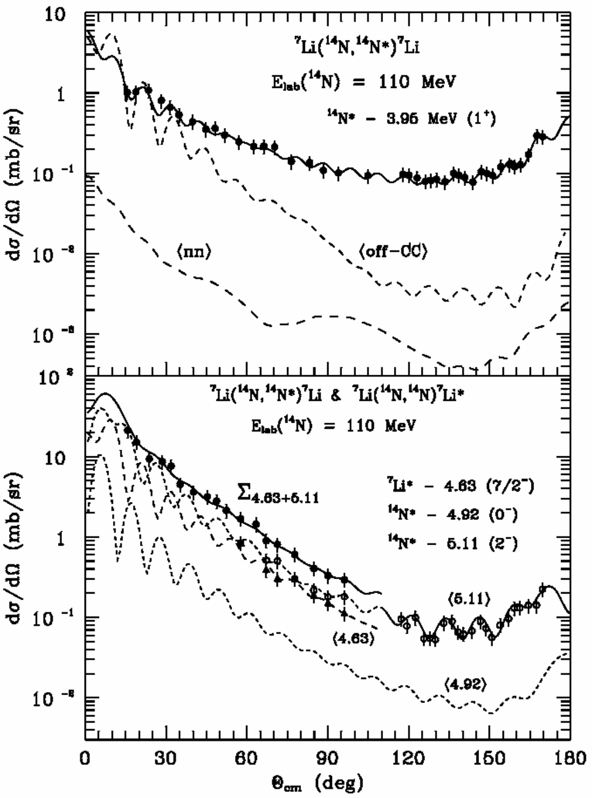

Fig. 4.3.2. Angular distributions of the inelastic scattering ^{14}N + ^{7}Li at E_{LAB}(^{14}N) = 110 MeV for the transitions to the 3.948 MeV (1^+) (see the upper panel) and to the 4.915 MeV (0^-) + 5.106 MeV (2^-) states of ^{14}N and to the 4.63 MeV ($7/2^-$) state of ^{7}Li (see the lower panel). The curves in the upper panel show the cross sections for the rotational transition with (solid curve) and without (curve <off-CC>) channel coupling and the CRC cross section for the successive exchange of neutrons corresponding to the second and third diagrams shown in Fig. 4.3.4 (curve <nn>). The solid curie $\Sigma_{4.63+5.11}$ in the lower panel represents the incoherent sum of CRC cross sections for transitions to the 4.63 MeV state of ^{7}Li and 5.106 MeV state of ^{14}N.

The angular distributions of the elastic and inelastic scattering of the ^{14}N ions on the ^{7}Li nuclei together with the reaction ^{7}Li(^{14}N, ^{15}N)^{6}Li at E_{LAB}(^{14}N) = 110 MeV were measured [7]. The results of the analysis of this reaction is presented in sub-Section 5.3.1. The obtained experimental results are shown in Figs. 4.3.1 – 4.3.3. The enhancement of the elastic scattering at backward angles is clearly visible. Therefore, the measured angular distribution for the elastic scattering can be useful in search for the dominant mechanism in the backward angle elastic scattering.

One can see in Figures 4.3.2 and 4.3.3 an enhancement in the backward inelastic scattering, similar to the one observed for the elastic scattering.

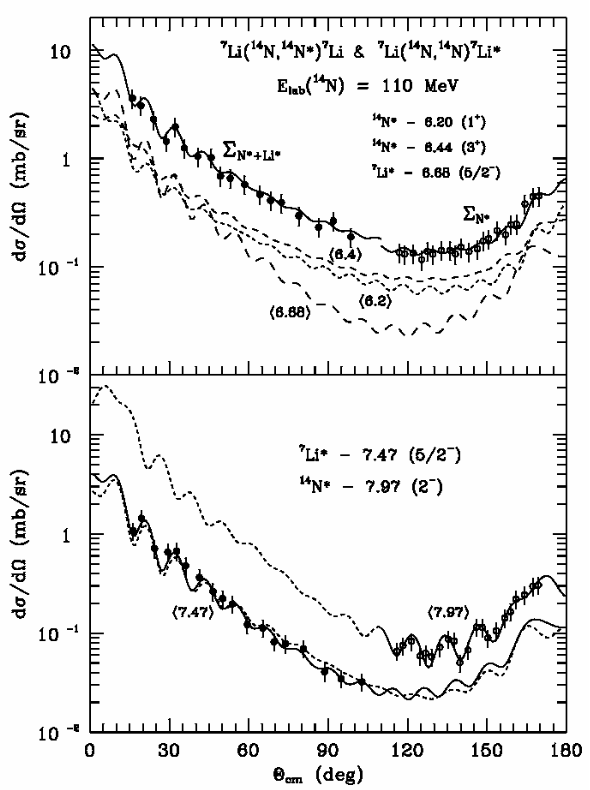

Fig. 4.3.3. Angular distributions of the inelastic scattering ^{14}N + ^{7}Li at E_{LAB}(^{14}N) = 110 MeV for the transitions to the 6.204 MeV (1^+), 6.444 MeV (3^+) and 7.967 MeV (2^-) states of ^{14}N and to the 6.68 MeV ($5/2^-$) and 7.47 MeV ($5/2^-$) states of ^{7}Li. The curves <E_x> present the CRC cross sections for the individual transitions. In the upper panel, the solid curves $\Sigma_{\mathrm{N*+Li*}}$ and $\Sigma_{\mathrm{N*}}$ show the incoherent sums of the CRC cross sections for the transitions to the states 1^+(^{14}N) + 3^+(^{14}N) + $5/2^-$(^{7}Li) and 1^+ + 3^+ of nitrogen, respectively. In the lower panel, the solid and dashed curve <7.47> represent the CRC cross sections in which the reorientation of ^{7}Li is included in the standard way or is artificially doubled, respectively.

The optical model with the potentials of the Woods-Saxon type were used in the OM- and CRC-calculations. The elastic and inelastic scattering for transitions to the excited states of ^{7}Li and ^{14}N as well as reorientation of ^{7}Li and ^{14}N were included in the coupling channel scheme. The deformation length parameters, δ_2 of ^{7}Li and δ_1, δ_2, δ_3 of ^{14}N, were used to describe the deformation of the optical potential. These parameters and the depth W_S of the imaginary part of the OM potential, obtained in the analysis of elastic scattering within optical model, were fitted to describe the elastic and inelastic scattering ^{7}Li + ^{14}N in the CRC method. The main effect of the explicit channel coupling relies on a reduction of the imaginary potential. Below, the depth of the imaginary optical potential used in the CRC analysis will be denoted by W_{CRC}. The obtained optical potential parameters and the deformation parameters δ_λ (universal for all the states) are listed in Tables 4.3.1 and 4.3.2.

In the analysis of the exit reaction channels, the corresponding transfer channels were added to the coupling scheme. The cross sections for the one- and two-step processes corresponding to the diagrams shown in Fig. 4.3.4, were calculated to estimate their contributions to the elastic and inelastic scattering. Both standard (d, t, ^{3}He, α) and exotic (^{4,5,6}Li, ^{6,7,8}Be) clusters were included in the present calculations.

Table 4.3.1 Parameters of Woods–Saxon optical potentials for the reactions ^{7}Li(^{14}N,X)
($R = r_i(A^{1/3}{}_T + A^{1/3}{}_P)$, $i = V,W$)

$T+P$	E_{LAB} (MeV)	E_{CM} (MeV)	V (MeV)	r_V (fm)	a_V (fm)	W_S (MeV)	W_{CRC} (MeV)	r_W (fm)	a_W (fm)	r_C (fm)
^{6}Li+^{14}N	19.5[a]	5.85	80.0	0.980	0.662	6.5	6.5	1.161	0.662	1.25
^{14}N+^{6}Li	32.0[b]	22.40	164.0	0.803	0.720	20.0	18.0	1.100	0.720	1.25
^{14}N+^{7}Li	36.0[c]	24.00	169.0	0.798	0.730	21.0	19.0	1.100	0.730	1.25
^{7}Li+^{14}N	110.0	36.67	205.0	0.798	0.740	22.5	20.5	1.000	0.740	1.25
^{8}Li+^{13}N		28.15	190.0	0.793	0.735		19.5	1.021	0.735	1.25
^{6}Li+^{15}N		40.25	208.0	0.805	0.740		9.0	1.000	0.740	1.25
^{8}Be+^{13}C		46.37	165.2	0.793	0.760		7.0	1.250	0.760	1.25
^{5}He+^{16}O		47.78	204.0	0.815	0.740		9.0	1.000	0.740	1.25
^{6}He+^{15}O		33.99	206.5	0.805	0.739		9.0	1.000	0.739	1.25
^{9}Be+^{12}C		43.09	157.0	0.789	0.799	19.4	17.5	1.250	0.661	1.25
^{10}B+^{11}B		33.72	122.5	0.788	0.782	10.9	9.6	1.240	0.570	1.25
^{10}Be+^{11}C		31.18	124.2	0.788	0.782		9.5	1.240	0.570	1.25

Data from: [a][124], [b][125], [c][123].

Table 4.3.2 Deformation parameters of the nuclei ^{6}Li, ^{7}Li and ^{14}N (β_λ for $R = 1.25A^{1/3}$ fm).

Nucleus	δ_1(fm)	β_1	δ_2(fm)	β_2	δ_3(fm)	β_3
^{6}Li			1.20	0.53		
^{7}Li			1.20	0.50		
^{14}N	0.40	0.13	0.10	0.03	1.00	0.33

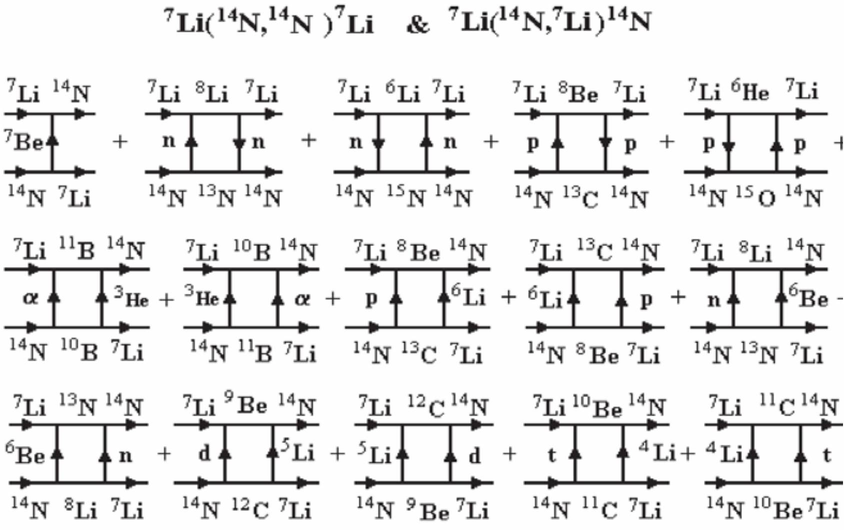

Fig. 4.3.4. Diagrams of the one- and two-step processes for the elastic and inelastic scattering of ^{7}Li(^{14}N, ^{14}N)^{7}Li and ^{7}Li(^{14}N, ^{7}Li)^{14}N included in the present analysis. Diagrams of the one- and two-step processes for the ^{7}Li(^{14}N, ^{15}N)^{6}Li and ^{7}Li(^{14}N, ^{6}Li)^{15}N reactions are show in Fig. 5.3.1.

At present only the data of elastic scattering ^{14}N + ^{7}Li for E_{LAB}(^{7}Li) = 36 MeV [123] exist. We included into the common analysis also the elastic scattering data for other isotopes of lithium and nitrogen. For instance, there are experimental data for the elastic scattering ^{14}N + ^{6}Li at E_{LAB}(^{14}N) = 19.5 MeV [124] and E_{LAB}(^{6}Li) = 32 MeV [125]. We have found that the OM parameters for the elastic scattering of ^{6}Li and ^{7}Li on ^{14}N at close energies 32 MeV and 36 MeV, respectively, differ only slightly. This can be seen from Table 4.3.1. The corresponding OM angular distributions are shown in Fig. 4.3.5 (curves <OM>). For this reason, we have used the above mentioned data of the elastic scattering ^{14}N + ^{6}Li and ^{14}N + ^{7}Li to obtain the energy dependence of the OM parameters, similarly as in [4, 6] for the elastic scattering ^{12}C + ^{9}Be and ^{12}C + ^{11}B.

As is seen from Fig. 4.3.1, the optical model (curve <OM>) with parameters fitted to the experimental angular distributions (see Table 4.3.1) does not describe the backward-angle enhancement of the elastic scattering ^{14}N + ^{7}Li. We have tried to explain this enhancement by means of several light- and heavy-cluster exchanges, the corresponding diagrams of which are shown in Fig. 4.3.4. The OM parameters for the intermediate channels were calculated using the corresponding energy dependences found in [3, 4, 5]. All these parameters are listed in Table 4.3.1. The corresponding CRC angular distributions are shown in the lower panel of Fig. 4.3.1. As expected, the cross sections of all transfer reactions leading to the elastic channel are very small.

The reorientations of ^{7}Li or ^{14}N are the alternative processes which can, at least potentially, provide the backward angle enhancement of the elastic scattering. The cross sections of these processes are determined by the quadrupole deformation of ^{7}Li and ^{14}N. The deformation length parameter δ_2 = 0.1 fm for ^{14}N was taken from our previous study [1] and was successfully tested in the analysis of the present data of inelastic scattering for the transition to the 3.95 MeV (1^+) state of ^{14}N. The parameter δ_2 for ^{7}Li was fitted to the data of both the elastic and inelastic scattering, i.e. for the transition to the ground and 7.467 MeV ($5/2^-$) excited states of ^{7}Li, respectively. In both cases we have obtained δ_2 = 1.2 fm for ^{7}Li. The contributions of the reorientations of ^{7}Li and ^{14}N are presented in the upper panel of Fig. 4.3.1. One can see that the reorientation of ^{7}Li dominates at large angles and satisfactorily describes the observed backward-angle enhancement of the elastic scattering ^{14}N + ^{7}Li.

The reorientation of ^{7}Li dominates in the backward elastic scattering ^{14}N + ^{7}Li also at energy $E_{\mathrm{LAB}}(^{7}\mathrm{Li})$ = 36 MeV, as one can see from the lowest panel in Fig. 4.3.5 (curve <reor>). In contrast, the elastic scattering ^{14}N + ^{6}Li at $E_{\mathrm{LAB}}(^{14}\mathrm{N})$ = 19.5 MeV is completely of the potential type (the upper panel of Fig. 4.3.5). However, at $E_{\mathrm{LAB}}(^{6}\mathrm{Li})$ = 32 MeV the CRC calculation predicts a backward angle enhancement in the angular distribution of elastic scattering (see the middle panel of Fig. 4.3.5).

The anomalous large-angle scattering is observed also in the inelastic channels ^{14}N* + ^{7}Li for the transitions to the 3.95MeV (1^+), 5.11 MeV (2^-), 6.20 MeV (1^+) + 6.44 MeV (3^+) and 7.97 MeV (2^-) excited states of ^{14}N (see Figs. 4.3.2 and 4.3.3). Due to a small quadrupole deformation of ^{14}N, the reorientation of ^{14}N* gives a small contribution to the large-angle inelastic scattering if the quadrupole deformation of excited ^{14}N* is the same as in the ground state (a suggestion of rotational nature of the excited state). Moreover, the CRC cross section for the transition to the 7.47 MeV ($5/2^-$) excited state of ^{7}Li with the artificially doubled reorientation amplitude of ^{7}Li* (dashed curve <7.47> in the lower panel of Fig. 4.3.3) differs very little from the cross section of this transition with the standard account of the reorientation of ^{7}Li* (solid curve <7.47>). Thus, the mechanism of the ALAS for inelastic scattering is different than that for elastic one.

Then, for understanding the mechanism of ALAS for the transition to the 3.95 MeV (1^+) state of ^{14}N, we have calculated the CRC cross sections for the exchange processes corresponding to the diagrams shown in Fig. 4.3.4 and for the corresponding DWBA cross sections without taking into account the channel couplings. These cross sections are shown in the upper panel of Fig. 4.3.2. The curve <nn> presents the CRC cross section for the sequential transfers of neutrons. The cross sections for transfers of other clusters are much smaller. Based on Fig. 4.3.2, one can conclude that the exchange processes play a rather marginal role in the inelastic scattering. The curve <off-CC> shows the DWBA cross section calculated with a code DWUCK4 [126] without channel coupling (CC). In this case, the weak absorption ($W/V \approx 0.1$) leads to an enhancement at backward angles which is, however, much smaller than that observed experimentally. The solid curve in the upper panel of Fig. 4.3.2 shows a very good CRC description of the inelastic scattering ^{14}N + ^{7}Li at $E_{LAB}(^{14}\text{N}) = 110$ MeV for the transition $1^+ \rightarrow 1^+$ to the 3.95 MeV (1^+) excited state of ^{14}N, suggesting the rotational nature of this state. Here the deformation length parameter $\delta_2 = 0.1$ fm for ^{14}N from [1] has been used. Now, one can conclude that the observed ALAS is due to the strong channel coupling and weak absorption.

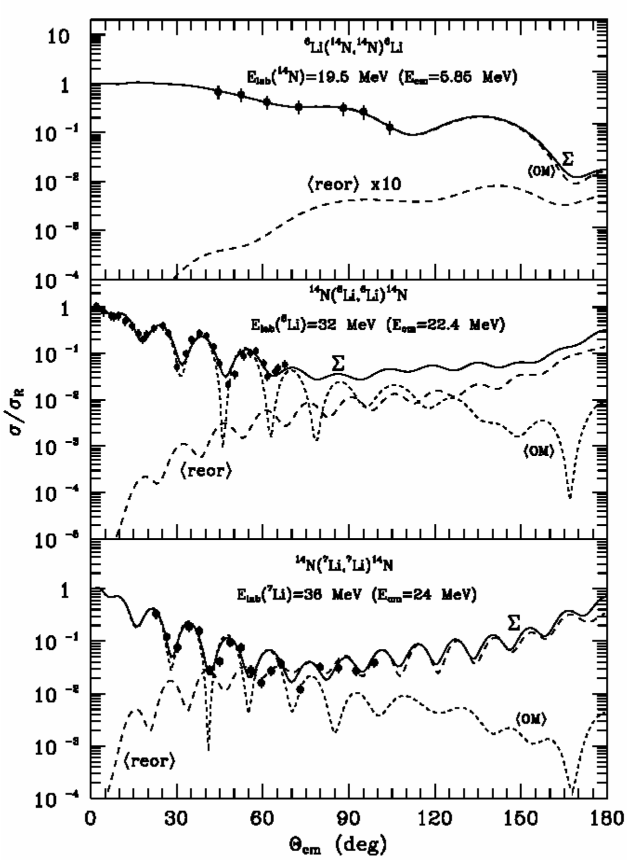

Fig. 4.3.5. Angular distributions of the elastic scattering ^{6}Li + ^{14}N at $E_{LAB}(^{14}\text{N}) = 19.5$ MeV (data from Ref. [127]) and $E_{LAB}(^{6}\text{Li}) = 32$ MeV [128] and the elastic scattering ^{7}Li + ^{14}N at $E_{LAB}(^{7}\text{Li}) = 36$ MeV [129]. The dashed curves <reor> and <OM> show the cross sections of reorientation of ^{7}Li and ^{14}N or ^{6}Li and ^{14}N and optical-model calculations, respectively. The solid curves Σ represent the coherent sums of potential elastic scattering and the relevant reorientation.

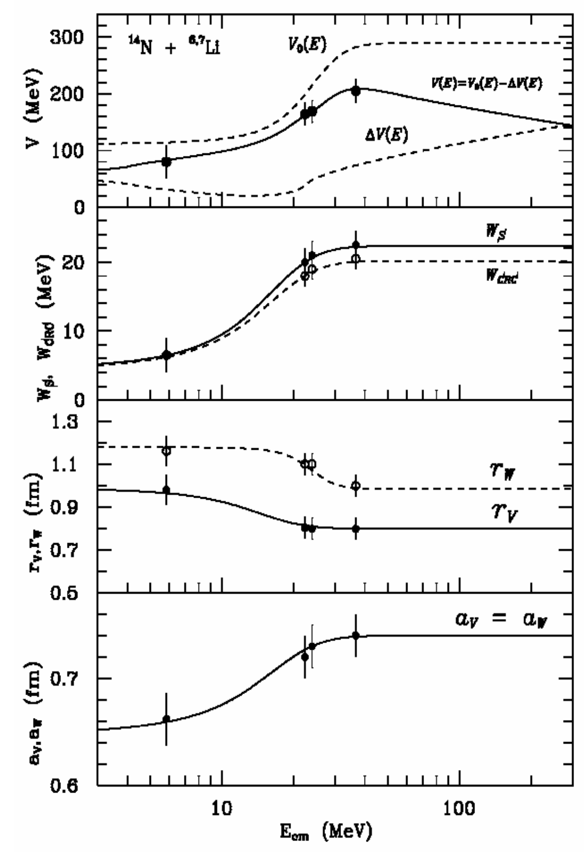

Fig. 4.3.6. Energy dependence of the OM potential parameters for the interaction ^{14}N+^{6,7}Li. The lines were obtained by fitting the parameterization to the experimentally found points.

The deformation length parameter $\delta_1 = 0.4$ fm for ^{14}N, which is in the good agreement with the value of 0.5 fm obtained earlier by us in [1] was found by fitting the backward-angle scattering data for the transition $1^+ \rightarrow 2^-$ to the data of 5.11 MeV (2^-) excited state of ^{14}N (open circles and curve <5.11> in the lower panel of Fig. 4.3.2). As the lower panel of Fig. 4.3.2 shows (curve <4.92>), the transition $1^+ \rightarrow 0^-$ to the 4.92 MeV (0^-) excited state of ^{14}N contributes very little to the experimental data. The transitions $1^+ \rightarrow 2^-$ ($\lambda = 1, 3$, $\delta_1 = 0.4$ fm, $\delta_3 = 1.0$ fm) and $3/2^- \rightarrow 7/2^-$ ($\lambda = 2, 4$, $\delta_2 = 1.2$

fm) to the 5.11 MeV state of ^{14}N and 4.63 MeV ($7/2^-$) state of ^{7}Li give comparable contributions at forward directions (curves <5.11> and <4.63>). The deformation length parameters δ_λ obtained in the analysis of the inelastic scattering for the transitions $1^+ \rightarrow 1^+$ (reorientation of ^{14}N and inelastic scattering), $1^+ \rightarrow 2^-$ (^{14}N excitation), $3/2^- \rightarrow 3/2^-$ (reorientation of ^{7}Li) and $3/2^- \rightarrow 7/2^-$ (^{7}Li excitation) are listed in Table 4.3.2 where we have also collected the corresponding deformation parameters $\beta_\lambda = \delta_\lambda/R$ calculated for $R = 1.25A^{1/3}$.

The deformation length parameters δ_λ from Table 4.3.2 have been used in the CRC calculations for the transitions to several excited states of ^{14}N and ^{7}Li. The corresponding angular distributions are shown in the upper panel of Fig. 4.3.3 (curves <6.2>, <6.4>, <6.68>).

The analytic parameterization of the energy dependence of the OM potential parameters for the elastic scattering ^{14}N + ^{6,7}Li were done. As was mentioned above, except of the ^{14}N + ^{7}Li elastic scattering data also the elastic scattering data for other isotopes of lithium and nitrogen were included into the common analysis. The values obtained from the fit are listed in Table 4.3.3 and the energy dependence of the OM potential parameters for the interaction ^{14}N + ^{6,7}Li is shown in Fig. 4.3.6.

Table 4.3.3 Parameters of energy dependence for OM parameters for the elastic scattering ^{6,7}Li + ^{14}N.

X_i	V_0 (MeV)	r_V (fm)	a_V (fm)	W_S (MeV)	$W_{\rm CRC}$ (MeV)	r_W (fm)	a_W (fm)
$X_i^{\min}$	109.5	0.800	0.64	3.4	3.2	0.987	0.64
$X_i^{\max}$	289.5	1.000	0.74	22.3	20.2	1.180	0.74
E_{Xi}(MeV)	22.5	12.000	13.00	13.4	13.2	23.200	13.00
ΔE_{Xi}(MeV)	4.5	4.000	5.00	4.6	4.8	3.200	5.00

It has been found that one- and two-step transfers of the standard (d, t, ^{3}He, α) and exotic (^{4,5,6}Li, ^{6,7,8}Be) clusters, which usually lead to the enhancement of the cross section, give rather negligible contribution to the elastic scattering ^{14}N + ^{7}Li. The results of the complete analysis of the data of the elastic scattering ^{14}N + ^{7}Li lead to the conclusion that the reorientation of ^{7}Li with its large quadrupole deformation provides the observed anomalous large-angle scattering (ALAS).

In distinction to other cases known from the literature, the deformation parameters of ^{7}Li and ^{14}N could be precisely deduced in the CRC analysis of both the elastic and inelastic scattering ^{14}N + ^{7}Li. The deformation parameter of ^{7}Li obtained from the backward-angle elastic scattering turned out to be identical to that obtained from the analysis of inelastic channels. Using different theoretical approaches in the analysis of the inelastic scattering ^{14}N + ^{7}Li at $E_{LAB}(^{14}\mathrm{N}) = 110$ MeV for the transitions to the low-energy excited states of ^{7}Li and ^{14}N, we have found that the cluster-exchange processes play here a negligible role and that the experimental data are well described by the CRC cross sections for the transitions to the collective (rotational) states of these nuclei. The observed anomalous large-angle inelastic scattering can be explained by weak absorption and a strong channel coupling.

It was found that the experimental angular distribution of the reaction ^{7}Li(^{14}N, ^{15}N)^{6}Li at $E_{LAB}(^{14}\mathrm{N}) = 110$ MeV is dominated by the neutron transfer. The heavy-cluster transfer of ^{8}Be and the two-step transfers were found to be completely negligible for this reaction.

4.3.2. Scattering of ^{14}N + ^{12}C nuclei, the optical potential and ^{12}C and ^{14}N deformation lengths.

The study of various quasi-elastic processes included in the collision of ^{14}N ions with ^{12}C nuclei at $E_{LAB}(^{14}N)$ = 116 MeV [1] are presented in this sub-Section. The interaction of ^{14}N ions with ^{12}C nuclei was already investigated at energies between 9 MeV and 280 MeV [201 - 215], but some unexplored intervals exist in this energy range, e.g. 100 MeV - 145 MeV.

The obtained angular distributions are shown in Figs. 4.3.7 and 4.3.9 − 4.3.13. The error bars presented in these figures include both the statistical errors and the uncertainties due to the fitting procedure. The error of the cross section normalization does not exceed 15%.

The quasi-elastic processes in the ^{14}N + ^{14}C reaction at the same beam energy have been already studied [216]. In the present sub-Section, we investigate isotopic effects for the ^{12}C and ^{14}C nuclei by comparison of the corresponding elastic scattering of the ^{14}N ions.

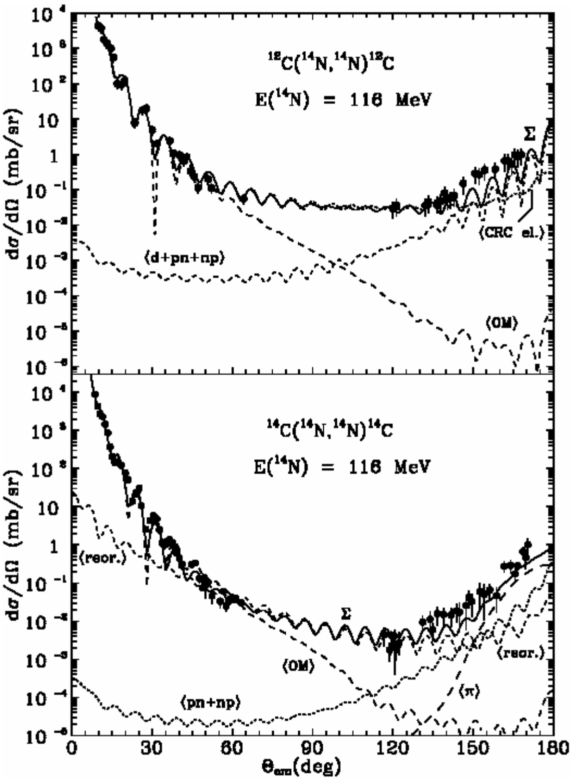

Fig. 4.3.7. Angular distributions of the ^{14}N + ^{12}C and ^{14}N + ^{14}C elastic scattering at $E_{LAB}(^{14}N)$ = 116 MeV. The curves show the cross sections by the optical model (curves <OM>) and CRC approach for the elastic channels (curve <CRC el.>), reorientation process (curve <reor.>), two-step transfers of p + n and n + p (curve <pn + np>) transfers of the d-cluster, p + n and n + p transfer (curve <d + pn + np>) and direct $\pi^{\pm}$ - exchange (curve <π>). The curves *Σ* correspond to total angular distributions including all the processes.

The angular distribution of the ^{14}N + ^{12}C elastic scattering at $E_{LAB}(^{14}N)$ = 116 MeV is shown in Fig. 4.3.7 (upper panel) and the angular distribution of the ^{14}N + ^{14}C [216] elastic scattering at the same beam energy is shown in Fig. 4.3.7 (lower panel). The experimental data were analyzed using the optical model (OM) and coupled reaction channels (CRC) models. The obtained parameters of the ^{14}N + ^{14}C OM potential are given in Table 4.3.4. The parameters of this potential were used as the starting point in the analysis of the ^{14}N + ^{12}C elastic scattering. At the second step, the a_V, a_W and W_S parameters, were fitted in order to describe the ^{14}N + ^{12}C angular distribution. The fitted parameters are close to the corresponding values of the ^{14}N + ^{14}C system (see Table 4.3.4). The calculated OM angular distribution is presented in Fig. 4.3.7 (upper panel). The pure OM potential cross section describes the data only at forward angles.

Table 4.3.4. Parameters of Woods-Saxon optical model potentials
($R = r_i(A^{1/2}_T + A^{1/3}_P)$, i = V, W)

T + P	V (MeV)	r_V (fm)	a_V (fm)	W_S (MeV)	r_W (fm)	a_W (fm)	r_C (fm)	Ref.
$^{14}C+^{14}N$	150	0.812	0.708	35.40	0.958	0.789	1.200	[216]
$^{12}C+^{14}N$	150	0.812	0.722	29.75 (35.75[a])	0.958	0.796	0.812	
$^{13}C+^{13}N$	150	0.812	0.900	35.75	0.958	0.500	0.812	
$^{11}C+^{15}N$	150	0.812	0.722	35.75	0.958	0.796	0.812	

[a] For optical model

Figure 4.3.7 shows that the OM angular distributions describe the $^{14}N + ^{12}C$ and $^{14}N + ^{14}C$ data only in the forward hemisphere. Other direct processes are expected to contribute at backward angles. The diagrams of the most probable one-step and two-step transfer contributions to the $^{14}N + ^{12}C$ and $^{14}N + ^{14}C$ data the backward hemisphere are shown in Fig. 4.3.8. The reorientation of the ^{14}N nucleus may also influence the backward angular region. All these processes, together with the potential scattering, were included in the CRC calculations in order to describe the data in the whole angular range.

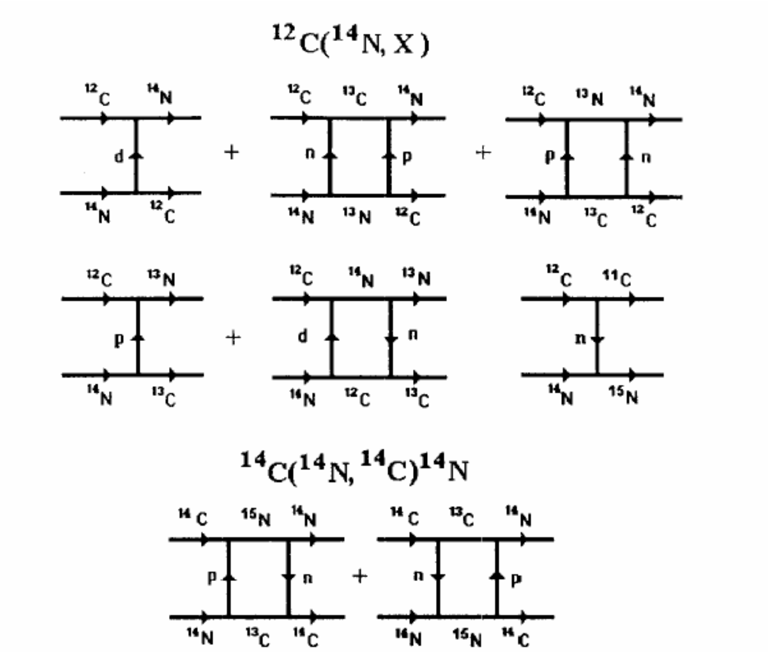

Fig. 4.3.8. Diagrams of possible transfer processes for the $^{12}C(^{14}N, X)$ and $^{14}C(^{14}N, ^{14}C)^{14}N$ reactions.

The elastic and inelastic scattering of $^{14}N + ^{14}C$ nuclei and the reorientation of the ^{14}N as well as all the transfers shown in Fig. 4.3.8, were included in the coupling scheme of the CRC calculation. The inclusion of the transfer processes into CRC calculations did not noticeably modify the CRC elastic and inelastic cross section. The potential determined in the CRC analysis is presented in Table 4.3.4.

The angular distribution of the $^{12}C(^{14}N, ^{13}C)^{13}N$ reaction is presented in Fig. 4.3.9. Both the p- and sequential d+n-transfer processes (Fig. 4.3.8) were included in the coupled reaction channel scheme. As a starting point of the fit, the OM parameters of the initial channel were used. Only the a_V and a_W parameters were fitted. The resulting parameters differ significantly from the corresponding values for the $^{14}N + ^{12}C$ initial channel. The fitted parameters of the $^{13}N + ^{13}C$ potential are given in Table 4.3.4. The p-transfer (<p> curve) is dominant in the $^{12}C(^{14}N, ^{13}C)^{13}N$ reaction. The two-step d+n-transfer (<d+n> curve) was rather negligible.

The $^{13}N + ^{13}C$ potential was successfully used in the CRC analysis of the $^{12}C(^{14}N, ^{13}C)^{13}N$ reaction for the transitions to the 3.68 MeV ($3/2^-$) and 3.85 MeV ($5/2^+$) excited states of the ^{13}C nucleus. The both states were unresolved in the experiment due to the beam energy spread. The $^{12}C(^{14}N, ^{15}N)^{11}C$ reaction peak is also expected at the same energy position due to the kinematical conditions. It was found that $^{12}C(^{14}N, {}^{13}N)^{13}C_{3.68}$ and $^{12}C(^{14}N, {}^{15}N)^{11}C$ reactions give only small contributions to the cross sections. The missing strength is expected to be due to the $^{12}C(^{14}N, {}^{13}N)^{13}C_{3.85}$ process. However, the $^{13}C_{3.85}$ state belongs to the *sd*-shell for which it is not possible to calculate the spectroscopic amplitude using the formalism of Chapter 2. Therefore, we determined S_x for $^{13}C_{3.85}$ by fitting the CRC cross section (sum of the $^{12}C(^{14}N, {}^{13}N)^{13}C_{3.68}$, $^{12}C(^{14}N, {}^{15}N)^{11}C$ and $^{12}C(^{14}N, {}^{13}N)^{13}C_{3.85}$ reactions) to the experimental data. The value of S_x found from the fit is similar to S_x of the 3.68 MeV ($3/2^-$) state (see Appendix). The cross sections including all processes discussed above is presented in Fig. 4.3.10.

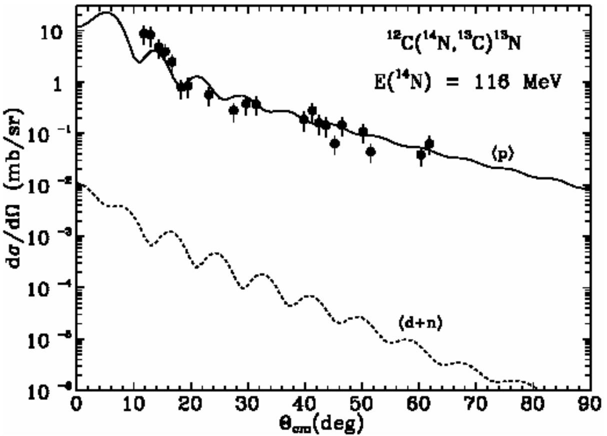

Fig. 4.3.9.. Angular distributions of the $^{12}C(^{14}N, {}^{13}C)^{13}N$ reaction at the energy $E(^{14}N)$ = 116 MeV. The curves show the CRC cross-sections for the p- and d+n transfers (curves <p> and <d+n>, respectively).

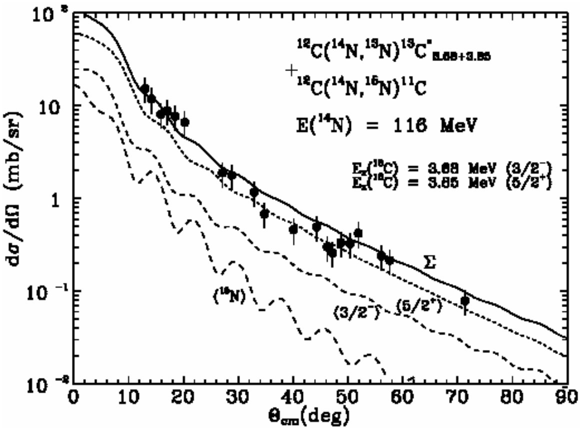

Fig. 4.3.10. Angular distribution of the $^{12}C(^{14}N, {}^{13}N)^{13}C^*_{3.68+3.85}$ + $^{12}C(^{14}N, {}^{15}N)^{11}C$ reactions at the energy $E(^{14}N)$ = 116 MeV for the transitions to the ground states of ejectiles and to the 3.68 Mev ($3/2^-$) + 3.85 MeV ($5/2^-$) excited states of the ^{13}C nucleus. The curves present the CRC cross-sections for the different reactions (curves <$5/2^-$>, <$3/2^-$> and <^{15}N>). The curve Σ represents an incoherent sum of the cross sections for these reactions.

Table 4.3.5. Deformation lengths δ_λ of the ^{12}C and ^{14}N nuclei.

Nuclei	E_x (MeV)	J^π	λ	δ_λ (fm)	Ref.
^{12}C	4.439	2^+	2	−1.07	[217]
^{14}N	3.948	1^-	2	0.10	
	4.915	0^-	1	0.50	
	5.106	2^-	1	0.50	
			3	1.10	

The summed angular distribution of the $^{12}C(^{14}N, {}^{14}N)^{12}C^*_{4.44}$ and $^{12}C(^{14}N, {}^{14}N^*_{3.95})^{12}C$ inelastic scattering to the 4.44 MeV (2^+) excited state of the ^{12}C nucleus and to the 3.95 MeV (1^+) excited state of the ^{14}N nucleus, unresolved in the experiment due to the beam energy spread, is shown in Fig. 4.3.11. These excited states were considered to have the rotational nature. The deformation length δ_2 for the $0^+ \rightarrow 2^+$ transition in the ^{12}C nucleus was taken from the $^{12}C + \alpha$ elastic scattering [217]. The deformation length δ_2 for the $1^+ \rightarrow 1^+$ transition in the ^{14}N nucleus was fitted. The deformation lengths δ_λ used in the CRC calculations are given in Table 4.3.5. The $1^+ \rightarrow 1^+$ transition (long dashed curve <1^+> in Fig. 4.3.11) turned out to be of minor importance at the forward angles ($\theta_{CM} < 30^o$). The $0^+ \rightarrow 2^+$ transition in the ^{12}C nucleus (short dashed curve <2^+>) dominates in this angular range. The incoherent sum of these two transitions (solid curve *Σ*) satisfactorily describes the data.

The summed angular distributions of the $^{12}C(^{14}N,\ ^{14}N_{4.9+5.1})^{12}C$ inelastic scattering to the 4.915 MeV (0^-) and 5.106 MeV (2^-) states of ^{14}N nucleus unresolved in the experiment due to the beam energy spread, and $^{12}C(^{14}N,\ ^{13}N)^{13}C$ reaction, unresolved from the inelastic scattering due to kinematical conditions is shown in Fig. 4.3.12. We found that the CRC angular distributions of the $^{12}C(^{14}N,\ ^{13}N)^{13}C$ reaction was not important at small angles (Fig. 4.3.12, short dashed curve <n>). The deformation lengths for the $1^+ \rightarrow 0^-$ and $1^+ \rightarrow 2^-$ transitions were determined in the fit of the CRC cross section to the experimental data. The obtained values of δ_1 and δ_3 are given in Table 4.3.5. Relative contributions of transitions between the $1^+ \rightarrow 0^-$ and $1^+ \rightarrow 2^-$ states are similar to those obtained in the α-particle inelastic scattering on ^{14}N target [218].

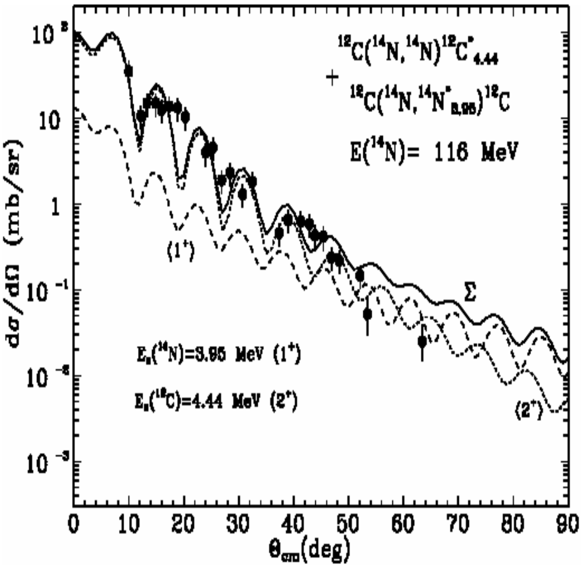

Fig. 4.3.11. Angular distribution of the $^{12}C(^{14}N,\ ^{14}N)^{12}C^*_{4.44}$+$^{12}C(^{14}N,\ ^{14}N^*_{3.95})^{12}C$ inelastic scattering at energy $E(^{14}N)$ = 116 MeV for the transitions to the ground and 4.44 MeV (2^+) excited state of ^{12}C nucleus and 3.95 MeV (1^+) excited state of the ^{14}N nucleus. The curves represent the CRC cross-sections for these two reactions (curves <2^+> and <1^+>). The curve *Σ* is an coherent sum of cross section for both reactions.

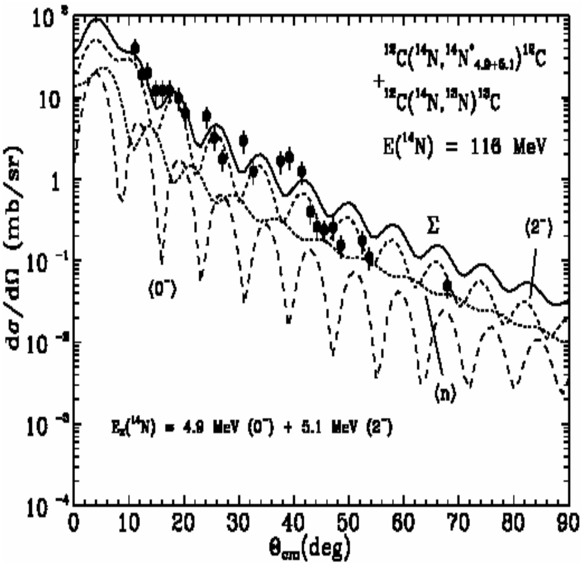

Fig. 4.3.12. Angular distribution of the $^{12}C(^{14}N,\ ^{14}N^*_{4.9+5.1})^{12}C$ inelastic scattering + $^{12}C(^{14}N,\ ^{13}N)^{13}C$ reaction at the energy $E(^{14}N)$ = 116 MeV for transitions to the 4.9 MeV (0^-) + 5.11 MeV (2^-) excited states for the ^{14}N nucleus. The curves correspond to the CRC cross-sections for the different reactions (curves <2^->, <0^-> and <n>). The curve *Σ* shows an incoherent sum of these cross sections.

The backward angles angular distributions of the ^{12}C + ^{14}N elastic scattering is presented in Fig. 4.3.13. The potential scattering, reorientation of the ^{14}N nucleus and p+n, n+p as well as d-cluster transfers contribute to the ^{12}C + ^{14}N elastic scattering. The inelastic channels included in the coupling scheme significantly modify the angular distributions of the ^{14}N + ^{12}C elastic scattering (see curves <OM> and <CRC el.> in Fig. 4.3.7). The CRC elastic cross section (curve <CRC el.> in Fig. 4.3.13) satisfactorily describes the data at $\theta_{CM} < 140^o$. The deuteron transfer (curve <d>) becomes noticeable at $\theta_{CM} > 160^o$. The reorientation of the ^{14}N nucleus (Fig. 4.3.13, curve <reor.>) and the sequential transfers p+n and n+p are rather negligible in the backward hemisphere.

In contrast to the $^{12}C(^{14}N,\ ^{14}N)^{12}C$ process in the $^{14}C(^{14}N,\ ^{14}N)^{14}C$ reaction, the reorientation of the ^{14}N nucleus is crucial, especially in the angular range $\theta_{CM} \approx 60^o - 140^o$.

The inclusion of the reorientation leads to better description of the experimental data of the $^{14}C(^{14}N, ^{14}N)^{14}C$ reaction in comparison to the earlier analysis [216].

Isotopic effects for the $^{14}N + ^{12}C$ and $^{14}N + ^{14}C$ elastic scattering were studied. No strong dependence of the optical potential on the difference in the structure of the ^{12}C and ^{14}C nuclei (^{14}C nucleus has the close 1p neutron shell) was observed. We have already studied quasi-elastic processes in the $^{14}N + ^{14}C$ reaction at the same beam energy [216]. The investigation of the isotopic effects for the ^{12}C and ^{14}C nuclei by the comparison of the corresponding elastic scattering of the ^{14}N ions is presented in this sub-Section. For a precise determination of difference between the angular distributions of the above mentioned scattering, the following function: $P(\theta) = (\sigma_{12C}(\theta) - \sigma_{14C}(\theta))/(\sigma_{12C}(\theta) + \sigma_{14C}(\theta))$ was introduced. $\sigma_{12C}(\theta)$ and $\sigma_{14C}(\theta)$ denote the angular distributions of the $^{14}N + ^{12}C$ and $^{14}N + ^{14}C$ elastic scattering, respectively. The $P(\theta)$ value obtained from the experimental data and from the OM calculations is presented in Figure 4.3.14.

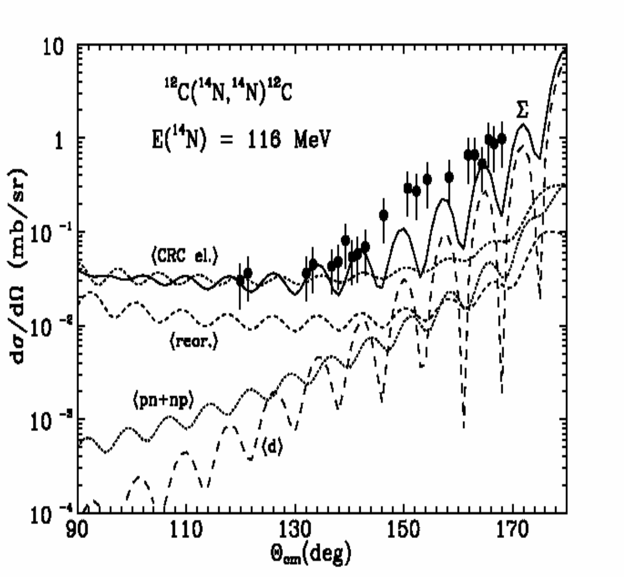

Fig. 4.3.13. Angular distribution of the $^{12}C + ^{14}N$ elastic channel in the backward hemisphere at the energy $E(^{14}N)$ = 116 MeV. The curves show the CRC cross-sections for the elastic channel (curve <CRC el.>), reorientation (curve <reor.>), two-step p + n and n + p (curve <pn+np>) transfers and the transfer of the d-cluster (curve <d>). The curve *Σ* represent the total angular distribution for all these processes.

A quite regular diffractive structure of $P(\theta)$ indicates that there is a systematic shift between the oscillations in the $^{14}N + ^{12}C$ and $^{14}N + ^{14}C$ angular distributions. The dashed curve (the same OM potential parameters for both the systems) satisfactorily describes all features of the experimental differences between the $^{14}N + ^{12}C$ and $^{14}N + ^{14}C$ angular distributions. This curve rather weakly differs from the solid curve (the best-fit parameters). It seems that the observed shift of the oscillations in $P(\theta)$ is primarily due to the difference between the ^{12}C and ^{14}C nuclear radii $R_{14C} - R_{12C} \approx 0.1$ fm, to the reduced mass μ and to the difference between the energies E_{CM} of the $^{14}N + ^{12}C$ and $^{14}N + ^{14}C$ channels ($E_{14C} - E_{12C} \approx 4.46$ MeV). The fit of the a_V, a_W and W_S parameters for the $^{14}N + ^{12}C$ potential leads only to quite small modifications. This means that the difference in the shell structure between the ^{12}C and ^{14}C nuclei (^{14}C nucleus has a close 1p neutron shell) does not have a significant influence on the OM potential parameters.

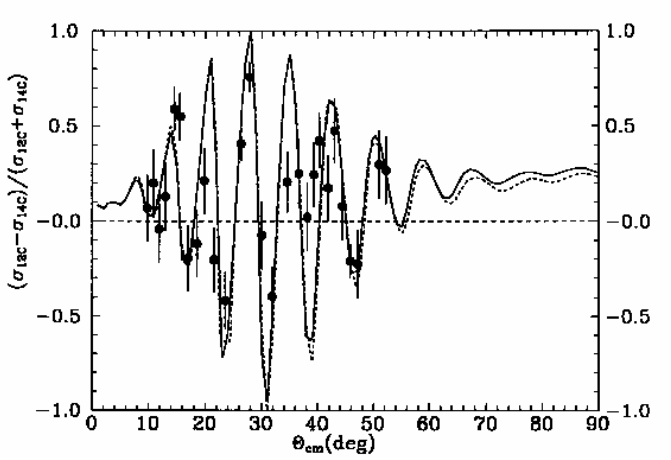

Fig. 4.3.14. The function $P(\theta)$ for the $^{14}N + ^{12}C$ and $^{14}N + ^{14}C$ elastic scattering at the energy $E(^{14}N)$ = 116 MeV.

The following conclusion can be drawn out: The contributions of the different processes to the backward ^{14}N + ^{12}C elastic scattering were calculated. It was found that in the backward elastic scattering both the CRC potential scattering and the deuteron transfer play an important role. The deformation parameters for the ^{12}C and ^{14}N nuclei were obtained by fitting to the ^{14}N + ^{12}C inelastic scattering data. The optical potential for the radioactive ^{13}N + ^{13}C channel was obtained using the data of the ^{12}C(^{14}N, ^{13}C)^{13}N reaction. The optical potential was successfully tested with the ^{12}C(^{14}N, ^{13}N)^{13}C and ^{12}C(^{14}N, ^{13}N)^{13}C$^{*}_{3.68+3.85}$ reactions.

4.4. The ^{7}Li + ^{16}O and ^{18}O + ^{7}Li scattering.

Scattering of ^{7}Li + ^{16}O and ^{18}O + ^{7}Li nuclei, optical potentials and ^{18}O deformation parameters.

The angular distributions of the ^{18}O + ^{7}Li elastic and inelastic scattering were measured at the energy E_{LAB}(^{18}O) = 114 MeV (E_{CM}(^{18}O) = 32 MeV) in the inverse kinematics [16]. The data were analyzed within the optical model and within the coupled reaction channels method to determine the potential parameters of the ^{18}O + ^{7}Li scattering and the reaction channels dominating the scattering. The deformation parameters for the ^{18}O inelastic scattering were obtained. The extracted potentials for ^{18}O + ^{7}Li system were compared to those previously obtained for the ^{7}Li + ^{16}O elastic scattering at E_{LAB}(^{7}Li) = 42 MeV. [20]. The structure and reaction Q-values for both the reactions are quite different.

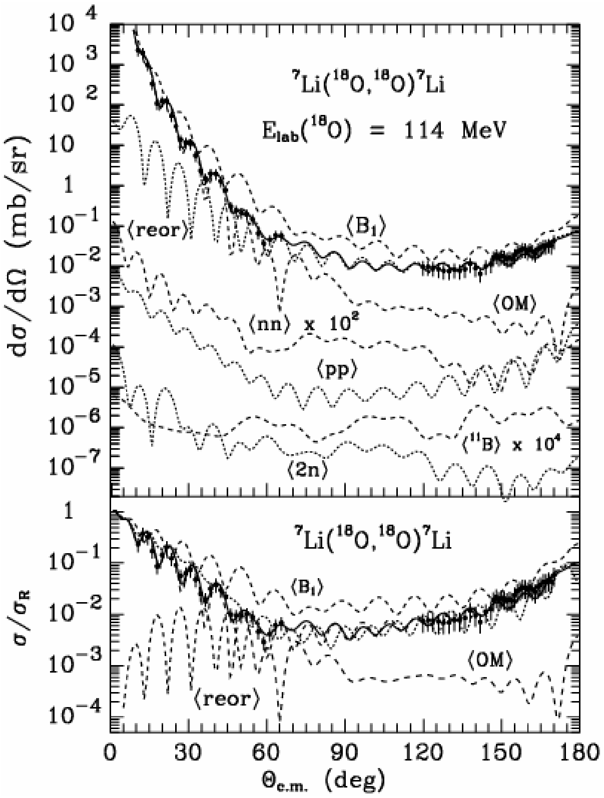

Fig. 4.4.1. The angular distributions of ^{18}O + ^{7}Li elastic scattering at energy E_{LAB}(^{18}O) = 114 MeV. The curves show the OM and CRC angular distributions of the potential scattering (curves <OM>), reorientation of ^{7}Li (curves <reor>) and transfers (other curves). The solid and dashed <B_1> curves represent the coherent sum of these processes, calculated with the potential parameters A and B_1 (see Table 4.4.2), respectively.

The measured angular distributions of the elastic and inelastic scattering of ^{18}O + ^{7}Li are shown in Figs. 4.4.1, 4.4.6, 4.4.7, while the data of the ^{7}Li + ^{16}O elastic scattering are presented in Fig. 4.4.2.

The optical model with potentials of the Woods-Saxon type were used in the OM- and CRC-calculations of the ^{7}Li + ^{18}O and ^{7}Li + ^{16}O data. The angular distribution data of the ^{7}Li+^{16}O elastic and inelastic scattering included in the analysis are shown in Figures 4.4.2, 4.4.3, 4.4.4 and 4.4.5 represent the OM and CRC calculations performed with the conventional potential parameters listed in Table 4.4.1 The sets A_i of these parameters were obtained with both the OM and CRC fitting procedures. The sets B_i were taken from the cited references. For each potential, Tables 4.4.1 and 4.4.2 contain also the numbers from relations between the potential parameters:

$$c_V = \ln C_V = \ln(V \exp(R_V/a_V)), \qquad c_W = \ln C_W = \ln(W_S \exp(R_W/a_W)).$$

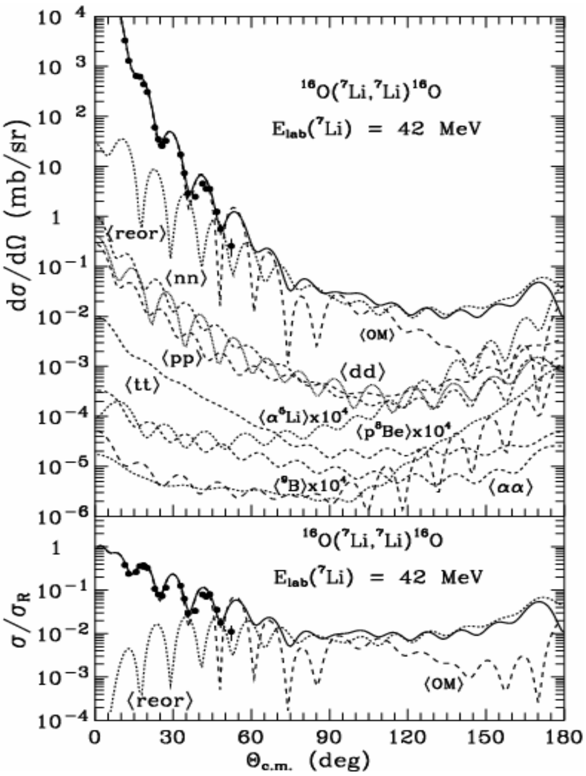

Fig. 4.4.2. Angular distribution of the ^{7}Li + ^{16}O elastic scattering at E_{LAB}(^{7}Li) = 42 MeV. The curves show the OM cross section (curves <M>) and CRC calculations for the reorientation of ^{7}Li (curves <reor>), ^{9}B-cluster transfer (curve <^{9}B>), sequential transfers of neutrons (curve <nn>), protons (curve <pp>), clusters *d*+*d* (curve <dd>), *t*+*t* (curve <tt>), *α*+*α* (curve <*αα*>), *p*+^{8}Be (curve <p^{8}Be>), and *α* + ^{5}Li (curve <*α*^{5}Li>). The solid curves show the coherent sum of all processes.

The solid curves in Figs. 4.4.2, 4.4.3 and 4.4.5 represent a coherent sum of the CRC cross-sections of the potential scattering calculated using the A_i parameters, ^{7}Li reorientation and most important transfers (n+n, p+p and ^{9}B cluster transfers). One can see that the potential scattering dominates at the forward angles (curves <*OM*>) and the ^{7}Li reorientation is most important at the backward angles (curves <*reor*>). Transfers, including the *α*-particle transfers (curves <*αα*>, <*α*^{5}*Li*>), are negligible at all energies (see Fig. 4.4.2). All the data are successfully described using the A_i parameters. Figures 4.4.3 and 4.4.5 show also the CRC-angular distributions calculated with the B_i parameters (curves <B_i >). One can see that the <A_i > and <B_i > curves shown in Figs. 4.4.3, 4.4.4 and 4.4.5 differ significantly at large angles, where the data are absent. The CRC cross sections for the both sets are very close only at the energies of 9 and 34 MeV (for this reason, the corresponding curves are not marked). These similarities can be explained by a dominance the Coulomb scattering at low energy E_{CM} = 6.26 MeV) and by the close values of c_V and c_W (see Table 4.4.1) for the A_i and B_i parameters at 34 MeV.

Table 4.4.1. Parameters of the ^{7}Li + ^{16}O potentials. The A_i parameters are the results of both OM and CRC fits. The B_i parameters are taken from the indicated references.

E_{LAB} (MeV)	E_{CM}. (MeV)	Sets	V (MeV)	r_V (fm)	a_V (fm)	W_S (MeV)	r_W (fm)	a_W (fm)	r_C (fm)	c_V	c_W
9 [133]	6.26	A$_1$	59.0	0.980	0.651	4.5	1.250	0.651	1.25	10.75	10.02
13 [133]	9.04	A$_2$	86.2	0.980	0.673	6.0	1.220	0.673	1.25	10.91	9.83
36(^{16}O) [131]	10.96	A_3	95.6	0.802	0.648	4.5	1.250	0.648	1.25	10.05	10.06
		B_3	10.5	0.848	0.658	3.4	0.848	0.658	0.56	8.06	6.94

		[131]								
20 [130]	13.91	A_4	154.3	0.970	0.690	11.3	1.283	0.690	1.25	11.27	10.67
		B_4[130]	33.1	0.980	0.850	10.3[b]	1.063	0.720	1.42	8.61	7.88
34 [135]	23.17[a]	A_5	181.0	0.860	0.730	15.4	1.300	0.730	1.25	10.42	10.63
		A_{15}	181.0	0.802	1.000	15.4	1.300	1.000	1.25	8.75	8.50
34 [135]	23.65	A_6	180.7	0.802	0.700	15.4	1.206	0.700	1.25	10.28	10.37
		B_6 [135]	240.6	0.676	0.730	16.3	1.182	0.710	0.74	9.59	10.17
36 [132]	25.04	A_7	179.6	0.807	0.700	15.6	1.203	0.700	1.25	10.30	10.37
		B_7 [132]	189.5	0.688	0.743	21.3	1.137	0.821	0.74	9.35	9.20
42	29.22	A_8	175.1	0.802	0.700	16.0	1.200	0.700	1.25	10.24	10.37
50 [134]	34.78	A_9	170.8	0.802	0.700	16.5	1.200	0.700	1.25	10.22	10.38
		B_9 [134]	170.3	0.688	0.777	11.4	1.194	0.951	0.74	9.06	8.00
9, 20, 36		B_{10} [133]	195.0	0.680	0.740	55.0[b]	0.680	0.740	0.68	9.35	8.08

[a] The potential parameters for the 0.478 MeV excited state of ^{7}Li.

[b] The surface imaginary potential.

The optical potential parameters for the ^{18}O + ^{7}Li elastic and inelastic scattering were obtained by fitting the elastic data with the OM and then independently through the CRC-calculations. First, the OM-analysis was carried out and then the parameters obtained were used as starting values for the CRC-calculations. These parameters are given in Table 4.4.2 (set *A*). For comparison, the ^{7}Li + ^{16}O optical-model parameters, derived from the energy dependent analysis of [20] (sets B_1–B_{12}), are given in Table 4.4.2. One can see that the values $\ln(C_V) \approx 10.7$ and $\ln(C_W) \approx 11.3$ are constant for all B_i -parameters, e.g., these parameters are almost energy independent in the given energy range.

Table 4.4.2 Parameters of Woods–Saxon potential for ^{7}Li + ^{18}O scattering.

E_{EX} (MeV)	J^π	E_{CM} (MeV)	Sets	V (MeV)	r_V (fm)	a_V (fm)	W_S (MeV)	r_W (fm)	a_W (fm)	$\ln C_V$	$\ln C_W$
				^{7}Li	+	^{18}O					
0.0		31.92	*A*	174.5	0.806	0.900	13.0	1.470	0.900	9.22	9.97
			B_1	172.9	0.802	0.660	14.9	1.250	0.660	10.66	11.29
				^{7}Li*	+	^{18}O					
0.478	$1/2^-$	31.44	B_2	173.3	0.802	0.660	14.8	1.250	0.660	10.66	11.28
4.652	$7/2^-$	27.29	B_3	176.7	0.804	0.660	14.5	1.250	0.660	10.70	11.26
6.604	$5/2^-$	25.24	B_4	178.3	0.807	0.660	14.2	1.250	0.660	10.73	11.24
7.454	$5/2^-$	24.45	B_5	178.9	0.808	0.660	14.1	1.250	0.660	10.74	11.23
				^{7}Li	+	^{18}O*					
1.982	2^+	29.94	B_6	174.5	0.803	0.660	14.7	1.250	0.660	10.68	11.27
3.555	4^+	28.36	B_7	175.8	0.803	0.660	14.6	1.250	0.660	10.69	11.27
3.634	0^+	28.28	B_8	174.3	0.803	0.660	14.8	1.250	0.660	10.68	11.28
			A_{2n}	77.0	1.050	0.950	29.6	0.878	0.810	9.35	8.30
3.920	2^+	28.00	B_9	176.1	0.804	0.660	14.6	1.250	0.660	10.69	11.27
4.456	1^-	27.46	B_{10}	176.6	0.804	0.660	14.5	1.250	0.660	10.70	11.26
5.098	3^-	26.82	B_{11}	177.1	0.805	0.660	14.5	1.250	0.660	10.71	11.26
5.255	2^+	26.66	B_{12}	177.2	0.805	0.660	14.4	1.250	0.660	10.71	11.25

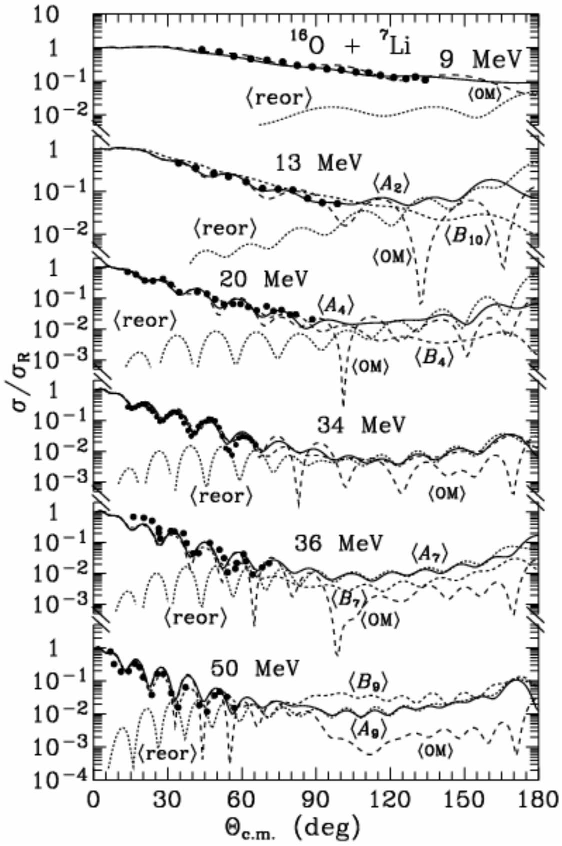

Fig. 4.4.3 Angular distributions of the ^{16}O(^{7}Li,^{7}Li)^{16}O elastic scattering at E_{LAB}(^{7}Li) = 9 and 13 MeV [133], 20 MeV [130], 34 MeV [135], 36 MeV [132], and 50 MeV [134]. The dashed curves show the OM (curves <OM>) and CRC angular distributions for the reorientation of ^{7}Li (curves <reor>) calculated with the A_i parameters (see Table 4.4.1). The $<A_i>$ and $<B_i>$ curves (i = 2, 4, 7, 9) represent the CRC coherent sum of potential scattering and ^{7}Li reorientation for the A_i and B_i parameters, respectively.

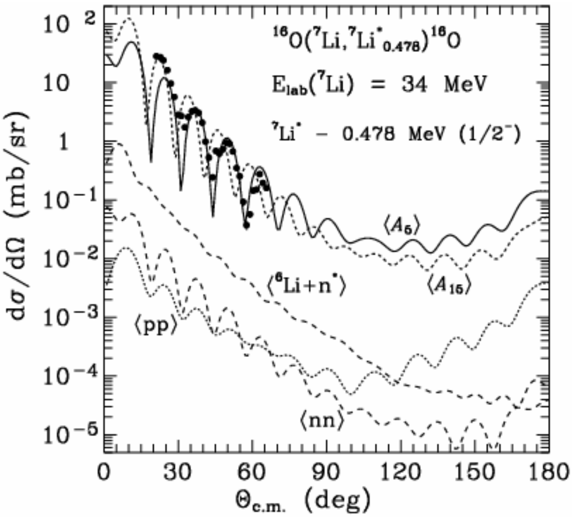

Fig. 4.4.4. Angular distribution of ^{7}Li+^{16}O inelastic scattering for the transition to the 0.478 MeV (1/2^{-}) state of ^{7}Li at E_{LAB}(^{7}Li)= 34 MeV [135]. The curve shows the CRC-calculations for the rotational model with the A_5 and A_{15} (see Tables 4.4.1 and 4.4.2) sets of potential parameters (curves $<A_5>$ and $<A_{15}>$, respectively), for the neutron excitation in the ^{7}Li = ^{6}Li+n system (curve <^{6}Li+n*>) and sequential transitions of neutrons and protons (curves <nn> and <pp>, respectively).

In the coupled-channel analysis of the elastic and inelastic scattering the possible reorientations of ^{7}Li and ^{18}O and the most important transfers were included. The diagrams of the investigated transfers are shown in Figs. 4.4.8 and 4.4.9. The elastic and inelastic transitions are shown in Figs. 4.4.10 and 4.1.40.

In the present calculations the deformation parameters from [136, 13] were used for ^{7}Li δ_2 = 2.0 fm, δ_4 = 1.0 fm. The ^{18}O deformation parameters δ_λ obtained in the present work and those from [137 - 145], are listed in Table 4.4.3.

The cross sections for the excited states of ^{7}Li for ^{7}Li+^{16}O were calculated within the rotational model. The deformation parameters obtained in analysis of the ^{7}Li+^{11}B scattering data [13] were used in the present calculations. The energy-dependent potential parameters estimated from the analysis of the elastic scattering at different energies were also used in the calculations.

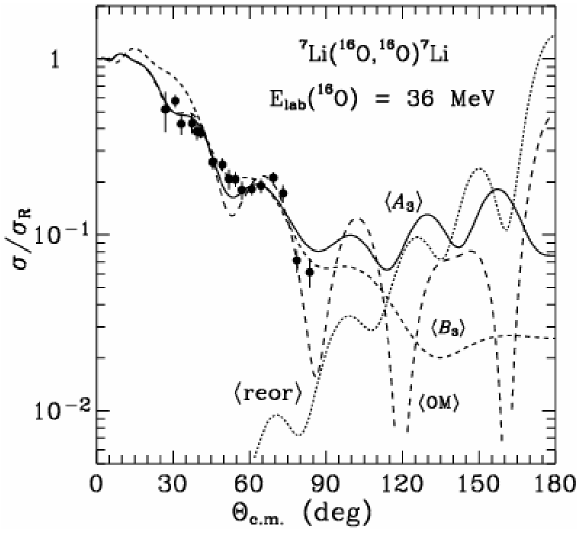

Fig. 4.4.5. Angular distribution of ^{7}Li(^{16}O, ^{16}O)^{7}Li elastic scattering at E_{LAB}(^{16}O) = 36 MeV [135]. The curves are the same as described for Fig. 4.4.3.

Table 4.4.3. Deformation parameters of ^{18}O

E_x (MeV)	J^π	λ	δ_λ	β_λ	Ref.	E_x (MeV)	J^π	λ	δ_λ	β_λ	Ref.
1.982	2^+	2	1.51	0.46	π^+ [137]	4.456	1^-	1	1.00	0.30	This work
			2.43	0.74	π^- [137]	5.098	3^-	3	1.38	0.42	n [138]
			1.07	0.33	n [138]				1.01	0.31	p [138]
			1.18	0.36	p [138]				1.45	0.44	p [39]
			1.04	0.32	p [139]				0.90	0.28	p [140]
			0.98	0.30	p [140]				1.61	0.49	p [141]
			1.07	0.33	p [141]				1.33	0.41	α [142]
			0.99	0.30	α [142]				0.68	0.21	^{18}O [145]
			1.00	0.30	^{18}O [143–145]				1.19	0.36	Average
			1.25	0.38	Average				1.00	0.30	This work
			1.00	0.30	This work	5.255	2^+	2	0.52	0.16	n [138]
3.555	4^+	4	0.92	0.28	p [141]				0.58	0.18	p [141]
			1.00	0.30	This work				0.55	0.17	Average
3.920	2^+	2	0.52	0.16	n [138]				1.00	0.30	This work
			0.43	0.13	p [138]						
			0.81	0.25	p [141]						
			0.62	0.19	α [142]						
			0.60	0.18	Average						
			1.00	0.30	This work						

$\beta_\lambda = \delta_\lambda/R$, $R = 1.25\,A^{1/3} = 3.28$ fm.

At present, there is only one set of the inelastic-scattering data for the system ^{7}Li+^{16}O and it consists of cross sections for the ^{7}Li 0.478 MeV state at at E_{LAB}(^{7}Li) = 34 MeV (E_{CM} = 23.65 MeV) [135]. The angular distribution of this inelastic scattering is shown in Fig. 4.4.4. The curves represent the CRC calculations for the transitions predicted by the rotational model using a ^{7}Li deformation length of δ_2 = 2.0 fm [13] and the potential parameters A_5 (see Tables 4.4.1 and 4.4.2) and A_{15} (curves <A_5> and <A_{15}>, respectively), the single-particle excitation model for neutron excitation in the system ^{7}Li = ^{6}Li+n (curve <$^6Li+n*$>) and sequential transfers of neutrons (curve <*nn*>) and protons (curve <*pp*>). The parameters A_{15} were used in the CRC calculations only for the rotational model. In Fig. 4.4.4 one can see that the rotational transition dominates the cross section. The parameters A_5 describe the data satisfactorily, except for the first oscillation maximum. They differ from the parameters A_6 for the ground state of ^{7}Li because they require larger values for the geometrical parameters r_V , r_W, a_V , and a_W. The parameters A_{15} with $a_V = a_W$ = 1.0 fm describe well the first oscillation, but fail in explaining the others.

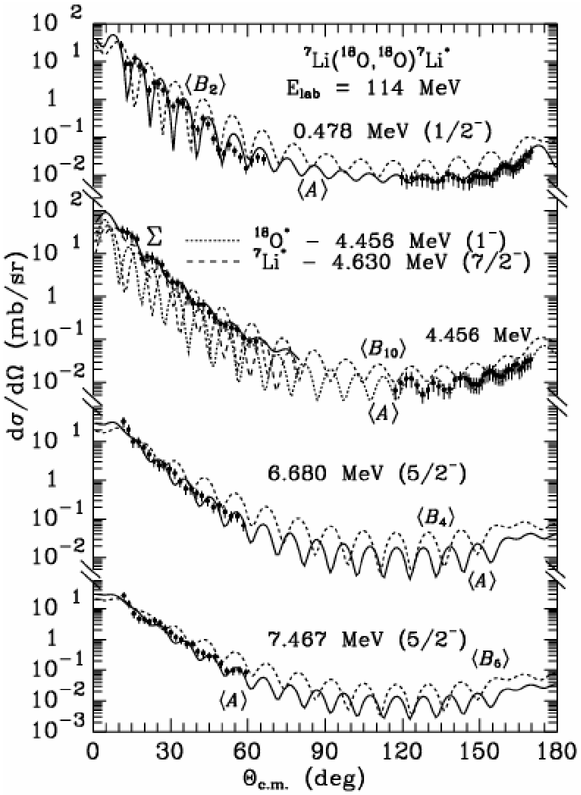

Fig. 4.4.6. The angular distributions of ^{18}O + ^{7}Li inelastic scattering at energy E_{LAB}(^{18}O) = 114 MeV for the transitions to the excited states of ^{7}Li and the 4.456 MeV state of ^{18}O. The curves <*A*> and <B_i > (i = 2, 4, 5, 10) (see Tables 4.4.1 and 4.4.2) show the CRC calculations for collective excitations using *A* and B_i potential parameters, respectively.

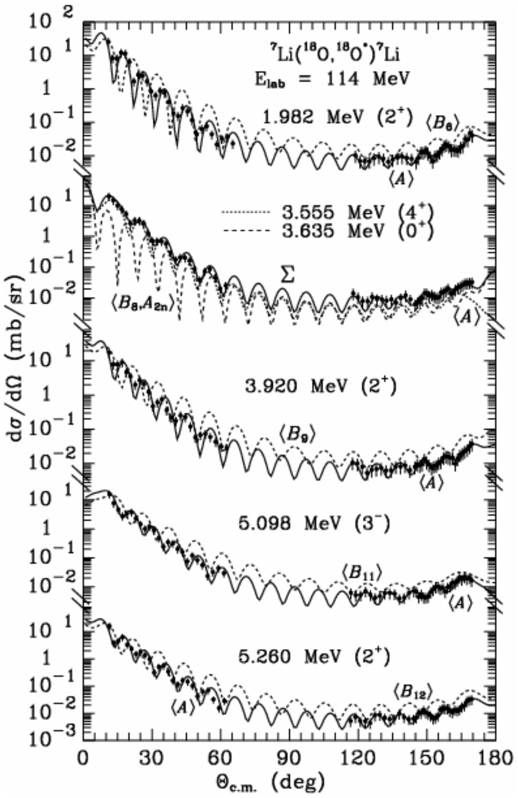

Fig. 4.4.7. The same as in Fig. 4.4.6 but for the excited states of ^{18}O. Curve *Σ* shows the incoherent sum of 3.555-MeV rotational model transition and 3.635-MeV 2n-cluster excitation of ^{18}O (curve <B_8,A_{2n}>), (see Tables 4.4.1 and 4.4.2).

Figure 4.4.6 shows the angular distributions of the ^{18}O + ^{7}Li elastic scattering data and OM and CRC calculations for the potential scattering (curves <OM>), reorientation of ^{7}Li (curves <reor>) and transfers. The solid and <B_1> curves represent the coherent sums of all the processes calculated with the potential parameters *A* and B_1, respectively. One can see that the potential scattering dominates at forward angles. The large-angle scattering is due to the reorientation of the ^{7}Li ground state. Transfer processes contribute weakly to the elastic scattering channel. The parameters B$_1$ (curves <B_1>), obtained from the energy dependence of the potential parameters for the ^{7}Li + ^{16}O elastic scattering [20], fail to describe the ^{18}O + ^{7}Li elastic scattering data. One can see, that the curve <B_1> has the smaller slope than the slope of experimental angular distribution. This curve is located above the experimental data for large angles. A good description of the data was achieved with the fitted parameters A, for which $\ln(C_V) \approx 9.2$ and $\ln(C_W) \approx 10.0$. These potential parameters are smaller than those for B_1 (see Table 4.4.2). The fitted A and predicted B_1 potentials differ mainly in the geometry parameters. While for the set A the values are $r_W = 1.47$ fm and $a_V = a_W = 0.9$ fm the corresponding values for the set B_1 are $r_W = 1.25$ fm and $a_V = a_W = 0.66$ fm. It was found that the slope of the calculated angular distribution mainly depends on the imaginary part of the ^{18}O + ^{7}Li potential. This is presented by the dotted curve in Fig. 4.4.1 (lower panel). This dotted curve represents the result of the calculation with the ^{18}O + ^{7}Li potential. It consists of the real part of the potential B_1 and of the imaginary part of the potential A.

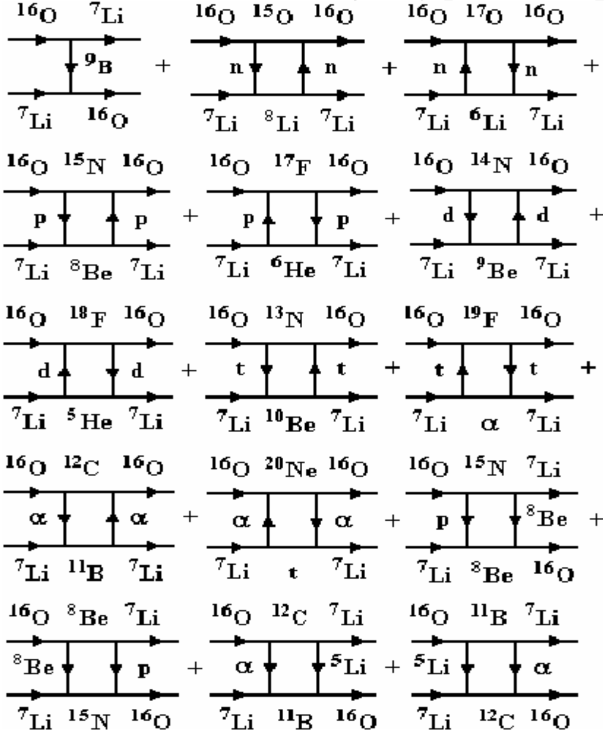

Fig. 4.4.9. Diagrams of one- and two-step transfers contributing to the ^{7}Li + ^{16}O elastic-scattering calculations.

The measured and calculated angular distributions of the ^{18}O + ^{7}Li inelastic scattering are shown in Figs. 4.4.6 and 4.4.7, which show the cross-sections for the excited states in ^{7}Li and ^{18}O. The solid <A> and dashed <B_1> curves represent the CRC-calculations within the rotational and vibrational models with the parameters A and B_1, respectively. One can see that the parameters B_1 fail to describe the data. A good description of the data was achieved using the potential parameters A and the deformation parameters δ_λ for ^{7}Li from [146, 147] and δ_λ for ^{18}O, which are listed in Table 4.4.1 with the notation of “This work”. In this table, we give also the δ_λ values taken from other works which were obtained from different analyses of the inelastic-scattering data of $\pi^{\pm}$-mesons, nucleons, α-particles and ^{18}O ions. One can see that in many cases the δ_λ values for ^{18}O obtained in the present work, are close to the average values taken from other work, with the exception of the transitions to the 3.92 MeV and 5.255 MeV states of ^{18}O.

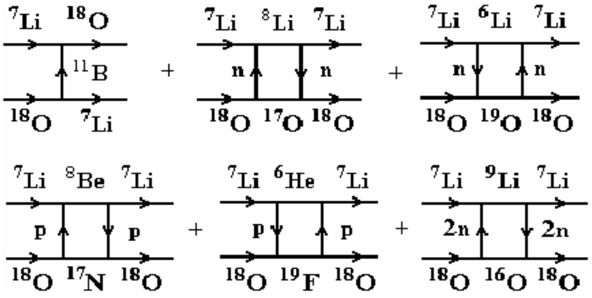

Fig. 4.4.8. Diagrams of one- and two-step transfers contributing to the ^{18}O + ^{7}Li elastic-scattering calculations.

The 3.555 MeV (4^+) and 3.635 MeV (0^+) states of ^{18}O were not resolved in the present experiment. The angular distribution for the sum of the transitions to these states is shown in Fig. 4.4.7. In this figure, the dotted curve <A> represents the rotational transition $0^+ \rightarrow 4^+$ to the 3.555 MeV (4^+) state of ^{18}O. The transition $0^+ \rightarrow 0^+$ to the 3.635 MeV (0^+) state of ^{18}O was assumed to be the 2n-cluster excitation in the system ^{18}O = ^{16}O + 2n. In the CRC-calculations for these transitions, the potentials B_8 and A_{2n} were used for ^{7}Li + ^{16}O and ^{7}Li + 2n interactions, respectively. The potential A_{2n} of the ^{7}Li + 2n interaction was assumed to be close to that of the ^{7}Li + d interaction [148]. In Figure 4.4.7, the curve $<B_8,A_{2n}>$ represent the CRC-calculation for the particle-excitation transition $0^+ \rightarrow 0^+$ to the 3.635 MeV (0^+) state of ^{18}O. The incoherent sum of both the transitions (solid curve Σ) describes the data satisfactorily.

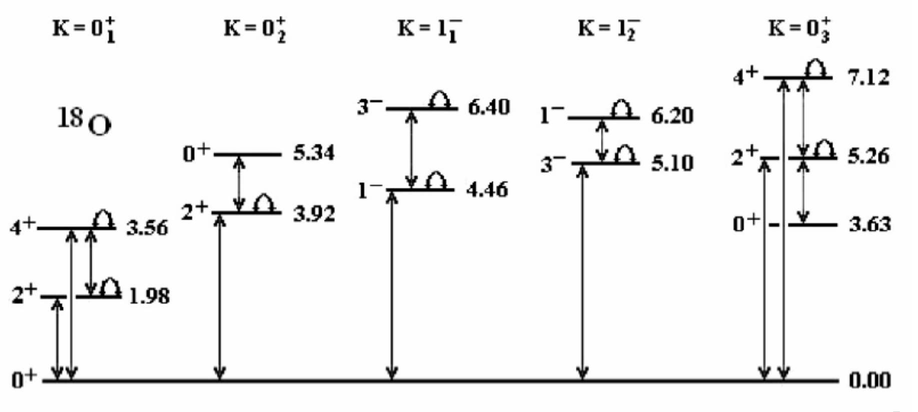

Fig. 4.4.10 Coupling schemes for the transitions to the excited states of ^{7}Li and ^{18}O. Coupling schemes for the transitions to the excited states of ^{7}Li are shown in Fig. 4.1.40.

The optical potential parameters, obtained from the ^{7}Li + ^{16}O experimental data analysis are shown in Fig. 4.4.11 as the full circles (see Table 4.4.1). The lines represent approximations of energy dependences of potential parameters. A similar energy dependences for the ^{7}Li + ^{11}B and ^{7}Li + ^{14}N potentials are also shown for comparison in Fig.4.4.11. Noticeable differences in the depths of the imaginary parts of these potentials are visible. This fact can be explained by differences of the inelastic cross sections for these pairs of nuclei.

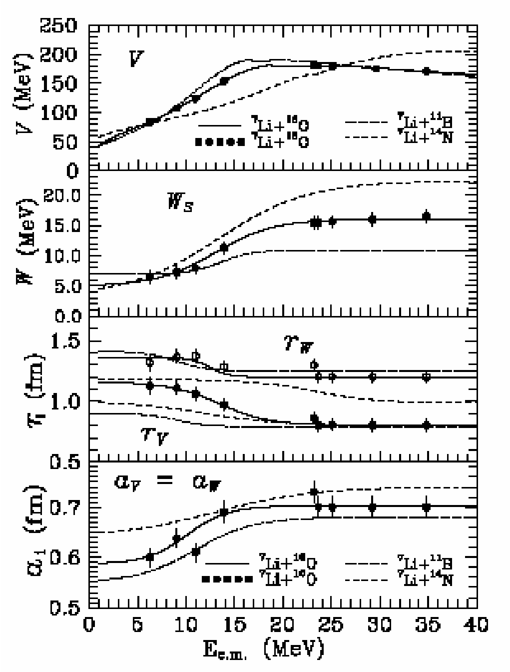

Fig. 4.4.11. Energy dependence of OM parameters for the ^{7}Li + ^{16}O scattering versus the same for the scattering of ^{7}Li + ^{11}B [13] and ^{7}Li + ^{14}N [7].

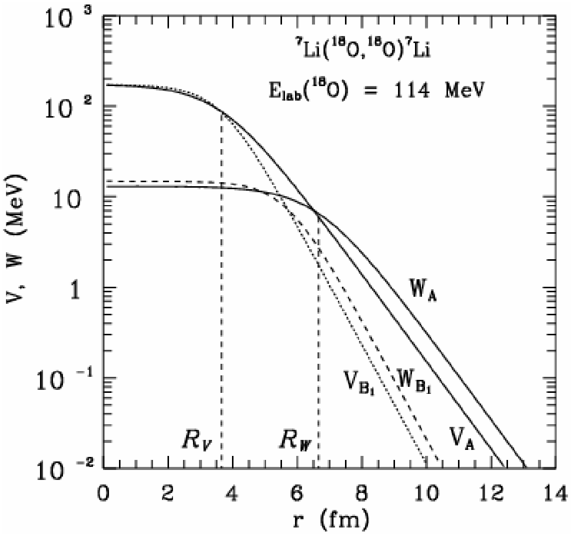

Fig. 4.4.12. Real V(r) and imaginary W(r) potentials of the ^{18}O + ^{7}Li elastic scattering for the parameters A (curves V_A and W_A) and B_1 (curves V_{B1} and W_{B1})

As it was already mentioned, for the investigation of isotopic differences of the nuclei interaction potentials, measurements of the elastic and inelastic scattering cross sections of the ^{18}O + ^{7}Li nuclei were done. There was no such experimental data in the literature before.

The ^{18}O + ^{7}Li potential parameters, obtained from the analysis of the ^{18}O + ^{7}Li scattering data for E_{CM} = 31.92 MeV are shown in Table 4.4.4. The ^{7}Li + ^{16}O potential parameters, calculated from their energy dependence at the same energy, are also presented in Table 4.4.4. The CRC cross sections calculated using the ^{7}Li + ^{16}O potential parameters for the ^{18}O + ^{7}Li scattering are shown in Fig. 4.4.1 as the <B$_1$>. One can see that the ^{18}O + ^{7}Li potential with the ^{7}Li + ^{16}O potential parameters cannot describe well the experimental data. It is visible from Table 4.4.4 that the ^{7}Li + ^{16}O and ^{18}O + ^{7}Li potentials differ in the parameters a_V, a_W and r_W. The real and imaginary parts of the ^{18}O + ^{7}Li potential with these two parameter sets are shown in Fig. 4.4.12. One can see that this potentials with the its "own" parameters have longer tails (V_A, W_A lines) than the potentials with the ^{7}Li + ^{16}O parameters (V_B, W_B lines). It can be concluded that the tail of the ^{18}O + ^{7}Li potential show the halo structure of the ^{18}O nucleus as in the case of ^{18}O = ^{16}O + 2n system (two neutrons and closed 1p-shell).

Table 4.4.4. The nucleus-nucleus Saxon-Woods potential parameters.

Interacting nuclei	E_{CM} (MeV)	V_0 (MeV)	r_V (fm)	a_V (fm)	W_S (MeV)	r_W (fm)	a_W (fm)
^{7}Li + ^{16}O	31.92	172.9	0.802	0.660	14.9	1.250	0.660
^{18}O + ^{7}Li	31.92	174.5	0.806	0.900	13.0	1.470	0.900

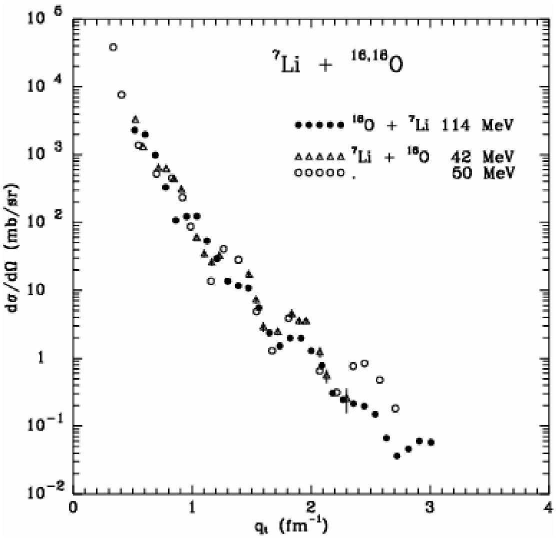

Fig. 4.4.13. ^{7}Li + ^{16,18}O data plotted as a function of momentum transfer. The data show that the elastic scattering from ^{18}O is more strongly absorbed than that for ^{16}O.

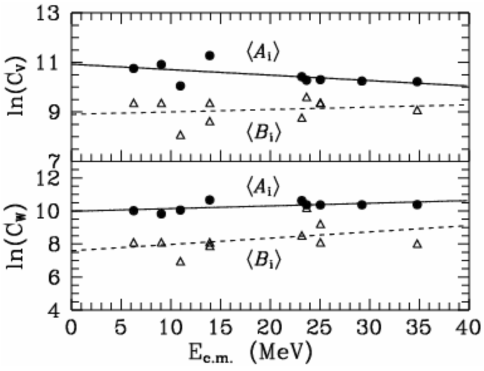

Fig. 4.4.14 Energy dependence of the c_V and c_W relations for the A_i and B_i parameters of the ^{7}Li + ^{16}O scattering potential.

Further evidence which shows that the ^{7}Li + ^{16}O scattering requires a different potential from that for the scattering by ^{18}O can be seen from Fig. 4.4.13, where the data for the two systems are plotted as a function of the momentum transfer [221]. This figure shows that the ^{16}O data does not decrease as rapidly at larger momentum transfer as does the ^{18}O data, which means that the imaginary potential for ^{16}O is weaker then that for ^{18}O. Figure 4.4.12 shows the actual potentials. As it has been anticipated, the ^{18}O potentials are stronger at large distances, where the more favorable Q-values for the transfer reactions decrease the chance for elastic scattering. Since the breakup threshold for both the ^{16}O and ^{18}O is almost the same and large (~ 6 MeV), it would not play a major role in the elastic scattering.

The energy dependence of the conventional-potential parameters of the ^{7}Li+^{16}O interaction, reported in Table 4.4.1 was fitted with the parameters $X_i\,(E) = X_{\rm i}^{\rm max}$, $X_{\rm i}^{\rm min}$, E_{Xi}, ΔE_{Xi}. These parameter sets are shown in Table 4.4.5 and the resulting fits are shown in Fig. 4.4.11. The relations

$C_V = V \exp(R_V/a_V)$, $\quad C_W = W \exp(R_W/a_W)$

have been found to be useful for representing the energy dependence of the scattering potential parameters. Figure 4.4.14 shows the energy dependence of the $c_V = \ln C_V$ and $c_W = \ln C_W$ values for both A_i and B_i parameters which are fitted to the lines:

$c_V\,(E) = -0.022E + 10.92$ for A_i sets,
$0.010E + 8.90$ for B_i sets,
$c_W(E) = 0.016E + 9.98$ for A_i sets,
$0.038E + 7.59$ for B_i sets,

where $E = E_{CM}$. The values of c_V and c_W are shown in Tables 4.4.1 and 4.4.2 and they were used to compare the parameter sets. The solid curves in Fig. 4.11.4 show the energy dependence fits of the ^{7}Li+^{16}O potential parameters.

Table 4.4.5. Energy dependence of the ^{7}Li + ^{16}O potential parameters.

X_i	V_0 (MeV)	W_S (MeV)	r_V (fm)	r_W (fm)	a_V (fm)	a_W (fm)
$X_{\min}$	92.6	5.0	0.802	1.200	0.587	0.587
$X^{i}_{\max}$	262.7	16.0	1.160	1.360	0.703	0.703
E_{Xi}(MeV)	13.0	13.0	13.400	12.400	10.100	10.100
ΔE_{Xi}(MeV)	3.9	3.0	2.600	0.958	2.100	2.100

A remarkable difference exists between the parameters of these interactions, especially for the values of W_S. The origin of this difference is still unknown. However, it can be an evidence of the dependence of the nuclear interaction on either the nuclear structure of the target or a discrete ambiguity of W_S, because

$c_W(^{11}\mathrm{B}) \approx 7.6$, $c_W(^{14}\mathrm{N}) \approx 8.8$,
$c_W(^{16}\mathrm{O}) \approx 10.3$, and $c_V\,(^{11}\mathrm{B}) \approx c_V\,(^{14}\mathrm{N}) \approx c_V\,(^{16}\mathrm{O}) \approx 10.4$.

The difference could be resolved when more scattering data were available for CRC analysis.

The following conclusions for this sub-Section can be done. The optical-model analysis showed that the scattering of ^{7}Li by ^{18}O produces the potential very different from that for the scattering by ^{16}O. The fact that the ^{7}Li + ^{18}O scattering system is more absorbing than the ^{7}Li + ^{16}O system can be seen when comparing the elastic data for ^{18}O scattering with that for ^{16}O. The radial difference in the optical-model potentials indicates that reactions that take place at larger distances produce the observed scattering difference. The fact that the breakup threshold is similar for the two target nuclei suggests that breakup of the target does not play a significant role in the difference in the observed scattering of the two system.

The coupled-reaction-channel analysis showed that the greater than expected large-angle elastic cross section arises from the ground state reorientation of ^{7}Li. Now, this effect has been observed for the targets of A = 7 to A = 18.

The existing ^{7}Li + ^{16}O scattering data at the energies of E_{CM} = 6.26 – 34.78 MeV were then analyzed to extract the energy-dependence parameters. The obtained energy-dependent potentials differ noticeably from those previously found for the systems ^{7}Li + ^{11}B and ^{7}Li + ^{14}N. This shows that the microscopic target structure influences the scattering. The unexpected result of the analysis is that the potential parameters are relatively energy independent between 20 and 50 MeV (CM).

CHAPTER 5.

Nuclear reactions with light exotic nuclei in the exit channel

5.1. The ^{9}Be(^{11}B, ^{10,12}B), ^{9}Be(^{11}B, ^{12}C) and ^{12}C(^{11}B, ^{15}N) reactions.

5.1.1. The ^{9}Be(^{11}B, ^{10}B)^{10}Be reaction, ALAS and isotopic effects. The ^{10}B + ^{10}Be optical potential.

The simple transfer reactions can be used as an alternative method to obtain the optical potential parameters when the direct nucleus–nucleus scattering is impossible for some reason (e.g., for unstable, short-living and non-existing in nature nuclei, or for other reasons). This approach is described in this sub-Section for the ^{10}B + ^{10}Be interaction using the one-nucleon transfer reaction ^{9}Be(^{11}B, ^{10}B)^{10}Be [10].

The ^{11}B + ^{9}Be elastic and inelastic scattering data at E_{LAB}(^{11}B) = 45 MeV (E_{CM} = 20.25 MeV) [8] and the data known from the literature at E_{CM} = 8.8 – 20.35 MeV [223] and 22.0 MeV [224] were already presented in sub-Section 4.1.4. The energy-dependent optical potential parameters were deduced for the ^{11}B + ^{9}Be scattering in sub-Section 4.1.4.

The study of isotopic effects in the ^{10}B + ^{9}Be, ^{11}B + ^{9}Be and ^{10}B +^{10}Be interactions using the ^{10}B + ^{9}Be scattering data at E_{CM} = 8.42 - 19.47 MeV [223], 21.05 MeV [224], 47.37 MeV [225] and the data for the ^{9}Be(^{11}B, ^{10}B)^{10}Be reaction at E_{LAB}(^{11}B) = 45 MeV for the transitions to the ground and excited states of ^{10}B and ^{10}Be (E_{CM} = 12.02 - 15.61 MeV for the ^{10}B + ^{10}Be channel) are also described.

The ^{9}Be(^{11}B, ^{10}B)^{10}Be reaction is also interesting due to its specific mechanism. The contributions to cross sections of the neutron (forward angles) and proton (backward angles) transfers are expected to be similar. Then, the angular distribution of this reaction will be quasi symmetric around θ_{CM} = 90^{o} and large interference phenomena at θ_{CM} ~ 90^{o} can be expected. There is also interest in the relative role of one-step and two-step processes in this reaction.

The angular distributions of the ^{9}Be(^{11}B, ^{10}B)^{10}Be reaction at E_{LAB}(^{11}B) = 45 MeV for the transitions to the ground and to the 0.718 MeV (1^{+}), 1.740 MeV (0^{+}), 2.154 MeV (1^{+}), 3.587 MeV (2^{+}) excited states of ^{10}B and to the 3.368 MeV (2^{+}) excited state of ^{10}Be were obtained from the analysis of the energy spectra of ^{10}B and ^{10}Be. These distributions are shown in Figs. 5.1.1 - 5.1.3. As it can be seen from the figures, all the distributions are quasi-symmetric around θ_{CM} = 90^{o}, which is due to similarity of the ^{9}Be(^{11}B, ^{10}B)^{10}Be and ^{9}Be(^{11}B, ^{10}Be)^{10}B reaction mechanisms.

The data for the ^{9}Be(^{11}B, ^{10}B)^{10}Be reaction at E_{LAB}(^{11}B) = 45 MeV were analyzed within the OM and the CRC method. For the entrance reaction channel (^{9}Be + ^{11}B) we used a set of the OM parameters $\{X_i\} = \{V, r_V, a_V, W_S, r_W, a_W\}$ obtained from our previous analysis of the ^{11}B + ^{9}Be elastic scattering at E_{CM} = 8.8 – 22.0 MeV [8]. The set of parameters $\{X_i\}$ at E_{CM} = 20.25 MeV (E_{LAB}(^{11}B) = 45 MeV) is listed in Table 5.1.1.

There are no data in the literature for the ^{10}B + ^{10}Be elastic scattering which can be used to obtain the OM potential for the exit channel of the ^{9}Be(^{11}B, ^{10}B)^{10}Be reaction. Therefore, the OM parameters for this channel were obtained from the energy-dependent OM parameters of the ^{11}B + ^{9}Be and ^{10}B + ^{9}Be elastic scattering. For this purpose, the study of energy dependence of the ^{10}B + ^{9}Be OM parameters using the data of [223, 224] are included. The energy dependence of the $^{11}B + ^{9}Be$ OM parameters was obtained in [8] (see Fig. 5.1.7).

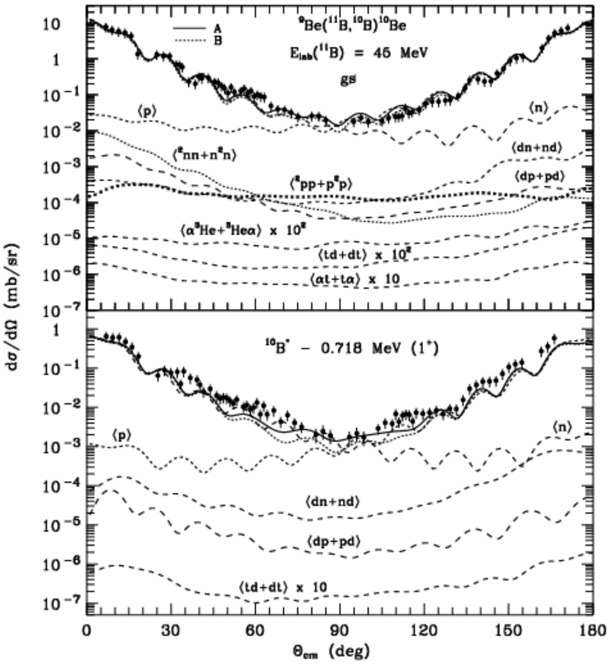

Fig. 5.1.1. Angular distribution of the $^{9}Be(^{11}B, ^{10}B)^{10}Be$ reaction at the energy $E_{LAB}(^{11}B)$ = 45 MeV for the transitions to ground states of ^{10}B and ^{10}Be (upper panel) and to the 0.718 MeV (1^{+}) excited state of ^{10}B (lower panel). The dashed curves represent the CRC angular distributions of individual processes corresponding to diagrams of Fig. 5.1.4. The solid and dotted curves show the coherent sums of the CRC angular distributions of the neutron and proton transfers for the sets A and B of the $^{10}B + ^{10}Be$ OM parameters, respectively.

In the OM and CRC calculations the $^{10}B + ^{9}Be$ the elastic and inelastic scattering as well as the reorientations of ^{9}Be and ^{10}B, and the proton transfer reaction $^{10}B(^{9}Be, ^{10}B)^{9}Be$ were included in the coupling scheme. The sets $\{X_i\}$ of the $^{10}B + ^{9}Be$ OM parameters obtained in the fitting procedure within the OM and CRC methods are listed in Table 5.1.1. The CRC-calculations for the $^{9}Be(^{11}B, ^{10}B)^{10}Be$ were also performed. One-step and two-step processes corresponding to the diagrams of Fig. 5.1.4 were calculated for this reaction.

Table 5.1.1 Parameters of the Woods–Saxon potentials for a $T + P$ scattering.

$T + P$	Ecm (MeV)		V (MeV)	r_V (fm)	a_V (fm)	W_S (MeV)	r_W (fm)	a_W (fm)	Ref.
$^{11}B + ^{9}Be$	20.25		187.3	0.788	0.730	10.4	1.236	0.730	[8]
$^{11}B + ^{9}Be$	8.80		81.0	1.150	0.690	7.0	1.350	0.690	[223]
	14.85		153.8	0.860	0.716	9.2	1.250	0.716	[223]
	20.35		180.0	0.788	0.750	11.4	1.236	0.750	[223]
	22.00		202.0	0.788	0.760	12.7	1.236	0.760	[224]
$^{10}B + ^{9}Be$	8.42		87.0	0.950	0.710	7.6	1.350	0.710	[223]
	14.21		140.0	0.790	0.710	12.0	1.260	0.710	[223]
	19.47		180.2	0.790	0.690	14.3	1.251	0.690	[223]
	21.05		185.1	0.788	0.690	14.8	1.250	0.690	[224]
	47.37		197.2	0.788	0.690	16.0	1.250	0.690	[225]
$^{10}B + ^{10}Be$	15.61	A	154.7	0.823	0.721	10.0	1.248	0.721	
		B	154.0	0.800	0.696	12.0	1.259	0.696	
$^{10}Be + ^{10}B_{0.71}$	14.89	A	147.6	0.850	0.716	9.7	1.254	0.716	
		B	147.8	0.805	0.696	11.5	1.262	0.696	
$^{10}Be + ^{10}B_{1.74}$	13.87	A	137.0	0.912	0.709	9.2	1.266	0.709	
		B	138.4	0.815	0.696	10.8	1.269	0.696	
$^{10}Be + ^{10}B_{2.15}$	13.45	A	132.6	0.944	0.707	9.0	1.272	0.707	
		B	134.4	0.820	0.696	10.5	1.273	0.696	
$^{10}Be_{3.36} + ^{10}B$	12.24	A	119.4	1.039	0.700	8.4	1.293	0.700	
		B	122.5	0.840	0.696	9.7	1.287	0.696	
$^{10}Be + ^{10}B_{3.59}$	12.02	A	117.0	1.053	0.699	8.3	1.298	0.699	
		B	120.3	0.845	0.696	9.5	1.290	0.696	

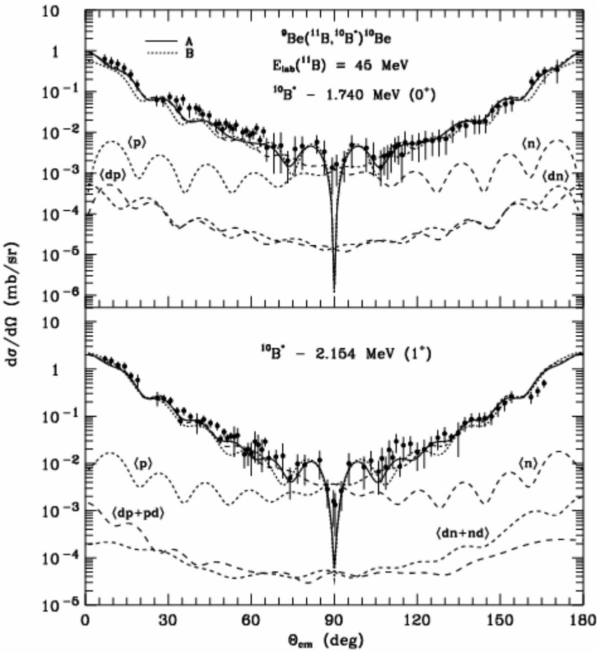

Fig. 5.1.2. The same as in Fig. 5.1.1 but for the transitions to the 1.74 MeV (0^+) (upper panel) and 2.154 MeV (1^+) (lower panel) excited states of ^{10}B.

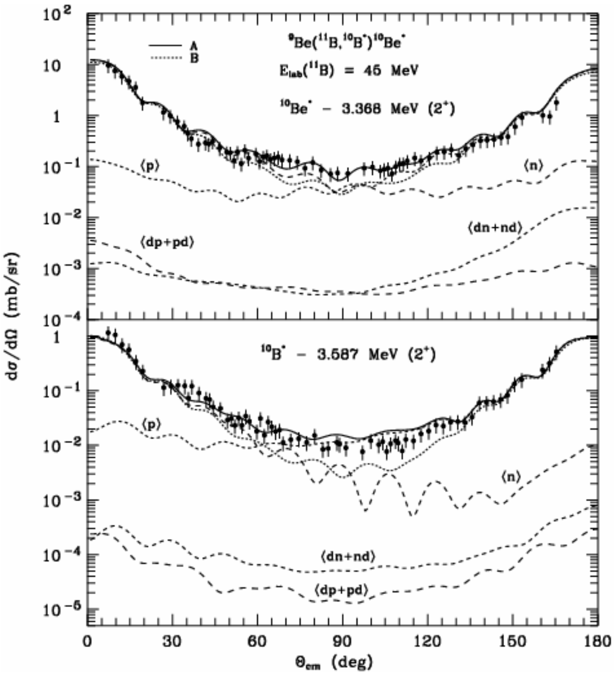

Fig. 5.1.3. The same as in Fig. 5.1.1 but for the transitions to the 3.368 MeV (2^+) excited state of ^{10}Be (upper panel) and 3.587 MeV (2^+) excited state of ^{10}B (lower panel).

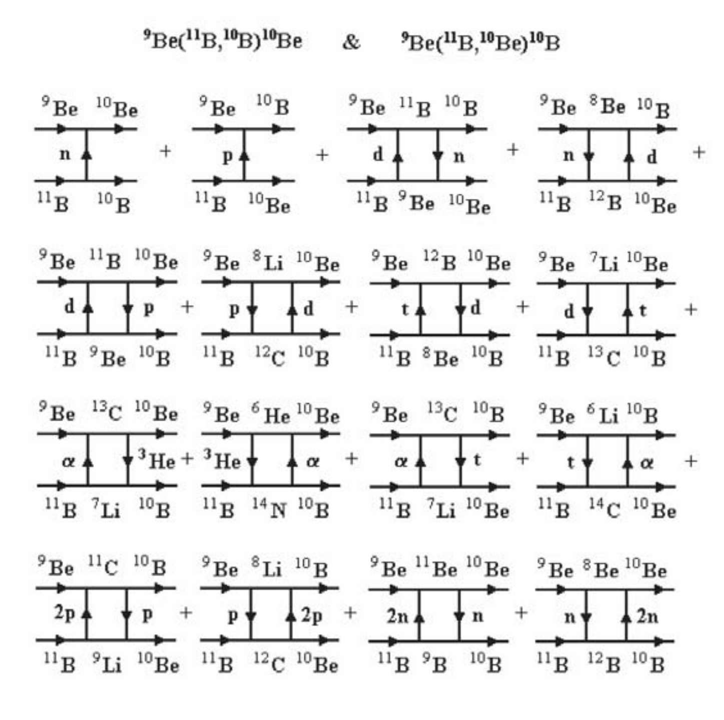

Fig. 5.1.4. Diagrams of the one- and two-step processes for the ^{9}Be(^{11}B,^{10}B)^{10}Be and ^{9}Be(^{11}B,^{10}Be)^{10}B reactions.

The angular distributions of the ^{9}Be + ^{10}B and of the ^{9}Be + ^{11}B elastic scattering for different energies are shown in Fig. 5.1.5. In both cases the optical model describes the angular distributions well only at forward angles (see dashed curves <OM> in Fig. 5.1.5). In both cases one can observe the effect of anomalously large angle scattering (ALAS).

In the CRC analysis of the ^{11}B + ^{9}Be elastic scattering data, it was found [8] that ALAS effect is mainly caused by the reorientations of ^{9}Be and ^{11}B (see dashed curves <reor> in the right panel of Fig. 5.1.5). Contributions to the cross-sections of the deuteron transfer and two-step processes were found to be small (see dashed curves <d>). In order to explain ALAS effect in the scattering of the ^{10}B + ^{9}Be the elastic scattering data were analyzed using the CRC method. The elastic and inelastic scattering, excitation of ^{9}Be (up to the level of 7.94 MeV), the reorientations of ^{9}Be and ^{10}B as well as the proton transfer were included into the coupling scheme. The deformation parameters of ^{9}Be were taken from [8]. Contributions of the two-step transfers to the $^{10}B + {}^{9}Be$ elastic scattering were also analyzed. They were found to be small.

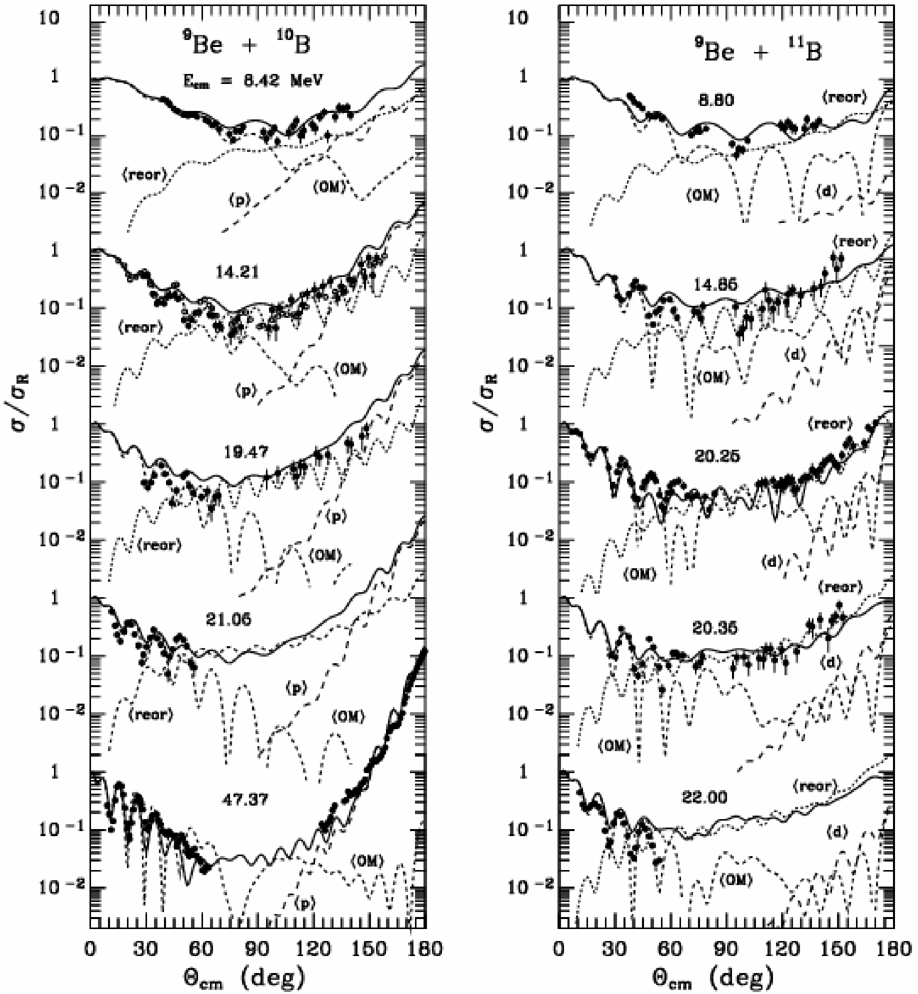

Fig. 5.1.5. Angular distributions of the $^{9}Be + {}^{11}B$ elastic scattering at the energies E_{CM} = 8.42, 14.21, 19.47 MeV [223], 21.05 MeV [224], 47.37 MeV [225] (left panel) and the $^{11}B + {}^{9}Be$ elastic scattering at the energies E_{CM} = 8.8, 14.85, 20.35 MeV [223], 20.25 MeV [8] and 22.0 MeV (right panel). The dashed curves <OM>, <d>, <p> and <reor> represent OM cross section, angular distributions for the deuteron, proton transfers and reorientation of ^{9}Be, respectively. The solid curves show the coherent sum of the cross sections of the individual processes.

In Figure 5.1.5 (left panel) one can see that the proton transfer (dashed curves <p>) dominates at large angles. At middle angles, the ^{9}Be reorientation is the dominant process. The $^{10}B + {}^{9}Be$ scattering at forward angles is of the potential type. The coherent sums (solid curves) of the individual processes satisfactorily describe the angular distributions in the full angular range.

As it was mentioned above, no data for the $^{10}B + {}^{10}Be$ elastic scattering was found in the literature. Therefore, in the analysis of the $^{9}Be(^{11}B, {}^{10}B)^{10}Be$ reaction, the OM parameters obtained in the analysis of the $^{11}B + {}^{9}Be$ and $^{10}B + {}^{9}Be$ elastic scattering data for the exit channel were used. These sets of the OM parameters are listed in Table 5.1.1 as the sets A and B, respectively.

The one-step or two-step transfers corresponding to the diagrams shown in Fig. 5.1.4 were included in the channel coupling scheme, together with the elastic and inelastic channels. The CRC-calculations for the one-step transfers were performed using the sets A and B of the OM parameters. In Figures 5.1.1 – 5.1.3, the curves show the CRC cross sections for the individual transfers or for their coherent sums.

The dashed curves <n> and <p> represent the angular distributions of the one-step neutron and proton transfers in the ^{9}Be(^{11}B, ^{10}B)^{10}Be and ^{9}Be(^{11}B, ^{10}Be)^{10}B reactions, respectively. One can see that the neutron transfers dominate at forward angles and the proton transfers dominate at backward angles. Both the experimental and theoretical angular distributions are quasi-symmetric around $\theta_{CM} = 90^{o}$. The solid and dotted curves in Figs. 5.1.1 – 5.1.3 represent the coherent sums of the neutron and proton transfers for the sets A and B of the OM parameters, respectively. One can see that only for the transitions to the 3.368 MeV (2^{+}) excited state of ^{10}Be or to 3.587 MeV (2^{+}) excited state of ^{10}B these sets give significantly different angular distributions around 90^{o}. The set A of the OM parameters for the exit channel of the reaction ^{9}Be(^{11}B, ^{10}B)^{10}Be provides satisfactory description of the data for all transitions in the whole angular range. The energy dependences of the ^{10}B + ^{10}Be OM parameters of the set A are shown in Fig. 5.1.7 using the solid circles. They are similar to the ones obtained for the ^{11}B + ^{9}Be elastic scattering in [8]. The optical potential parameters for the interactions of ^{10}B + ^{10}B (open squares) and ^{10}B + ^{11}B (solid squares) at $E_{CM} \approx 4$ - 19 MeV [5] are also placed for comparison in Figure 5.1.7. One can see that the energy dependence of the ^{10}B + ^{10,11}B OM parameters differ somewhat from the energy dependence of the+ ^{10,11}B + ^{9,10}Be OM parameters, especially at low energies. This difference can be caused probably by a different Coulomb interaction in the ^{10}B + ^{10,11}B and ^{10,11}B + ^{9,10}Be systems. The different Coulomb interaction at close inter-nuclear distances can be responsible for different "formation" of the effective nucleus– nucleus OM potential at low energies.

The contributions of the individual two-step processes (see diagrams in Fig. 5.1.5) to the ^{9}Be(^{11}B, ^{10}B)^{10}Be reaction are displayed in Figs. 5.1.1 – 5.1.3. The angular distributions of this reaction for the transition to the ground states of ^{10}B and ^{10}Be are shown in the upper panel of Fig. 5.1.1. The dashed curves <^{2}pp+p^{2}p>, <^{2}nn+n^{2}n>, <dn+nd>, <dp+pd>, <α^{3}He+^{3}Heα> and <αt+tα> present the coherent sums of the sequential transfers of 2p + p and p + 2p, 2n+n and n +2n, d +n and n+ d, d +p and p+ d, α + ^{3}He and ^{3}He + α, t+d and d+ t, α + t and t + α, respectively. One can see that for the transition to the ground states of ^{10}B and ^{10}Be all these two-step transfers give only small contributions. The sequential transfers with the t-, ^{3}He- and α-cluster exchanges are less important than those with the nucleon and d-cluster exchanges.

The two-step processes of the type specified above are also negligible for the transitions to the excited states of ^{10}B or ^{10}Be in the ^{9}Be(^{11}B, ^{10}B)^{10}Be reaction. This is demonstrated in Fig. 5.1.1 (lower panel) and Figs. 5.1.2, 5.1.3, where the angular distributions for the most important two-step transfers such as the deuteron + nucleon and nucleon + deuteron (curves <dn + nd> and <dp + pd>) are shown. The coherent sum of the p- and n-transfers (solid curves) at $\theta_{CM} = 90^{o}$ have deep minima (due to interference of the p- and n-transfers) for the transitions to the 1.74 MeV (0^{+}) and 2.154 MeV (1^{+}) excited states of ^{10}B (see Fig. 5.1.3). The coherent sum of two-step processes are represented by the dashed curves. These minima are substantially reduced when the one-step and two-step processes are added together. If the experimental angular resolution were ideal, then the degree of reduction of the minima could be used to estimate the contribution of the two-step processes.

To analyze in detail the difference (isotopic effect) between the angular distributions of the ^{10}B + ^{9}Be and ^{11}B + ^{9}Be elastic scattering, an auxiliary quantity $D(\theta)$ is shown in Fig. 5.1.6

$$D(\theta) = \frac{\sigma_{10B}(\theta) - \sigma_{11B}(\theta)}{\sigma_{10B}(\theta) + \sigma_{11B}(\theta)},$$

where $\sigma_{10\mathrm{B}}(\theta)$ and $\sigma_{11\mathrm{B}}(\theta)$ are the cross sections $\sigma(\theta)/\sigma_R(\theta)$ ($\sigma_R(\theta)$ is the Rutherford cross-sections) for the ^{10}B + ^{9}Be and ^{11}B + ^{9}Be elastic scattering, respectively. The data at the same laboratory energies for both reactions are taken. One can see that the $D(\theta)$ function has regular oscillations with the amplitude of about 50%. Such an oscillatory structure can be caused by a small difference between the potential radii $R_{9\mathrm{Be}+10\mathrm{B}}$ and $R_{9\mathrm{Be}+11\mathrm{B}}$. This difference of radii is correctly accounted for in the CRC calculations. As the result, $D(\theta)$ calculated using CRC (solid curves) satisfactorily describes the observed structure of oscillations in the experimental $D(\theta)$. The value of $D(\theta)$, calculated using CRC for the ^{10}B + ^{9}Be elastic scattering with the OM parameters of the ^{11}B + ^{9}Be elastic scattering (dashed curves) is also presented in Fig. 5.1.6. It is visible that in this case the description of the experimental $D(\theta)$ is worse, especially at large angles.

The energy dependent OM parameters for the ^{10}B + ^{9}Be and^{11}B + ^{9}Be elastic scattering, listed in Table 5.1.1, are also shown in Fig. 5.1.7 using the solid and empty circles, respectively. As in the previous analyses (see [1] and references therein), the energy dependences of the OM parameters $\{X_i\} = \{V, r_V, a_V, W_S, r_W, a_W\}$ were parameterized by the functional forms described in Chapter 3.

The E_{Xi}, ΔE_{Xi}, $X_i^{\max}$ and $X_i^{\min}$ parameters deduced from fits to the energy dependence are listed in Table 5.1.2. The corresponding curves are shown in Fig. 5.1.7. One can see that only imaginary parts of the ^{10}B + ^{9}Be and ^{11}B + ^{9}Be OM parameters are clearly different. Some differences are also observed for the parameters r_V and $a_V = a_W$ at low energies.

Table 5.1.2 Energy dependence of the ^{10}B + ^{9}Be optical potential parameters.

X_i	V_0 (MeV)	W_S (MeV)	r_V (fm)	r_W (fm)	a_V (fm)	a_W (fm)
$X_i^{\min}$	29.5	1.9	0.788	1.250	0.690	0.690
$X_i^{\max}$	250.5	16.9	1.000	1.400	0.700	0.700
E_{Xi}(MeV)	12.5	11.9	10.000	10.000	10.000	10.000
ΔE_{Xi}(MeV)	5.5	5.1	2.000	2.000	10.000	10.000

A following conclusion can be made for this sub-Section. The ^{9}Be(^{11}B,^{10}B)^{10}Be reaction proceeds mainly through the one-step neutron and proton transfers and therefore can be successfully used for estimation of the ^{10}B + ^{10}Be OM parameters as an alternative method to the standard analysis of the ^{10}B + ^{10}Be elastic scattering data.

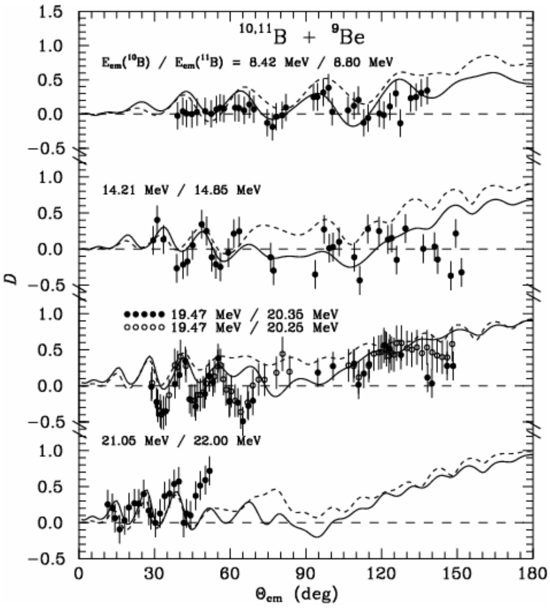

Fig. 5.1.6. The difference $D(\theta) = [\sigma_{10B}(\theta) - \sigma_{11B}(\theta)]/[\sigma_{10B}(\theta) + \sigma_{11B}(\theta)]$ between the cross sections $\sigma_{10B}(\theta) = \sigma/\sigma_R(\theta)$ of the ^{10}B + ^{9}Be elastic scattering and $\sigma_{11B}(\theta) = \sigma/\sigma_R(\theta)$ of the ^{11}B + ^{9}Be elastic scattering at energies $E_{CM}(^{10}B + ^9Be)$ and $E_{CM}(^{11}B + ^9Be)$, respectively (marked by $E_{CM}(^{10}B)/E_{CM}(^{11}B)$). The curves represent the CRC $D(\theta)$ calculated for respective OM parameters of the ^{10}B + ^{9}Be and ^{11}B + ^{9}Be scattering (solid curve) and for the case when the ^{11}B + ^{9}Be OM parameters were used for the both scattering (dashed curve).

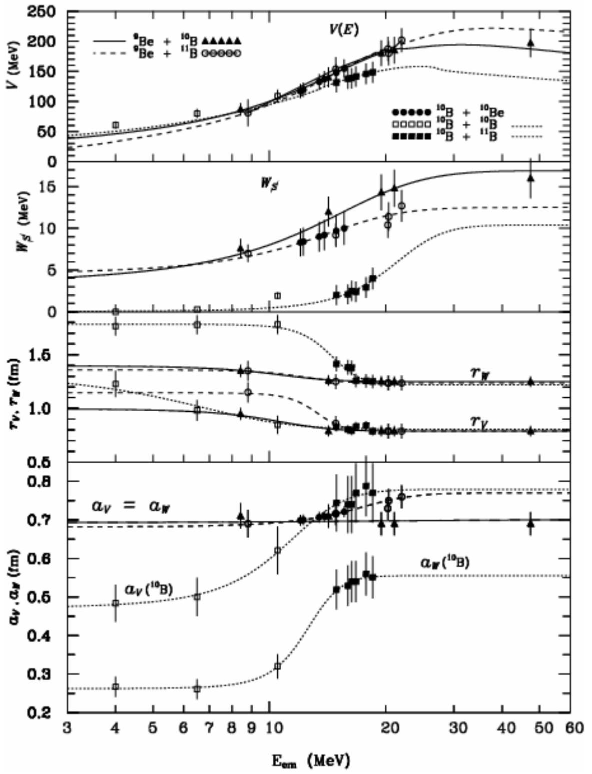

Fig. 5.1.7. Energy dependence of the OM parameters of ^{10}B + ^{9}Be (solid triangles and solid curves), ^{11}B + ^{9}Be (empty circles and dashed curves), ^{10}B + ^{10}Be (solid circles), ^{10}B + ^{10}B (empty circles and dotted curves) and ^{10}B + ^{11}B (solid circles and dotted curves).

5.1.2. The ^{9}Be(^{11}B, ^{12}B)^{8}Be reaction and the ^{12}B + ^{8}Be optical potential.

This sub-Section is devoted to the study of the ^{9}Be(^{11}B, ^{12}B)^{8}Be reaction (see [18]). For the ^{9}Be(^{11}B, ^{12}B)^{8}Be reaction the obtained previously experimental data were used [8]. The experimental data for this reaction are not accessible in the literature. This reaction is interesting because it can be used for determining the optical potential of interactions of the short-lived unstable nuclei ^{12}B + ^{8}Be. Such determination can be done in the framework of the coupled-reactions-channel method. The angular distributions of the ^{9}Be(^{11}B, ^{12}B)^{8}Be reaction at E_{LAB}(^{11}B) = 45 MeV for the ground excited states of ^{12}B and ^{8}Be nuclei are shown in Figs. 5.1.8 and 5.1.9.

The differential cross sections of the ^{9}Be(^{11}B, ^{12}B)^{8}Be reactions were analyzed using the optical model and the CRC method with inclusion of the elastic and inelastic scattering of ^{9}Be + ^{11}B nuclei and also the one-step and two-step transfers of nucleons and clusters into the coupling scheme. The optical model potentials of the Woods-Saxon type were used in the calculations. The diagrams of these transfers are shown in Fig. 5.1.10.

The values of the optical-potential parameters for the entrance and exit channels of the ^{9}Be(^{11}B, ^{12}B)^{8}Be reaction are shown in Table 5.1.3. The CRC cross sections of the ^{9}Be(^{11}B, ^{12}B)^{8}Be reaction for one-step and two-step sequential are shown in Fig. 5.1.8. The solid curve presents a coherent sum of the cross sections for the neutron and triton transfer reaction. One can see that in this reaction the neutron transfer process dominates

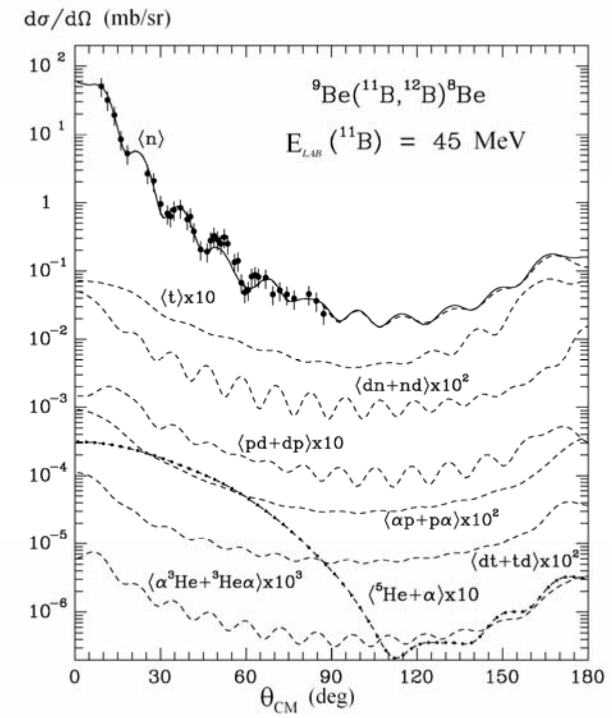

Fig. 5.1.8. The differential cross sections of the ^{9}Be(^{11}B, ^{12}B)^{8}Be reaction for E_{LAB}(^{11}B) = 45 MeV energy for transitions to ground states of the ^{12}B and ^{8}Be nuclei. The lines – the CRC-cross sections of nucleons and cluster transfers. The explanations are included in the text.

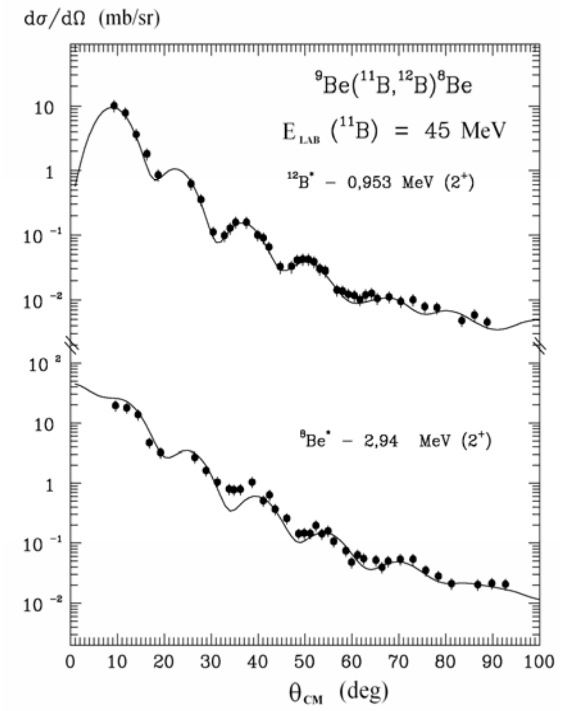

Fig. 5.1.9. The differential cross sections of the ^{9}Be(^{11}B, ^{12}B)^{8}Be reaction for E_{LAB}(^{11}B) = 45 MeV energy for excited states of the ^{12}B and ^{8}Be nuclei. The curves – CRC-cross sections for neutron transfer reactions.

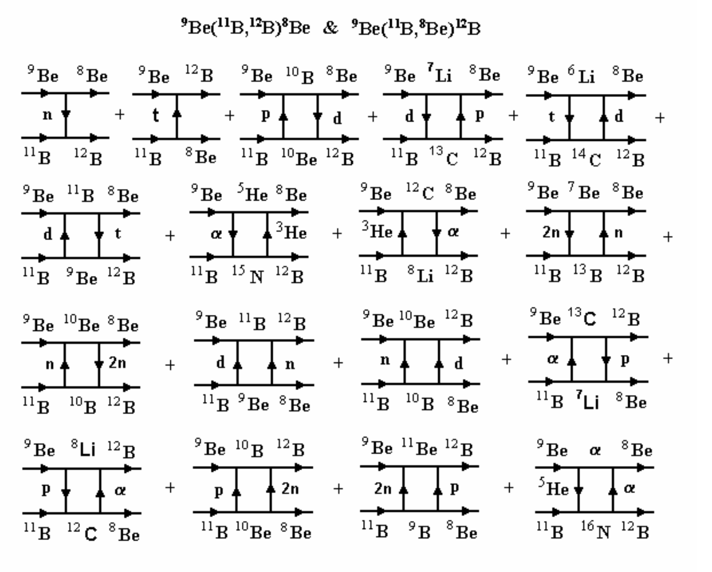

Fig. 5.1.10. The diagrams of one- and two-step transfer reactions of ^{9}Be(^{11}B, ^{12}B)^8 and ^{9}Be(^{11}B, ^{8}Be)^{12}B.

in the full angular range. The CRC cross sections well describe the experimental data for the optical-potential parameters of the exit ^{12}B + ^{8}Be channel (see Table 5.3.1). It is also visible that this potential is different from the entrance ^{9}Be + ^{11}B channel potential in the W_S value (less by about 3 MeV).

Analysis of the ^{9}Be(^{11}B, ^{12}B)^{8}Be reaction for the excited states of ^{12}B and ^{8}Be (see Fig. 5.1.9) has shown that also in this case the t-cluster transfer and the two-step transfers are small.

The neutron transfer dominates (solid curves in Fig. 5.1.9) in the cross sections. It was found that the optical potential of the ^{12}B$^*_{0.953}$ + ^{8}Be and ^{12}B + ^{8}Be$^*_{2.94}$ nuclei interaction in the excited states is almost equal to that for the ^{12}B + ^{8}Be nuclei interaction in the ground states.

Table 5.1.3. Parameters of optical model potentials.

Reaction channel	V, MeV	r_V, fm	a_V, fm	W_S, MeV	r_W, fm	a_W, fm
^{9}Be + ^{11}B	187,3	0,788	0,730	10,4	1,236	0,730
^{8}Be + ^{12}B	187,3	0,791	0,730	7,0	1,250	0,730

It was concluded from the CRC-analysis of the experimental data of the ^{9}Be(^{11}B, ^{12}B)^{8}Be reaction for the ground and excited states of the ^{12}B and ^{8}Be nuclei that the neutron transfer is the dominating process and the two-step transfers are small. Then, this reaction can be used for determining the optical potential for the unstable ^{12}B + ^{8}Be nuclei interactions.

5.1.3. The ^{9}Be(^{11}B, ^{12}C)^{8}Li reaction and comparison with the ^{9}Be(^{11}B, ^{12}B)^{8}Be and ^{9}Be(^{11}B, ^{10}Be)^{10}Be reactions.

This sub-Section is devoted to comparison of the ^{9}Be(^{11}B, ^{12}B)^{8}Be**,** ^{9}Be(^{11}B, ^{12}C)^{8}Li, ^{9}Be(^{11}B, ^{12}B)^{8}Be, and ^{9}Be(^{11}B, ^{10}B)^{10}Be reactions for E_{LAB}(^{11}B) = 45 MeV (see [19]). For the ^{9}Be(^{11}B, ^{12}B)^{8}Be and ^{9}Be(^{11}B, ^{10}B)^{10}Be reactions, the obtained previously experimental data were used [8]. For the ^{9}Be(^{11}B, ^{12}C)^{8}Li reaction, the differential cross sections for transitions to the ground states of ^{12}C and ^{8}Li nuclei and to the levels 4.439 MeV (2^+) of ^{12}C nucleus and 0.981 MeV (1^+), 2.261 MeV (3^+), 3.21 MeV (1^+), 5.4 MeV (2^+) of the ^{8}Li nucleus were measured at E_{LAB}(^{11}B) = 45 MeV [10].

A comparison of reactions with the identical nuclei in the entrance channels and with different isotopes and isobars in the exit channels for close values of the Q-reaction is important for investigation of isotopic and isobaric effects in the structure of nuclei and in the nucleus-nucleus interaction potentials. A comparison of the ^{9}Be(^{11}B, ^{12}B)^{8}Be [18] and ^{9}Be(^{11}B, ^{12}C)^{8}Li reactions is important for investigation of the shell structure of the ^{9}Be, ^{11}B, ^{12}B and ^{12}C nuclei and for studies of isobaric effects in the optical potential of interaction of the ^{12}B + ^{8}Be and ^{12}C + ^{8}Li nuclei. The structure peculiarities of these nuclei are taken into account in the spectroscopic amplitudes of nucleons in the ^{12}B → ^{11}B + n, ^{12}C → ^{11}B + p, ^{9}Be → ^{8}Be + n and ^{9}Be → ^{8}Li + p systems. The absolute values of the reaction cross sections depend on these amplitudes, while the angular distributions depend on the optical potentials of nuclear interactions. Then, comparison of the ^{9}Be(^{11}B, ^{12}B)^{8}Be and ^{9}Be(^{11}B, ^{12}C)^{8}Li reactions can give some information about nuclear structures and nuclear interactions.

Besides the isobaric effects mentioned above, also isotopic effects in the ^{9}Be(^{11}B, ^{12}B)^{8}Be [18] and ^{9}Be(^{11}B, ^{10}B)^{10}Be [10] reactions for the same energy can be investigated. These reactions give a possibility of experimental verification of the spectroscopic amplitudes for neutrons in the ^{12}B → ^{11}B + n and ^{11}B → ^{10}B + n, ^{9}Be → ^{8}Be + n and ^{10}Be → ^{9}Be + n systems, which were obtained from the shell model. These reactions give also a possibility of investigation of isotopic effects in the optical potentials of the ^{9}Be + ^{11}B, ^{12}B + ^{8}Be and ^{10}B + ^{10}Be nuclei interactions. Some of these nuclei are unstable. As it was already mentioned in Chapter 1, direct investigation of the nucleus-nucleus interaction for unstable short-living nuclei, performed using the secondary radioactive beams, is very difficult. Investigations of the transfer reactions with not complicated mechanisms are an alternative. For investigation of the optical potentials for the ^{12}C + ^{8}Li nuclei interactions, the ^{9}Be(^{11}B, ^{12}C)^{8}Li reaction was used. The optical potential for the entrance channel was taken from the analysis of the elastic scattering of ^{9}Be + ^{11}B nuclei in the wide energy range [8]. Earlier our group obtained the optical potentials of the ^{12}B + ^{8}Be and ^{10}B + ^{10}Be nuclei interactions from the ^{9}Be(^{11}B, ^{12}B)^{8}Be [18] and ^{9}Be(^{11}B, ^{10}B)^{10}Be [10] reactions.

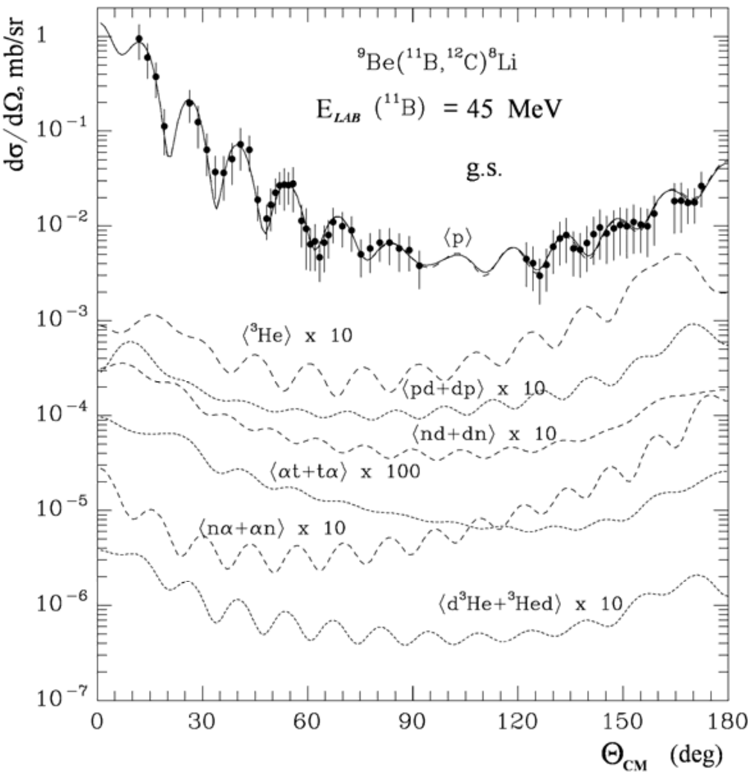

Fig. 5.1.11. The differential cross sections for the ^{9}Be(^{11}B, ^{12}C)^{8}Li reaction at E_{LAB}(^{11}B) = 45 MeV energy and for ground states of ^{12}C and ^{8}Li nuclei. Lines – the CRC cross sections for one- and two-step transfer reactions. The reaction diagrams are shown in Fig. 5.1.13.

The differential cross sections for transitions to ground and excited states of ^{12}C and ^{8}Li nuclei in the ^{9}Be(^{11}B, ^{12}C)^{8}Li reaction for E_{LAB}(^{11}B) = 45 MeV are shown in Figs. 5.1.11 and 5.1.12. For transitions to the ground states of ^{12}C and ^{8}Li (Fig. 5.1.11) and to the levels 0.981 MeV (1^{+}) of ^{8}Li and 4.439 MeV (2^{+}) of ^{12}C (Fig. 5.1.12, left side), the differential cross sections were measured in the full angular range, except of a small region around middle angles. The differential cross sections for large angles were obtained from the analysis of the lithium-isotope spectra. For transitions to the 2.261 MeV (3^{+}), 3.21 MeV (1^{+}) and 5.40 MeV (2^{+}) levels of ^{8}Li, the differential cross sections (Fig. 5.1.12, right side) were obtained from the analysis of the carbon-isotope spectra only, because ^{8}Li in these states decays to fragments, not achieving the detectors. Then, for these transitions, the cross sections for $\theta_{\mathrm{CM}} < 90^{\mathrm{O}}$ only were obtained.

One can see that only for transitions to the ground states of ^{12}C and ^{8}Li (Fig. 5.1.11) and to the 0.981 MeV (1^{+}) level of ^{8}Li (Fig. 5.1.12, left side), sharp oscillations at $\theta_{\mathrm{CM}} < 90^{\mathrm{o}}$ can be observed in the differential cross sections of the ^{9}Be(^{11}B, ^{12}C)^{8}Li reactions. For other transitions, the angular dependences have rather poor oscillation structure.

The experimental differential cross sections for transitions to the ground and excited states of ^{12}C and ^{8}Li in the ^{9}Be(^{11}B, ^{12}C)^{8}Li reaction were analyzed using the CRC method with the elastic and inelastic scattering of the ^{11}B + ^{9}Be nuclei. Also, the one-step and two-step transfers of nucleons and clusters were included into the coupled-channel scheme, accordingly to the diagrams in Fig. 5.1.13. For the CRC calculations in the entrance and exit channels, the optical Saxon-Woods potential with volume absorption was used.

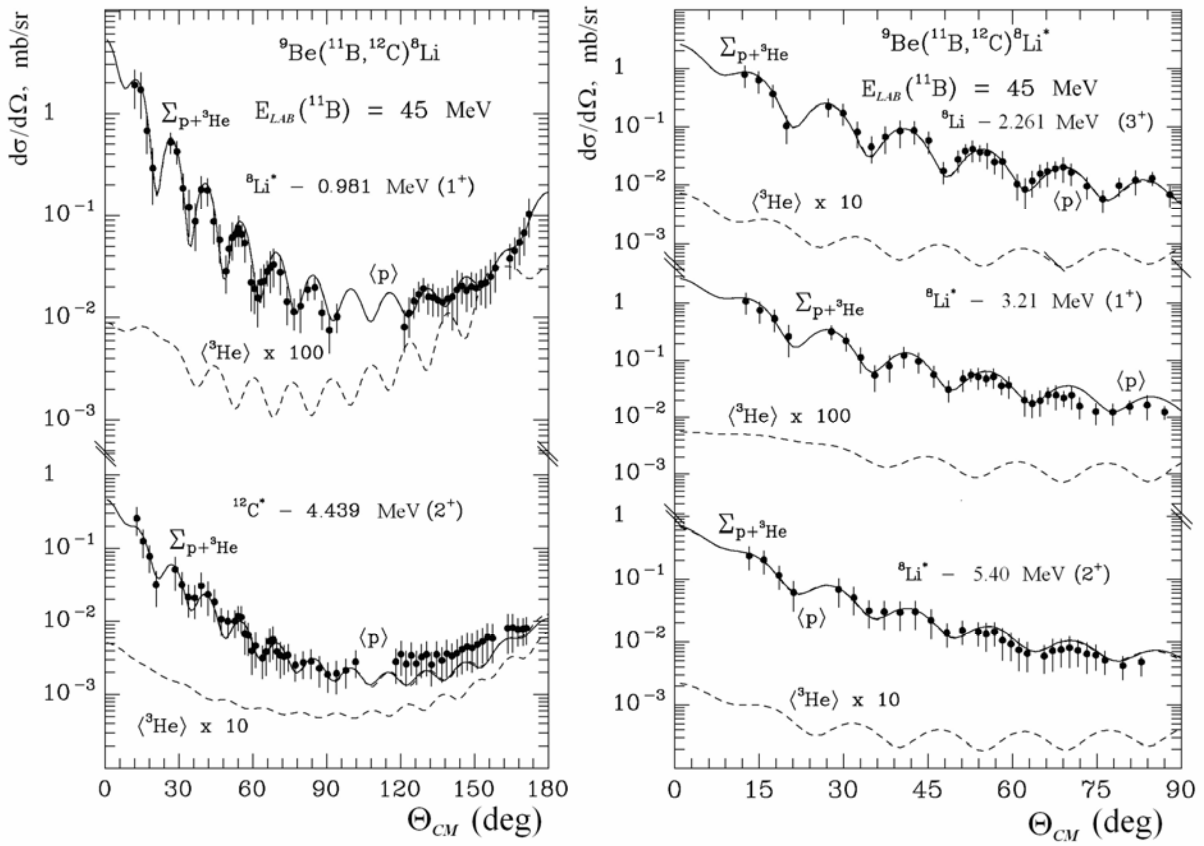

Fig. 5.1.12. The differential cross sections at the $E_{\mathrm{LAB}}(^{11}\mathrm{B})$ = 45 MeV energy and for transfers to levels of 0.981 MeV (1^+) of ^{8}Li nuclei and 4.439 MeV (2^+) of ^{12}C nuclei (left panel) and to levels of 2.261 MeV (3^+), 3.21 MeV (1^+) and 5.4 MeV (2^+) of ^{8}Li nuclei (right panel). Lines – the CRC- cross sections for for proton transfers (curves <p>) and ^{3}He cluster transfers (lines <^{3}He>).

Table 5.1.4. Parameters of optical model potentials.

Reaction channel	E_{CM} MeV	V, MeV	r_V, fm	a_V, fm	W_S, MeV	r_W, fm	a_W, fm	Ref.
^{9}Be + ^{11}B	20.25	187.3	0.788	0.730	10.4	1.236	0.730	
^{8}Li + ^{12}C	19.32	187.3	0.791	0.730	5.0	1.236	0.730	
^{8}Be + ^{12}B	21.95	187.3	0.791	0.730	7.0	1.236	0.730	[18]
^{10}Be + ^{10}B	15.61	154.7	0.823	0.721	10.0	1.248	0.721	[10]

For the entrance channel of the ^{9}Be(^{11}B, ^{12}C)^{8}Li reaction, the energy-dependent optical potentials obtained from the experimental data of elastic scattering of ^{11}B + ^{9}Be nuclei in a wide energy range were used [8]. The parameters of these potentials are shown in Table 5.1.4.

The parameters of the optical potentials for the exit channel of the ^{9}Be(^{11}B, ^{12}C)^{8}Li reaction were fitted to the experimental data. The obtained parameters of the optical potentials of the ^{12}C + ^{8}Li interactions are also shown in Table 5.1.4. One can see that the optical potentials of the ^{11}B + ^{9}Be and ^{12}C + ^{8}Li interactions noticeably differ only in the depth of imaginary parts (W_S = 10.4 MeV for ^{11}B + ^{9}Be and W_S = 5.0 MeV for ^{12}C + ^{8}Li).

The parameters of optical potentials for interactions of the ^{12}B + ^{8}Be [18] and ^{10}B + ^{10}Be [10] nuclei, necessary for analysis of the ^{9}Be(^{11}B, ^{12}B)^{8}Be and ^{9}Be(^{11}B, ^{12}C)^{8}Li, ^{9}Be(^{11}B, ^{10}B)^{10}Be, ^{9}Be(^{11}B, ^{11}B)^{9}Be and ^{9}Be(^{11}B, ^{12}B)^{8}Be reactions are also shown in Table 5.1.4.

The CRC cross sections of the ^{9}Be(^{11}B, ^{12}C)^{8}Li reaction for the ground states of the ^{12}C + ^{8}Li nuclei are shown in Fig. 5.1.11. It is visible that for these reactions the proton transfers dominate the cross section in the full angular range. On the other hand, the ^{3}He-cluster transfers and two-step transfers are small. The solid line in Fig. 5.1.11 represents the coherent sum of the CRC cross sections for proton and ^{3}He transfers. This curve is practically the same as the CRC cross sections for proton transfers. One can see that the CRC cross sections, obtained using the optical potentials shown in Table 5.1.4, well describe the experimental data in the full angular range.

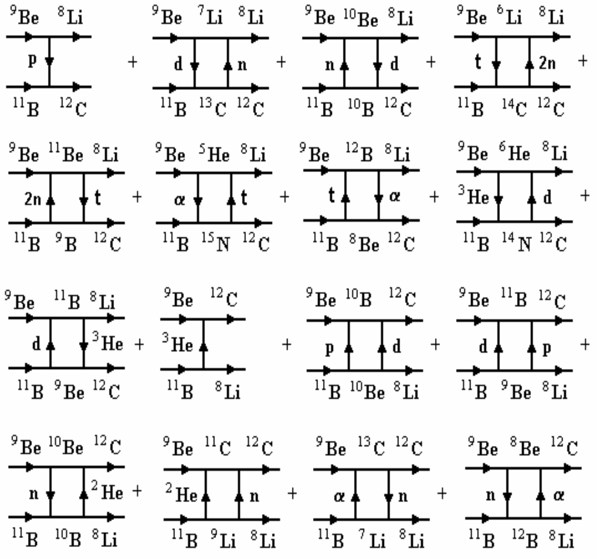

Fig. 5.1.13. The diagrams of one- and two-step transfers in the ^{9}Be(^{11}B, ^{12}C)^{8}Li and ^{9}Be(^{11}B, ^{8}Li)^{12}C reactions.

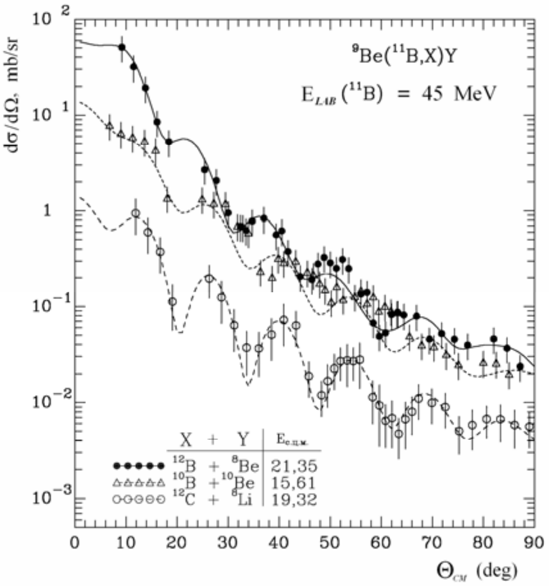

Fig. 5.1.14. The differential cross sections of the ^{9}Be(^{11}B ,^{10}B)^{10}Be, ^{9}Be(^{11}B, ^{12}B)^{8}Be and ^{9}Be(^{11}B, ^{12}C)^{8}Li reactions for E_{LAB}(^{11}B) = 45 MeV energy and ground states of nuclei in exit channels. Lines – the CRC-cross sections.

The CRC cross sections for the ^{9}Be(^{11}B, ^{12}C)^{8}Li reaction for the excited states of ^{12}C and ^{8}Li are shown in Fig. 5.1.12. This is apparent that the proton transfers (line <p>) also dominate here and the ^{3}He transfers and two-step transfers are also small. The coherent sum of the CRC cross sections for the proton and ^{3}He transfers (solid lines Σ_{p+3He}) are practically equal to the CRC cross sections for proton transfers. Then, the experimental data of the ^{9}Be(^{11}B, ^{12}C)^{8}Li reaction for the excited states of the ^{12}C and ^{8}Li are also well described by the CRC cross sections.

Isobaric effects appears in the ^{9}Be(^{11}B, ^{12}B)^{8}Be and ^{9}Be(^{11}B, ^{12}C)^{8}Li reactions. The differential cross sections for the ^{9}Be(^{11}B, ^{12}B)^{8}Be reaction (full points and solid line) and ^{9}Be(^{11}B, ^{12}C)^{8}Li reaction (open points and dotted line) for the ground states of nuclei in exit channels for E_{LAB}(^{11}B) = 45 MeV are shown in Fig. 5.1.14. It is apparent, that the values of the cross sections of these reactions noticeably differ. These differences cannot be a result of energy dependence of the cross sections since for the ^{12}B + ^{8}Be channel E_{CM} = 21.35 MeV and for the ^{12}C + ^{8}Li channel E_{CM} = 19.32 MeV. The difference of kinetic energies of these reaction products equals ~2 MeV only and this is not a reason for differences of these cross sections. These energy differences in the exit channels of reactions can explain only shifting of the angular cross sections of oscillations and differences in their mean slopes only. The absolute values of these reactions cross section depend on products of the spectroscopic amplitudes $A_{12B+8Be} = S_{12B\to 11B+n}\cdot S_{9Be\to 8Be+n} \approx 1{,}35$ and $A_{12C+8Li} = S_{12C\to 11B+p}\cdot S_{9Be\to 8Li+p} \approx 1.04$ and also on the binding energy of neutrons in the ^{12}B → ^{11}B + n (E_n = 3.370 MeV) and ^{9}Be → ^{8}Be + n (E_n = 1.665 MeV) systems and the binding energy of protons in the ^{12}C → ^{11}B + p (E_p = 15.957 MeV) and ^{9}Be → ^{8}Li + p (E_p = 16.887 MeV) systems. Then, a larger probability of the ^{9}Be(^{11}B, ^{12}B)^{8}Be reaction in comparison to the ^{9}Be(^{11}B,^{12}C)^{8}Li reaction is due to $A_{12B+8Be} > A_{12C+8Li}$, relation and also due to fact that the binding energy of neutrons in the ^{12}B and ^{9}Be nuclei is smaller than the proton binding energy in the ^{12}C and ^{9}Be nuclei. The neutron transfers are more probable energetically and have greater spectroscopic factors than the proton transfers in interactions of these nuclei.

For a more detailed investigation of differences of the cross sections for the ^{9}Be(^{11}B, ^{12}B)^{8}Be and ^{9}Be(^{11}B, ^{12}C)^{8}Li reactions, the asymmetry $D_1(\theta)$ (full points and solid line) is shown in Fig. 5.1.15

$$D_1(\theta) = \frac{\sigma_{12B}(\theta) - \sigma_{12C}(\theta)}{\sigma_{12B}(\theta) + \sigma_{12C}(\theta)} .$$

As one sees from Fig. 5.1.15, the asymmetry D_1 has an oscillatory shape, accordingly to the relative shift of oscillations in the angular distributions of the ^{9}Be(^{11}B, ^{12}B)^{8}Be and ^{9}Be(^{11}B, ^{12}C)^{8}Li reactions. The mean value of asymmetry is $D_1 \approx 1$.

One can conclude from Table 5.1.4, that the optical potentials for the ^{12}B + ^{8}Be and ^{12}C + ^{8}Li channels are different only in W_S (W_S = 7 MeV for ^{12}B + ^{8}Be and W_S = 5 MeV for ^{12}C + ^{8}Li) parameters. The isobaric effects in the ^{9}Be(^{11}B, ^{12}B)^{8}Be and ^{9}Be(^{11}B, ^{12}C)^{8}Li reactions only slightly affect the optical potentials in exit channels.

Isotopic effects appear also in the ^{9}Be(^{11}B, ^{12}B)^{8}Be and ^{9}Be(^{11}B, ^{10}B)^{10}Be reactions. The differential cross sections for these reactions at E_{LAB}(^{11}B) = 45 MeV are shown in Fig. 5.1.14. It is visible that the cross sections of these reactions slightly differ for $\theta_{CM} > 25^{\circ}$, although differences of the kinetic energies are 5.74 MeV. This energy difference can explain larger differences in the cross sections only for small angles. Small differences of the differential cross sections for the ^{9}Be(^{11}B, ^{12}B)^{8}Be and ^{9}Be(^{11}B, ^{10}B)^{10}Be reactions can be explained in the following way. The values of product of the spectroscopic amplitudes $A_{10B+10Be} \approx 1.89$ for the is larger than similar value $A_{12B+8Be} \approx 1.35$ for the ^{9}Be(^{11}B, ^{12}B)^{8}Be reaction. But the binding energies of neutrons in the^{12}B → ^{11}B + n (E_n = 3.370 MeV), ^{9}Be → ^{8}Be + n (E_n = 1.665 MeV) system are smaller than binding energies of neutrons in the ^{11}B → ^{10}B + n (E_n = 11.454 MeV), ^{10}Be → ^{9}Be + n (E_n = 6.812 MeV) systems. The asymmetry

$$D_2(\theta) = \frac{\sigma_{12B}(\theta) - \sigma_{10B}(\theta)}{\sigma_{12B}(\theta) + \sigma_{10B}(\theta)}$$

of the differential cross sections for the ^{9}Be(^{11}B, ^{12}B)^{8}Be and ^{9}Be(^{11}B, ^{10}B)^{10}Be reactions at E_{LAB}(^{11}B) = 45 MeV is shown in Fig. 5.1.15. Oscillations of this asymmetry display the angular shifts of oscillations of the differential cross sections, due to differences in kinetic energies of the exit channels of these reactions. These differences explain the increase of the asymmetry $D_2(\theta)$ for small angles.

One can see from Table 5.1.4 that the optical potentials of the ^{12}B + ^{8}Be and ^{10}B + ^{10}Be channels noticeably differ only in depths of the real and imaginary parts.

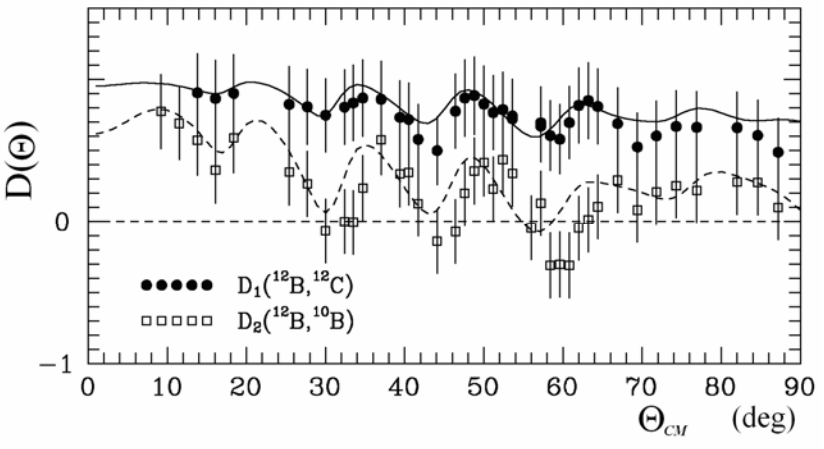

Fig. 5.1.15. The angular dependence of asymmetry $D_1(\theta)$ of cross sections of the ^{9}Be(^{11}B, ^{12}B)^{8}Be and ^{9}Be(^{11}B, ^{12}C)^{8}Li reactions (full circles and solid line) and $D_2(\theta)$ of cross sections of the ^{9}Be(^{11}B, ^{12}B)^{8}Be and ^{9}Be(^{11}B, ^{10}B)^{10}Be reactions (open circles and dashed line) for E_{LAB}(^{11}B) = 45 MeV energy and ground states of nuclei in exit channels. The curves D_1 and D_2 are the CRC-cross sections asymmetries.

As a conclusion of this sub-Section we emphasize that big differences (isobaric effect) in the differential cross sections for the ^{9}Be(^{11}B, ^{12}B)^{8}Be and ^{9}Be(^{11}B, ^{12}C)^{8}Li reactions were found. The isotopic effects in the differential cross sections for ^{9}Be(^{11}B, ^{12}B)^{8}Be and ^{9}Be(^{11}B, ^{10}B)^{10}Be reactions at E_{LAB}(^{11}B) = 45 MeV were also observed.

5.1.4. The ^{12}C(^{11}B, ^{15}N)^{8}Be reaction and ^{8}Be + ^{15}N optical-model potential.

The analysis of the ^{12}C(^{11}B, ^{15}N)^{8}Be reaction, measured for the transitions to the ground and excited states of ^{8}Be and ^{15}N at E_{LAB}(^{11}B) = 49 MeV is presented in this sub-Section (see [11]). We have found in the literature only the experimental data of the ^{12}C(^{11}B, ^{8}Be)^{15}N reaction for a few angles at $E_{CM} \approx$ 10 - 17 MeV [226]. Those data were used together with our data to study the energy dependence of the ^{8}Be + ^{15}N OM parameters. This is impossible when a standard method using elastic scattering is applied because ^{8}Be is unbound. The ^{12}C(^{11}B, ^{15}N)^{8}Be and ^{12}C(^{11}B, ^{8}Be)^{15}N reactions are also used to investigate the two-step transfers which include the sequential nucleon and two- nucleon cluster exchanges, in addition to the α- and t-cluster transfers.

As a result, the angular distributions of the ^{12}C(^{11}B, ^{15}N)^{8}Be reaction at E_{LAB}(^{11}B) = 49 MeV were obtained for the transitions to the ground and excited states of ^{8}Be and ^{15}N are shown in Figs. 5.1.16 - 5.1.18, together with the results of theoretical calculations. The errors shown in the figures include the statistical errors and uncertainties from the analysis of the spectra. We assumed that the areas under the isolated and unresolved peaks are obtained with the accuracy of about 20% - 30%.

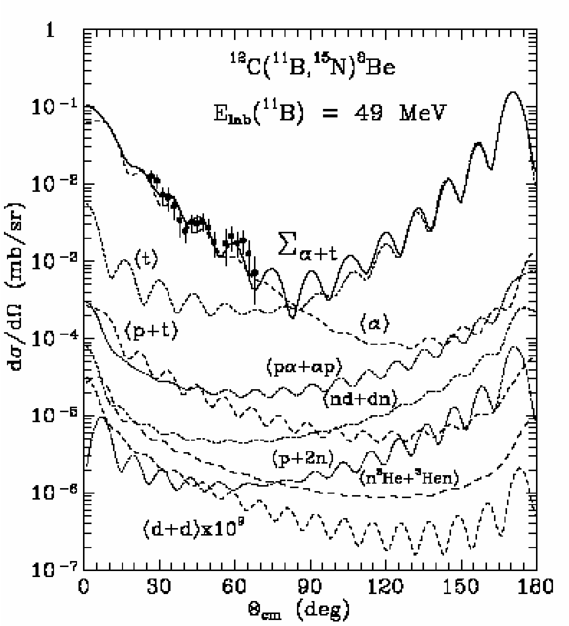

Fig. 5.1.16. Angular distribution of the ^{12}C(^{11}B, ^{15}N)^{8}Be reaction for the transitions to the ground states of ^{15}N and ^{8}Be at the energy E_{LAB}(^{11}B) = 49 MeV. The dashed curves represent the CRC cross-sections for the individual transfers or their coherent sums corresponding to the diagrams shown in Fig. 5.1.20 (see text for more details). The solid curve $\Sigma_{\alpha+t}$ shows the coherent sum of the α- and t-cluster transfers (see curves <α> and <t>, respectively).

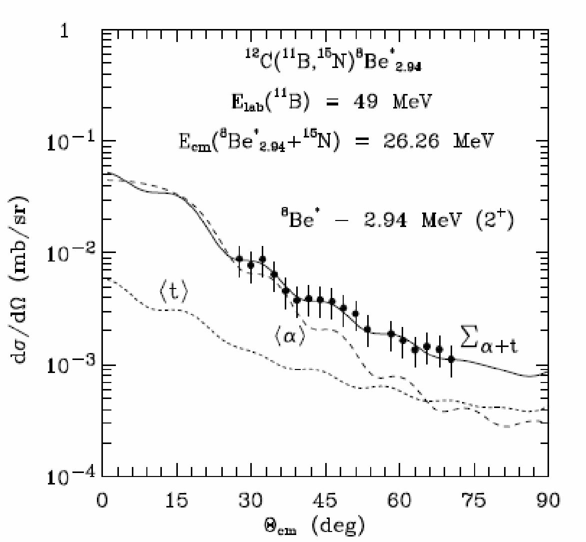

Fig. 5.1.17. Angular distribution of the ^{12}C(^{11}B, ^{15}N)^{8}Be reaction at the energy E_{LAB}(^{11}B) = 49 MeV for the transition to the 2.94 MeV (2^{+}) excited state of ^{8}Be. The dashed curves <α> and <t> present the angular distributions for the α- and t- cluster transfers, respectively. The solid curve $\Sigma_{\alpha+t}$ shows the coherent sum of these transfers.

The angular distributions of the ^{12}C(^{11}B, ^{15}N)^{8}Be reaction for the ground and excited states of ^{8}Be and ^{15}N at E_{LAB}(^{11}B) = 49 MeV (E_{CM} = 25.57 MeV), as well as the data of the ^{12}C(^{11}B, ^{8}Be)^{15}N reaction at E_{CM} = 10 - 17 MeV [226], which are known from the literature, were analyzed within the coupled-reaction-channel method. The data of the ^{12}C(^{11}B, ^{8}Be)^{15}N reaction at CM energies ranging from 10 MeV up to 17 MeV in the step of 1 MeV were obtained from the differential cross-sections $\sigma(\theta,E)$ given in [226] at θ_{CM} = 12.2°, 20.0°, 36.2°, 44.2° and 52.0°. These angular distributions are shown in Fig. 5.1.19.

The OM parameters $\{X_i\} = \{V;\ r_V;\ a_V;\ W_S;\ r_W;\ a_W\}$ for the entrance ^{11}B + ^{12}C channel were taken from the energy-dependent parameterization based on the elastic-scattering data obtained in [6]. These OM parameters are listed in Table 5.1.5.

Table 5.1.5. Parameters of OM potentials (r_C = 1.25 fm).

E_{CM} (MeV)	V (MeV)	r_V (fm)	a_V (fm)	W_S (MeV)	r_W (fm)	a_W (fm)
^{11}B + ^{12}C						
10.00	114.0	0.808	0.669	4.0	1.289	0.669
12.00	147.0	0.795	0.670	4.5	1.262	0.670
13.50	175.7	0.791	0.670	5.0	1.255	0.670
15.00	202.6	0.789	0.670	5.5	1.253	0.670
16.00	217.5	0.789	0.670	5.9	1.252	0.670
17.00	229.3	0.788	0.670	6.2	1.251	0.670
25.57 [2]	241.6	0.788	0.670	9.0	1.250	0.670
^{8}Be + ^{15}N						
13.63	68.0	0.799	0.400	1.0	1.255	0.400
15.63	102.0	0.796	0.400	1.4	1.255	0.400
17.13	128.9	0.796	0.400	1.9	1.250	0.400

18.63	177.8	0.796	0.400	2.6	1.250	0.400
19.63	211.0	0.796	0.400	3.0	1.250	0.400
20.63	231.0	0.796	0.400	3.8	1.250	0.400
21.63	238.0	0.796	0.400	4.0	1.250	0.400
22.04	241.5	0.796	0.400	4.1	1.250	0.400
22.88	246.8	0.796	0.400	4.2	1.250	0.400
23.90	247.2	0.796	0.400	4.3	1.250	0.400
26.26	252.0	0.796	0.400	4.3	1.250	0.400
29.20	252.6	0.796	0.400	4.3	1.250	0.400

The angular distributions were calculated for the one-step and two-step transfers corresponding to the diagrams shown in Fig. 5.1.20. First of all, the angular distributions for each individual transfer were calculated using the same OM parameters for both the entrance and exit reaction channels. An individual transfer or a group of sequential transfers (e.g., n + d and d + n) were included into the coupling scheme, together with the elastic scattering and the transitions to the excited states of ^{11}B or ^{12}C, which correspond to the diagrams presented in Fig. 5.1.20. It was found that, in the ^{12}C(^{11}B, ^{15}N)^{8}Be reactions, the α- and t-cluster transfers dominate at the forward and backward angles, respectively, for all transitions to the ground and excited states of ^{8}Be and ^{15}N. Next, a coherent sum of the α- and t-cluster transfers was fitted to the data for each transition by the variation of the OM parameters for the ^{8}Be + ^{15}N channel. As a result, the OM parameters for this channel were obtained for a few different energies. These parameters are listed in Table 5.5.1. The corresponding coherent sums of the α- and t-cluster transfers are shown in Figs. 5.5.3 - 5.5.6 using the solid curves. More details of the angular distribution analysis are presented below.

Figure 5.1.16 shows the angular distribution of the ^{12}C(^{11}B, ^{15}N)^{8}Be reaction for the transition to the ground states of ^{8}Be and ^{15}N. The curves present the CRC cross-sections for the one- and two-step transfers corresponding to the diagrams of Fig. 5.1.20. One can see that the α-transfer (curve <α>) is dominant at forward angles where the angular distribution was measured. The t-cluster transfer is not important in this angular range. The CRC calculations predict that this transfer is dominant at backward angles (curve <t>). The coherent sum of the α- and t-cluster transfers (solid curve $\Sigma_{\alpha+t}$) satisfactorily describes the data. The sequential transfers of p + t (curve <p + t>), p + 2n (curve <p + 2n>), d + d (curve <d + d>), n + ^{3}He and ^{3}He + n (curve <n^{3}He + ^{3}Hen> shows their coherent sum), n + d and d + n (curve <nd + dn>), p + α and α + p (curve <pα + αp>) contribute weakly to the ^{12}C(^{11}B, ^{15}N)^{8}Be reaction.

The angular distribution of the ^{12}C(^{11}B, ^{15}N)^{8}Be reaction for the transition to the 2.94 MeV (2^+) excited state of ^{8}Be and to the ground state of ^{15}N is shown in Fig. 5.1.17. One can see that the α-cluster transfer (dashed curve <α>) dominates at the angles $\theta_{CM} < 50^o$ and that contributions of the α- and t-cluster transfers (curves <α> and <t>, respectively) appear in the region $\theta_{CM} \approx 50^o - 90^o$. As in the case presented above, the two-step transfers are negligible for this transition. The coherent sum of the α- and t-cluster transfers (solid curve $\Sigma_{\alpha+t}$) satisfactorily describes the data.

The angular distributions of the ^{12}C(^{11}B, ^{15}N)^{8}Be reaction at E_{LAB}(^{11}B) = 49 MeV for the transitions to the 5.270 MeV ($5/2^+$) + 5.299 MeV ($1/2^+$), 6.324 MeV ($3/2^-$), 7.155 MeV ($5/2^+$) + 7.301 MeV ($3/2^+$) and 7.567 MeV ($7/2^+$) excited states of ^{15}N are shown in Fig. 5.1.18. The contributions of the α-cluster transfers (dashed curves <α>) to the data are dominant for all these transitions. In the forward hemisphere the t-cluster transfers (curves <t>) modify the angular distributions only around $\theta_{CM} = 90^o$. The coherent sums of the α- and t-cluster transfers (solid curves) satisfactorily describe all data. The transition to the 5.299 MeV ($1/2^+$) excited state of ^{15}N only weakly contributes to the data of unresolved transitions to the 5.270 MeV ($5/2^+$) + 5.299 MeV ($1/2^+$) excited states of ^{15}N. The transition to the 7.301 MeV ($3/2^+$) excited state of ^{15}N is also weak in comparison to the 7.155 MeV ($5/2^+$) excited state of ^{15}N.

The experimental angular distributions of the ^{12}C(^{11}B, ^{8}Be)^{15}N reaction at the energies E_{CM} = 10 - 17 MeV taken from Ref. [226], are shown in Fig. 5.1.19. The curves present the CRC angular distributions.

Table 5.1.6. Energy dependence of the ^{8}Be + ^{15}N OM parameters.

X_i	V_0 (MeV)	W_S (MeV)	r_V (fm)	r_W (fm)	a_V (fm)	a_W (fm)
X_i^{min}	69.7	0.8	0.8	1.25	0.30	0.30
X_i^{max}	270.3	4.4	1.1	1.60	0.40	0.40
E_{Xi}(MeV)	18.1	18.6	5.0	5.00	4.80	4.80
ΔE_{Xi}(MeV)	1.7	1.7	2.0	2.00	1.13	1.13

The optical-model parameters for the ^{8}Be + ^{15}N channel deduced from the CRC analysis of the ^{12}C(^{11}B, ^{15}N)^{8}Be and ^{12}C(^{11}B, ^{8}Be)^{15}N reactions at different energies, are listed in Table 5.1.5 and presented in Fig. 5.1.21 using the solid circles. These sets of the OM parameters $\{X_i\}$ for different energies were parameterized by the functional forms introduced in Section 3.4.

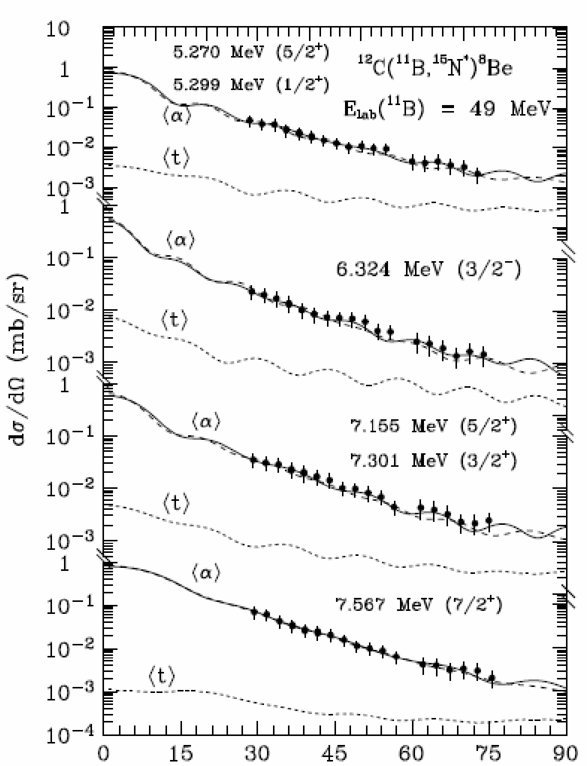

Fig. 5.1.18. Angular distributions of the ^{12}C(^{11}B, ^{15}N)^{8}Be reaction at the energy E_{LAB}(^{11}B) = 49 MeV for the transitions to the 5.27 MeV ($5/2^+$) + 5.299 MeV ($1/2^+$), 6.324 ($3/2^-$), 7.155 MeV ($5/2^+$) + 7.301 MeV ($3/2^+$) and 7.567 MeV ($7/2^+$) excited state of ^{15}N. The angular distributions for the α- and t-cluster transfers are presented by dashed curves <α> and <t>, respectively. The solid curves represent the coherent sums of the α- and t-cluster transfers.

The energy-dependent parameters X_i^{min}, X_i^{max}, E_{Xi} and ΔE_{Xi} were fitted in order to describe the energy dependences of the OM parameters X_i. As the result, the sets of these parameters were estimated for the ^{8}Be + ^{15}N channel. These parameters are listed in Table 5.1.6. In Fig. 5.1.21 we show also the energy dependence of the OM parameters for the ^{8}Be + ^{13}C channel (open triangles and dashed curves) obtained in our previous work [3]. Except for r_V and r_W , rather large differences between the OM parameters of the ^{8}Be + ^{13}C and ^{8}Be + ^{15}N channels can be seen. At energies E_{CM} > 0 MeV the parameters a_V and a_W are much smaller for the ^{8}Be + ^{15}N channel than for the ^{8}Be + ^{13}C one (see the lower panel in Fig. 5.1.21). This is probably caused by closing the neutron p-shell in the ^{15}N nucleus. The energy interval of the fast rise of W_S for the ^{8}Be + ^{15}N channel is shifted relatively to its counterpart for the ^{8}Be + ^{13}C channel (see panel for W_S in Fig. 5.1.21). To characterize this shift quantitatively it is convenient to use points in the middle of the regions of the fast growths of W_S (E_N = 18.6 MeV for ^{8}Be + ^{15}N and E_C = 11.39 MeV [3] for ^{8}Be + ^{13}C). The corresponding points E_N and E_C are marked on the E_{CM} axis of W_S in Fig. 5.1.21. The energy shift $\Delta E_{NC} = E_N - E_C$ = 7.21 MeV is probably due to differences between the ^{8}Be + ^{13}C and ^{8}Be + ^{15}N potential barriers. The fast W_S rise must correspond to an intensive opening of new inelastic channels. For nucleus-nucleus collisions inelastic processes take place mainly nearby the surfaces of interacting nuclei. Therefore, we analyze barriers of the effective potential for both interacting systems in the vicinity of grazing orbital momenta l_g. The V_{eff}(r) potentials were calculated using the ^{8}Be + ^{13}C OM parameters from ref. [3] At E_{CM} = 11.39 MeV (V_0 = 159.0 MeV, r_V = 0.87 fm, a_V = 0:723 fm, r_C = 0.87 fm) and the ^{8}Be + ^{15}N OM parameters at E_{CM} = 18.63 MeV from Table 5.1.5. It was found that for both the ^{8}Be + ^{13}C and ^{8}Be + ^{15}N systems the grazing orbital momenta are l_g = 21. This is illustrated in Fig. 5.1.22 where the effective potentials V_{eff}(r) are shown: dashed curve: for the ^{8}Be + ^{13}C system, solid curves: for the ^{8}Be + ^{15}N system. The grazing potential barrier for the ^{8}Be + ^{13}C system at E_C = 11.39 MeV is

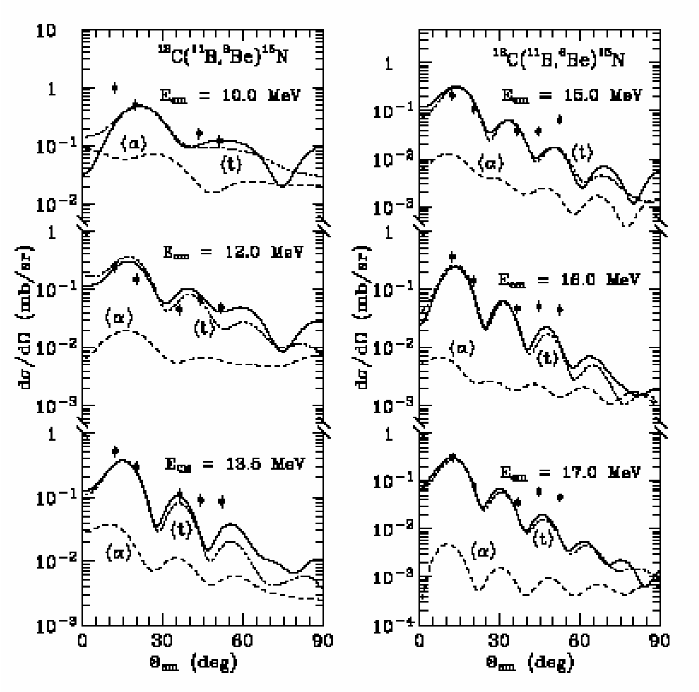

Fig. 5.1.19. Angular distributions of the ^{12}C(^{11}B, ^{8}Be)^{15}N reaction at the energies E_{CM} = 10 - 17 MeV for the transitions to the ground states of ^{8}Be and ^{15}N (data from [226]). The dashed curves <α> and <t> show the angular distributions of the α- and t-cluster transfers, respectively. The solid curves present the coherent sum of these transfers.

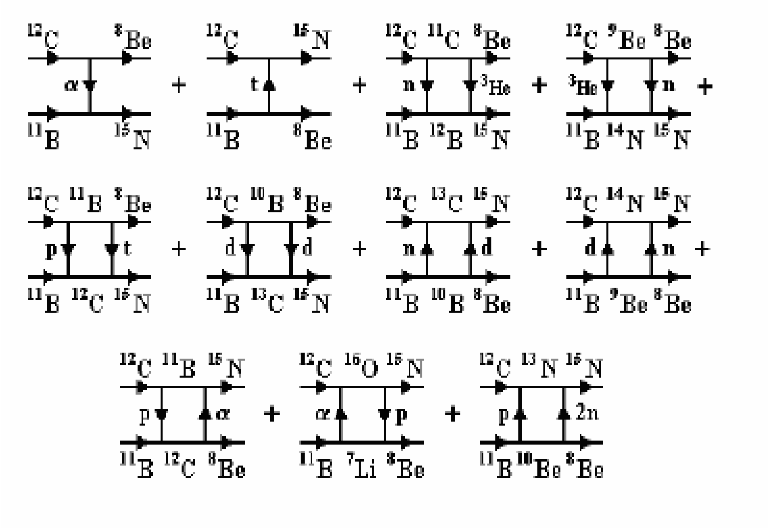

Fig. 5.1.20. Diagrams of the one- and two-step processes for the ^{12}C(^{11}B, ^{15}N)^{8}Be and ^{12}C(^{11}B, ^{8}Be)^{15}N reactions.

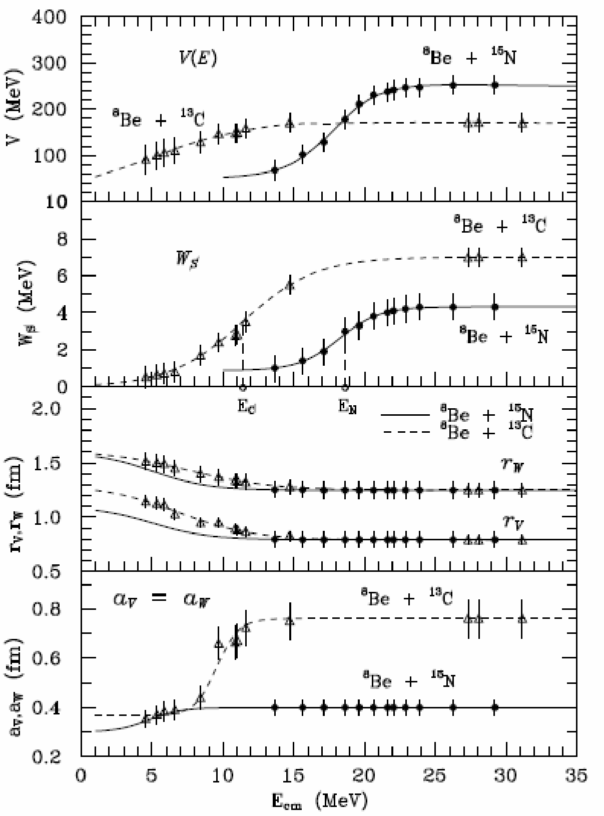

Fig. 5.1.21. Energy dependence of the OM potential parameters for the ^{8}Be + ^{13}C (open triangles and dashed curves) (E_{Coul} = 5.59 MeV (CM)) [3] and ^{8}Be + ^{15}N (solid circles and curves) (E_{Coul} = 6.27 MeV (CM)) channels. E_N and E_C are the points of fast growths of W_S.

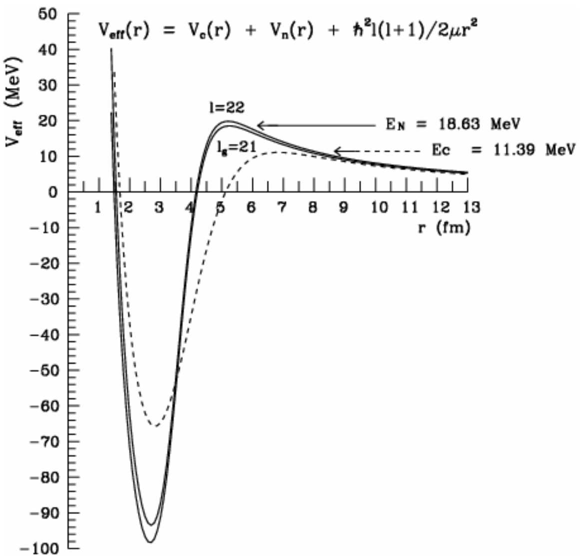

Fig. 5.1.22. Effective potential V_{eff}(r) for the ^{8}Be + ^{15}N (solid curves) and ^{8}Be + ^{13}C (dashed curve) channels. Parameters of the OM potential for the ^{8}Be + ^{13}C channel are taken from Ref. [3].

lower than for the ^{8}Be + ^{15}N system at E_N = 18.63 MeV. Such a difference between the grazing potential barriers for these systems is probably the reason of the energy shift of the fast growth of W_S discussed above. The OM parameters V(E) of ^{8}Be + ^{15}N and ^{8}Be + ^{13}C are also shifted in a similar way.

The following conclusion can be made. The two-step processes are negligible in the ^{12}C(^{11}B, ^{15}N)^{8}Be and ^{12}C(^{11}B, ^{8}Be)^{15}N reactions for all transitions. The coherent sums of the α- and t-cluster transfers satisfactorily describe the angular distributions of these reactions for all transitions. Using the energy-dependent OM parameters for the entrance channel of the ^{12}C(^{11}B, ^{15}N)^{8}Be and ^{12}C(^{11}B, ^{8}Be)^{15}N reactions and the cluster spectroscopic amplitudes, the OM parameters for the ^{8}Be + ^{15}N channel were obtained from the analysis of experimental data at different energies. The energy dependence of the OM parameters for the ^{8}Be + ^{15}N channel was derived as a result of our procedure. Differences between the energy dependence of the OM parameters for the ^{8}Be + ^{15}N and ^{8}Be + ^{13}C channels were discussed and explained by the differences of potential barriers in both channels.

5.2. The ^{9}Be(^{12}C, ^{13}C) and ^{9}Be(^{12}C, ^{11}B) reactions.

5.2.1. The ^{9}Be(^{12}C, ^{13}C)^{8}Be reaction and the optical potential for the ^{8}Be + ^{13}C interaction.

This sub-Section is devoted to investigation of the ^{9}Be(^{12}C, ^{13}C)^{8}Be reaction [3]. The energy-dependent optical-model potential for the ^{12}C + ^{9}Be elastic scattering (entrance channel) was recently obtained in the work [4] and described in Section 4.2.

The mechanism of the ^{9}Be(^{12}C, ^{13}C)^{8}Be reaction was carefully studied and the results are presented in this sub-Section. Two OM potentials for the ^{13}C + ^{8}Be interaction were used in the CRC calculations: the same as for the entrance channel and the OM potential obtained in the fitting procedure. The energy dependence of these potentials were studied. The results were compared with the energy dependence of the OM potential for the ^{12}C + ^{9}Be elastic scattering. Some differences were found.

The angular distributions for the ^{9}Be(^{12}C, ^{13}C)^{8}Be reaction at E_{LAB}(^{12}C) = 65 MeV for the transitions to the ground states of the ^{8}Be and ^{13}C nuclei and to excited states of the ^{13}C nucleus are shown in Figs. 5.2.1 and 5.2.2.

The angular distributions of the ^{9}Be(^{12}C, ^{13}C)^{8}Be reaction at E_{LAB}(^{12}C) = 65 MeV (E_{CM} = 27.86 MeV) for the transitions to the ground and excited states of ^{13}C and ^{8}Be nuclei together with similar data at E_{LAB}(^{12}C) = 12, 15 MeV (E_{CM} = 5.14, 6.43 MeV) [222] and E_{LAB}(^{9}Be) = 20 MeV (E_{CM} = 11.43 MeV) for the ^{12}C(^{9}Be, ^{8}Be)^{13}C reaction [153] were analyzed within the CRC model. This model uses the energy-dependent OM potential found in [4] for the ^{12}C + ^{9}Be interaction in the entrance reaction channel. The parameters of this potential are given in Table 5.2.1. The OM potential parameters for the exit ^{13}C + ^{8}Be channel were fitted to the reaction data using the OM potential of the entrance channel as the starting potential in the fitting procedure.

The angular distributions of the ^{9}Be(^{12}C, ^{13}C)^{8}Be reaction at E_{LAB}(^{12}C) = 65 MeV (E_{CM} = 27.86 MeV) for the transitions to the ground and excited states of ^{13}C and ^{8}Be nuclei together with similar data at E_{LAB}(^{12}C) = 12, 15 MeV (E_{CM} = 5.14, 6.43 MeV) [222] and E_{LAB}(^{9}Be) = 20 MeV (E_{CM} = 11.43 MeV) for the ^{12}C(^{9}Be, ^{8}Be)^{13}C reaction [153] were analyzed within the CRC model. This model uses the energy-dependent OM potential found in [4] for the ^{12}C + ^{9}Be interaction in the entrance reaction channel. The parameters of this potential are given in Table 5.2.1. The OM potential parameters for the exit ^{13}C + ^{8}Be channel were fitted to the reaction data using the OM potential of the entrance channel as the starting potential in the fitting procedure.

The diagrams for the one-step and two-step transfer reactions are presented in Fig. 5.2.3. The elastic and inelastic scattering for the transitions to the 1.68 MeV (1/2^{+}) and 2.43 MeV (5/2^{-}) excited states of the ^{9}Be nucleus were included in the coupled channel-scheme. The excited states of ^{9}Be were assumed to be rotational and the deformation parameters obtained in [4] were used in the CRC calculations.

The spectroscopic amplitudes S_x for the 1p-shell states of nuclei are listed in Appendix. The spectroscopic amplitudes for the 3.09 MeV (1/2^{+}) and 3.85 MeV (5/2^{+}) excited sd-shell states of ^{13}C were fitted to the corresponding data at E_{LAB}(^{12}C) = 12, 15 MeV [222] . The fitting procedure is reasonable because the CRC angular distributions of these reactions at small angles are only slightly dependent on the variation of the OM potential parameters for the exit channels of these reactions.

The angular distributions calculated within the CRC model are shown in Figs. 5.2.1, 5.2.2, 5.2.4 – 5.2.6 by the solid and dashed curves. In Figs. 5.2.1, 5.2.4 – 5.2.6 the dotted curves marked by the Σ_0 label illustrate the CRC cross sections obtained using the same potentials in the entrance and exit channels. Figures 5.2.1, 5.2.4 – 5.2.6 show that the n-transfer (dashed curves <n>) dominates in the ^{9}Be(^{12}C, ^{13}C)^{8}Be and ^{12}C(^{9}Be, ^{8}Be)^{13}C reactions at all beam energies considered here. The α transfer (dashed curves <α>) contributes to the angular distributions only at large angles. Figure 5.2.1 shows that the two-step transfers ^{3}He + n and d + d (dashed curves <^{3}He+n> and <d+d>) in these reactions are negligible. The other two-step reactions give also small contributions to the cross section for these reactions. Therefore, the ^{9}Be(^{12}C, ^{13}C)^{8}Be and ^{12}C(^{9}Be, ^{8}Be)^{13}C reactions are suitable for studying the ^{8}Be + ^{13}C interaction at different energies.

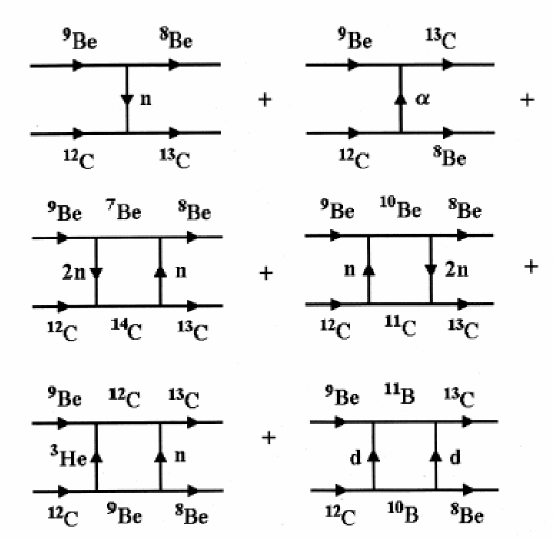

Fig. 5.2.3. Diagrams of one- and two-step transfer processes relevant for the ^{9}Be(^{12}C, ^{13}C)^{8}Be reaction.

Fig. 5.2.3. Diagrams of one- and two-step transfer processes relevant for the ^{9}Be(^{12}C, ^{13}C)^{8}Be reaction.

The values of the OM potential parameters V, $W_S = W_{CRC}$, r_V,r_W, a_V, a_W, $r_C = r_V$ obtained in the fitting procedure. The parameters a_V and a_W were fitted independently from each other. It was found that the CRC angular distributions are more sensitive to the variation of the parameter a_V than to the variation of the parameter a_W. The best description of the data was observed for almost identical values of a_V and a_W . Thus, in the following we put $a_V = a_W$. The CRC cross sections calculated as a coherent sum of the n- and α- transfer transition amplitudes for the ^{9}Be(^{12}C, ^{13}C)^{8}Be and ^{12}C(^{9}Be, ^{8}Be)^{13}C reactions are shown in Figs. 5.2.1, 5.2.2 and Figs. 5.2.4 – 5.2.6 using the solid curves Σ, $\Sigma_{2.94+3.09}$ and $\Sigma_{3.68+3.85}$. As it can be seen from the figures, a good description of all experimental data is achieved.

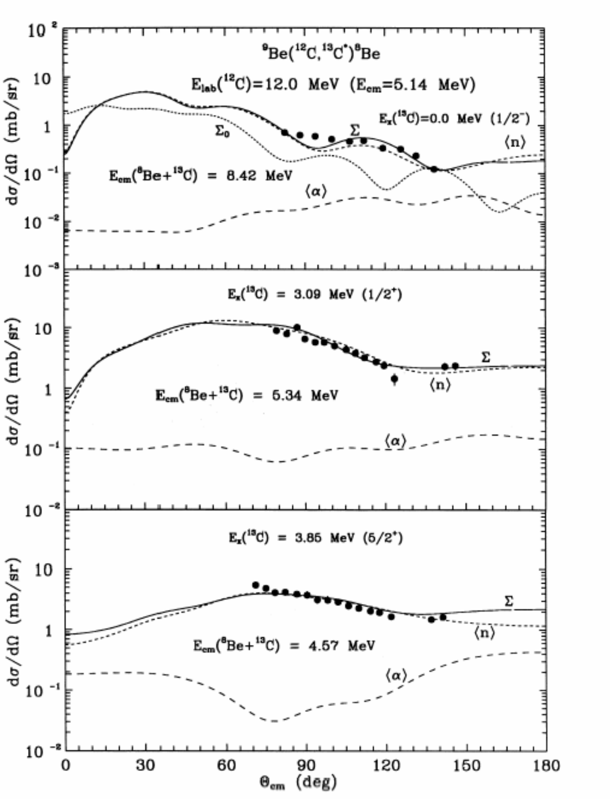

Fig. 5.2.4. Angular distributions of the ^{9}Be(^{12}C, ^{13}C)^{8}Be reaction at the energy E_{LAB}(^{12}C) = 12 MeV [222] for the transitions to the ground states of the ^{13}C and ^{8}Be nuclei upper panel and to the 3.09 MeV (1/2^{+}) and 3.85 MeV (5/2^{+}) excited states of the ^{13}C nucleus middle and lower panels, respectively . The dashed curves <n>, <α> and solid curve Σ show the angular distributions corresponding to the n, α transfers and a coherent sum of these processes calculated within the CRC model, respectively. The meaning of the dotted curve Σ_0 is the same as in Fig. 5.2.1 but at E_{LAB}(^{12}C) = 12 MeV.

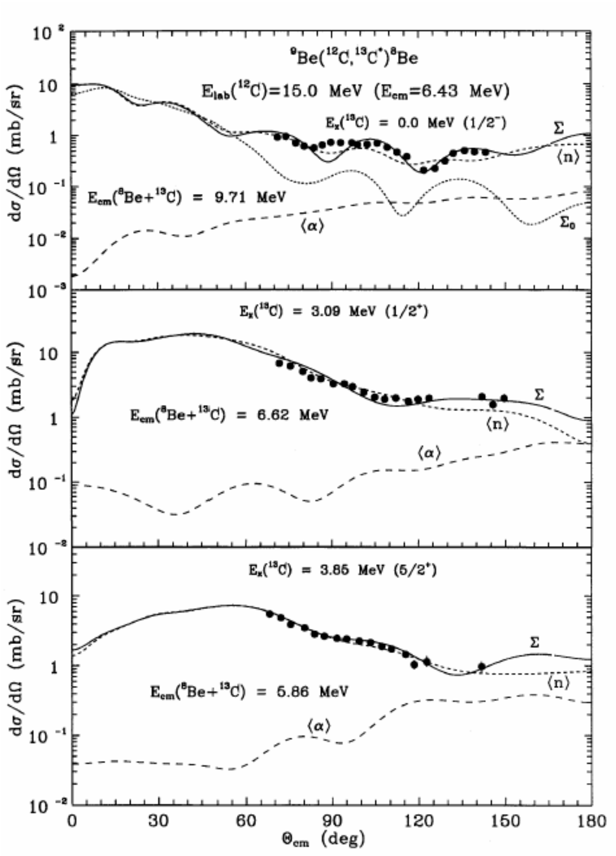

Fig. 5.2.5. The same as in Fig. 5.2.2 at the energy E_{LAB}(^{12}C) = 15 MeV [222] .

It should be noticed that the OM potentials for the interactions of the ^{8}Be and ^{13}C nuclei in their ground and excited states can differ only by their spin-dependent parts. The depth of the spin-dependent part of the OM potential for the nucleus–nucleus interaction is considerably smaller than the corresponding depth of its central part. For this reason, the values of OM potential parameters obtained for the excited states of nuclei (ignoring spin effects) in order to study the energy dependence of the ^{13}C + ^{8}Be OM potential at the corresponding relative center-of-mass energies (see Table 5.2.1) were used.

Table 5.2.1. Parameters of the Woods–Saxon optical potentials.

System	E_{CM} (MeV)	V (MeV)	r_V (fm)	a_V (fm)	W_{CRC} (MeV)	r_W (fm)	a_W (fm)	r_C (fm)	Ref.
^{9}Be+^{12}C	5.14	108.0	0.843	0.760	3.50	1.350	0.600	0.843	[4]
	6.43	115.0	0.810	0.790	3.80	1.340	0.600	0.810	[4]
	11.43	167.1	0.789	0.800	8.00	1.270	0.680	0.789	[4]
	27.86	181.4	0.789	0.760	14.50	1.250	0.680	0.789	[4]
^{8}Be+^{13}C$_{3.85}$	4.57	91.3	1.146	0.354	0.52	1.517	0.354	1.146	
^{8}Be+^{13}C$_{3.09}$	5.34	100.0	1.127	0.371	0.64	1.500	0.371	1.127	
^{8}Be+^{13}C$_{3.85}$	5.86	105.5	1.114	0.385	0.70	1.490	0.385	1.114	
^{8}Be+^{13}C$_{3.09}$	6.62	110.0	1.030	0.390	0.80	1.451	0.390	1.030	
^{8}Be+^{13}C	8.42	129.0	0.950	0.440	1.70	1.400	0.440	0.950	
^{8}Be+^{13}C	9.71	147.0	0.950	0.660	2.40	1.370	0.670	0.950	
^{8}Be+^{13}C$_{3.85}$	10.86	148.0	0.894	0.664	2.76	1.336	0.664	0.894	
^{8}Be+^{13}C$_{3.68}$	11.03	149.0	0.885	0.671	2.81	1.333	0.671	0.885	
^{8}Be+^{13}C$_{3.09}$	11.62	159.0	0.870	0.723	3.50	1.325	0.723	0.870	
^{8}Be+^{13}C	14.71	170.0	0.830	0.750	5.50	1.280	0.750	0.830	
^{8}Be+^{13}C$_{3.85}$	27.28	170.9	0.793	0.760	6.97	1.250	0.760	0.793	
^{8}Be+^{13}C$_{3.68}$	27.45	170.9	0.793	0.760	6.97	1.250	0.760	0.793	
^{8}Be+^{13}C$_{3.09}$	28.05	171.5	0.793	0.760	7.00	1.250	0.760	0.793	
^{8}Be$_{2.94}$+^{13}C	28.20	171.5	0.793	0.760	7.00	1.250	0.760	0.793	
^{8}Be+^{13}C	31.14	170.2	0.793	0.760	7.00	1.250	0.760	0.793	
^{10}B+^{11}B	18.00	169.6	0.788	0.760	10.00	1.250	0.760	0.788	

The measured ^{9}Be(^{12}C, ^{13}C)^{8}Be reaction data, together with the angular distribution of the ^{9}Be(^{12}C, ^{13}C)^{8}Be reaction at E_{LAB}(^{12}C) = 12, 15 MeV and the ^{12}C(^{9}Be, ^{8}Be)^{13}C reaction at E_{LAB}(^{9}Be) = 20 MeV [153] for the transitions to the ground states of the ^{8}Be and ^{13}C nuclei and to the 3.09 MeV, 3.85 MeV excited states of the ^{13}C nucleus were analyzed using the coupled reaction channel (CRC) model. This model employed the energy-dependent OM potential found recently in Ref. [4] for the ^{12}C + ^{9}Be channel and spectroscopic amplitudes. It was found that the *n*-transfer dominates in the ^{9}Be(^{12}C, ^{13}C)^{8}Be and ^{12}C(^{9}Be, ^{8}Be)^{13}C reactions at all energies studied. This simplified the fit of the OM potential to the ^{8}Be + ^{13}C channel experimental data. A good description of the experimental data is achieved at all energies.

The values of the OM potential parameters listed in Table 5.2.1 for the ^{13}C + ^{8}Be interaction are plotted in Fig. 5.2.7 as functions of the center-of-mass energy. The simple parametric forms of the Woods–Saxon type were chosen (see Section 3.4) to parameterize the observed energy dependence of the OM parameters. The values of the energy dependence parameters $X_i^{\min}$, $X_i^{\max}$, E_{Xi} and ΔE_{Xi} obtained from the fitting procedure are listed in Table 5.2.2. In the region of the Coulomb barrier, one may expect a fast evolution of the parameters of the nucleus–nucleus potential.

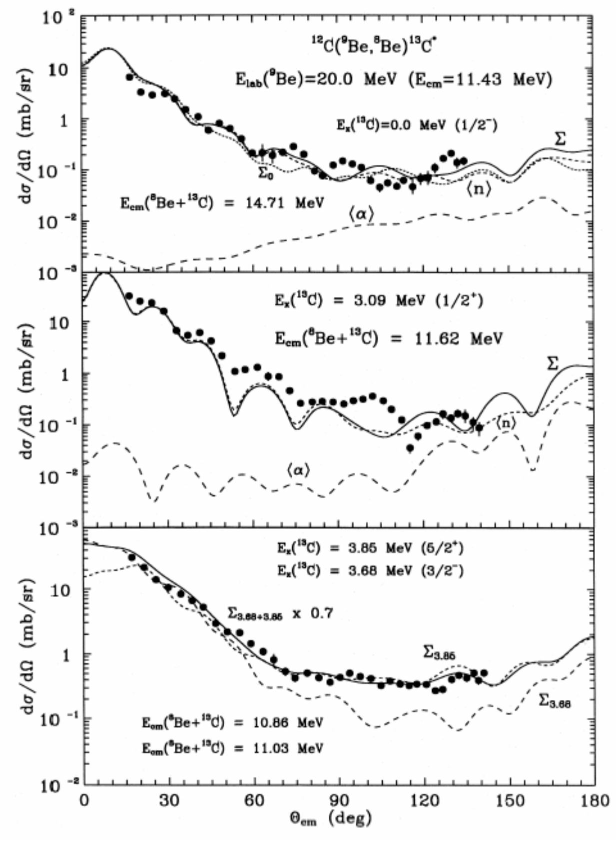

Fig. 5.2.6. Angular distributions of the ^{9}Be(^{12}C,^{8}Be)^{13}C reaction at the energy E_{LAB}(^{8}Be) = 20 MeV [153] for the transitions to the ground states of the ^{13}C and ^{8}Be nuclei upper panel and to the 3.09 MeV (1/2$^+$) and 3.68 MeV (3/2$^-$) + 3.85 MeV (5/2$^+$) excited states of the ^{13}C nucleus (middle and lower panels), respectively. The dashed curves <n>, <α> and solid curve Σ show the angular distributions corresponding to the *n*, α transfers and coherent sum of these processes calculated within the CRC model, respectively. The dashed curves $\Sigma_{3.68}$, $\Sigma_{3.85}$ and solid curve $\Sigma_{3.68+3.85}$ show the angular distributions calculated within the CRC model for the transitions to the 3.68 MeV, 3.85 MeV excited states of the ^{13}C nucleus and incoherent sum of these distributions, respectively. The meaning of the dotted curve Σ_0 is the same as in Fig. 5.1.1 but at E_{LAB}(^{12}C) = 20 MeV.

The energy dependences of the OM potential parameters for the ^{13}C + ^{8}Be and ^{12}C + ^{9}Be [4] interactions are shown in Fig. 5.2.7 using the solid and dashed curves, respectively. It can be seen that differences between the real parts *V(E)* of the OM potentials are rather small at E_{CM} < 50 MeV. The curve *V(E)* for the ^{13}C + ^{8}Be interaction shows only a smaller threshold anomaly in comparison with its counterpart for the ^{12}C + ^{9}Be interaction. This is due to the fact that $W_S(E) = W_{CRC}(E)$ for the ^{13}C + ^{8}Be OM potential is smaller than for the OM potential of ^{12}C + ^{9}Be interaction (the second panel of Fig. 5.2.7). Large differences are observed between the values of the parameters $r_V(E)$, $r_W(E)$ for the ^{13}C + ^{8}Be and ^{12}C + ^{9}Be interactions (the third panel of Fig. 5.2.7) at energies E_{CM} < 10 MeV. However, the parameters for both the systems take similar values at larger energies. Very large differences are also observed for the energy dependences of $a_V(E)$, $a_W(E)$ for the ^{13}C + ^{8}Be and ^{12}C + ^{9}Be systems at E_{CM} < 15 MeV (lower panel of Fig. 5.2.7). For the ^{12}C + ^{9}Be interaction, the functions $a_V(E)$ and $a_W(E)$ are almost constant, whereas for the $^{13}C + {}^{8}Be$ interaction these functions show a rapid variation at the energy $E_{CM} \approx 9$ MeV slightly above the Coulomb barrier energy ($E_{Coul.} = 5.59$ MeV (CM)). These differences can be explained by the different structure and the breakup threshold of the ^{8}Be and ^{9}Be nuclei.

Table 5.2.2. Energy dependence of the $^{13}C + {}^{8}Be$ optical potential parameters.

X_i	V_0 (MeV)	$W_S = W_{CRC}$ (MeV)	r_V (fm)	r_W (fm)	a_V (fm)	a_W (fm)
$X_i^{\min}$	0.00	0.00	0.793	1.250	0.37	0.37
X_i^{max}	199.38	7.00	1.300	1.620	0.76	0.76
E_{Xi}(MeV)	3.76	11.39	6.850	7.480	9.57	9.57
ΔE_{Xi}(MeV)	5.48	2.56	2.650	3.020	0.78	0.78

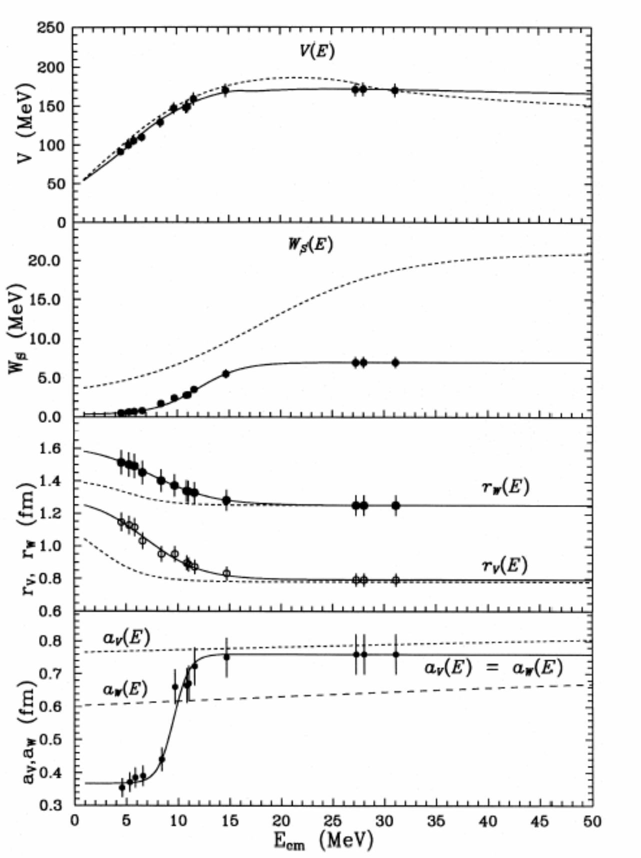

Fig. 5.2.7. Energy dependence of Woods–Saxon optical potential parameters for the $^{8}Be + {}^{13}C$ (solid curves) ($E_{Coul} = 5.59$ MeV (CM)) and $^{9}Be + {}^{12}C$ [4] (dashed curves) interactions.

The following conclusion can be made. The data were analyzed using the OM and CRC models. The one- and two-step transfer reactions as well as elastic and inelastic scattering for the transitions to the low energy excited states of ^{9}Be were included in the coupled channel scheme. It was found that the *n*-transfer dominates in the $^{9}Be(^{12}C, {}^{13}C)^{8}Be$ and $^{12}C(^{9}Be, {}^{8}Be)^{13}C$ reactions at all energies studied. This simplified the fit of the OM potential to the $^{13}C + {}^{8}Be$ channel experimental data. A regular behavior of the energy dependence of the OM potential parameters for the $^{13}C + {}^{8}Be$ interaction was found. A rapid variation of the a_V and a_W parameters was found at the energy slightly above to the Coulomb barrier ($E_{CM} = 5.59$ MeV). Energy dependences of the optical potentials for the $^{13}C + {}^{8}Be$ and $^{12}C + {}^{9}Be$ interactions were compared. Large differences were found for W_S in the whole energy range and for r_V, r_W, a_V, a_W at the energies $E_{CM} < 15$ MeV. These differences can be explained by the difference in the structure and breakup threshold for the ^{8}Be and ^{9}Be nuclei.

5.2.2. The ^{9}Be(^{12}C, ^{11}B)^{10}B reaction, one- and two-step mechanisms.

This sub-Section is devoted to the study of one- and two-step mechanisms in the $^{9}Be(^{12}C;{}^{11}B)^{10}B$ reaction at $E_{LAB}(^{12}C) = 65$ MeV(see [5]). The angular distributions of this reaction were measured for transitions to the ground and low-excited states of ^{11}B and ^{10}B. The estimated total statistical errors for each angle was lower than 10%. The data were normalized to the $^{12}C + {}^{9}Be$ elastic scattering with the experimental uncertainty smaller than 20%. The total (statistical + systematical) errors of the data were estimated to be equal about 30%. The ^{9}Be(^{12}C;^{11}B)^{10}B reaction is often an intermediate step in other processes with light exotic nuclei.

Because the lack of data for the ^{11}B + ^{10}B elastic scattering, the study of the ^{9}Be(^{12}C;^{11}B)^{10}B reaction is difficult because both the OM potential for the ^{11}B + ^{10}B channel and the reaction mechanisms must be obtained in the analysis of the reaction data. It is, however, possible in our case, because the energy-dependent OM potential for the entrance ^{12}C + ^{9}Be channel was obtained in [4]. The data of the ^{10}B + ^{10}B elastic scattering from [249] and the ^{9}Be(^{12}C;^{11}B)^{10}B reaction were included in the fitting procedure in order to obtain the energy dependence of the OM potential for the ^{10}B + ^{10}B and ^{11}B + ^{10}B interactions. The energy dependence of the OM potentials for different systems such as ^{11}B + ^{10}B, ^{12}C + ^{9}Be [4] and ^{13}C + ^{8}Be [3] are compared in this sub-Section.

The angular distributions for the ^{9}Be(^{12}C, ^{11}B)^{10}B reaction are shown in Figs. 5.2.8 and 5.2.9. All these distributions are almost symmetric around $\theta_{CM} = 90^o$. This is typical for heavy ion reactions with a small difference of the reaction product masses.

The parameters of the OM potential for the ^{12}C + ^{9}Be channel were taken from [14]. Probably, there are no published experimental data for the ^{11}B + ^{10}B elastic scattering. Therefore, the parameters of the OM potential for the ^{11}B+ ^{10}B channel were fitted using the data of the ^{9}Be(^{12}C, ^{11}B)^{10}B reaction for the transitions to the ground and excited states of the ^{10}B and ^{11}B nuclei. Due to a small kinetic energy of the ejectiles (E_{CM} = 14.5 - 18.5 MeV), the parameters of the OM potentials for different transitions are strongly energy dependent. The best results can be achieved if the data from a broad energy range are used in the analysis of the energy dependence of optical model parameters. Due to the lack of data for the ^{11}B + ^{10}B scattering, the ^{10}B + ^{10}B scattering data at E_{CM} = 4.0 – 10.5 MeV [249] (no data at other energies are published) were included into the analysis of the energy dependence. There are no reasons of considerable differences of the OM potential parameters for the ^{11}B + ^{10}B and ^{10}B + ^{10}B interactions at energies close to the Coulomb barrier. Thus, the data at E_{CM} = 4.0 - 18.5 MeV were used in the analysis of energy dependence of the OM potential parameters for the ^{11}B + ^{10}B channel.

The parameters of the OM potential for the ^{10}B + ^{10}B elastic scattering at E_{CM} = 4.0 - 10.5 MeV [4] were fitted. These parameters are given in Table 5.2.3. The OM cross-sections are shown in Fig. 5.2.11. As it can be seen, a good description of the data is achieved. It was found that the ^{10}B + ^{10}B OM cross section nearby $\theta_{CM} = 90^o$ is very sensitive to the Coulomb radius r_C, at such low energies. The best description of the ^{10}B + ^{10}B angular distributions at E_{CM} = 4.0 - 10.5 MeV were achieved for r_C = 1.33 fm. The same value was used for r_C in the ^{11}B + ^{10}B channel.

The parameters of the OM potential for the ^{13}C + ^{8}Be intermediate channel were taken from [3]. The OM potential parameters for the ^{11}C + ^{10}Be intermediate channel were assumed to be the same as for the ^{11}B + ^{10}B channel. All the potential parameters used in the CRC calculations are given in Table 5.2.3.

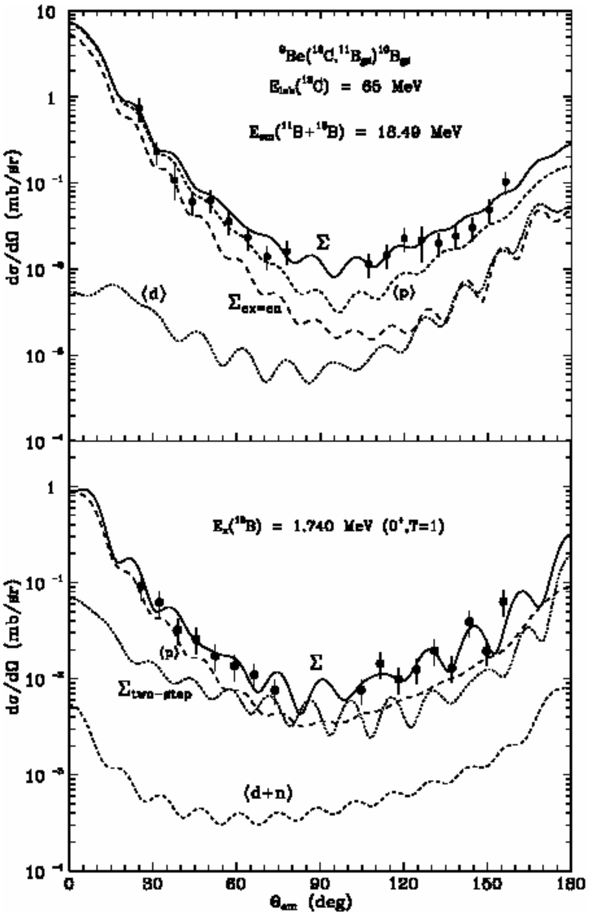

Fig. 5.2.8. Angular distributions of the ^{9}Be(^{12}C, ^{11}B)^{10}B reaction at the energy E_{LAB}(^{12}C) = 65 MeV for the transitions to the ground states of the ^{11}B and ^{10}B nuclei (upper panel) and 1.74 MeV (0^+, $T = 1$) excited state of the ^{10}B nucleus (lower panel). The dashed curves <p>, <d> and <d+n> show the CRC angular distributions for the transfers marked in brackets. The solid curve Σ shows a sum of all processes calculated with the fitted OM parameters. The long dashed line $\Sigma_{\text{ex=en}}$ represents calculations with the same OM potential parameters for the entrance and exit channel (see text). The curve $\Sigma_{\text{two-step}}$ presents a sum of all two-step processes.

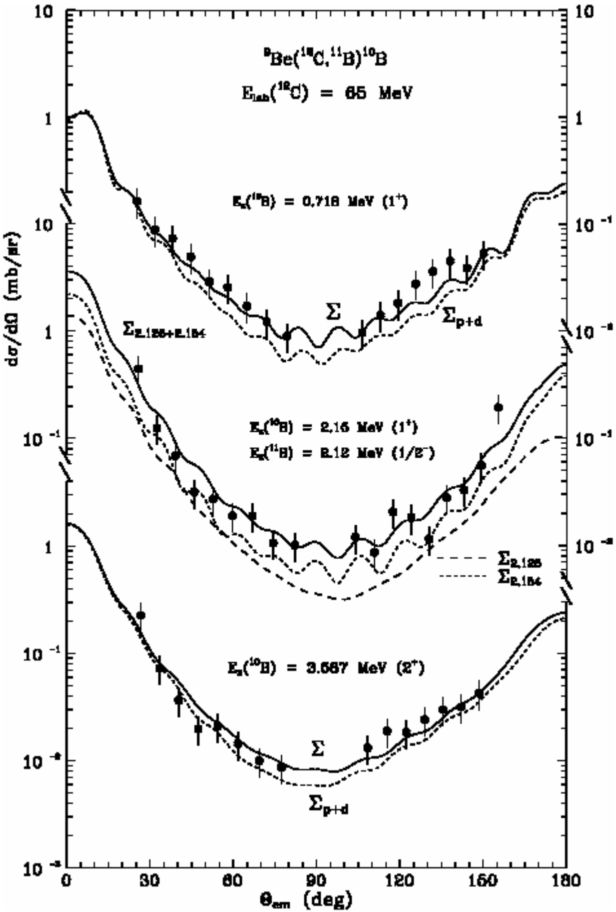

Fig. 5.2.9. Angular distributions of the ^{9}Be(^{12}C, ^{11}B)^{10}B reaction at the energy E_{LAB}(^{12}C) = 65 MeV for the transitions to the 0.718 MeV (1^+), 2.154 MeV (1^+) and 3.587 MeV (2^+) excited state of the ^{10}B nucleus and 2.125 MeV ($1/2^-$) excited state of the ^{11}B nucleus. The dashed curve $\Sigma_{\text{p+d}}$ shows the CRC angular distribution for a sum of the proton and deuteron transfers and the curves Σ, $\Sigma_{2.125}$, $\Sigma_{2.154}$ and $\Sigma_{2.125+2.154}$ show the sums of all processes for the transitions to the corresponding excited states of the ^{10}B and ^{11}B nuclei.

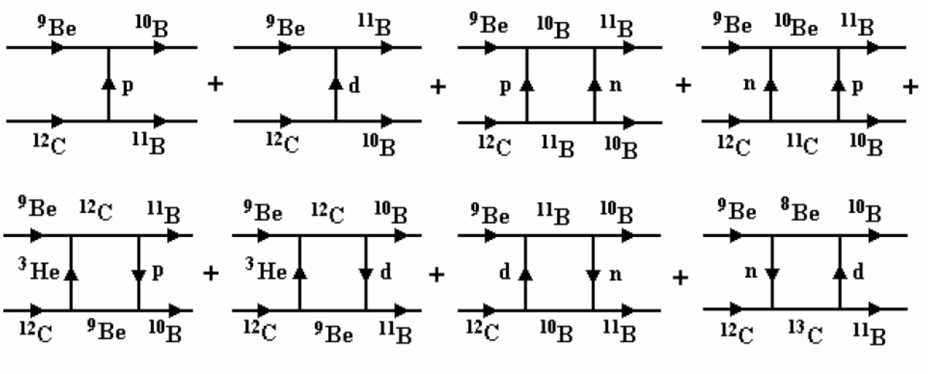

Fig. 5.2.10 Diagrams of the one- and two-step transfers for the ^{9}Be(^{12}C,^{11}B)^{10}B reaction.

The angular distributions of the ^{9}Be(^{12}C, ^{11}B)^{10}B reaction at $E_{\rm LAB}$(^{12}C) = 65 MeV were analyzed within the CRC model. The elastic and the inelastic scattering for the transitions to the low-energy excited states of the ^{9}Be nucleus, together with one- and two-step transfers corresponding to the diagrams presented in Fig. 5.2.10, were included in the coupled-channel scheme. The excited states of ^{9}Be were assumed to be rotational and deformation parameters obtained in [4] were used in the CRC calculations.

The CRC angular distributions of the ^{9}Be(^{12}C, ^{11}B)^{10}B reaction for the transitions to the ground and excited states of the ^{10}B and ^{11}B nuclei are shown in Figs. 5.2.8 and 5.2.9.

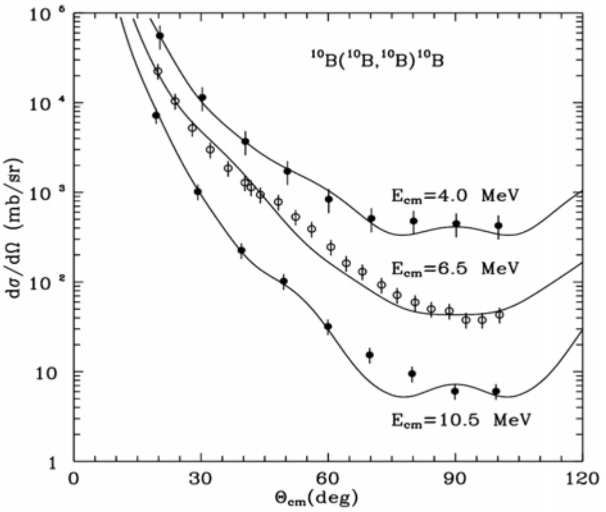

Fig. 5.2.11 Angular distributions of the ^{10}B + ^{10}B elastic scattering at the energies E_{CM} = 4, 6.5 and 10.5 MeV [249]. The solid curves show the OM angular distributions.

As a starting point of the CRC analysis, we have used the OM potential parameters of the ^{12}C + ^{9}Be entrance channel for the ^{10}B + ^{11}B exit channel as well as for the intermediate channels. In the upper panel of Fig. 5.2.8, the curve $\Sigma_{\rm ex+en}$ presents the CRC cross-section for such parameters. It is apparent that the curve $\Sigma_{\rm ex+en}$ does not describe the experimental data of the ^{9}Be(^{12}C, ^{11}B)^{10}B reaction for the transition to the ground states of the ^{10}B and ^{11}B nuclei, especially at large angles. The same phenomenon is observed also for other transitions. This was a reason to fit the scattering potential parameters for the ^{10}B + ^{11}B channel within the CRC model for each transition separately, using the ^{9}Be(^{12}C, ^{11}B)^{10}B reaction data. The potential parameters found in the fitting procedure are given in Table 5.2.3.

The CRC cross sections for the individual processes corresponding to the diagrams shown in Fig. 5.2.10 are presented in Figs. 5.2.8 and 5.2.9 as the curves marked by <name of the transferred cluster>. The curves corresponding to the coherent sums of relevant amplitudes are marked by Σ (a sum of all processes) or $\Sigma_{\rm index}$ (a sum for a few selected processes). Figure 5.2.8 (upper panel) shows that the proton transfer (curve <p>) dominates for the transition to the ground states of the ^{10}B and ^{11}B in the whole angular range. The deuteron transfer (curve <d>) gives only a small contribution to the cross section. One can see from Fig. 5.2.8 that the CRC cross section corresponding to a coherent sum of the amplitudes of all the one-step and two-step processes (curve Σ) satisfactorily describes the data of the ^{9}Be(^{12}C; ^{11}B)^{10}B reaction for the transition to the ground states of the ^{10}B and ^{11}B nuclei.

For the transition to the 1.74 MeV (0^+, T = 1) state of the ^{10}B nucleus, the deuteron transfer is forbidden due to the isospin conservation. Figure 5.2.8 (lower panel) shows that the proton transfer (curve <p>) dominates at small angles and stays also very important at large angles. The cross section corresponding to a coherent sum of all the two-step processes (curve $\Sigma_{\rm two\text{-}step}$) is important only at large angles. The CRC cross section for this transition corresponding to the sum of all processes (curve Σ) gives a good description of the data in the whole angular range.

The angular distributions for transitions to the 0.718 MeV (1^+) and 3.587 MeV (2^+) states are shown in Fig. 5.2.9 (upper and lower figures, respectively). Here, as for the transition to the ground states of ^{10}B and ^{11}B, the proton transfer dominates in the whole angular range. The curves $\Sigma_{\mathrm{p+d}}$ present the CRC cross section for the sum of the proton and deuteron transfers. The two-step processes are important only nearby $\theta_{\mathrm{CM}} = 90^{\mathrm{o}}$, as one can see by comparing the sum of all the processes (curves Σ) with the sum of one-step processes (curves $\Sigma_{\mathrm{p+d}}$).

The angular distribution for the transitions to the 2.125 MeV ($1/2^-$) state of the ^{11}B and to the 2.154 MeV (1^+) state of the ^{10}B nucleus, unresolved in the experiment, is shown in the central part of Fig. 5.2.9. The dashed curves $\Sigma_{2.125}$ and $\Sigma_{2.154}$ represent the CRC cross sections for relevant transitions corresponding to the coherent sum of amplitudes of all the one-step and two-step processes. As it can be seen from Fig. 5.2.9 the cross-sections for these two transitions differ only slightly. Their incoherent sum (curve $\Sigma_{2.125+2.154}$) well describes the experimental data.

Table 5.2.3 Parameters of Woods–Saxon optical potentials.

System	E_{CM} (MeV)	V (MeV)	r_V (fm)	a_V (fm)	W_{CRC} (MeV)	r_W (fm)	a_W (fm)	r_{C} (fm)	Ref.
^{9}Be + ^{12}C	27.86	181.4	0.789	0.760	14.500	1.250	0.680	0.789	[4]
^{10}B + ^{11}B	18.49	148.4	0.787	0.770	4.000	1.250	0.551	1.330	
^{10}B$_{0.72}$ + ^{11}B	17.78	145.9	0.840	0.788	2.900	1.257	0.560	1.330	
^{10}B$_{1.74}$ + ^{11}B	16.75	141.5	0.832	0.770	2.400	1.250	0.540	1.330	
^{10}B + ^{11}B$_{2.12}$	16.33	138.5	0.792	0.740	2.500	1.377	0.540	1.330	
^{10}B$_{2.15}$ + ^{11}B	16.33	138.5	0.792	0.740	2.500	1.377	0.540	1.330	
^{10}B$_{3.59}$ + ^{11}B	14.50	131.4	0.828	0.744	2.000	1.415	0.519	1.330	
^{10}Be + ^{11}C	15.95	136.7	0.813	0.754	2.200	1.354	0.536	1.330	
^{8}Be + ^{13}C	31.14	170.2	0.793	0.760	7.000	1.250	0.760	0.793	[3]
^{10}B + ^{10}B	4.00	60.7	1.228	0.484	0.015	1.767	0.267	1.330	
	6.50	80.0	0.982	0.500	0.295	1.780	0.261	1.330	
	10.50	108.7	0.848	0.621	1.930	1.782	0.320	1.330	

The optical potential energy dependence parameters X_i^{min}, X_i^{max}, E_{Xi} and ΔE_{Xi}, obtained using the fitting procedure for the OM potential of the ^{10,11}B + ^{10}B interactions, are listed in Table 5.2.4. The functional dependences of $X_i(E)$ are shown in Fig. 5.2.12. The OM parameters obtained by the fitting procedures are located in the low-energy part of the threshold anomaly and they strongly depend on energy. In spite of a small number of the experimental points, the curves shown in Fig. 5.2.12 can be considered as a first prediction for the energy dependence of the ^{10}B + ^{10}B and ^{11}B + ^{10}B interactions.

Table 5.2.4 Energy dependence of the ^{10}B + ^{11}B and ^{10}B + ^{10}B OM potential parameters.

X_i	V_0 (MeV)	W_S(^{10}B+^{10}B) (MeV)	W_{CRC}(^{10}B+^{11}B) (MeV)	r_V (fm)	r_W (fm)	a_V (fm)	a_W (fm)
X_i^{min}	0.0	0.0	0.0	0.807	1.220	0.47	0.26
X_i^{max}	179.9	9.2	10.4	1.420	1.785	0.78	0.56
E_{Xi}(MeV)	4.9	15.2	20.4	5.000	14.345	10.69	12.39
ΔE_{Xi}(MeV)	6.9	3.2	3.4	2.400	1.364	2.16	1.34

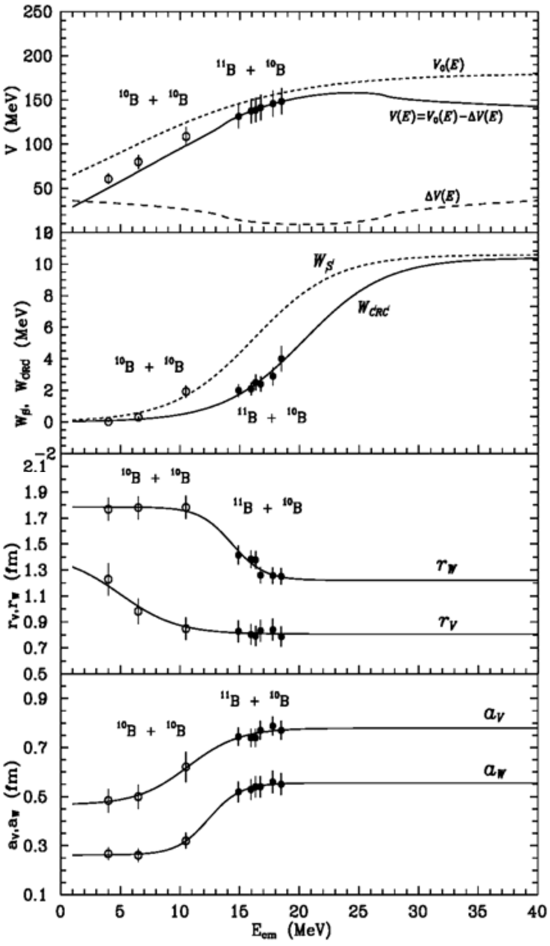

Fig. 5.2.12. Energy dependence of the OM potential parameters for the ^{10,11}B+ ^{10}B interactions (E_{Coul} = 5.80 MeV (CM) for ^{10}B+ ^{10}B and E_{Coul} = 5.71 MeV (CM) for ^{11}B+ ^{10}B).

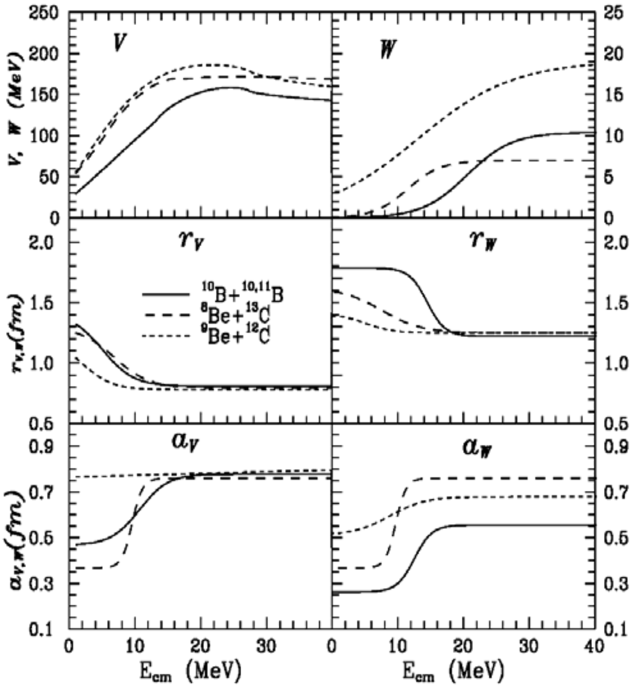

Fig. 5.2.13. A comparison of the energy dependence of the OM potential parameters for the ^{10,11}B+^{10}B (solid curves), ^{8}Be + ^{13}C (long-dashed curves) and ^{9}Be + ^{12}C (short-dashed curves) interactions.

There is a possibility to compare the energy dependence of the OM potential parameters for the ^{12}C + ^{9}Be [4] and ^{13}C + ^{8}Be [3] channels with the prediction for the ^{10,11}B + ^{10}B channel described in present sub-Section. The corresponding curves are shown in Fig. 5.2.13. One can see significant differences for the depth W_S and for the diffuseness a_W of the imaginary part of the OM potentials. The other parameters differ only in the threshold-anomaly region. Then, we tried to reduce the difference between W_S for the ^{12}C + ^{9}Be, ^{13}C + ^{8}Be and ^{10,11}B + ^{10}B channels by modification of a_W, using the correlation between W_S and a_W. Some increase of W_S for the ^{13}C + ^{8}Be channel is possible but it gives somewhat poorer description of the angular distributions. This suggests that the energy dependence of the OM potential parameters is correlated with the structure of a nucleus.

Then, a following conclusion can be made. The obtained experimental data were analyzed using the CRC model with the coupled-channel scheme including the elastic and inelastic scattering, as well as the one-step and two-step transfer reaction channels. It was found that the one-step processes dominate in the ^{9}Be(^{12}C, ^{11}B)^{10}B reaction. The two-step processes are important only in the angular region near θ_{CM} = 90^{o} and at large angles for the transitions to the 1.74 MeV (0^{+}, T = 1) excited states of the ^{10}B nucleus.

From the present analysis of the experimental data of the ^{9}Be(^{12}C, ^{11}B)^{10}B reaction one can conclude that if a few nucleon transfer reactions are used to obtain the OM potential parameters for the exit channels, the one- and two-step processes must be included in the coupled channel scheme.

5.3. The ^{7}Li, ^{12}C(^{14}N, $^{13,\,15}$N) reactions.

The ^{7}Li(^{14}N,^{15}N) ^{6}Li reaction and the ALAS phenomenon.

This sub-Section is devoted to study of the backward angle enhancement in the nucleus–nucleus elastic scattering, the so called anomalous large-angle scattering (ALAS). The investigation of the reaction ^{7}Li(^{14}N, ^{15}N)^{6}Li at $E_{\rm LAB}$(^{14}N) =110 MeV was done since the final state of this reaction is an intermediate channel in some two-step cluster-exchange mechanisms leading to the elastic scattering. This reaction was investigated in order to explain ALAS, discussed already in sub-Section 4.3.1.

The results of Ref. [7] are presented in this sub-Section. The angular distributions of the reactions ^{7}Li(^{14}N, X) were measured at E_{LAB} = 110 MeV using the ^{14}N ion beam. The angular distribution of the reaction ^{7}Li(^{14}N, ^{15}N)^{6}Li was obtained simultaneously at the same energy. The results are shown in Fig. 5.3.2.

The experimental data of the reactions ^{7}Li(^{14}N, X) were analyzed within the CRC method. The elastic and inelastic scattering and the reorientation of ^{7}Li and ^{14}N were included in the coupling channel scheme. The deformation length parameters, δ_2 of ^{7}Li and δ_1, δ_2, δ_3 of ^{14}N, were used to describe the deformation of the optical potential. These parameters and the depth $W_{\rm S}$ of the imaginary part of the OM potential, obtained in the analysis of elastic scattering within optical model, were fitted to describe the elastic and inelastic scattering ^{14}N + ^{7}Li in the CRC method. The main effect of the explicit channel coupling relies on a reduction of the imaginary potential. The depth of the imaginary optical potential used in the CRC analysis will be denoted below as $W_{\rm CRC}$. The optical potential parameters V , $r_{\rm V}$, $a_{\rm V}$, $W_{\rm S}$, $W_{\rm CRC}$, $r_{\rm W}$, $a_{\rm W}$, $r_{\rm C}$ and the deformation parameters δ_λ (universal for all the states) used in the final CRC calculations are already listed in sub-Section 4.3.1.

In the analysis of the exit reaction channels, the corresponding transfer channels were added to the coupling scheme mentioned above (see Fig. 5.3.1). The cross sections for the one- and two-step processes, corresponding to the diagrams already shown in sub-Section 4.3.1, were calculated in order to estimate their contributions to the elastic and inelastic scattering and to the reaction ^{7}Li(^{14}N, ^{15}N)^{6}Li. Both the standard (d, t, ^{3}He, α) and exotic (^{4,5,6}Li, ^{6,7,8}Be) clusters were included in the present calculations.

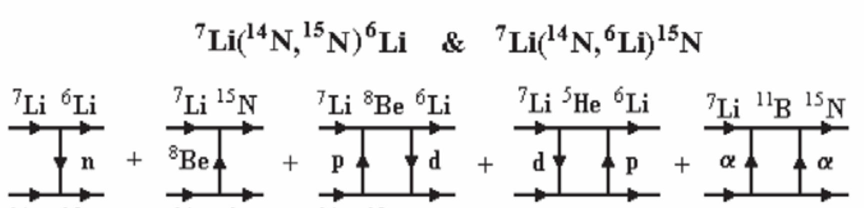

Fig. 5.3.1. Diagrams of the one- and two-step processes for the ^{7}Li(^{14}N, ^{15}N)^{6}Li and ^{7}Li(^{14}N, ^{6}Li)^{15}N reactions included in the present analysis. Diagrams of the one- and two-step processes for the elastic and inelastic scattering of ^{7}Li(^{14}N, ^{14}N)^{7}Li and ^{7}Li(^{14}N, ^{7}Li)^{14}N are shown in Fig. 4.3.4.

The experimental angular distribution of the reaction ^{7}Li(^{14}N, ^{15}N)^{6}Li at E_{LAB}(^{14}N) = 110 MeV is presented in Fig. 5.3.2. One can see an enhancement of the cross section at backward angles. As in the case of the elastic scattering, we have calculated the CRC angular distributions for several one- and two-step transfers which lead to the final channel of this reaction. The diagrams corresponding to these transfers are shown in the bottom of Fig. 5.3.1. According to our knowledge, there are no experimental data for the elastic scattering ^{15}N + ^{6}Li. Therefore, it is not possible to obtain the OM parameters for the channel ^{6}Li + ^{15}N, using our standard method. In this situation, we applied the OM parameters predicted by the energy dependence for the elastic scattering ^{6,7}Li + ^{14}N, In the CRC calculation only the parameter W_{CRC} for the channel ^{15}N + ^{6}Li was fitted. It was found that W_{CRC} (^{15}N + ^{6}Li) = 9 MeV allows to describe well the angular distribution for the ^{7}Li(^{14}N, ^{15}N)^{6}Li.

The CRC angular distributions for the one- and two-step transfers corresponding to the diagrams in Fig. 5.3.1, obtained with the parameters described already in sub-Section 4.3.1 are shown in Fig. 5.3.2. One can see that the cross sections for transfers of the ^{8}Be-cluster (curve <^{8}Be>) and for the sequential transfer of two alpha particles (curve <$\alpha\alpha$>) are a few orders of magnitude smaller than the experimental data. The neutron transfer (curve <n>) in the reaction ^{7}Li(^{14}N, ^{15}N)^{6}Li at E_{LAB}(^{14}N) = 110 MeV is the dominant process in the whole angular range.

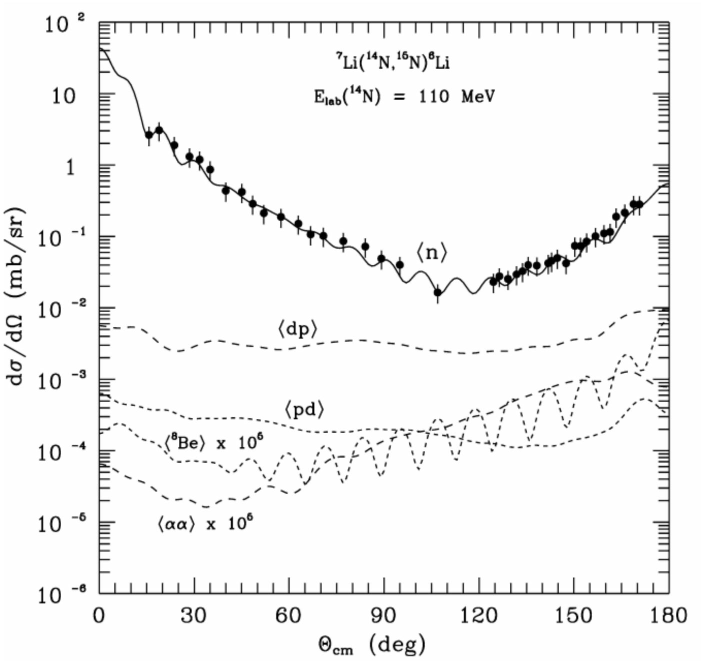

Fig. 5.3.2. Angular distribution of the reaction ^{7}Li(^{14}N, ^{15}N)^{6}Li at E_{LAB}(^{14}N) = 110 MeV. The curves show the CRC angular distributions for the transfers of neutron (curve <n>), ^{8}Be-cluster (<^{8}Be>) and the sequential transfers α + α (<$\alpha\alpha$>), p + d (<pd>) and d + p (<dp>), corresponding to the diagrams shown in Fig. 5.3.1.

It has been found that one- and two-step transfers of the standard (d, t, ^{3}He, α) and exotic (^{4,5,6}Li, ^{6,7,8}Be) clusters, which usually lead to an enhancement of the cross section, give a negligible contribution to the elastic scattering ^{7}Li + ^{14}N. The results of complete analysis of the data of the elastic scattering ^{7}Li + ^{14}N lead to the conclusion that it is the reorientation of ^{7}Li with its large quadruple deformation which provides the observed ALAS.

In distinction to other cases known from the literature, the deformation parameters of ^{7}Li and ^{14}N could be precisely estimated in the CRC analysis of both the elastic and inelastic scattering ^{7}Li + ^{14}N. The deformation parameter of ^{7}Li obtained from the backward-angle elastic scattering turned out to be identical to that obtained from the analysis of inelastic channels. Using different theoretical approaches in the analysis of the inelastic scattering ^{7}Li + ^{14}N at E_{LAB}(^{14}N) = 110 MeV for the transitions to the low-energy excited states of ^{7}Li and ^{14}N, we have found that the cluster-exchange processes play here a negligible role and that the experimental data are well described by the CRC cross sections for the transitions to the collective (rotational) states of these nuclei. The observed anomalous large-angle inelastic scattering can be explained by the weak absorption and strong channel coupling.

It was found that the experimental angular distribution of the reaction ^{7}Li(^{14}N, ^{15}N)^{6}Li at E_{LAB}(^{14}N) = 110 MeV is dominated by the neutron transfer. The heavy-cluster transfer of ^{8}Be and the two-step transfers were found to be completely negligible for this reaction.

5.4. The ^{14}C(^{6}Li, ^{6}He) and ^{12}C(^{7}Li, ^{7}Be) charge exchange reactions.

5.4.1. The ^{14}C(^{6}Li, ^{6}He)^{14}N reaction (direct charge-exchange versus sequential nucleon transfers).

The ^{14}C(^{6}Li, ^{6}He)^{14}N reaction, investigated at the ^{6}Li ion energy of 93 MeV is described in this sub-Section (see [2]). The angular distributions for several natural and unnatural parity states of the ^{14}N nucleus were compared with the DWBA and the CRC calculations, assuming direct the charge exchange and two-step sequential nucleon transfers.

After the first investigations of the (^{6}Li, ^{6}He) reaction [227 228], many experimental studies have shown that the direct charge-exchange mechanism dominates at ^{6}Li energies of 30 – 50 MeV, and that its contribution increases with increasing beam energy [229 – 237]. Thus for a good description of the (^{6}Li, ^{6}He) reaction, a contribution of the two-step processes connected with the sequential one-nucleon transfers must be taken into account in the theoretical calculations because in some cases, the cross sections for these processes can be comparable to the cross section of the one-step charge-exchange processes. This problem has not been studied enough in the literature. The necessity of including the sequential one-step pickup/stripping in the description of the (^{6}Li, ^{6}He) reaction was pointed out in the past [231 – 233], but no detailed calculations were made.

The experimental angular distributions for transitions to the ground and excited states of the ^{14}N nucleus measured in the angular range of 7° - 26° in the *LAB* system are shown in Figs. 5.4.1a and 5.64.1b. The angular distributions corresponding to the 5.1 MeV and 5.7 MeV excitation energies shown in Fig. 5.4.1b include the sum of the unresolved states $J^{\pi} = (0^{-}, 2^{-})$ and $J^{\pi} = (1^{-}, 3^{-})$, respectively. It is visible from Fig. 5.4.1a that the angular distributions for the 0^{+} transition is out of phase in comparison with both 1^{+} transitions. This is consistent with the fact that 1^{+} states are excited mainly in the one-step mechanism and the transition to the 0^{+} state proceeds through the two-step mechanism. In accordance with the selection rules for the two-step process of a sequential nucleon transfer, the $0^{+} \rightarrow 0^{+}$ transition is characterized by a transferred angular momentum of $l = 0$, whereas in the case of direct charge-exchange mechanism, the transition to the 1^{+} states proceeds through the $l = 0$ and $l = 2$ transfers. The role of the two-step mechanism in the excitation of the 1^{+} states can be roughly estimated by the cross section ratio of the 0^{+} to 1^{+} transitions. These ratios are equal to ~ 1/8 and to ~1/40 for the ground and the 3.95 MeV states, respectively.

The best fit potentials taken from [238] are given in Table 5.4.1 (sets A and B). I_V and I_W are the real and imaginary volume integrals per interacting nucleon, respectively. The OM cross sections for the potential A, together with the experimental data at 93 MeV [238], are shown in Fig. 5.4.2 (dashed line). The theoretical cross sections strongly underestimate the experimental data at the maxima corresponding to the angles of 25° and 35°. This was the reason to search for another potential, which would give a better description at small angles.

The investigation of the elastic scattering data [238] was done using the OM model. The parameters of the potential found in the present work are given in Table 5.4.1

(set C). The radius and the diffuseness of this potential are close to those for the potential B. However, its real part is considerably deeper. The calculations with the potential C reproduce the data rather well, both in the region of small and large angles. We have used this potential in the DWBA and CRC analyses. However, to satisfactorily describe the elastic scattering data [238] in the CRC analysis we had to decrease the value of the depth W by 3.7 MeV (see Table 5.4.2).

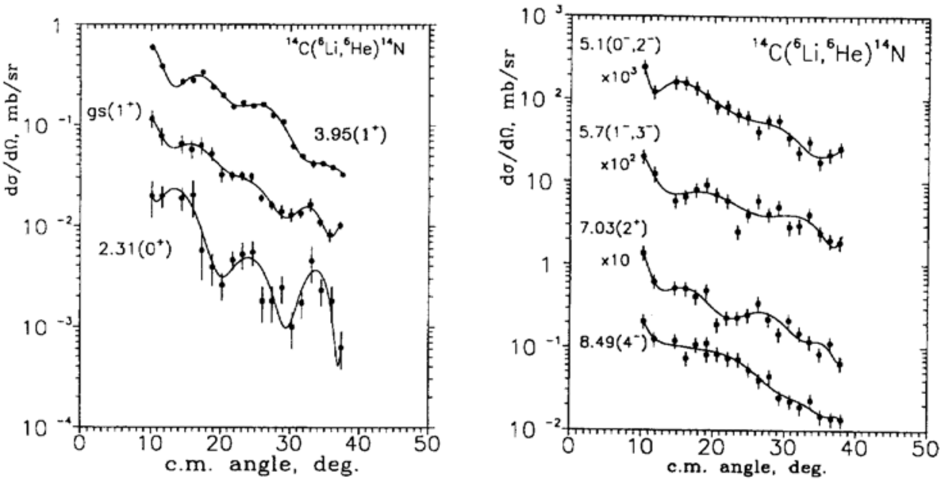

Fig. 5.4.1. (a) Angular distributions of the $^{14}C(^6Li, ^6He)^{14}N$ reaction at 93 MeV for the first three states of ^{14}N: gs ($J^\pi = 1^+$), $E_x = 2.31$ MeV ($J^\pi = 0^+$, $T = 1$) and $E_x = 3.95$ MeV ($J^\pi = 1^+$). The curves were obtained by a polynomial fit of the 10th order to the experimental data. (b) The same as in (a) but for states at $E_x = 4.92 - 5.11$ MeV ($J^\pi = 0^-, 2^-$), $E_x = 5.69 - 5.83$ MeV ($J^\pi = 1^-, 3^-$), $E_x = 7.03$ MeV ($J^\pi = 2^+$) and $E_x = 8.49$ MeV ($J^\pi = 4^-$).

Table 5.4.1. The Woods-Saxon optical model parameters for $^{14}C + {}^6Li$ used in the DWBA analysis.

Set	V_0 MeV	r_V fm	a_V fm	W_0 MeV	r_W fm	a_W fm	r_C fm	I_V MeVfm^3	I_W MeVfm^3	χ^2/N
A	254.0	0.580	0.787	67.0	0.666	1.043	0.741	378.16	177.08	13.9
B	134.5	0.799	0.634	83.7	0.687	0.925	0.741	348.35	205.48	18.8
C	160.6	0.803	0.657	61.7	0.803	0.924	0.803	429.13	208.72	16.6

Table 5.4.2. The Woods-Saxon optical model parameters for A + a used in the CRC analysis.

A+a	V_0 MeV	r_V fm	a_V fm	W_0 MeV	r_W fm	a_W fm	r_C fm
$^{14}C+^6Li$	160.6	0.803	0.657	58.0	0.803	0.924	0.803
$^{13}C+^7Li$	160.6	0.800	0.614	61.7	0.800	0.833	0.800
$^{15}N+^5He$	160.6	0.812	0.657	61.7	0.812	0.924	0.812
$^{14}N+^6He$	160.6	0.803	0.657	61.7	0.803	0.924	0.803

The potentials for the intermediate channels $^7Li + {}^{13}C$ in the np-transfer and for $^5He + {}^{15}N$ in the pn-transfer were chosen as follows. The OM potential for the $^5He + {}^{15}N$ interaction was taken to be the same as for the $^6Li + {}^{14}C$ channel, except for the parameters r_V, r_W and r_C, which were excluded from the fitting procedure. The radii of the potential in the $^7Li + {}^{13}C$ channel were treated in the same way. The parameters V and W for this channel were taken to be the same as for the $^6Li + {}^{14}C$ channel. The diffuseness parameters for the $^7Li + {}^{13}C$ and $^6Li + {}^{14}C$ channels were fitted using the experimental data for $^{7}Li + ^{13}C$ scattering at $E(^{7}Li) = 34$ MeV [239]. The parameters of the OM potentials are presented in Table 5.4.2. The agreement of the calculated and experimental cross sections is rather good as it can be seen from Fig. 5.4.2.

The direct charge-exchange process was calculated in the framework of the DWBA method using an effective NN-interaction which included the spin-isospin central and tensor forces [2].

The differential cross sections for the direct charge-exchange process were calculated in the zero-range approximation using the DWUCK4 code [126]. The projectile size and exchange effects were neglected in these calculations. The OM potential C from Table 5.4.1 was used for the entrance and exit channels. The bound state wave functions of valence nucleons in the ^{14}C and ^{14}N nuclei were calculated using the Saxon-Woods potential ($r_0 = 1.25$ fm, a = 0.65 fm) with the depth of the potential fitted according to the binding energies. The angular distributions were calculated for following most intense transitions to the unnatural parity states of the ^{14}N nucleus: 1^{+} (ground and 3.95 MeV states), 2^{-} (5.1 MeV) and 4^{-} (8.49 MeV).

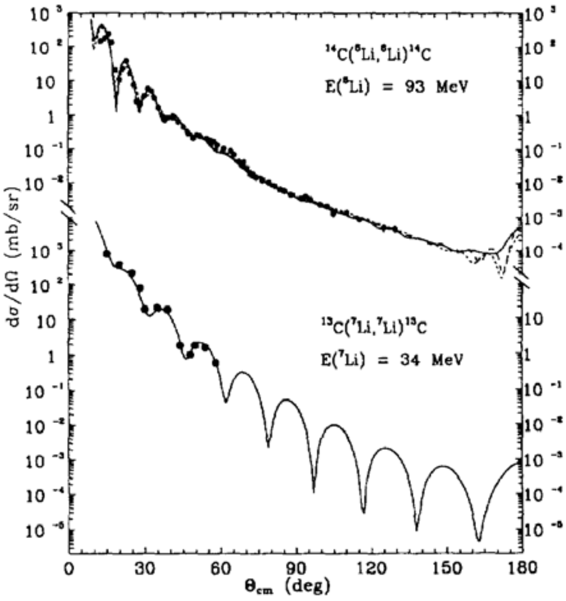

Fig. 5.4.2. Optical model fits for the ^{6}Li elastic scatering on ^{14}C at 93 MeV and ^{7}Li elastic scattering at 34 MeV on ^{13}C. The dashed and solid lines for ^{6}Li scattering correspond to the potentials A and C from Table 5.4.1, respectively. The solid line for ^{7}Li scattering shows elastic scattering calculated with the potential C from Table 5.4.2. The experimental data were taken from [238, 239].

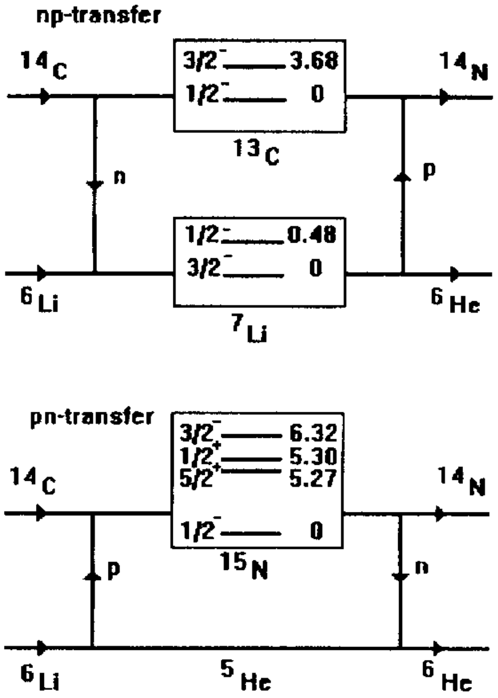

Fig. 5.4.3. Diagrams of two-step sequential one-nucleon *np*- and *pn*-transfers for the $^{14}C(^{6}Li, ^{6}He)^{14}N$ reaction.

Since the cross sections for the charge-exchange processes are typically smaller than the transfer reaction cross sections, it is possible that in some cases the two-step transfer mechanism, leading to the same final nuclei as the charge-exchange reaction, will be dominant. There are many two-step processes and the one-nucleon sequential transfer reaction can be the most important. The cross section for such a mechanism can be calculated in the second-order DWBA.

The consideration about the two-step sequential one-nucleon transfer, presented in this Section, are restricted only to the reactions $^{14}C(^{6}Li, ^{7}Li)^{13}C(^{7}Li, ^{6}He)^{14}N$ and $^{14}C(^{6}Li,$

^{5}He)^{15}N(^{5}He, ^{6}He)^{14}N. These reactions are presented in Fig. 5.4.3. Not only the ground states, but also the excited states of the ^{13}C, ^{15}N and ^{7}Li intermediate nuclei were included in the analysis.

The two-step sequential transfers were calculated in the framework of the CRC with the optical model parameters from Table 5.4.2. The spectroscopic amplitudes for the transitions within the 1p-shell were calculated and presented in Appendix.

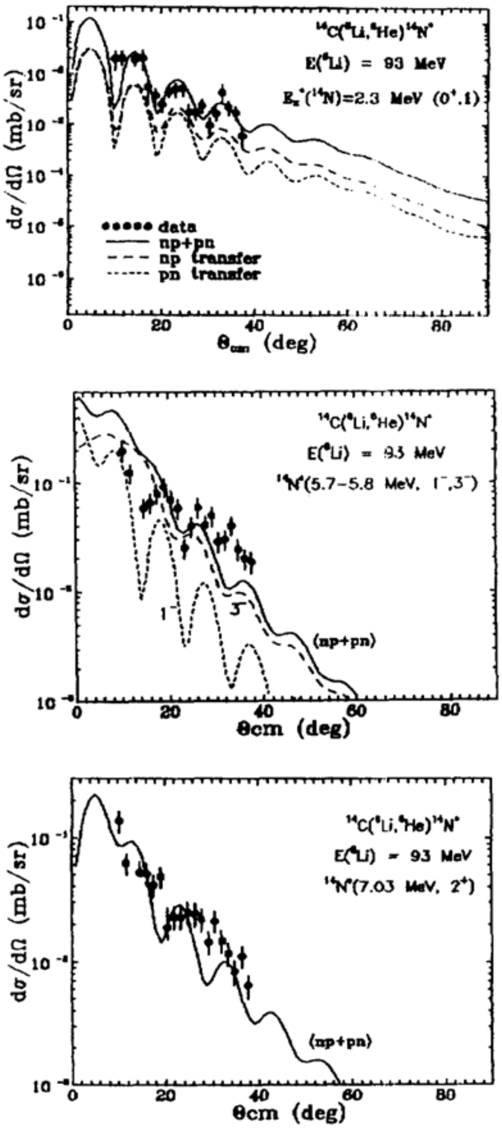

Fig. 5.4.4. Angular distributions for the ^{14}C(^{6}Li, ^{6}Li)^{14}N reaction leading to the states of ^{14}N at E_x = 2.31 MeV (J^π = 0$^+$, T = 1), E_x = 5.69 − 5.83 MeV (J^π = 1$^-$, 3$^-$) and E_x = 7.03 MeV (J^π = 2$^+$). The solid curves represent results of calculations for two-step sequential one-nucleon transfers. The short dashed and long dashes curves for the 0$^+$ transitions correspond to the calculations of pn- and np-transfers. The short dashed and long dashed curves describe contributions for 1$^-$ and 3$^-$ levels, respectively.

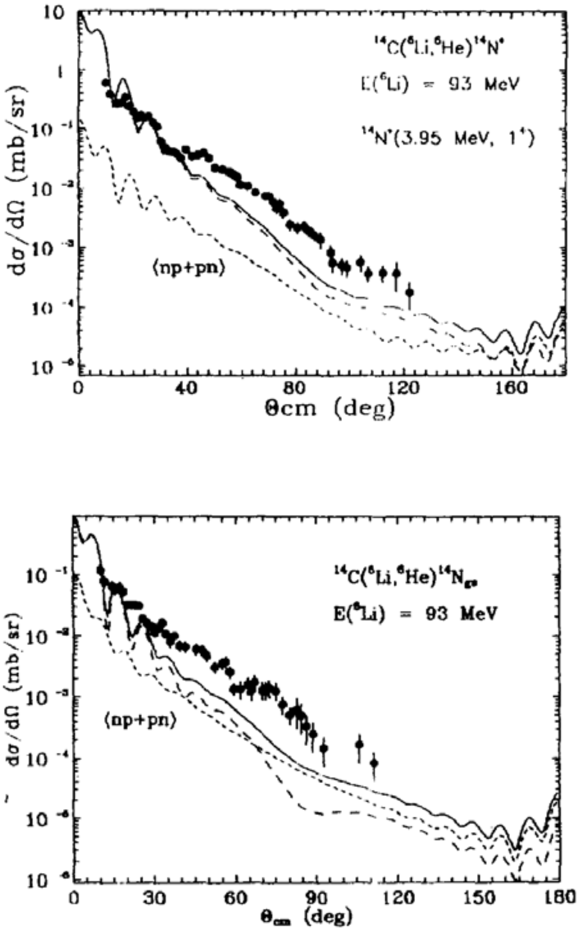

Fig. 5.4.5. Angular distributions for the ^{14}C(^{6}Li, ^{6}He)^{14}N reaction for transitions to the 1$^+$ states of ^{14}N. The short dashed lines represent two-step transfer contributions. The long dashed lines correspond to the direct charge-exchange contributions with $V^c_{\sigma\tau} = V^t_\tau$ = 3.7 MeV. The solid line is an incoherent sum of both processes. The $V^c_{\sigma\tau}$ and V^t_τ parameters are strengths of the central spin-isospin and the tensor interaction, respectively [2].

The prior- and post-interactions were used for the first and second steps of sequential transfers, respectively. The one-particle bound-state wave functions were calculated using the standard procedure by fitting the depth of Woods-Saxon potential to obtain the nucleon binding energy. The geometrical parameters of the bound state potentials were fixed at a = 0.65 fm and $r = r_0A^{1/3}/(A_C^{1/3}+1)$ fm, where A and A_C are the masses of the composite system and the core, respectively and $r_0 = 1.25$ fm.

Figure 5.4.4 shows the angular distributions calculated under the assumption of a two-step mechanism for the sequential nucleon transfers, which are compared with the experimental data for the above mentioned transitions. A coherent sum for the sequential *np*- and *pn*-transfers gives an excellent description of the magnitude and shape of the experimental angular distribution for excitation of the 0^+ ($T = 1$) state (see Fig. 5.6.4a), without an extra normalization factor for the theoretical cross section. The absolute cross sections for the 1^-, 3^- states (Fig. 5.4.4b) are also well reproduced. However, in the case of 2^+ state (Fig. 5.4.4c), the calculated angular distribution was increased by the extra factor of 2 to fit the experimental data. The disagreement between theory and experiment in this case can be caused by our insufficient knowledge of the 2^+ state wave function.

A good description of the experimental angular distributions for the natural parity states (0^+, 1^-, 3^-, 2^+) supports validity of the reaction model. This allows us to use the same parameters (OM potentials, spectroscopic amplitudes) in the calculations of the two-step transfer contributions in excitation of the unnatural parity states (1^+, 2^-, 4^-). The results of these calculations are shown in Figs. 5.4.5 and 5.4.6. As one sees in Fig. 5.4.5 for the 1^+ transitions, the two-step mechanism accounts only for a small fraction of the experimental cross sections: about 15% for the ground state and less than 10% for the excited state. In contrast, the contribution of two-step mechanism is significant for the 2^- and 4^- states (≈ 50% and ≈ 70%, respectively) (Fig. 5.4.6).

The calculated differential cross sections for the direct charge-exchange mechanism in the case of the transitions to 1^+ state (long dashed lines) are compared with experiment in Fig. 5.4.5. The similar experimental angular distributions for the both 1^+ states, together with the discussion above gives the evidence for a large tensor force contribution. A similar observation was already made in the work of Winfield et al. [237] for 35 MeV/n energy in the angular range $0^o - 12.5^o$. Figure 5.4.6 shows the calculated cross sections for the other unnatural parity states ($J^\pi = 2^-$, 4^-). It is visible that the coherent sum of the direct and two-step transfer mechanisms describes quite well the experimental cross sections (solid lines), without any extra renormalization of the theoretical cross sections.

As it can be seen from Fig. 5.4.5, the angular distribution obtained within the direct charge-exchange mechanism well describe the experimental data at relatively small angles (up to 40^o). For larger angles, the theoretical cross sections are approximately one third of the experimental ones. The same result was also obtained in the previous analysis of the (^{6}Li, ^{6}He) reaction, in which the calculations were made using another optical potential and a somewhat different form of the effective interactions [238].

It should be noticed that the difficulty in the description of the cross sections at large angles is not only a feature of the (^{6}Li, ^{6}He) reaction. Similar difficulties were found in the other charge-exchange reactions, particularly in (^{3}He,*t*), (*p,n*) and in the inelastic proton scattering $^{14}N(p,p')^{14}N$ for the transition to the 2.31 MeV ($T = 1$) state. The latter process is analogous to the $^{14}C(p,n)^{14}N_{g.s.}$ reaction.

Then, a following conclusion can be made.

1). The two-step transfer mechanism well reproduces the experimental cross sections for the states of natural parity (0^+ (E_x = 2.31 MeV, T = 1), 1^-,3^- (E_x = 5.69 – 5.83 MeV) and 2^+ (E_x = 7.03 MeV)) of the ^{14}N nucleus.

2). The direct charge-exchange mechanism dominates in transitions to the ground and excited (E_x = 3.95 MeV) 1^+ states. The two-step transfer mechanism is responsible only for ~ 15% and less than 10% of the experimental cross sections, respectively.

3). For transitions to the other unnatural parity states (2^-, 4^-) the two-step mechanism is more important. Its contributions are about 50% and 70%, respectively.

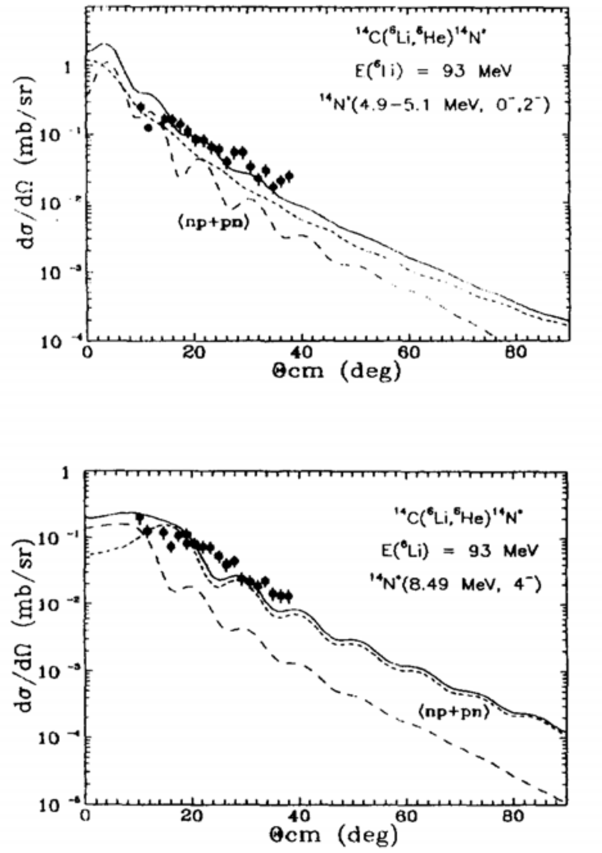

Fig. 5.4.6. The same as in Fig. 5.4.5 but for transitions to the 2^- and 4^- states in ^{14}N.

5.4.2. The ^{12}C(^{7}Li, ^{7}Be)^{12}B reaction (direct charge-exchange versus sequential nucleon transfers)

The measurements of the angular distributions for transitions to the ground and excited states of ^{12}B from the ^{12}C(^{7}Li, ^{7}Be)^{12}B reaction at 82 MeV are described in this sub-Section (see [14]). The data were analyzed in the framework of the DWBA for the direct charge-exchange processes and in the framework of the CRC method for the two-step sequential nucleon transfers. It was shown that the two-step sequential nucleon transfer is dominant mechanism in the investigated angular range and that the direct mechanism becomes important only for small angles ($\theta_{\mathrm{CM}} < 10^{\mathrm{o}}$). The problem of the direct charge-exchange versus the two-step-sequential transfer reactions was already discussed in the previous sub-Section 5.4.1.

Up to now, the ratio of one- and two-step mechanisms in the ^{12}C + ^{7}Li reaction was directly estimated in Ref. [241] only. This work does not allow to answer the questions about the dominance of direct processes.

An example of the measured spectrum at 2.5^{o} for the ^{12}C(^{7}Li, ^{7}Be)^{12}B reaction is given in Fig. 5.4.7. There is no pronounced diffraction structure in the experimental angular distributions which are shown in Figs. 5.4.9 – 5.4.13. Error bars include the contributions of statistical origin and the inaccuracy of the fitting procedure. The systematic errors connected to the target thickness, the solid angle and the integrated current are not included. The uncertainty of the absolute cross section is estimated to be less than 30%.

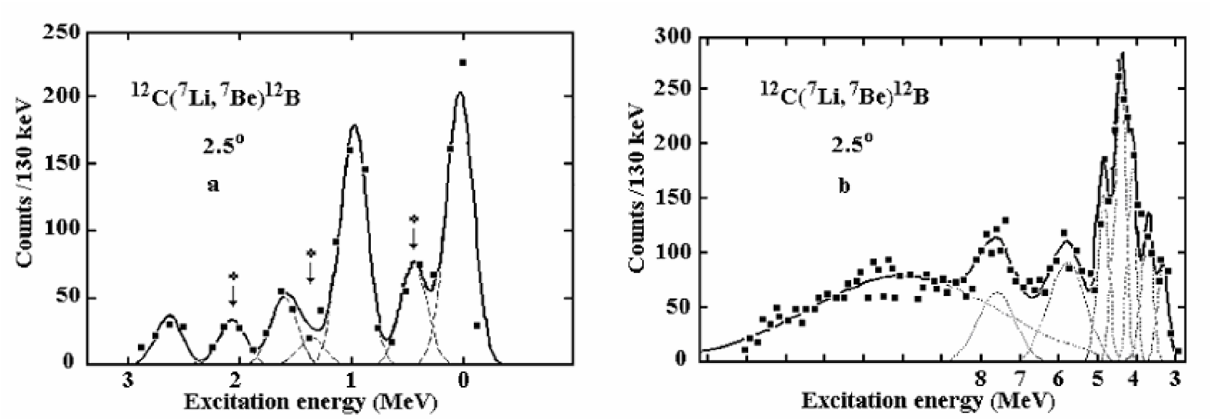

Fig. 5.4.7. Energy spectra of ^{7}Be from the ^{12}C(^{7}Li, ^{7}Be)^{12}B reaction at 2.5° for the 0 – 3 MeV (a) and 3 – 8 MeV (b) transitions. The transitions with mutual excitation of ^{12}C (E_x = 0.0, 0.95 and 1.67 MeV) and ^{7}Be (E_x= 0.43 MeV, J^π= 1/2$^-$) nuclei are marked by* .

The differential cross sections for the direct one-step charge exchange process was calculated in the DWBA using the well-known program DWUCK [126], which was modified in order to permit calculations for particles with spin 3⁄2 scattered in an optical potential without spin–orbit forces [242]. The same optical potential obtained from the ^{7}Li elastic scattering on the ^{12}C nuclei at energy of 78.7 MeV [243] was used for the calculation of distorted waves in the entrance and exit channels. All the parameters are collected in Table 5.4.3.

Table 5.4.3. Optical potential parameters used in our calculations within DWBA and CRC methods.

System	E (MeV)	V (MeV)	r_V (fm)	a_V (fm)	$-W$ (MeV)	r_W (fm)	a_W (fm)	r_C (fm)	Ref.
^{12}C+^{7}Li	78.7	140.2	1.02*	0.97	21.3	1.88*	0.81	1.3	[30]
	131.8	119.1	0.69	0.89	30.0	0.912	0.99	1.3	[41]
^{13}C+^{6}Li	93.0	257.5	0.577	0.82	60.6	0.71	1.07	0.73	[34]
^{11}B+^{8}Be		165.6	0.79	0.76	7.0	1.25	1.25	0.76	[35]

$\beta^T_2 = -1.17$, $\beta^P_2 = 2.45$.
$R = r_i(A^{1/3}_T + A^{1/3}_P)$, $i = V,W$.
* $R = r_i(A^{1/3}_T)$, $i = V,W$.

The calculation of two-step processes were done with taking into account the sequential *pn*- and *np*-transfers, which proceed through the intermediate ^{6}Li, ^{13}C, ^{8}Be and ^{11}B nuclei. The ground and excited states were included in the calculation scheme. The relevant diagrams are shown in Figs. 5.4.8(b) and 5.4.8(c).

The calculations were done also in the framework of the CRC method. The potential used in the one-step process (Table 5.4.3) was used as a starting point for the description of the relative motion in the entrance ^{12}C + ^{7}Li and exit ^{12}B + ^{7}Be channels of the two-step process. The cross-sections for elastic and inelastic scattering of ^{7}Li on ^{12}C into the excited 4.44 MeV (2^+) (^{12}C) and 0.48 MeV (1⁄2$^-$) (^{7}Li) states were calculated in the framework of the rotational model. The coupling between the 0^+ and 2^+ states for the target nuclei and between the 3⁄2$^-$ and 1⁄2$^-$ channels for the projectile, as well as reorientation effects, were taken into account.

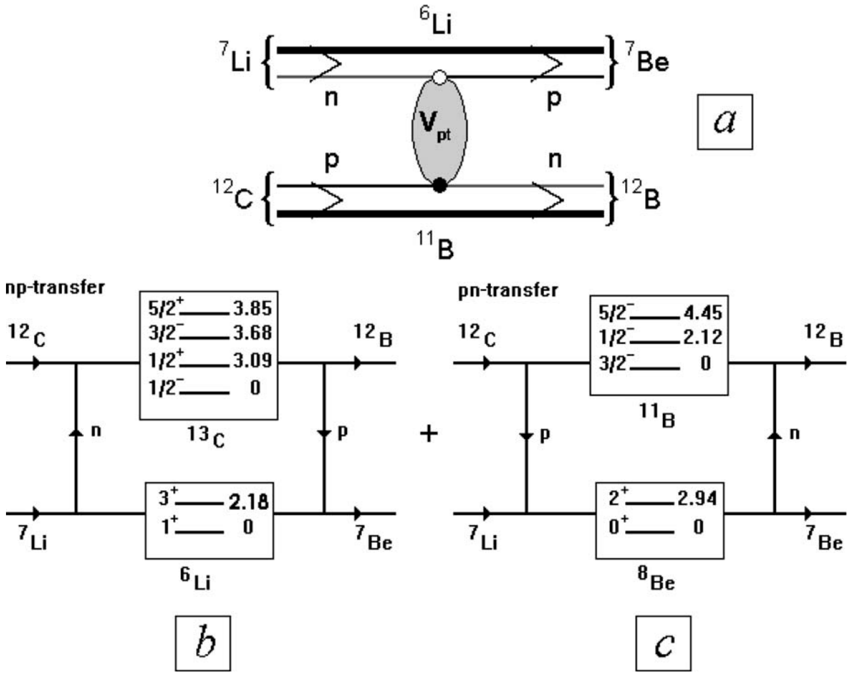

Fig. 5.4.8. A schematic representation of the direct one-step charge-exchange mechanism for the ^{12}C(^{7}Li, ^{7}Be)^{12}B reaction (a) and diagrams for two-step sequential *np*—(b) and *pn*—(c) transfers.

The identical deformation lengths for the real and imaginary parts of the potential were assumed. Only the depth of the imaginary potential W and the quadrupole deformation length δ_2 for the target and projectile were modified during the fitting procedure. The calculated cross sections well reproduce the experimental angular distributions [242] for elastic and inelastic scattering to the ^{12}C (2^+) and ^{7}Li($1/2^-$) states with parameters $W = -19$ MeV, $\delta_2(^{12}\text{C}) = -1.17$ fm and $\delta_2(^{7}\text{Li}) = 2.45$ fm (Fig. 5.4.9). This is in a good agreement with the coupled-channel analysis performed at 34 MeV [244].

The potentials for the intermediate ^{6}Li + ^{13}C and ^{8}Be + ^{11}B channels were taken from previous studies [17, 18] and are presented in Table 5.4.3. The one-nucleon spectroscopic amplitudes (S_x) for the *p*-shell transitions were calculated and shown in Appendix. The one-particle wave functions were calculated by modifying the depth of Woods–Saxon potential, in order to obtain corresponding binding energies. In this procedure the geometric parameters of the potential were fixed ($a = 0.65$ fm and $r = 1.25$ fm) for the appropriate bound states. The total cross sections were calculated as a coherent sum of all the considered reaction channels.

The experimental angular distributions for the transitions to the ground (1^+) and excited $E_x = 0.95$ MeV (2^+), 4.5 MeV (2^-, 4^-), 1.67 MeV (2^-), 2.62 MeV (1^-), 3.39 MeV (3^-), 3.76 MeV (2^+), 5.8 MeV(3^-) and 7.6 MeV(1^-, 2^-) states of ^{12}B are shown in Figs. 5.4.10 – 5.4.13. The differential cross sections for the three lowest excited states of ^{12}B populated in the ^{12}C(^{7}Li, ^{7}Be)^{12}B reaction, are shown in Fig. 5.4.13.

A simple comparison of the calculated and experimental angular distributions shows that one-step charge-exchange mechanism cannot explain the experimental data (too steep fall-off of the corresponding distributions (curves 1 in Figs. 5.4.10, 5.4.11 and 5.4.13)). In contrast, the shape of the angular distributions for the two-step sequential nucleon transfer is in a good agreement with the experimental cross sections, as it can be seen from the figures (curves 2). This clearly points towards importance of the two-step mechanism in (^{7}Li, ^{7}Be) reaction.

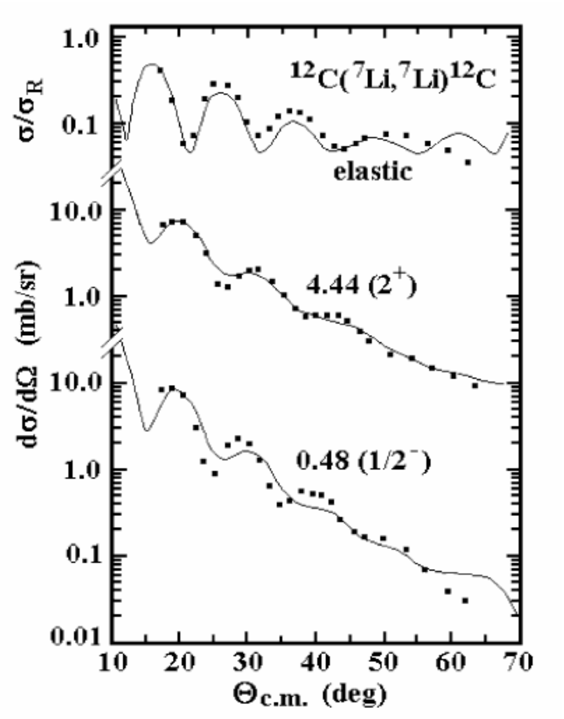

Fig. 5.4.9. Elastic and inelastic scattering of the ^7Li ions on the ^{12}C nuclei at 78.7 MeV with excitation of 4.44 MeV (2^+) state of ^{12}C and 0.48 MeV ($1/2^-$) of ^7Li. The dots show the experimental data [244]. The solid curves represent coupled reaction channel calculations. The optical potential from Table 5.4.3 with $W = -19$ MeV and deformation lengths $\delta_2(^{12}C) = -1.17$ fm and $\delta_2(^7Li) = 2.45$ fm was used in these calculations.

Table 5.4.4. Normalization factors for calculated differential cross sections.

E_x [MeV]	J^π	One-step	Two-step
		DWUCK	FRESCO
0	1^+	2.7	2.5
0*	1^+	2.6	1.0
0.95	2^+	2.7	1.8
0.95*	2^+	2.7	0.9
1.67	2^-	1.3	1.0
1.67*	2^-	3.3	1.0
2.62	1^-	0.6	0.3
3.39	3^-	1.0	0.7
3.76	2^+		3.0
4.3	2^-		1.0
4.46+4.52	2^-+4^-	1.0	1.5
7.6	1^-	1.0	

The calculated cross sections for the two-step mechanism were normalized to the experimental data in a large-angle region because the contribution from this process increases with the value of the angle. The normalization coefficients are presented in Table 5.4.4. They are close to unity, which means that the truncation of the included processes (with the intermediate ^6Li, ^{13}C (diagram 3(b)) and ^8Be, ^{11}B (diagram 3(c)) nuclei is reasonable. The contributions of diagrams (b) and (c) in Fig. 5.4.8 to the coupling scheme turned out to be comparable, as it can be seen for the transition to the ground state of ^{12}B (top panel of Fig. 5.4.10).

The theoretical cross sections for the one-step charge-exchange process shown in Figs. 5.4.10, 5.4.11 and 5.4.13 were normalized by the factors taken from a comparison of the calculated cross sections and the experimental data at E(^7Li) = 147 MeV [245], because for this energy there is no doubt about the dominant nature of the one-step mechanism. The optical potential was taken from the analysis of the elastic scattering of ^7Li on ^{12}C at E(^7Li) = 131.8 MeV [246]. The corresponding parameters are presented in Table 5.4.3. The calculated and the experimental cross sections for some low-lying states of ^{12}B at 147 MeV are compared in Fig. 5.4.14. It can be seen that the experimental data are well reproduced at small angles ($\theta \leq 10^o$) by the direct mechanism and they are underestimated at large angles. This can be explained by the pn + np two-step mechanism. The normalization coefficients for the one-step processes are presented in Table 5.4.4.

The theoretical total cross sections being an incoherent sum of the one- and two-step mechanisms are presented in Figs. 5.4.10, 5.4.11 and 5.4.13 using the thick solid curves. The agreement with the experimental data at small angles is improved by adding the one-step charge-exchange mechanism. Simultaneously, the fraction of this mechanism in the total cross section at angles smaller than 10^o equals about 50% for transition to the ground state and about 20 – 30% for transitions to the excited states.

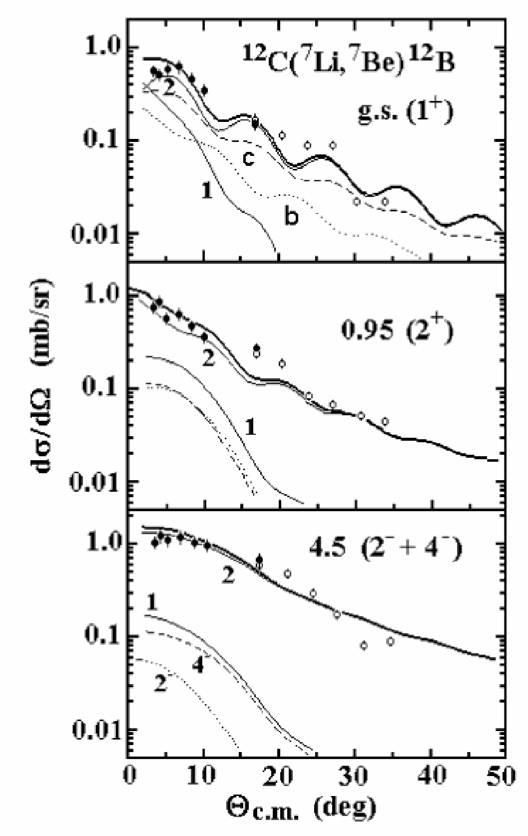

Fig. 5.4.10 Angular distributions for the transitions to the ground (1^+) state and the excited 0.95 MeV (2^+) and 4.5 MeV (2^-, 4^-) states of the ^{12}B nucleus populated in the ^{12}C(^{7}Li, ^{7}Be)^{12}B reaction. The open dots were obtained by the $\Delta E - E$ technique. The thin solid curves correspond to the DWBA and CRC calculations assuming the direct charge-exchange mechanism (1) and the two-step sequential *np*- and *pn*-transfers (2). The dotted and dashed curves in the top panel correspond to calculations with diagrams (b) and (c) (see Fig. 5.4.8), respectively. The dashed and dotted curves for the 0.95 MeV (2^+) state show contributions of the spin-flip (ΔS = 1) and non-spin-flip (ΔS = 0) processes for the direct charge-exchange mechanism. The thick solid curves represent an incoherent su m of the direct (1) and two-step (2) mechanisms.

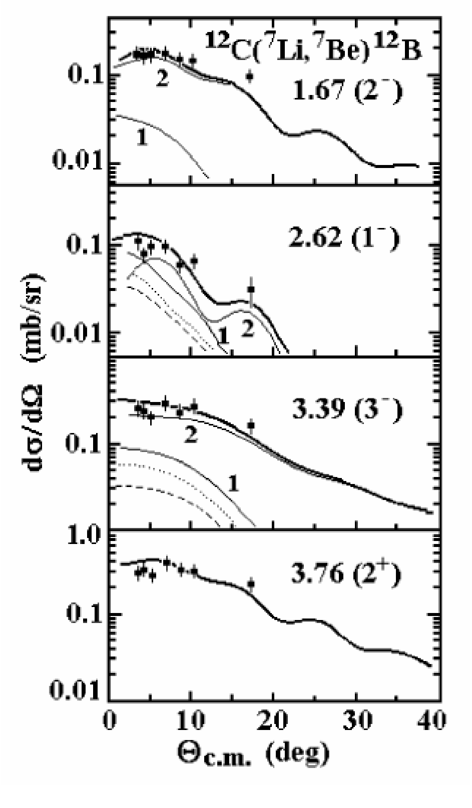

Fig. 5.4.11. Angular distributions for the transitions to the 1.67 MeV (2^-), 2.62 MeV (1^-), 3.39 MeV (3^-) and 3.76 MeV (2^+) excited states of ^{12}B from the ^{12}C(^{7}Li, ^{7}Be)^{12}B reaction. Calculated one-step charge-exchange (1) and two-step sequential nucleon transfer (2) processes are represented by the thin solid curves. Contributions of the direct charge-exchange process with ΔS = 0 and ΔS = 1 are shown by the dotted and dashed curves, respectively. The thick solid curves are incoherent sums of 1 (direct charge-exchange mechanism) and 2 (two-step sequential *np*- and *pn*-transfers).

For the angles larger than 10°, the total cross sections is almost completely defined by the two-step mechanism. The contributions to the cross-sections of the spin-flip (ΔS = 1) and non spin-flip (ΔS = 0) processes for the transitions to the states of ^{12}B with normal parity in the (^{7}Li, ^{7}Be) reaction are comparable accordingly to calculations. This is visible in Figs. 5.4.10, 5.4.12 for the transitions to the 2^+, 1^- and 3^- states. In contrast, the spin-flip process for the transition to the 0.95 MeV (2^+) state with ^{7}Be (E_x = 0.43 MeV, $J^\pi = 1/2^-$) in the exit channel gives the main contribution to the cross sections. Due to this peculiarity, the (^{7}Li, ^{7}Be) reaction could be the unique tool to study the spin–isospin ($\Delta S = 1$, $\Delta T = 1$) excitations of nuclei. Including the two-step processes into the analysis can facilitate description of the (^{7}Li, ^{7}Be) reactions at low energies (30 – 80 MeV).

The excitation function could give an additional information on the mechanism of the (^{7}Li, ^{7}Be) reaction. The cross sections of this reaction for the transitions to the ground (1^+) and excited 0.95 MeV (2^+) and 1.67 MeV (2^-) states, measured around 0^o at energies 14, 21 and 26 MeV/n [247] are presented in Fig. 5.4.15. The data from the present study for ^{7}Li at energy 11.7 MeV/n are shown in the same figure using the open circles. Theoretical predictions of the energy dependence for the one- and two-step mechanisms [248] are shown by the solid and dashed curves, respectively. In contrast to the case of 21 and 26 MeV/n, the theoretical cross section for the one-step mechanism at 14 MeV/n and particularly at 11.7 MeV/n underestimates the experimental data.

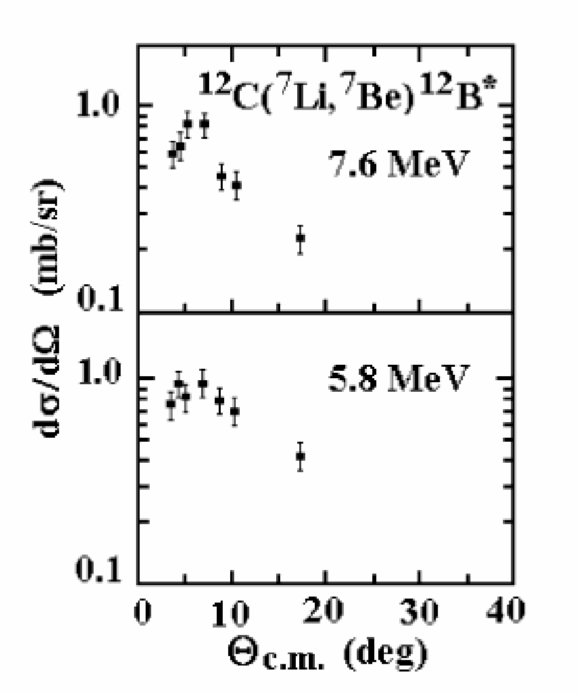

Fig. 5.4.12. Experimental angular distributions for the structures at $E_x \approx 5.8$ MeV and 7.6 MeV of ^{12}B nucleus.

The analysis of the measured angular distributions using the DWBA and CRC methods were done assuming direct one-step charge-exchange mechanism and two-step sequential nucleon transfer. It was shown that the two-step sequential mechanism gives a better description of the shape of the experimental angular distributions and, in practice, is the dominant process for the angles above 10^o. The one-step process gives a significant contribution only in the region of small angles ($< 10^o$). The fraction of this process in the transition to the ground (1^+) state is about 50% and is about 20–30% for all other transitions.

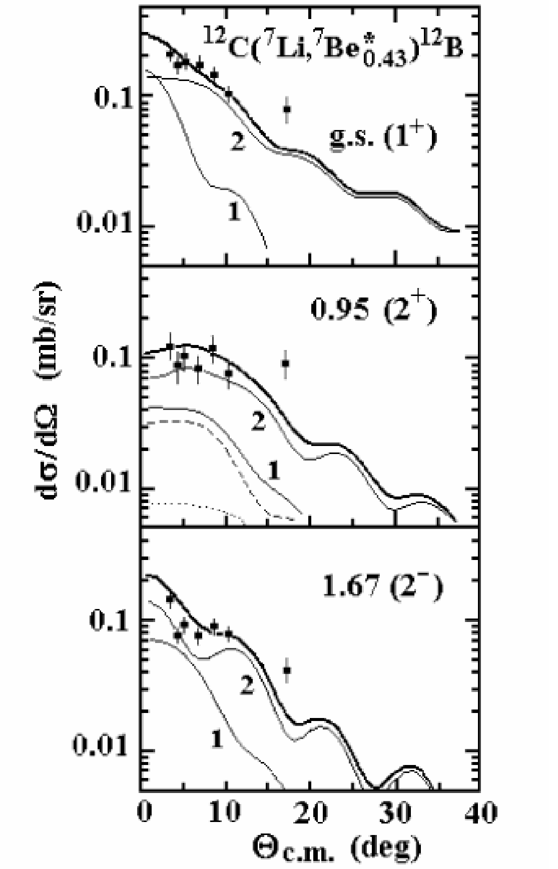

Fig. 5.4.13. Angular distributions for the transitions to the ground (1^+) and excited 0.95 MeV (2^+) and 1.67 MeV (2^-) states of the ^{12}B nucleus which are accompanied by excited outgoing ^7Be (E_x = 0.43 MeV, $1/2^-$). The meaning of the curves is the same as in Figs. 5.4.10, 5.4.11.

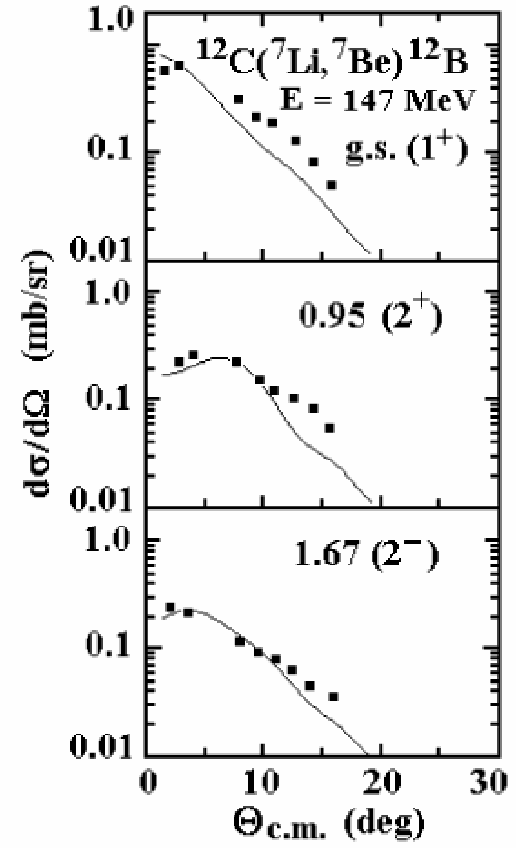

Fig. 5.4.14. Angular distributions of the differential cross sections for the transitions to the ground (1^+) and excited states of the ^{12}B nucleus produced in the $^{12}C(^7Li, ^7Be)^{12}B$ reaction at $E(^7Li)$ = 147 MeV. Experimental data are taken from Ref. [245]. The curves show the DWBA calculations for direct charge-exchange mechanism.

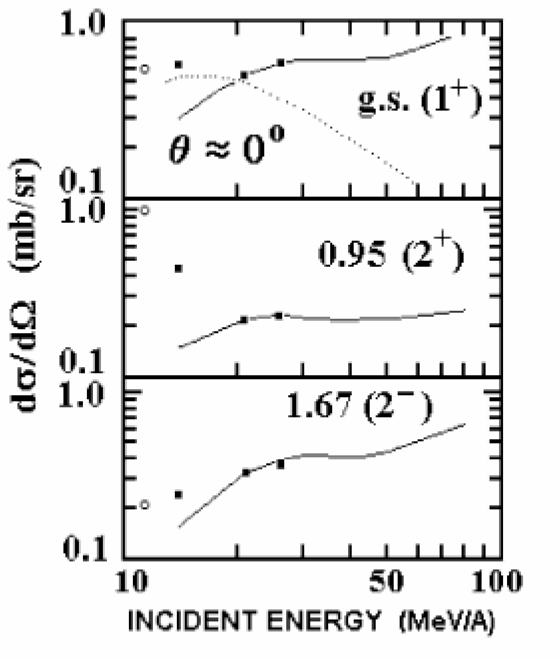

Fig. 5.4.15. Excitation functions of the $^{12}C(^7Li, ^7Be)^{12}B$ reaction for the transitions to the ground (1^+) and excited E_x = 0.95 MeV (2^+) and 1.67 MeV (2^-) states of ^{12}B. Differential cross sections from the present work are presented by the open circles. The squares represent the data from Ref. [247]. Predictions for one- and two-step mechanisms [247] are shown by the solid and dotted curves, respectively.

SUMMARY AND CONCLUSIONS

In this thesis the interaction of exotic, short-living and stable nuclei has been studied. Development of nuclear reaction theory, computational methods and computer technique gave the possibility of revival the subject area presented in this work including the elastic and inelastic scattering as well as transfers of nucleons and light clusters data. The following results of our investigation has been obtained:

Creation of the data base of the elastic scattering, inelastic scattering and transfer reaction angular cross-sections. This data base include the following new experimental data:

- the ^{14}C(^{6}Li, ^{6}He)^{14}N reaction at energy E_{LAB}(^{6}Li) = 93 MeV,
- elastic scattering of the ^{7}Li + ^{16}O nuclei at energy E_{LAB}(^{7}Li) = 42 MeV,
- the ^{12}C(^{7}Li, ^{7}Be)^{12}B reaction. at energy E_{LAB}(^{7}Li) = 82 MeV,
- elastic and inelastic scattering of the ^{10}B + ^{7}Li nuclei at energy E_{LAB}(^{10}B) = 51 MeV,
- elastic and inelastic scattering of the ^{11}B + ^{7}Li nuclei at energy E_{LAB}(^{11}B) = 44 MeV,
- elastic and inelastic scattering of the ^{11}B + ^{9}Be, ^{13}C, ^{14}C nuclei and the ^{9}Be(^{11}B, ^{10}B)^{10}Be, ^{9}Be(^{11}B, ^{12}B)^{8}Be, ^{9}Be(^{11}B, ^{12}C)^{8}Li reactions for the transitions to the ground and low excited states of the exit channel nuclei at energy E_{LAB}(^{11}B) = 45 MeV,
- elastic and inelastic scattering of the ^{11}B + ^{12}C nuclei and the ^{12}C(^{11}B, ^{15}N)^{8}Be reaction at energy E_{LAB}(^{11}B) = 49 MeV,
- elastic and inelastic scattering of the ^{12}C + ^{9}Be nuclei and the ^{9}Be(^{12}C, ^{13}C)^{8}Be, ^{9}Be(^{12}C, ^{11}B)^{10}B reaction for transitions to the ground and low excited states of the exit channel nuclei, at energy E_{LAB}(^{12}C) = 65 MeV,
- elastic and inelastic scattering of the ^{7}Li + ^{14}N nuclei and the ^{7}Li(^{14}N, ^{15}N) ^{6}Li reaction at energy E_{LAB}(^{14}N) = 110 MeV, elastic and inelastic scattering of the ^{14}N + ^{12}C nuclei at energy E_{LAB}(^{14}N) = 116 MeV,
- elastic and inelastic scattering of the ^{18}O + ^{7}Li nuclei at the energy E_{LAB}(^{18}O) = 114 MeV,

Creation of the data base of the optical potential parameters, which were obtained from the Optical Model, Distorted Wave Born Approximation and Coupled Reaction Channels methods analysis, for the mentioned above light nuclei interactions in the ground and excited states of nuclei in the exit channels. In particular, except of the optical-potential parameters for stable nuclei, this data base contains the data also for the following unstable and short-living nuclei: ^{5}He + ^{16}O, ^{6}He + ^{15}O, ^{8}Li + ^{12}C, ^{8}Li + ^{13}N, ^{8}Be + ^{13}C, ^{8}Be + ^{12}B, ^{8}Be + ^{13}C, ^{8}Be + ^{15}N, ^{10}Be + ^{10}B, ^{10}Be + ^{11}C, ^{11}C + ^{15}N, ^{13}C + ^{13}N, ^{14}C + ^{6}Li and ^{14}C +^{14}N,

Creation of the spectroscopic amplitudes (SA) data base for the nucleon and light-cluster interactions with nuclei. Those calculations for nucleons and clusters, can be made in the frame of the Translationary Invariant Shell Model (TISM) using the method of Ref. [33] for the 1s-1p-shell nuclei. Therefore, the reactions investigated in the presented work include the nuclear processes for the interactions of the 1s-1p-shell nuclei only. These spectroscopic amplitudes are presented in Appendix.

Investigation of the energy dependence of the optical-potential parameters have been performed using the data obtained in the described experiments and also the data taken from the literature. The dispersion relation between the real V(r, E) and imaginary W(r, E) parts of the OM potential, introduced on the basis of the causality principle was used. Data base for the energy-dependence coefficients of the optical potential (useful for further CRC calculations) was created. It was found that this dependence may differ for the interaction of various heavy ions and that it is tightly bound with their nuclear structure.

Study of isobaric and isotopic effects in the investigated reactions has been made. For example, it was found that the energy dependence of the $^{10}B + {}^{7}Li$ interaction is different from that of the $^{11}B + {}^{7}Li$ interaction, especially for the imaginary potential. Another example is the energy dependence of the OM potentials for the $^{13}C + {}^{8}Be$ and $^{12}C + {}^{9}Be$ interactions. Large differences were found for the imaginary surface part, W_S(E) of the optical potential in the investigated energy range and for the r_V(E), r_W(E), a_V(E), a_W(E) optical potential parameters at energies $E_{CM} < 15$ MeV. These differences can be explained by distinctions of the structure and the breakup threshold in the ^{8}Be and ^{9}Be nuclei. In another experiment for the $^{9}Be(^{11}B, {}^{10}B)^{10}Be$ reaction, a strong isotopic effect for the imaginary potentials of the $^{10}B + {}^{9}Be$ and $^{11}B + {}^{9}Be$ scattering and isobaric effects for the $^{10}B + {}^{10}Be$ and $^{10}B + {}^{10,11}B$ OM parameters were found.

The deformation parameters for the rotational and vibrational excitations of some nuclei are included in the mentioned above data bases. These parameters were determined for the following nuclei: $^{6,7}Li$, ^{9}Be, $^{10,11}B$, $^{12,13,14}C$, ^{14}N and ^{18}O. The influence of these excitations on the scattering cross sections were investigated. For example, the rotational excitations of ^{7}Li and ^{11}B dominate in the $^{11}B + {}^{7}Li$ inelastic channels, while the contributions of one-step and two-step transfers to the elastic and inelastic channels are small. Interesting results concerning the carbon isotopes have been observed. The quadrupole deformation of the ^{14}C nucleus in ground state was found to be negative, while the ^{13}C quadrupole deformation was found to be positive.

Investigation of influence of the reorientation processes in reactions between light nuclei has been performed. The reorientation processes are the quadrupole rotational transitions without energy change, allowed by the selection rules. The following examples of the role of reorientation mechanism in the light nuclei interaction have been found:

- in the $^{10}B + {}^{7}Li$ and $^{11}B + {}^{7}Li$ elastic scattering channels, the reorientation processes of the ^{7}Li and ^{10}B nuclei dominate at the backward angles.
- in the $^{14}N + {}^{7}Li$ elastic scattering, the reorientation of ^{7}Li with its large quadrupole deformation provides the observed anomalous large-angle scattering (ALAS).
- in the $^{11}B + {}^{9}Be$ elastic and inelastic scattering it was found that the ^{9}Be and ^{11}B nuclei reorientations processes in the ground states combined with a weak absorption dominate in the large angle scattering. On the contrary, the reorientations of these nuclei in the excited states is rather marginal, being a higher-order process.
- in the $^{9}Be(^{12}C, {}^{12}C)$ elastic and inelastic scattering, the ^{9}Be nucleus reorientation processes dominate in the cross section at large angles.
- in the $^{12}C + {}^{11}B$ elastic scattering, the potential (Coulomb + nuclear) scattering plus reorientation of ^{11}B play an important role at the intermediate angular region.
- in the $^{11}B + {}^{7}Li$ elastic channel, the potential scattering dominates at the forward angles, while the reorientations of ^{7}Li and ^{11}B dominate at the backward angles.

Investigation of the role of different one-step and two-step transfers was made for the following reactions:

- ^{9}Be(^{12}C, ^{9}Be)^{12}C, ^{9}Be(^{12}C, ^{13}C)^{9}Be and ^{9}Be(^{12}C ^{10,11}B)^{11,10}B. It was found that the one-step transfers are dominant in these reactions and that the two-step transfers play a significant role at the separate angular ranges.
- the transfer reactions have small contribution for ^{11}B + ^{7}Li scattering.
- in the ^{12}C(^{11}B, ^{15}N)^{8}Be reaction, the α-cluster transfer dominates at the forward angles, while the t-cluster transfer dominates at the backward angles. The two-step transfers of nucleons and clusters don't play any significant role.
- the one-step and two-step transfers of the standard (d, t, ^{3}He, α) and exotic (^{4,5,6}Li, ^{6,7,8}Be) clusters, which usually lead to the enhancement of the cross section, give a negligible contribution to the elastic scattering ^{14}N + ^{7}Li.
- the contributions from one-step and two-step transfer reactions to the ^{11}B + ^{14}C elastic and inelastic scattering were found to be negligible.
- in the ^{9}Be(^{12}C, ^{13}C)^{8}Be reaction, the n- and α-transfers dominate.
- in the ^{9}Be(^{11}B, ^{10}B)^{10}Be reaction, the direct neutron and proton transfers dominate at the forward and backward angles, respectively. Contributions of the two-step processes to this reaction were found to be negligible.
- in the ^{9}Be(^{11}B, ^{12}B)^{8}Be reaction for $\theta_{CM} < 90^{o}$ angles, the neutron transfer dominates. The two-step processes are small.
- the one-step processes dominate in the ^{9}Be(^{12}C, ^{11}B)^{10}B reaction. The two-step processes are important only in the angular region nearby $\theta_{CM} = 90^{o}$ and at large angles.

Generally, the contributions of one-step and two-step transfers to the elastic and inelastic cross sections of the reactions described in this thesis are small.

Investigation of influence of the ALAS processes in reactions between light nuclei has been performed:

- the results of the data analysis of the elastic scattering ^{14}N + ^{7}Li lead to the conclusion that the observed anomalously large-angle scattering is the result of reorientation of ^{7}Li, due to its large quadrupole deformation. Different explanations of the ALAS phenomenon in the elastic scattering were proposed in the literature, e.g., a weak absorption in the collision process (a small imaginary part of the optical potential), the direct cluster transfer or the compound-nucleus process. Also, for the ^{11}B + ^{9}B elastic and inelastic scattering, it was found that the ^{9}Be and ^{11}B reorientations in the ground states, combined with a weak absorption, dominate in the large angle elastic scattering. On the contrary, the reorientations of these nuclei in the excited states are rather small, being a higher-order processes.
- the one-step and two-step transfers of the standard (d, t, ^{3}He, α) and exotic (^{4,5,6}Li, ^{6,7,8}Be) clusters, which usually lead to the enhancement of the cross section, give a negligible contribution to the elastic scattering ^{14}N + ^{7}Li. The results of the complete analysis of the data for the elastic scattering ^{14}N + ^{7}Li lead to the conclusion that the reorientation of ^{7}Li with its large quadruple deformation which provides the observed anomalous large-angle scattering.
- it is very interesting to compare the ALAS phenomenon for the ^{11}B + ^{12}C and ^{11}B + ^{13}C reactions. The ALAS is much stronger for the ^{11}B + ^{12}C than for the ^{11}B + ^{13}C reaction. For the ^{11}B + ^{12}C, ALAS is described satisfactorily by the sum of the CRC cross section for the potential scattering, the ^{11}B reorientation and the proton transfer. In the case of ^{11}B + ^{13}C, ALAS is caused by the two first mechanisms only. The proton transfer in the ^{11}B + ^{12}C elastic scattering leads to the observed difference between

the large angle scattering of ^{11}B on ^{12}C and on ^{13}C. One can see that the ^{11}B + ^{12}C inelastic ALAS is stronger than the ALAS for the ^{11}B + ^{13}C inelastic scattering, due to the proton transfer dominating in the ^{11}B + ^{12}C inelastic scattering.

The interesting results concerning the so called threshold anomaly were obtained. Due to the causality principle, a scattered wave cannot be emitted before the interaction has occurred. Then, this principle implies the existence of a dispersion relation between the real and the imaginary parts of the optical potential. In the case of nucleus-nucleus scattering, the dispersion relation predicts that the absolute value of the real part of the optical potential as a function of energy has a bell-shaped maximum, while the imaginary part approaches minimum, mainly for energies near the top of the Coulomb barrier. This is so called threshold anomaly. The existence of threshold anomaly in the ^{9}Be + ^{12}C (Section 4.2) ^{13}C + ^{8}Be, ^{12}C + ^{9}Be (sub-Section 5.2.1) and ^{10,11}B + ^{10}B (sub-Section 5.2.2) reaction was found. The decrease of absolute value of the imaginary potential occurs at energies above the top of the Coulomb barrier. It was also observed for another systems e.g. ^{16}O + ^{28}Si [255] and α + ^{40}Ca [252, 253, 254]. It is probably due to contributions of other channels, coupling to the elastic scattering and modifying the real potential [255].

The threshold anomaly effect is well established for the scattering of tightly bound nuclei, although there are some conclusions that the breakup of weakly bound nuclei influence the threshold anomaly [257]. This is probably the explanation of the differences in threshold anomaly for the ^{8}Be and ^{9}Be nuclei.

The problem of differences of optical potential parameters for stable and radioactive (short-living) nuclei was also considered. For example, the parameters for the^{13}C + ^{8}Be and ^{12}C + ^{9}Be interactions (see Fig. 5.2.7) are shown. The parameters for both the systems have similar values at larger energies. The differences are observed for the energy dependences of $a_V(E)$, $a_W(E)$ for the ^{13}C + ^{8}Be and ^{12}C + ^{9}Be systems at E_{CM} < 15 MeV. For the ^{12}C + ^{9}Be interaction, the functions $a_V(E)$ and $a_W(E)$ are almost constant, whereas for the ^{13}C + ^{8}Be interaction these functions show a rapid variation at the energy $E_{CM} \approx 9$ MeV slightly above the Coulomb barrier energy ($E_{Coul.}$ = 5.59 MeV (CM)). These differences can be explained by the different structure and the breakup threshold of the ^{8}Be and ^{9}Be nuclei.

The OM parameters for mentioned above ^{12}C + ^{9}Be and ^{13}C + ^{8}Be interactions were compared with the OM parameters for the ^{10,11}B + ^{10}B scattering (see Fig. 5.2.13). The significant differences for the depth W_S and for the diffuseness a_W of the imaginary part of the OM potentials are visible. The other parameters differ only in the threshold-anomaly region. This suggests that the energy dependence of the OM potential parameters is correlated with the structure of a nucleus.

The OM parameters of the ^{8}Be + ^{13}C and ^{8}Be + ^{15}N interactions were also compared (see Fig. 5.1.21). We show also the energy dependence of the OM parameters for the ^{8}Be + ^{13}C channel (open triangles and dashed curves) obtained in our previous work [3]. Except for r_V and r_W , rather large differences between the OM parameters of the ^{8}Be + ^{13}C and ^{8}Be + ^{15}N channels can be seen. At energies E_{CM} > 10 MeV the parameters a_V and a_W are much smaller for the ^{8}Be + ^{15}N channel than for the ^{8}Be + ^{13}C one (see the lower panel in Fig. 5.1.21). This is probably caused by closing the neutron p-shell in the ^{15}N nucleus. The energy interval of the fast rise of W_S for the ^{8}Be + ^{15}N channel is shifted relatively to its counterpart for the ^{8}Be + ^{13}C channel. Probably the difference between the grazing potential barriers for these systems is the reason of the energy shift of the fast growth of W_S discussed above. The energy interval of the fast rise of V of ^{8}Be + ^{15}N and ^{8}Be + ^{13}C are also shifted in a similar way.

It seems that there is no significant differences of optical potential parameters for stable and radioactive (short-living) nuclei. The only differences are caused by the structure of these nuclei.

The results presented in this thesis were used in many other works. The ground state quadrupole effect, evidenced by the CRC calculations, where the reorientation of ^{7}Li produces a large effect at backward angles in the elastic scattering of 110 MeV ^{14}N on ^{7}Li [7] has been cited in Ref.[260]. The deformation parameters and the spectroscopic factors for the ^{7}Li (g.s.) and ^{6}Li (g.s.) overlap the $1P_{3/2}$ and $1P_{1/2}$ components, taken from Ref. [13] were used in Ref.[261]. In the review article [262] the data from author and collaborators' papers (Refs [3, 5 and 10]) are reported. The theoretical methods, used in this thesis [92] were also used in many works, e.g. [263, 264, 265, 266, 267]. The importance of reorientation in the elastic scattering of the odd-mass nucleus [4] at large angles was reported in Ref. [268]. The deformation parameters and OM parameters of ^{7}Li nucleus, taken from Ref. [7] were used in [269]. The deformation parameters of the ^{9}Be nucleus for excited states 1.680 MeV and 2.430 MeV presented in Ref. [4] has been used in [270]. The optical potential parameters, and spectroscopic amplitudes from Ref. [4] were used in [271].

The optical potential parameters obtained from the experiments with the radioactive (secondary) beams (direct method) (see Table 1.2) are presented in Refs [70, 72, 74], although in some cases for different energies than are concerned in this thesis. It seems that they are similar to the ones presented in this thesis.

The present thesis clearly shows that the second method - the stable ion beam experiments with the nucleon-transfer and cluster-transfer reactions is a very useful tool for obtaining the main goal of the present work. This goal is the investigation of reaction mechanisms (nucleon and cluster transfers), obtaining the optical potential parameters and their energy dependences for the exotic and stable nuclei interactions. Simultaneously it is possible to found the important other features of these interactions, e.g. influence of reorientation processes and threshold anomaly effects.

The results presented in this thesis prove that the investigation of interaction of the exotic and short-living nuclei together with stable light nuclei using the stable ion beams is a very useful tool in nuclear physics. It would be interesting to perform the investigation of ^{7,6}Li, ^{9}Be, ^{12,13,14}C(^{15}N, X), ^{7,6}Li, ^{9}Be,^{12,13,14}C(^{13}N, X), ^{7,6}Li, ^{9}Be, ^{12,13,14}C(^{17}O, X), ^{7,6}Li, ^{9}Be, ^{12,13,14}C(^{18}O, X) reactions, to obtain the information about their mechanisms as well as about interaction of ^{5}Li with ^{18,19}O, ^{14,16}N, unstable nucleus ^{8}Li with ^{16,17}O, ^{12,14}N, unstable ^{8}Be with ^{18,19}O, ^{16,17}N and so on.

ACKNOWLEDGEMENTS

I would like to express my deep gratitude to all Colleagues who helped me during my work: in performing experiments, analyzing the data and writing publications.

Especially I would like to thank Prof. dr hab. Andrzej Budzanowski for good collaboration and helping during all my scientific way of life and also encouraging and helping in the process of preparing this thesis.

I am grateful to Prof. dr hab. Adam Tichonowich Rudchik from Kiev, Ukraine for many years cooperation, encouraging and great support during writing this thesis.

Many thanks for Colleagues from Krakow-Kiev-Warsaw collaboration working with me since many years:
Prof. dr hab. Andrzej Budzanowski,
Prof. dr hab. Adam T. Rudchik,
Prof. dr hab. Antoni Szczurek,
Prof. dr hab. Krzysztof Rusek,
Prof. dr hab. Stanisław B. Sakuta,
Dr Regina Siudak,
Dr Irena Skwirczyńska,
Dr Marianna Makowska-Rzeszutko,
Eng. Bronisław Czech,
Eng. Wiesław Kantor,
Dr Leopoldyna Głowacka,
Dr Andriy A. Rudchik,
Dr Vladislav K. Chernievsky,
Dr Evgen I. Koschyi,
Dr Valentin M. Kiryanchuk,
Dr Oleksandr A. Momotyuk,
Dr Valeriy M. Pirnak,
Dr hab. Eryk Piasecki,
Prof. dr hab. Vadim V. Volkov,
Dr Anatoliy G. Artukh.

I am grateful to Prof. dr hab. Hartmut Machner from Juelich, Germany for many years friendly and fruitful cooperation in another area of scientific activity – meson physics.

Many thanks for Colleagues working with me since many years in meson physics, in the GEM, HIRES and PISA collaborations in Forschungszentrum Juelich, Germany:
Prof. dr hab. Andrzej Budzanowski,
Prof. dr hab. Hartmut Machner,
Prof. dr hab. Kurt Kilian
Dr Regina Siudak,
Dr Ludwik Freindl,

Dr Peter von Rossen,
Prof. dr hab. Frank Hinterberger,
Dr hab. Frank Goldenbaum,
Dr. hab. Stanisław Kistryn,
Dr Małgorzata Kistryn,
Dr Valentin M. Kiryanchuk,
Prof. dr hab. Lucjan Jarczyk,
Prof. dr hab. Andrzej Magiera,
Prof. dr hab. Bogusław Kamys,
Prof. dr hab. James Ritman,
Dr Krzysztof Pysz,
Dr Paweł Kulessa,
Dr Ambar Chatterjee,
Dr Bidyut J. Roy,
Dr. Nikolai M. Piskunov,
Dr Igor M. Sitnik,
Dr Dimitri A. Kirillov,
Dr Dimitri Kolev,
Prof. dr Roumen Tsenov,
Prof. dr hab. Gabriela Martinska,
Dr Josef Urban,
Dr Maria Kravcikova.

Above all, I am deeply grateful to my wife Barbara for her patience, love and constant support.

REFERENCES

[1] V.A. Ziman, A.T. Rudchik, A. Budzanowski, V.K. Chernievsky, L. Głowacka, E.I. O.A. Ponkratenko, R. Siudak, I. Skwirczyńska, A. Szczurek, J. Turkiewicz, Nucl. Phys. **A 624** (1997) 459.

[2] S.B. Sakuta, Yu.A. Glukhov, A.T. Rudchik, V.M. Pirnak, A. Budzanowski, S. Kliczewski, R. Siudak, I. Skwirczyńska, A. Szczurek, Nucl. Phys. **A 639** (1998) 599.

[3] A.T. Rudchik, O.A. Momotyuk, A. Budzanowski, A. Szczurek, V.K. Chernievsky, A.V. Mokhnach, V.A. Ziman, E.I. Koshchy, S. Kliczewski, R. Siudak, I. Skwirczyńska, J. Turkiewicz, Nucl. Phys. **A 660** (1999) 267.

[4] A.T. Rudchik, O.A. Momotyuk, V.A. Ziman, A. Budzanowski, A. Szczurek, I. Skwirczyńska, S. Kliczewski, R. Siudak, Nucl. Phys. **A 662** (2000) 44.

[5] A.T. Rudchik, O.A. Momotyuk, A. Budzanowski, V.K. Chernievsky, E.I. Koshchy, A.V. Mokhnach, V.A. Ziman, S. Kliczewski, R. Siudak, I. Skwirczyńska, A. Szczurek, M. Makowska-Rzeszutko, L. Głowacka, J. Turkiewicz, Nucl. Phys. **A 677** (2000) 61.

[6] A.T. Rudchik, A. Budzanowski, V.K. Chernievsky, B. Czech, L. Głowacka, S. Kliczewski, A.V. Mokhnach, O.A. Momotyuk, S.E. Omelchuk, V.M. Pirnak, K. Rusek, R. Siudak, I. Skwirczyńska, A. Szczurek, L. Zemło, Nucl. Phys. **A 695** (2001) 51.

[7] A.T. Rudchik, V.M. Pirnak A. Budzanowski, A. Szczurek, V.K. Chernievsky, L. Głowacka, S. Kliczewski, E.I. Koshchy, A.V. Mokhnach, R. Siudak, I. Skwirczyńska, J. Turkiewicz V.A. Ziman, Nucl. Phys. **A 700** (2002) 25.

[8] A.T. Rudchik, V.M. Kyryanchuk, A. Budzanowski, V.K. Chernievsky, B. Czech, T. Czosnyka, L. Głowacka, S. Kliczewski, E.I. Koshchy, S.Yu. Mezhevych, A.V. Mokhnach, K. Rusek, S.B. Sakuta, R. Siudak, I. Skwirczyńska, A. Szczurek, L. Zemło, Nucl. Phys. **A 714** (2003) 391.

[9] S.Yu. Mezhevych, K. Rusek, A.T. Rudchik, A. Budzanowski, V.K. Chernievsky, B. Czech, J. Choiński, L. Głowacka, S. Kliczewski, E.I. Koshchy, V.M. Kyryanchuk, A.V. Mokhnach, A.A. Rudchik, S.B. Sakuta, R. Siudak, I. Skwirczyńska, A. Szczurek, L. Zemło, Nucl. Phys. **A 724** (2003) 29.

[10] V.M. Kyryanchuk, A.T. Rudchik, A. Budzanowski, V.K. Chernievsky, T. Czosnyka, B. Czech, L. Głowacka, S. Kliczewski, E.I. Koshchy, S.Yu. Mezhevych, A.V. Mokhnach, K. Rusek, S.B. Sakuta, R. Siudak, I. Skwirczyńska, A. Szczurek, L. Zemło, Nucl. Phys. **A 726** (2003) 231.

[11] A.A. Rudchik, A.T. Rudchik, A. Budzanowski, A. Szczurek, B. Czech, T. Czosnyka, J. Choiński, L. Głowacka, S. Kliczewski, E.J. Koshchy, S.Yu. Mezhevych, A.V. Mokhnach, O.A. Momotyuk, V.M. Pirnak, R. Siudak, I. Skwirczyńska, Eur. Phys. J. **A 23** (2005) 445.

[12] S.Yu. Mezhevych, A.T. Rudchik, K. Rusek, A. Budzanowski, B. Czech, T. Choiński, L. Głowacka, S. Kliczewski, E.J. Koshchy, V.M. Kiryanchuk, A.V. Mokhnach, A.A. Rudchik, S.B. Sakuta, R. Siudak, I. Skwirczyńska, A. Szczurek, Nucl. Phys. **A 753** (2005) 13

[13] A.A. Rudchik, A.T. Rudchik, G.M. Kozeratska, O.A. Ponkratenko, E.I. Koshchy, A. Budzanowski, B. Czech, S. Kliczewski, R. Siudak, I. Skwirczyńska, A.

Szczurek, S.Yu. Mezhevych, K.W. Kemper, J. Choiński, T. Czosnyka and L. Głowacka, Phys. Rev. **C 72** (2005) 034608.
[14] S.B. Sakuta, Yu.A Glukhov, A.T. Rudchik, V.M. Pirnak, V.A. Ziman, A. Budzanowski, S. Kliczewski, R. Siudak, I. Skwirczyńska and A. Szczurek, Nucl. Phys. **A 773** (2006) 187.
[15] A.T. Rudchik, V.O. Romanyshyn, E.I. Koshchy, A. Budzanowski, K.W. Kemper, K. Rusek, V.D. Chesnokova, T. Choiński, B. Czech, L. Głowacka, S. Kliczewski, V.M. Kyryanchuk, S.Yu. Mezhevych, O.A. Mokhnach, O.A. Momotyuk, O.A. Ponkratenko, R. Siudak, I. Skwirczyńska, A. Szczurek, Eur. Phys. J. **A 33** (2007) 325.
[16] A.A. Rudchik, A.T. Rudchik, S. Kliczewski, E.I. Koshchy, O.A. Ponkratenko, K.W. Kemper, K. Rusek, A.Budzanowski, T. Czosnyka, V.D. Chesnokova, B. Czech, L. Głowacka, E. Kozik, V.M. Kyryanchuk, S.Yu. Mezhevych, A.V. Mokhnach, I. Skwirczyńska, R. Siudak, A. Szczurek, Nucl. Phys. **A 785** (2007) 293.
[17] V.K. Chernievsky, K. Rusek, A. Budzanowski, A.T. Rudchik, J. Dworski, L. Zemło, V.M. Kyryanchuk, S. Kliczewski, E.I. Koshchy, S.Yu. Mezhevych, W. Mielczarek, I. Skwirczyńska, R. Siudak, B. Czech, Scientific papers of the Institute for Nuclear Research. – Kyiv. – 2002 – **2(8) -** p. 216.
[18] V.M. Kyryanchuk, A.T. Rudchik, A. Budzanowski, B. Czech, T. Czosnyka L. Głowacka, S. Kliczewski, E.I. Koshchy, S.Yu. Mezhevych, O.A. Momotyuk, G.W. Mokhnach, K. Rusek, S.B. Sakuta, R. Siudak, I. Skwirczyńska, A. Szczurek, Scientific papers of the Institute for Nuclear Research. – Kyiv. – 2004 – **1(12) -** p. 16.
[19] V.M. Kyryanchuk, A.T. Rudchik, A. Budzanowski, B. Czech, T. Czosnyka L. Głowacka, S. Kliczewski, E.I. Koshchy, S.Yu. Mezhevych, G.W. Mokhnach, K. Rusek, S.B. Sakuta, R. Siudak, I. Skwirczyńska, A. Szczurek, Scientific papers of the Institute for Nuclear Research. – Kyiv. – 2004 – **2(13) -** p. 7.
[20] A.T. Rudchik, K.W. Kemper, A.A. Rudchik, A.M. Crisp, V.D. Chesnokova, V.M. Kyryanchuk, F. Marechal, O.A. Momotyuk, O.A. Ponkratenko, B.T. Roeder and K. Rusek, Phys. Rev. **C 75** (2007) 024612.
[21] B. Jonson, Phys. Rep. **389** (2004) 1.
[22] H.J. Kluge, Nucl. Phys. **A 701** (2002) 495c.
[23] Z. Janas, Post. Fiz. **57** (2206) 174. (in polish)
[24] A. Ozawa et al., Nucl. Phys. **A 693** (2002) 32.
[25] P. Egelhof, Prog. Part. Nucl. Phys. **46** (2001) 397.
[26] P.G. Hansen et al., Nucl. Phys. **A 693** (2001) 133.
[27] V.Z. Goldberg et al., Yad. Fiz. **56** (1993) 31 [Phys. At. Nucl. **56** (1993) 17].
[28] R.B. Wiringa et al., Phys. Rev. **C 62** (2000) 014001.
[29] A. Dote et al., Phys. Rev. **C 56** (1997) 1844.
[30] B.J. Greenhalgh et al., Phys. Rev. **C 66** (2002) 027302.
[31] J. Dobaczewski et al., Phys. Rev. **C 53** (1996) 2809.
[32] T. Motobayashi et al., , Phys. Lett. **B 346** (1995) 9.
[33] T. Otsuka et al., Prog. Part. Nucl. Phys. **47** (2001) 319.
[34] A. Ozawa et al., Phys. Rev. Lett. **84** (2000) 5493.
[35] T. Otsuka et al., Phys. Rev. Lett. **87** (2001) 082502.

[36] R. Kanungo et al., Phys. Lett. **B 528** (2002) 58.
[37] G. Audi et al., Nucl. Phys. **A 624** (1997) 1.
[38] M.J.G. Borge et al., Z. Phys. **A 340** (1991) 255.
[39] E.M. Burbridge et al., Rev. Mod. Phys. **29** (1957) 547.
[40] R. Harkewicz et al., Phys. Rev. **C 44** (1991) 2365.
[41] G. Raimann et al., Phys. Rev. **C 53** (1996) 453.
[42] K.W. Scheller et al., Nucl. Phys. **A 582** (1995) 109.
[43] A. Ozawa et al., Nucl. Phys. **A 592** (1995) 244.
[44] K. Yoneda et al., Phys. Rev. **C 67** (2003) 014316.
[45] S. Kubono, Nucl. Phys. **A 693** (2001) 221.
[46] T. Motobayashi, Nucl. Phys. **A 693** (2001) 258.
[47] A. M. Mukhamedzhanov et al., Phys. Rev. **C 56** (1997) 1302.
[48] Xiaodong Tang et al., Phys. Rev. **C 67** (2003) 015804.
[49] H.M. Xu et al., Phys. Rev. Lett. **73** (1994) 2027.
[50] Z.R. Iwinski et al., Phys. Rev. **C 29** (1984) 349.
[51] L.D. Blokhintsev et al., Phys. Rev. **C 48** (1993) 2390.
[52] A. M. Mukhamedzhanov et al., Phys. Rev. **C 51** (1995) 3472.
[53] C.A. Gagliardi et al., Nucl. Phys. **A 588** (1995) 327c.
[54] P.D. Kunz, Computer code CHUCK,
available at: http://spot.colorado.edu/~kunz/DWBA.html.
[55] D. Habs et al., Hyperfine Interactions **129** (2000) 43.
[56] M. Lewitowicz, Nucl. Phys. **A 746** (2004) 118c.
[57] G D Alton et al., J. Phys. **G 24** (1998) 1347.
[58] O. Kester et al., Nucl. Instr. Meth. **B 204** (2003) 20.
[59] H. Geissel et al., Nucl. Instr. Meth. **B 70** (1992) 286.
[60] Alex C. Mueller et al., Nucl. Instr. Meth. **B 56/57** (1991) 559.
[61] I. Tanihata et al., Phys. Rev. Lett. **55** (1985) 2676.
[62] Michiharu Wada, Nucl.Instr.Meth. **A 532** (2004) 40.
[63] D.J. Morrissey et al., Nucl. Instr. Meth. **B204** (2003) 90.
[64] A.G. Artukh et al., Nucl. Instr. Meth. **B 204** (2003) 159.
[65] A.G. Artukh et al., Nucl. Instr. Meth. **A 426** (1999) 605.
[66] A. Azhari et al., Phys. Rev. Lett. **82** (1999) 3960.
[67] S. Barua et al., Nucl. Phys. **A 746** (2004) 467c.
[68] G. Tabacaru et al., Phys. Rev. **C 73** (2006) 025808.
[69] K. Perajarvi et al., Phys. Rev. **C 74** (2006) 024306.
[70] E. Lienard et al., Phys. Rev. **C 54** (1996) 2477.
[71] J.F. Liang et al., Phys. Lett. **B 491** (2000) 23.
[72] D. Gupta et al., Nucl. Phys. **A 646** (1999) 161.
[73] L. Trache et al., Phys. Rev. **C 61** (2000) 024612,
[74] Ian J. Thompson, Comp. Phys. Rep. **7** (1988) 167,
available at: http://www.fresco.org.uk/
[75] P.E. Hodgson, The Nucleon Optical Model, World Scientific,
Singapore, New Jersey, London, Hong Kong, 1994,
[76] Ian J. Thompson, Nuclear Reactions for Astrophysics,
Cambridge University Press, Cambridge 2009,
[77] N. Austern, Direct Nuclear Reaction Theories, Wiley Interscience,

New York, 1970,
[78] P. Froebrich and R. Lipperheide, Theory of Nuclear Reactions, Clarendon Press, Oxford, (1996).
[79] G.R. Satchler, Direct Nuclear Reactions, Clarendon Press, Oxford, (1983).
[80] N.K. Glendenning, Direct Nuclear Reactions, Academic Press, New York, (1983), World Scientific Publishing Co. Pte. Ltd., (2004).
[81] B.S. Nilsson, SPI-GENOA: an Optical Model Search Code.,The Niels Bohr Institute Report, (1976).
[82] N. Austern et al., Phys.Rev. **B133** (1964) 3.
[83] T. Tamura, Rev. Mod. Phys. **37** (1965) 679.
[84] T. Tamura et al., Phys. Rep. **65** (1980) 345.
[85] A. Bohr, B.R. Mottelson, Nuclear structure. Vol. **2**. Nuclear deformations., W. A. Benjamin Inc., New York, (1974).
[86] A. G. Sitenko, V. K. Tartakovskii, Theory of Nuclear Structure and Nuclear Interaction, Kluwer Academic Publishers Group (Netherlands), (1997).
[87] F. Videbaek et al., Nucl. Phys. **A 256** (1976) 301.
[88] A.T. Rudchik, Yu.M. Tchuvilsky, A code DESNA, The Kiev Institute for Nuclear Research, Report KIYAI-**82-12**, (1982).
[89] A.T. Rudchik, Yu.M. Tchuvilsky, Calculation of the Clebsch-Gordan and Racah coefficients (SU(3) group), The Kiev Institute for Nuclear Research, Report KIYAI-**82-11**, (1982).
[90] A.T. Rudchik, Yu.M. Tchuvilsky, Ukr. Fiz. Zh. **30** (1985) 819.
[91] Yu.F. Smirnov, Yu.M. Tchuvilsky, Phys. Rev. **C 15** (1977) 84.
[92] O.F. Nemets, V.G. Neudatchin, A.T. Rudchik, Yu.F. Smirnov, Yu.M. Tchuvilsky, The nucleon associations in atomic nuclei and multi-nucleon transfer reactions, Naukova Dumka, Kyiv, (1988).
[93] V.G. Neudatchin, Yu.F. Smirnov, The nucleon associations in light nuclei, Nauka, Moscow, (1969).
[94] D.A. Varshalovich, A.N. Moskalev, V.K. Khersonskii, Quantum theory of angular momentum, World Scientific, Singapore, (1988).
[95] A.T. Rudchik, The multi-nucleon transfer reactions in deuteron-light nuclei interactions, Thesis, Kyiv, (1983).
[96] I.S. Guseva, Yu.F. Smirnov, V.N. Tolstoi, Yu.I. Kharitonov, The Clebsch-Gordan coefficients of SU(3) group, Leningrad Institute for Nuclear Research, Report Nr **678**, (1981).
[97] D. Chlebowska, $< p^n \mid p^{n-3}, p^3 >$ fractional parentage coefficients. Institute of Nuclear Research Report; No. **449/VII**, Warsaw, (1963), p. 77c.
[98] A.N. Boyarkina, Structure of 1p-Shell Nuclei, Moscow State University, (1973).
[99] M. Kowalczyk, SMAN: The multi-parameter data acquisition system in the CAMAC standard, Warsaw University, (1997).
[100] PEAKFIT Program Code, http://www.scientific-solutions.ch/tech/peakfit/index.html
[101] A.A. Rudchik et al., Scientific papers of the Institute for Nuclear Research. – Kyiv. – 2005 – **3(16)** - p. 9.
[102] K.A. Weber et al., Nucl. Phys. **A 186** (1972) 145.
[103] A. Etchegoyen et al., Phys. Rev. **C 38** (1988) 2124.

[104] G.T.A. Squier et al., Nucl. Phys. **A 119** (1968) 369.

[105] H. Stocker et al., Phys. Rev. **C 9** (1974) 102.

[106] B. Vaucher et al., Helv. Phys. Acta **43** (1970) 237.

[107] R. de Swiniarski et al., Helv. Phys. Acta **49** (1976) 227.

[108] J. Cook et al., Nucl. Phys. **A466** (1987) 168.

[109] J. Cook et al., Phys. Rev. **C 35** (1987) 126.

[110] W. Sciania et al., Nucl. Phys. **A 620** (1997) 91.

[111] L.F. Canto et al., Phys. Rev. Lett. **51** (1983) 95.

[112] J.E. Poling et al., Phys. Rev. **C 5** (1972) 1819.

[113] K.A. Weber et al., Nucl. Phys. **A 186** (1972) 145

[114] J. Cook et al., Phys. Rev. **C 33** (1986) 915.

[115] Yu.A. Glukhov et al., Yad. Fiz. (Sov. J. Nucl. Phys.) **34** (1981) 312.

[116] M.F. Vineyard et al., Phys. Rev. **C 30** (1984) 916.

[117] J. Cook, Nucl. Phys. **A 445** (1985) 350.

[118] J. Carter et al., Nucl. Phys. **A 591** (1985) 349.

[119] D.E. Trcka et al., Phys. Rev. **C 41** (1990) 2134.

[120] P.L. Kerr et al., Phys. Rev. **C 54** (1996) 1267.

[121] F. Brau et al., Phys. Rev. **C 57** (1998) 1386.

[122] A.S.B. Tariq et al., Phys. Rev. **C 59** (1999) 2558.

[123] M.E. Cobern et al., Phys. Rev. **C 14** (1976) 491.

[124] H. Kumpf et al., Yad. Fiz. (Sov. J. Nucl. Phys.) **25** (1977) 481.

[125] K.O. Groeneveld et al., Phys. Rev. Lett. **27** (1971) 1806.

[126] P.D. Kunz, Computer code DWUCK4,
available at http://spot.colorado.edu/~kunz/DWBA.html.

[127] H. Kumpf et al., Yad. Fiz. (J. Nucl. Phys.) **25** (1977) 481.

[128] K.O. Groeneveld et al., Phys. Rev. Lett. **27** (1971) 1806.

[129] M.E. Cobern et al.,Phys. Rev. **C 14** (1976) 491.

[130] K. Bethge et al., Nucl. Phys. **A 123** (1969) 521.

[131] J. Orloff et al., Phys. Rev. **C 3** (1971) 430.

[132] P. Schumacher et al., Nucl. Phys. **A 212** (1973) 573.

[133] J. E. Poling et al., Phys. Rev. **C 13** (1976) 648.

[134] J. Cook et al., Phys. Rev. **C 30** (1984) 1538.

[135] K. W. Kemper et al., Phys.Rev. **C 38** (1988) 2664.

[136] J. Cook et al., Phys. Rev. **C 35** (1987) 126.

[137] Md.A. Rahman et al., Phys. Rev. **C 44** (1991) 2484.

[138] P. Grabmayr et al., Nucl. Phys. **A 350** (1980) 167.

[139] D.T. Khoa, Phys. Rev. **C 68** (2003) 011601.

[140] E. Khan et al., Phys. Lett. **B 490** (2000) 45.

[141] J.L. Escudie et al., Phys. Rev. **C 10** (1974) 1645.

[142] H.F. Lutz et al., Nucl. Phys. **81** (1966) 423.

[143] H. Essel et al., Phys. Rev. **C 19** (1979) 2224.

[144] A. Christy et al., Data Tables **A 11** (1972) 281.

[145] K.E. Rehm et al., Phys. Rev. **C 26** (1982) 1010.

[146] K. Rusek et al., Phys. Rev. **C 70** (2004) 014603.

[147] R. Kakuee et al., Nucl. Phys. **A 728** (2003) 339.

[148] H.G. Bingham et al., Nucl. Phys. **A 173** (1971) 265.

[149] L.M. Comer et al., Phys. Rev. **C 45** (1992) 1803.
[150] L. Fante Jr. et al., Nucl. Phys. **A 552** (1993) 82.
[151] J. Cook, Nucl. Phys. **A 375** (1982) 238.
[152] P.H. Barker et al., Nucl. Phys. **A 155** (1970) 401.
[153] E. Ungricht et al., Nucl. Phys. **A 313** (1979) 376.
[153] L. Jarczyk et al., Nucl. Phys. **A 316** (1979) 139.
[154] J.F. Mateja et al., Phys. Rev. **C 20** (1979) 176.
[155] J. Carter et al., Nucl. Phys. **A 591** (1995) 349.
[156] D.P. Stahel et al., Phys. Rev. **C 16** (1977) 1456.
[157] G.R. Satchler et al., Phys. Lett. **128B** (1983) 147.
[158] V.N. Bragin et al., Sov. J. Nucl. Phys. **31** (1980)14,
Yad. Fiz. **31** (1980) 29 .
[159] M.A. Nagarajan et al., Phys. Lett. **54** (1985) 1136.
[160] C. Mahaux et al., Nucl. Phys. **A 449** (1986) 354.
[161] I.J. Thompson et al., Nucl. Phys. **A 505** (1989) 84.
[162] N. Keeley et al., Nucl. Phys. **A 571** (1994) 326.
[163] N. Keeley et al., Phys. Rev. **C 56** (1997) 3421.
[164] A.M.M. Maciel et al., Phys. Rev. **C 59** (1999) 2103.
[165] S. Roy et al., Phys. Rev. **C 52** (1995) 1524.
[166] E. Muskat et al., Nucl. Phys. **A 581 (**1995) 42.
[167] J. Cook et al., Phys. Rev. **C 31** (1985) 1745.
[168] V. Hnizdo et al., Phys. Rev. Lett. **46** (1981) 590.
[169] W. von Oertzen et al., Phys. Lett. **26B** (1968) 291.
[170] M. Liu et al., Nucl. Phys. **A 165** (1971) 118.
[171] W. Bohne et al., Nucl. Phys. **A 222** (1974) 117.
[172] P. Dück et al., Nucl. Phys. **A 251** (1975) 344.
[173] J.F. Mateja et al., Phys. Rev. **C 25** (1982) 2963.
[174] J. Sromicki et al., Nucl. Phys. **A 406** (1983) 390.
[175] L. Jarczyk et al., Phys. Rev. **C 31** (1985) 12.
[176] J.F. Mateja et al., Phys. Rev. **C 31** (1985) 867.
[177] J.F. Mateja et al., Phys. Rev. **C 33** (1986) 1307.
[178] S. Albergo et al., Phys. Rev. **C 43** (1991) 2704.
[179] L. Jarczyk et al., Nucl. Phys. **A 518** (1990) 583.
[180] Y. Kudo et al., Prog. Theor. Phys. **59** (1978) 101.
[181] J. Specht et al., Nucl. Phys. **A 171** (1971) 65.
[182] K.P. Artemov et al., Yad. Fiz. **9** (1969) 266,
Sov. J. Nucl. Phys. **9** (1969) 157.
[183] N.N. Pavlova et al., Yad. Fiz. **23** (1976) 252,
Sov. J. Nucl. Phys. **23** (1976) 131.
[184] G.S. Blanpied, et al., Phys. Rev. **C 18** (1978) 1436.
[185] J.H. Mitchell et al., Phys. Rev. **C 37** (1988) 710.
[186] P.J. Simmonds et al., Nucl. Phys. **A 482** (1988) 653.
[187] Y. Kanada-Enyo et al., Phys. Rev. **C 55** (1997) 2860.
[188] M. Milin et al., Eur. Phys. J. **A 14** (2002) 295.
[189] N. Itagaki et al., Phys. Rev. Lett. **92** (2004) 142501.
[190] W. von Oertzen et al., Eur. Phys. J. **A 21** (2004) 193.

[191] G. Murillo et al., Nucl. Phys. **A 579** (1994) 125.
[192] R.J. Peterson et al., Nucl. Phys. **A 425** (1984) 469.
[193] V. Burjan et al., Z. Phys. **A 354** (1996) 163.
[194] N. Keeley et al., Phys. Rev. **C 66** (2002) 027603.
[195] Z.H. Liu et al., Phys. Rev. **C 68** (2003) 024305.
[196] E.K. Warburton et al., Phys. Rev. **C 22** (1980) 2330.
[197] N. Vinh Mau, Nucl. Phys. **A 592** (1995) 33.
[198] S.Yu. Mezhevych et al., Acta Phys. Pol. **B 34** (2003) 2415.
[199] J.H. Dave et al., Phys. Rev. **C 28** (1983) 2212.
[200] Z.H. Liu et al., Phys. Rev. **C 64** (2001) 034312.
[201] H. –D. Helb et al., Phys. Rev. Lett. **23** (1969) 176.
[202] W. von Oertzen et al., Nucl. Phys. **A 143** (1970) 34.
[203] W. von Oertzen et al., Phys. Lett. **34 B** (1971) 51.
[204] I. Kohno et al., Phys. Soc. Japan. **30** (1971) 910.
[205] R.M. de Vries et al., Phys. Rev. Lett. **32** (1974) 680.
[206] K.G. Nair et al., Phys. Rev. Lett. **23** (1969) 176.
[207] K.G. Nair et al., Phys. Rev. **C 12** (1975) 838.
[208] J.S. Eck et al., Phys. Rev. Lett. **35** (1975) 1973.
[209] P.J. Moffa et al., Phys. Rev. Lett. **35** (1975) 992.
[210] C.W. Towsley et al. Phys. Rev. **C 15** (1977) 281.
[211] T. Motobayashi et al., Nucl. Phys. **A 331** (1979) 193.
[212] J. Gomez del Campo et al., Phys. Rev. **C 19** (1979) 2170.
[213] K.R. Cordell et al., Phys. Rev. **C 23** (1981) 2035.
[214] K.P. Artemov et al., Yad. Fiz. **48** (1988) 1228.
[215] M.E. Brandan et al., Phys. Rev. **C 42** (1990) 2236.
[216] A.T. Rudchik et al., Nucl. Phys. **A 589** (1995) 535.
[217] J. Specht et al., Nucl. Phys. **A 171** (1971) 65.
[218] R.J. Peterson et al., Z. Phys. **A 305** (1982) 275.
[219] C. Mahaux et al., Phys. **A 449** (1986) 354.
[220] A.T. Rudchik, a code PARE, unpublished.
[221] O.A. Momotyuk et al., Phys. Lett. **B 640** (2006) 13.
[222] P.H. Barker et al., Nucl. Phys. **A 155** 1970 401.
[223] L. Fante Jr. et al., Nucl. Phys. **A 552** (1993) 82.
[224] L.M. Comer et al., Phys. Rev. **C 45** (1992) 1803M.
[225] A.M. Mukhamedzhanov et al., Phys. Rev. **C 56** (1997) 1302.
[226] A.D. Flawley et al., Phys. Rev. **C 19** (1979) 2215.
[227] V.I. Chuev et al., Phys. Lett. **B 31** (1970) 624,
[228] V.I. Chuev et al., J. Phys (Paris) **C32** (1971) 6,
[229] H.H. Duhm et al., **B 33** (1972) 306,
[230] C. Gaarde et al., Nucl. Phys. **A 221** (1974) 238,
[231] H.H. Duhm et al., Phys. Lett. **B 48** (1974) 1,
[232] C. Gaarde et al., Nucl. Phys. **A 222** (1974) 579,
[233] C. Gaarde et al., Phys. Lett. **B 51** (1974) 451,
[234] G. Ciangaru et al., Nucl. Phys. **A 380** (1980) 147,
[235] W.R. Wharton et al., Phys. Rev. **C 22** (1980) 1138,
[236] Yu.A. Glukhov et al., Yad. Fizika, **40** (1984) 62,

[237] J.S. Winfield et al., Phys. Rev. **C 35** (1987) 1734,
[238] A.S. Demyanova et al., Nucl. Phys. **A 501** (1989) 336,
[239] J. Cook et al., Nucl. Phys. **A 388** (1982) 173,
[240] S. Rakers et al., Phys. Rev. **C 65** (2002) 044323;
[241] S.B. Sakuta et al., Nucl. Phys. **A 587** (1995) 355,
[242] J. Bang et al., Nucl. Phys. **A 429** (1984) 330,
[243] A.F. Zeller et al., Phys. Rev. **C 22** (1980) 134,
[244] J. Cook et al., Phys. Rev. **C 33** (1986) 915,
[245] S. Nakayama et al., Nucl. Phys. **A 507** (1990) 515,
[246] K. Katory et al., Nucl. Phys. **A 480** (1988) 323,
[247] S. Nakayama et al., Phys. Lett. **B 246** (1990) 342,
[248] T. Tanabe et al., Nucl. Phys. **A 311** (1978) 38,
[249] G. Dietl et al., Nucl. Phys. **A 250** (1975) 322,
[250] W.W. True, Phys. Rev. **130** (1963) 1530,
[251] G. Pollarolo et al., Nucl. Phys. **A 406** (1983) 369,
[252] M. Lassaut, Phys. Lett. **B 105** (1981) 252,
[253] F. Michel et al., Phys. Lett. **B 82** (1979) 183,
[254] H.P. Gubler et al., Nucl. Phys. **A 351** (1981) 29,
[255] A.M. Kobos et al., Nucl. Phys. **A 427** (1984) 589,
[256] G.R. Satchler, Phys. Rep. **199** (1991) 147,
[257] J.M. Figueira et al., Phys. Rev. **C 73** (2006) 054603,
[258] A. Pakou et al., Phys. Rev. **C 69** (2004) 054602,
[259] J.O. Fernandez Niello et al., Nucl. Phys. **A 787** (2007) 484c,
[260] M. Avrigeanu et al., Nucl. Phys. **A 759** (2005) 327,
[261] J. Lubian et al., Nucl. Phys. **A 791** (2007) 24,
[262] D.R. Tilley et al., Nucl. Phys. **A 745** (2004) 155,
[263] N. Keeley et al, Prog. Part. Nucl. Phys. **59** (2007) 579,
[264] Yu.A. Lurie et al.,Ann. Phys. **312** (2004) 284,
[265] G. Kim et al., Nucl. Phys. **A 679** (2001) 304,
[266] A. Diaz Torres et al., Nucl. Phys. **A 679** (2001) 410,
[267] G.G. Adamian et al., Nucl. Phys. **A 646** (1999) 29,
[268] B. Shorto et al., Phys. Rev. **C 78** (2008) 064610,
[269] S. Barua et al. Phys. Rev. **C 72** (2005) 044602,
[270] N. Alamanos et al., Phys. Rev. **C 65** (2002) 054606,
[271] N. Keeley et al., Phys. Rev. **C 64** (2001) 031602,

APPENDIX

The spectroscopic amplitudes S_x of x-clusters in the $A = C + x$ systems.

The spectroscopic amplitudes needed for the CRC calculations were obtained within Translationary Invariant Shell Model (TISM) [22] using a code DESNA [23,24] and Boyarkina's wave function tables [25]. Spectroscopic amplitudes S_x of x-clusters (or nucleons) in the $A = C + x$ systems are given here in Appendix. Here the nL_j are the quantum numbers of the wave function for the relative motion of the cluster x and the core C in the $A = C + x$ system.

A	C	x	nL_j	S_x	Ref.
He					
^{4}He	^{3}H	p	$1S_{1/2}$	1.414	[20]
^{5}He	^{3}H	d	$1P_{1}$	0.456	[20]
			$1P_{2}$	1.021	[20]
^{6}He	^{3}H	t	$2S_{1/2}$	−1.333	[20]
^{6}He	^{5}He	n	$1P_{3/2}$	1.437	[2]
Li					
^{6}Li	^{3}H	^{3}He	$2S_{1/2}$	0.943	[20]
^{6}Li	^{5}He	p	$1P_{1/2}$	0.572	[2]
			$1P_{3/2}$	−0.722	[2]
^{7}Li	^{3}H	α	$2P_{1}$	1.091	[20]
^{7}Li	^{4}He	t	$2P_{3/2}$	−1.091	[20]
^{7}Li	^{5}He	d	$2S_{1}$	−0.674	[20]
			$1D_{1}$	−1.205	[20]
			$1D_{3}$	0.676	[20]
^{7}Li	^{6}He	p	$1P_{3/2}$	0.805	[2, 7, 13, 15, 16, 20]
$^{7}\text{Li}^{*}_{0.478}$	^{6}He	p	$1P_{1/2}$	0.805	[13, 20]
^{7}Li	^{6}Li	n	$1P_{1/2}$	−0.657	[7, 13, 14, 15, 16, 20]
			$1P_{3/2}$	−0.735	[7, 13, 14, 15, 16, 20]
$^{7}\text{Li}^{*}_{0.478}$	^{6}Li	n	$1P_{1/2}$	0.329	[20]
			$1P_{3/2}$	0.930	[20]
^{7}Li	$^{6}\text{Li}^{*}_{2.18}$	n	$1P_{3/2}$	0.738	[14]
^{8}Li	^{5}He	t	$2P_{1/2}$	−0.427	[19]
			$1F_{5/2}$	−0.581	[19]
			$1F_{7/2}$	0.570	[19]
^{8}Li	^{6}He	d	$1D_{1/2}$	0.149	[19]
^{8}Li	^{7}Li	n	$1P_{1/2}$	0.478	[7, 13, 15, 16, 19, 20]
^{8}Li	$^{7}\text{Li}^{*}_{0.478}$	n	$1P_{3/2}$	0.478	[20]
Be					
^{7}Be	^{6}Li	p	$1P_{1/2}$	−0.657	[14]
			$1P_{3/2}$	−0.735	[14]
^{7}Be	$^{6}\text{Li}^{*}_{2.18}$	p	$1P_{3/2}$	0.738	[14]
$^{7}\text{Be}^{*}_{0.43}$	^{6}Li	p	$1P_{1/2}$	0.329	[14]
			$1P_{3/2}$	0.930	[14]
^{8}Be	α	α	$3S_{0}$	1.225	[18]
^{8}Be	^{5}He	^{3}He	$2P_{3/2}$	1.102	[18]

^{8}Be	^{6}Li	d	2S$_{1}$	1.217	[18]
^{8}Be	^{7}Li	p	1P$_{3/2}$	1.234	[7, 11, 13, 14, 15, 16, 18, 20]
^{8}Be	^{7}Li$^{*}_{0.478}$	p	1P$_{1/2}$	0.873	[13, 20]
^{8}Be	^{7}Be	n	1P$_{3/2}$	−1.234	[3, 14, 18]
^{8}Be	^{7}Be$^{*}_{0.43}$	n	1P$_{1/2}$	−0.873	[14]
^{8}Be$^{*}_{2.94}$	^{7}Li	p	1P$_{1/2}$	−0.730	[14]
			1P$_{3/2}$	−0.730	[14]
^{8}Be$^{*}_{2.94}$	^{7}Be	n	1P$_{1/2}$	0.730	[14]
			1P$_{3/2}$	0.730	[14]
^{8}Be$^{*}_{2.94}$	^{7}Be$^{*}_{0.43}$	n	1P$_{3/2}$	−0.730	[14]
^{9}Be	α	^{5}He	3S$_{3/2}$	0.810	[18]
			2D$_{3/2}$	0.536	[18]
^{9}Be	^{5}He	α	3S$_{0}$	−0.810	[19]
			2P$_{3/2}$	0.194	[19]
^{9}Be	^{6}He	^{3}He	2P$_{3/2}$	−0.236	[10, 19]
^{9}Be	^{6}Li	t	2P$_{1/2}$	−0.192	[10, 18]
			2P$_{3/2}$	−0.215	[10, 18]
^{9}Be	^{7}Li	d	2S$_{1}$	−0.226	[7, 8, 10, 13, 15, 18, 19, 20]
			1D$_{1}$	0.111	[7, 8, 10, 13, 15, 18, 19, 20]
			1D$_{3}$	−0.624	[7, 8, 10, 13, 15, 19, 20]
^{9}Be	^{8}Li	p	1P$_{1/2}$	−0.162	[18]
			1P$_{3/2}$	−0.324	[18]
^{9}Be	^{8}Li$^{*}_{0.981}$	p	1P$_{1/2}$	0.362	[19]
			1P$_{3/2}$	0.648	[19]
^{9}Be	^{8}Li$^{*}_{2.261}$	p	1P$_{1/2}$	−0.628	[19]
^{9}Be	^{8}Li$^{*}_{3.210}$	p	1P$_{1/2}$	−0.362	[19]
			1P$_{3/2}$	0.648	[19]
^{9}Be	^{8}Li$^{*}_{5.4}$	p	1P$_{1/2}$	−0.375	[19]
^{9}Be	^{7}Be	2n	2S$_{1}$	0.247	[18]
			1D$_{1}$	−0.122	[18]
			1D$_{3}$	0.683	[18]
^{9}Be	^{8}Be	n	1P$_{3/2}$	0.866	[3, 4, 5, 8, 10, 11, 18, 19]
^{9}Be	^{8}Be$^{*}_{2.94}$	n	1P$_{1/2}$	−0.573	[3, 18]
			1P$_{3/2}$	0.573	[3, 18]
^{10}Be	^{6}He	α	2S$_{1}$	−0.802	[10]
^{10}Be	^{7}Li	t	2P$_{3/2}$	0.392	[7, 10, 13, 20]
^{10}Be	^{8}Li	d	1D$_{2}$	0.646	[10, 19]
^{10}Be	^{9}Li	p	1P$_{3/2}$	−1.217	[10]
^{10}Be	^{8}Be	2n	2S$_{0}$	−0.833	[3, 10]
^{10}Be	^{9}Be	n	1P$_{3/2}$	1.406	[3, 4, 5, 8, 10, 18, 19]
^{10}Be$^{*}_{3.368}$	^{8}Li	d	2S$_{1}$	−0.722	[10]
			1D$_{1}$	0.065	[10]
			1D$_{3}$	−0.242	[10]
^{10}Be$^{*}_{3.368}$	^{9}Be	n	1P$_{1/2}$	0.968	[10]
			1P$_{3/2}$	0.968	[10]
^{11}Be	^{9}Be	2n	3P$_{1}$	0.644	[10]
^{11}Be	^{10}Be	n	2S$_{2}$	−0.606	[10]
B					
^{9}B	^{7}Li	2p	2S$_{0}$	−0.247	[15]

			$1D_2$	−0.430	[15]
^{9}B	^{8}Be	p	$1P_{3/2}$	0.866	[18]
^{10}B	^{6}Li	α	$2D_2$	−0.125	[10, 15]
^{10}B	^{7}Li	^{3}He	$1P_{3/2}$	0.419	[7, 10, 13, 15]
			$1F_{5/2}$	−0.104	[7, 10, 13, 15]
			$1F_{7/2}$	0.347	[7, 10, 13, 15]
^{10}B	^{8}Li	2p	$1D_2$	0.307	[10, 15]
^{10}B	^{8}Be	d	$1D_3$	0.811	[3, 5, 10, 11, 15, 18]
^{10}B*$_{0.718}$	^{8}Be	d	$1D_1$	0.811	[5, 10]
^{10}B*$_{2.154}$	^{8}Be	d	$2S_1$	−0.833	[5, 10]
^{10}B*$_{3.587}$	^{8}Be	d	$1D_2$	0.811	[5, 10]
^{10}B	^{9}Be	p	$1P_{3/2}$	1.185	[4, 8, 18, 19]
^{10}B*$_{0.718}$	^{9}Be	p	$1P_{1/2}$	−0.361	[5, 10]
			$1P_{3/2}$	−0.323	[5, 10]
^{10}B*$_{1.740}$	^{9}Be	p	$1P_{3/2}$	0.994	[5, 10]
^{10}B*$_{2.154}$	^{9}Be	p	$1P_{1/2}$	−0.663	[5, 10]
			$1P_{3/2}$	0.741	[5, 10]
^{10}B*$_{3.587}$	^{9}Be	p	$1P_{1/2}$	0.838	[5, 10]
^{10}B	^{9}B	n	$1P_{3/2}$	−1.185	[10, 15]
^{11}B	^{7}Li	α	$3S_0$	−0.638	[7, 8, 10, 11, 13, 15, 18, 19, 20]
			$2D_2$	−0.422	[7, 8, 10, 11, 13, 15, 18, 19, 20]
^{11}B	^{7}Li*$_{0.478}$	α	$2D_2$	−0.422	[13]
^{11}B	^{7}Li*$_{4.63}$	α	$2D_2$	0.362	[13]
			$1G_4$	0.429	[13]
^{11}B	^{7}Li*$_{6.68}$	α	$2D_2$	0.148	[13]
			$1G_4$	0.575	[13]
^{11}B	^{7}Li*$_{9.67}$	α	$2D_2$	0.362	[13]
			$1G_4$	0.429	[13]
^{11}B	^{7}Li*$_{9.85}$	α	$3S_0$	−0.638	[13]
			$2D_2$	−0.422	[13]
^{11}B*$_{2.125}$	^{7}Li	α	$2D_2$	0.596	[13]
^{11}B*$_{4.445}$	^{7}Li	α	$2D_2$	−0.049	[13]
			$1G_4$	−0.192	[13]
^{11}B*$_{5.020}$	^{7}Li	α	$3S_0$	−0.638	[13]
			$2D_2$	−0.422	[13]
^{11}B*$_{6.743}$	^{7}Li	α	$2D_2$	0.104	[13]
			$1G_4$	0.124	[13]
^{11}B*$_{6.793}$	^{7}Li	α	$2D_2$	0.596	[13]
^{11}B*$_{7.286}$	^{7}Li	α	$2D_2$	−0.049	[13]
			$1G_4$	−0.192	[13]
^{11}B	^{8}Li	^{3}He	$1P_{1/2}$	0.160	[8, 13, 18, 19]
			$1F_{5/2}$	0.218	[8, 13, 18, 19]
			$1F_{7/2}$	0.214	[8, 13, 19]
^{11}B	^{8}Li*$_{0.98}$	^{3}He	$2P_{1/2}$	0.053	[19]
			$2P_{3/2}$	−0.048	[19]
			$1F_{5/2}$	0.268	[19]

^{11}B	^{8}Li*$_{2,261}$	^{3}He	$2P_{3/2}$	0.268	[19]
			$1F_{5/2}$	0.078	[19]
			$1F_{7/2}$	0.268	[19]
^{11}B	^{8}Li*$_{3,21}$	^{3}He	$2P_{1/2}$	0.053	[19]
			$2P_{3/2}$	−0.048	[19]
			$1F_{5/2}$	0.268	[19]
^{11}B	^{8}Li*$_{5.4}$	^{3}He	$2P_{1/2}$	0.160	[19]
			$1F_{5/2}$	0.218	[19]
			$1F_{7/2}$	0.214	[19]
^{11}B	^{9}Li	2p	$2S_{0}$	0.576	[10]
			$1D_{2}$	0.456	[10]
^{11}B	^{8}Be	t	$2P_{3/2}$	0.641	[6, 8, 10, 11, 13, 18, 19]
^{11}B	^{8}Be*$_{2.94}$	t	$2P_{1/2}$	−0.424	[11, 18]
			$2P_{3/2}$	0.424	[11, 18]
			$1F_{5/2}$	0.148	[11, 18]
			$1F_{7/2}$	−0.363	[11, 18]
^{11}B	^{9}Be	d	$2S_{1}$	−0.607	[3, 4, 5, 6, 8, 9, 10, 11, 13, 18, 19]
			$1D_{1}$	−0.109	[3, 4, 5, 6, 8, 9, 10, 11, 13, 18, 19]
			$1D_{3}$	0.610	[3, 4, 5, 6, 8, 9, 10, 11, 13, 18, 19]
^{11}B*$_{2.125}$	^{9}Be	d	$2S_{1}$	−0.768	[5, 8]
			$1D_{1}$	0.172	[5, 8]
			$1D_{2}$	0.515	[5, 8]
^{11}B*$_{4.44}$	^{9}Be	d	$2S_{1}$	0.576	[8]
			$1D_{1}$	−0.064	[8]
			$1D_{2}$	0.220	[8]
			$1D_{3}$	−0.394	[8]
^{11}B*$_{5.02}$	^{9}Be	d	$2S_{1}$	−0.607	[8]
			$1D_{1}$	−0.109	[8]
			$1D_{3}$	0.610	[8]
^{11}B*$_{6.74}$	^{9}Be	d	$1D_{2}$	0.316	[8]
			$1D_{3}$	0.387	[8]
^{11}B*$_{8.56}$	^{9}Be	d	$2S_{1}$	−0.384	[8]
			$1D_{1}$	0.279	[8]
			$1D_{2}$	−0.432	[8]
			$1D_{3}$	0.241	[8]
^{11}B	^{10}Be	p	$1P_{3/2}$	0.699	[5, 6, 8, 9, 10, 11, 13, 18, 19]
			$1P_{5/2}$	−0.788	[8]
^{11}B	^{10}Be*$_{3.368}$	p	$1P_{1/2}$	−0.930	[10]
			$1P_{3/2}$	0.930	[10]
^{11}B*$_{2.125}$	^{10}Be	p	$1P_{1/2}$	0.699	[5, 13]
^{11}B	^{9}B	2n	$2S_{0}$	−0.665	[10]
			$1D_{2}$	0.421	[10]
^{11}B	^{10}B	n	$1P_{3/2}$	−1.347	[5, 6, 9, 10, 11, 13, 15, 18, 19]
^{11}B	^{10}B*$_{0.718}$	n	$1P_{1/2}$	−0.268	[5, 10]
			$1P_{3/2}$	0.240	[5, 10]
^{11}B	^{10}B*$_{1.740}$	n	$1P_{3/2}$	−0.494	[5, 10]
^{11}B	^{10}B*$_{2.154}$	n	$1P_{1/2}$	−0.571	[5, 10]
			$1P_{3/2}$	−0.638	[5, 10]

^{11}B	^{10}B*$_{3.587}$	n	$1P_{1/2}$	−0.805	[5, 10]
^{12}B	^{8}Li	α	$2D_2$	0.496	[18]
^{12}B	^{8}Li	α	$2D_2$	0.544	[19]
^{12}B	^{9}Be	t	$2P_{1/2}$	0.102	[8, 10, 18, 19]
			$2P_{3/2}$	0.091	[8, 10, 18, 19]
			$1F_{5/2}$	0.512	[8, 10, 18, 19]
^{12}B*$_{0.953}$	^{9}Be	t	$2P_{1/2}$	−0.237	[18]
			$1F_{5/2}$	−0.323	[18]
			$1F_{7/2}$	0.316	[18]
^{12}B	^{10}Be	d	$1D_1$	0.380	[10, 18]
^{12}B	^{10}Be*$_{3.368}$	d	$2S_1$	0.746	[10]
			$1D_1$	0.046	[10]
			$1D_2$	0.060	[10]
			$1D_3$	0.020	[10]
^{12}B	^{10}B	2n	$1D_2$	−0.777	[10]
^{12}B	^{11}B	n	$1P_{1/2}$	−0.734	[6, 9, 10, 11, 14, 18, 19]
			$1P_{3/2}$	0.821	[11, 14, 18, 19]
^{12}B	^{11}B*$_{2.12}$	n	$1P_{1/2}$	−0.260	[14]
			$1P_{3/2}$	0.734	[14]
^{12}B*$_{0.95}$	^{11}B	n	$1P_{1/2}$	0.330	[12, 14]
^{12}B*$_{0.95}$	^{11}B*$_{2.12}$	n	$1P_{3/2}$	0.330	[14]
^{12}B*$_{3.76}$	^{11}B	n	$1P_{1/2}$	0.330	[14]
^{12}B*$_{3.76}$	^{11}B*$_{2.12}$	n	$1P_{3/2}$	0.330	[14]
^{13}B	^{11}B	2n	$2S_0$	0.623	[12]
			$1D_2$	0.197	[12]
^{13}B	^{12}B	n	$1P_{1/2}$	−0.238	[18]
			$1P_{3/2}$	0.213	[18]
C					
^{11}C	^{7}Li	^{4}Li	$2P_1$	−0.007	[7]
			$2P_2$	0.464	[7]
			$2P_3$	0.233	[7]
			$1F_1$	−0.063	[7]
			$1F_3$	0.190	[7]
^{11}C	^{8}Be	^{3}He	$2P_{3/2}$	0.641	[11]
^{11}C	^{9}Be	2p	$2S_0$	0.665	[4, 10]
			$1D_2$	−0.421	[4, 10]
^{11}C	^{10}B	p	$1P_{3/2}$	1.347	[15, 10]
^{11}C	^{10}B*$_{0.718}$	p	$1P_{1/2}$	−0.268	[5]
			$1P_{3/2}$	0.240	[5]
^{11}C	^{10}B*$_{1.740}$	p	$1P_{3/2}$	0.494	[5]
^{11}C	^{10}B*$_{2.154}$	p	$1P_{1/2}$	−0.571	[5]
			$1P_{3/2}$	−0.638	[5]
^{11}C	^{10}B*$_{3.587}$	p	$1P_{1/2}$	−0.805	[5]
^{12}C	^{7}Li	^{5}Li	$3S_{3/2}$	−0.793	[7, 20]
			$2D_{3/2}$	−0.525	[7, 20]
^{12}C	^{8}Be	α	$3S_0$	0.821	[3, 4, 6, 11, 18, 19]
^{12}C	^{8}Be*$_{2.94}$	α	$2D_2$	−0.919	[3, 11]
^{12}C	^{9}Be	^{3}He	$2P_{3/2}$	1.224	[3, 4, 5, 6, 8, 11, 18, 19]

^{12}C	^{9}B	t	2P$_{3/2}$	−1.124	[19]
^{12}C	^{10}Be	2p	2S$_{0}$	0.800	[4, 6, 10]
^{12}C	^{10}B	d	1D$_{3}$	1.780	[3, 4, 6, 10, 11, 19]
^{12}C	^{10}B$^*_{0.718}$	d	1D$_{1}$	1.165	[5, 10]
^{12}C	^{10}B$^*_{2.154}$	d	2S$_{1}$	−1.386	[5]
^{12}C	^{10}B$^*_{3.587}$	d	1D$_{2}$	1.504	[5]
^{12}C	^{11}B	p	1P$_{3/2}$	−1.706	[4, 5, 6, 8, 9, 10, 11, 13, 14, 18, 19]
^{12}C	^{11}B$^*_{2.125}$	p	1P$_{1/2}$	−1.206	[5, 6, 13, 14]
^{12}C	^{11}B$^*_{5.021}$	p	1P$_{3/2}$	−1.706	[6, 13]
^{12}C	^{11}B$^*_{6.793}$	p	1P$_{1/2}$	−1.206	[13]
^{12}C$^*_{4.44}$	^{11}B	p	1P$_{1/2}$	−0.505	[6, 19]
			1P$_{3/2}$	−0.505	[6, 19]
^{12}C	^{11}C	n	1P$_{3/2}$	1.706	[1, 3, 4, 5, 6, 11]
^{13}C	^{7}Li	^{6}Li	3S$_{1}$	−0.124	[7]
			2D$_{1}$	−0.039	[7]
			2D$_{2}$	−0.116	[7]
^{13}C	^{9}Be	α	2D$_{2}$	0.504	[3, 4, 8, 9, 10, 18, 19]
^{13}C$^*_{3.088}$	^{9}Be	α	3P$_{1}$	0.500	[3]
^{13}C$^*_{3.684}$	^{9}Be	α	3S$_{0}$	−0.539	[3]
			2D$_{2}$	−0.356	[3]
^{13}C$^*_{3.854}$	^{9}Be	α	3P$_{1}$	−0.400	[3]
^{13}C	^{10}Be	^{3}He	2P$_{1/2}$	0.170	[9, 10]
^{13}C	^{10}B	t	1F$_{5/2}$	0.108	[9, 10]
			1F$_{7/2}$	0.747	[9, 10]
^{13}C	^{10}B$^*_{0.718}$	t	2P$_{1/2}$	−0.654	[10]
			2P$_{3/2}$	0.231	[10]
^{13}C	^{11}B	d	2S$_{1}$	−0.263	[3, 5, 6, 8, 9, 10, 11, 18, 19]
			1D$_{1}$	−0.162	[3, 5, 6, 8, 9, 10, 11, 18, 19]
			1D$_{2}$	−0.485	[3, 5, 6, 8, 9, 10, 11, 18, 19]
^{13}C	^{11}B$^*_{2.12}$	d	2S$_{1}$	0.093	[5, 9]
			1D$_{1}$	−0.457	[5, 9]
^{13}C	^{11}B$^*_{4.44}$	d	1D$_{2}$	−0.111	[9]
			1D$_{3}$	−0.417	[9]
^{13}C	^{11}B$^*_{5.02}$	d	2S$_{1}$	−0.263	[9]
			1D$_{1}$	−0.162	[9]
			1D$_{2}$	−0.485	[9]
^{13}C	^{11}B$^*_{6.74}$	d	1D$_{3}$	0.814	[9]
^{13}C	^{11}B$^*_{8.56}$	d	2S$_{1}$	−0.263	[9]
			1D$_{1}$	−0.162	[9]
			1D$_{2}$	−0.485	[9]
^{13}C$^*_{3.68}$	^{11}B	d	2S$_{1}$	−0.208	[9]
			1D$_{1}$	0.102	[9]
			1D$_{3}$	−0.573	[9]
^{13}C	^{12}B	p	1P$_{1/2}$	0.283	[9, 14]
			1P$_{3/2}$	0.801	[9, 14]
^{13}C	^{12}B$^*_{0.95}$	p	1P$_{3/2}$	−0.736	[14]
^{13}C	^{12}B$^*_{3.76}$	p	1P$_{3/2}$	−0.736	[14]

$^{13}\text{C}^{*}_{3.68}$	^{12}B	p	$1P_{1/2}$	−0.448	[14]
			$1P_{3/2}$	0.401	[14]
$^{13}\text{C}^{*}_{3.68}$	$^{12}\text{B}^{*}_{0.95}$	p	$1P_{1/2}$	−0.520	[14]
$^{13}\text{C}^{*}_{3.68}$	$^{12}\text{B}^{*}_{3.76}$	p	$1P_{1/2}$	−0.520	[14]
^{13}C	^{11}C	2n	$1D_{2}$	−0.559	[3]
^{13}C	^{12}C	n	$1P_{1/2}$	0.601	[1, 3, 4, 5, 6, 9, 11, 14, 19]
^{13}C	$^{12}\text{C}^{*}_{4.44}$	n	$1P_{3/2}$	−1.124	[1]
^{13}C	$^{12}\text{C}^{*}_{9.64}$	n	$1D_{5/2}$	0.111	[12, 197]
$^{13}\text{C}^{*}_{3.08}$	^{12}C	n	$2S_{1/2}$	0.957	[12, 197]
$^{13}\text{C}^{*}_{3.08}$	$^{12}\text{C}^{*}_{4.44}$	n	$1D_{5/2}$	0.291	[12, 197]
$^{13}\text{C}^{*}_{3.68}$	^{12}C	n	$1P_{3/2}$	0.601	[1, 3, 14]
$^{13}\text{C}^{*}_{3.68}$	$^{12}\text{C}^{*}_{4.44}$	n	$1P_{1/2}$	0.745	[1]
			$1P_{3/2}$	−0.745	[1]
$^{13}\text{C}^{*}_{3.85}$	^{12}C	n	$1D_{5/2}$	0.550	[3]
^{14}C	^{10}Be	α	$3S_{0}$	−0.566	[10]
^{14}C	^{11}B	t	$2P_{3/2}$	−0.368	[9, 10, 18]
^{14}C	^{12}B	d	$1D_{1}$	−1.01	[18]
^{14}C	^{12}C	2n	$2S_{0}$	0.615	[3, 12]
$^{14}\text{C}^{*}_{7.01}$	^{12}C	2n	$1D_{2}$	0.300	[12]
$^{14}\text{C}^{*}_{8.32}$	^{12}C	2n	$2D_{2}$	0.300	[12]
^{14}C	^{13}C	n	$1P_{1/2}$	−1.094	[3, 9]
^{14}C	$^{13}\text{C}^{*}_{3.68}$	n	$1P_{3/2}$	−1.024	[2]
$^{14}\text{C}^{*}_{6.09}$	^{13}C	n	$2S_{1/2}$	−0.994	[12, 250]
			$1D_{3/2}$	0.105	[12, 250]
N					
^{13}N	^{7}Li	^{6}Be	$2D_{2}$	0.134	[7]
^{13}N	^{11}B	2p	$1D_{2}$	0.559	[6]
^{13}N	^{12}C	p	$1P_{1/2}$	0.601	[1, 6, 11]
^{13}N	$^{12}\text{C}^{*}_{4.44}$	p	$1P_{3/2}$	−1.124	[1]
^{14}N	^{7}Li	^{7}Be	$3S_{3/2}$	−0.048	[7]
			$2D_{1/2}$	−0.050	[7]
			$2D_{3/2}$	0.097	[7]
			$2D_{5/2}$	0.062	[7]
			$1G_{5/2}$	−0.072	[7]
^{14}N	^{8}Li	^{6}Be	$2D_{2}$	−0.243	[7]
^{14}N	^{8}Be	^{6}Li	$2D_{1}$	−0.167	[7]
^{14}N	^{9}Be	^{5}Li	$3S_{3/2}$	−0.056	[7]
			$2D_{1/2}$	−0.059	[7]
			$2D_{3/2}$	−0.037	[7]
			$2D_{5/2}$	−0.089	[7]
			$1G_{5/2}$	−0.348	[7]
^{14}N	^{10}Be	^{4}Li	$2P_{1}$	0.024	[7]
			$1F_{1}$	0.219	[7]
^{14}N	^{10}B	α	$2D_{2}$	0.111	[7]
			$1G_{4}$	0.740	[7]
^{14}N	^{11}B	^{3}He	$2P_{1/2}$	−0.107	[6, 7, 9, 10, 11, 19]
			$2P_{3/2}$	−0.096	[6, 7, 9, 10, 11, 19]
			$1F_{5/2}$	−0.292	[6, 7, 9, 10, 11, 19]

^{14}N	^{11}C	t	2P$_{1/2}$	0.107	[7]
			2P$_{3/2}$	0.096	[7]
			1F$_{5/2}$	0.292	[7]
^{14}N	^{12}C	d	1D$_1$	0.246	[6, 7, 11, 19]
^{14}N	^{12}C$^*_{4.44}$	d	1D$_1$	0.515	[1]
			1D$_2$	−0.664	[1]
			1D$_3$	0.786	[1]
^{14}N$^*_{3.95}$	^{12}C	d	2S$_1$	0.615	[1]
^{14}N	^{13}C	p	1P$_{1/2}$	0.461	[7, 9]
			1P$_{3/2}$	0.163	[7, 9]
^{14}N	^{13}C$^*_{3.68}$	p	1P$_{1/2}$	0.729	[1]
			1P$_{3/2}$	−0.815	[1]
^{14}N$^*_{2.31}$	^{13}C	p	1P$_{1/2}$	−0.421	[2]
^{14}N$^*_{2.31}$	^{13}C$^*_{3.68}$	p	1P$_{3/2}$	−0.724	[2]
^{14}N$^*_{3.95}$	^{13}C	p	1P$_{1/2}$	0.186	[2]
			1P$_{3/2}$	−0.811	[2]
^{14}N$^*_{3.95}$	^{13}C$^*_{3.68}$	p	1P$_{1/2}$	0.729	[1]
			1P$_{3/2}$	−0.819	[1]
^{14}N$^*_{4.92}$	^{13}C	p	1P$_{1/2}$	0.028	[2]
^{14}N$^*_{4.92}$	^{13}C$^*_{3.68}$	p	1P$_{3/2}$	−0.012	[2]
^{14}N$^*_{5.11}$	^{13}C	p	1P$_{3/2}$	0.103	[2]
^{14}N$^*_{5.11}$	^{13}C$^*_{3.68}$	p	1P$_{1/2}$	0.369	[2]
			1P$_{3/2}$	−0.348	[2]
^{14}N$^*_{5.69}$	^{13}C	p	1P$_{1/2}$	−0.146	[2]
			1P$_{3/2}$	0.188	[2]
^{14}N$^*_{5.69}$	^{13}C$^*_{3.68}$	p	1P$_{1/2}$	0.106	[2]
			1P$_{3/2}$	0.233	[2]
^{14}N$^*_{5.83}$	^{13}C$^*_{3.68}$	p	1P$_{3/2}$	0.539	[2]
^{14}N$^*_{7.03}$	^{13}C$^*_{3.68}$	p	1P$_{1/2}$	0.369	[2]
			1P$_{3/2}$	−0.348	[2]
^{14}N$^*_{8.49}$	^{13}C$^*_{3.68}$	p	1D$_{5/2}$	1.000	[2]
^{14}N	^{13}N	n	1P$_{1/2}$	−0.461	[7]
			1P$_{3/2}$	−0.163	[7]
^{14}N$^*_{3.95}$	^{13}N	n	1P$_{1/2}$	−0.258	[1, 7]
			1P$_{3/2}$	0.729	[1, 7]
^{15}N	^{7}Li	^{8}Be	2D$_2$	0.226	[20]
^{15}N	^{11}B	α	2D$_2$	0.435	[6, 9, 11, 18, 19]
^{15}N$^*_{5.27}$	^{11}B	α	3P$_1$	−0.471	[11]
^{15}N$^*_{6.32}$	^{11}B	α	3S$_0$	−0.465	[11]
			2D$_2$	−0.308	[11]
^{15}N$^*_{7.15}$	^{11}B	α	3P$_1$	−0.471	[11]
^{15}N$^*_{7.56}$	^{11}B	α	2F$_3$	0.290	[11]
^{15}N	^{12}B	^{3}He	2P$_{1/2}$	0.254	[11, 18]
			2P$_{3/2}$	−0.090	[11, 18]
^{15}N	^{12}C	t	2P$_{1/2}$	0.380	[6, 11, 19]
^{15}N$^*_{5.27}$	^{12}C	t	1D$_{5/2}$	−0.540	[11]

$^{15}N^*_{6.32}$	^{12}C	t	$2P_{3/2}$	0.380	[11]
$^{15}N^*_{7.15}$	^{12}C	t	$1D_{5/2}$	−0.540	[11]
$^{15}N^*_{7.56}$	^{12}C	t	$1G_{7/2}$	0.258	[11]
^{15}N	^{13}C	d	$2S_1$	0.248	[7, 9, 11]
			$1D_1$	0.444	[7, 9, 11]
^{15}N	^{14}C	p	$1P_{1/2}$	−1.006	[2]
^{15}N	^{13}N	2n	$2S_0$	−0.608	[11]
^{15}N	^{14}N	n	$1P_{1/2}$	−1.091	[7, 11]
			$1P_{3/2}$	0.386	[7, 11]
^{15}N	$^{14}N^*_{2.31}$	n	$1P_{1/2}$	0.711	[2]
^{15}N	$^{14}N^*_{3.95}$	n	$1P_{1/2}$	−0.599	[2]
			$1P_{3/2}$	−0.639	[2]
^{15}N	$^{14}N^*_{5.11}$	n	$1P_{3/2}$	−1.157	[2]
^{15}N	$^{14}N^*_{5.69}$	n	$1P_{1/2}$	−0.737	[2]
			$1P_{3/2}$	−0.171	[2]
^{15}N	$^{14}N^*_{7.03}$	n	$1P_{3/2}$	−1.157	[2]
$^{15}N^*_{5.27}$	^{14}C	p	$1P_{3/2}$	1.000	[2]
$^{15}N^*_{5.27}$	$^{14}N^*_{8.49}$	n	$1P_{3/2}$	1.000	[2]
$^{16}N^*_{3,355}$	^{11}B	^{5}He	$3D_{1/2}$	0.254	[18]
			$3D_{3/2}$	−0.199	[18]
$^{16}N^*_{3.355}$	^{12}B	α	$4S_0$	0.514	[18]
O					
^{15}O	^{14}N	p	$1P_{1/2}$	−1.091	[7]
			$1P_{3/2}$	0.386	[7]
^{15}O	$^{14}N^*_{3.95}$	n	$1P_{1/2}$	−0.244	[7]
			$1P_{3/2}$	−0.690	[7]
^{16}O	^{7}Li	^{9}B	$3S_{3/2}$	−0.533	[20]
			$1D_{3/2}$	−0.353	[20]
^{16}O	^{8}Be	^{8}Be	$3S_0$	0.365	[20]
^{16}O	^{11}B	^{5}Li	$3S_{3/2}$	−0.677	[20]
			$2D_{3/2}$	−0.448	[20]
^{16}O	^{12}C	α	$3S_0$	0.544	[11, 20]
^{16}O	^{13}N	t	$2P_{1/2}$	−0.910	[20]
^{16}O	^{14}N	d	$1D_1$	1.400	[20]
^{16}O	^{15}N	p	$1P_{1/2}$	−1.461	[11, 20]
^{16}O	^{15}O	n	$1P_{1/2}$	1.461	[20]
^{17}O	^{16}O	n	$1D_{5/2}$	0.500	[20]
^{18}O	^{7}Li	^{11}B	$4S_{3/2}$	−0.184	[16]
			$3D_{3/2}$	−0.121	[16]
^{18}O	^{17}N	p	$1P_{1/2}$	−1.198	[16]
^{18}O	^{16}O	2n	$3S_0$	−0.833	[16]
$^{18}O^*_{3.635}$	^{16}O	2n	$3S_0$	0.615	[16]
^{18}O	^{17}O	n	$1D_{5/2}$	0.891	[16]
^{19}O	^{18}O	n	$1D_{5/2}$	−0.155	[16]
F					
^{17}F	^{16}O	p	$1D_{5/2}$	−0.500	[20]
^{18}F	^{16}O	d	$3S_1$	1.061	[20]
^{19}F	^{16}O	t	$4S_{1/2}$	−1.091	[20]

^{19}F	^{18}O	p	$2S_{1/2}$	0.633	[16]
Ne					
^{20}Ne	^{16}O	α	$5S_0$	1.225	[20]
^{20}Ne	^{17}O	^{3}He	$3D_{5/2}$	−1.102	[20]
^{20}Ne	^{17}F	t	$3D_{5/2}$	−1.102	[20]
^{20}Ne	^{18}F	d	$3S_1$	1.217	[20]
^{20}Ne	^{19}F	p	$2S_{1/2}$	1.234	[20]